frontiers | Research Topics

Insights in brain imaging methods 2023

Edited by
Xi-Nian Zuo, Federico Giove and Vince D. Calhoun

Published in
Frontiers in Neuroscience
Frontiers in Neuroimaging

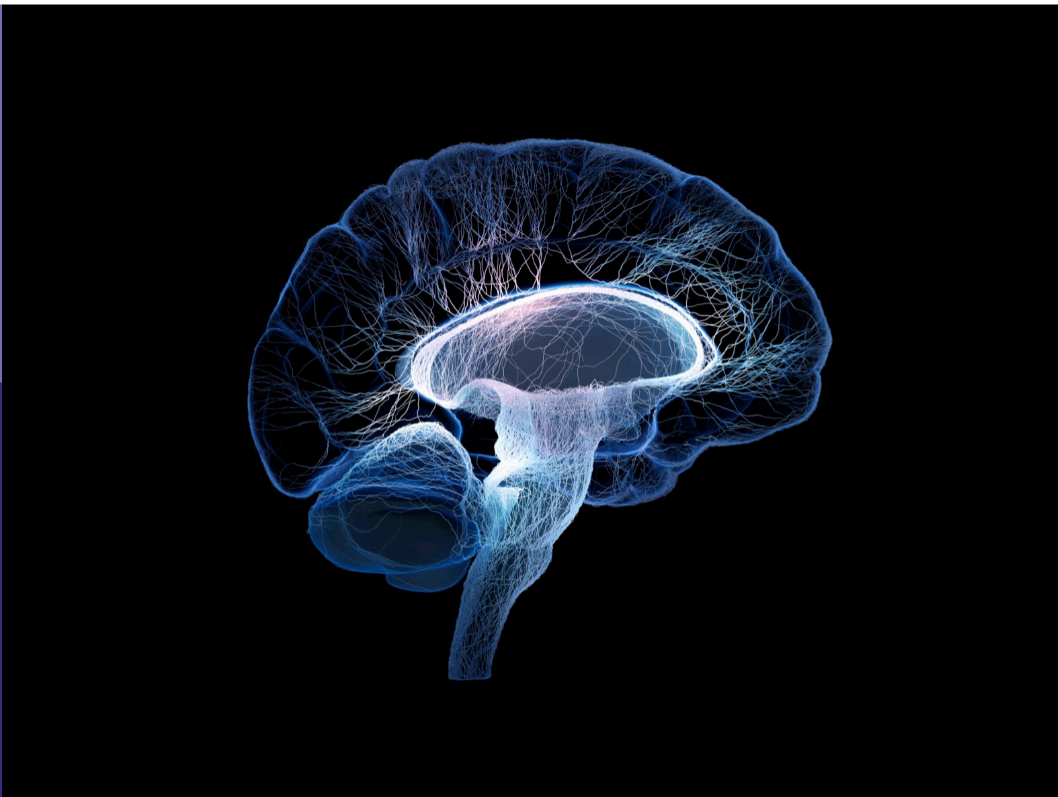

ISSN 1664-8714
ISBN 978-2-8325-5521-7
DOI 10.3389/978-2-8325-5521-7

About Frontiers

Frontiers is more than just an open access publisher of scholarly articles: it is a pioneering approach to the world of academia, radically improving the way scholarly research is managed. The grand vision of Frontiers is a world where all people have an equal opportunity to seek, share and generate knowledge. Frontiers provides immediate and permanent online open access to all its publications, but this alone is not enough to realize our grand goals.

Frontiers journal series

The Frontiers journal series is a multi-tier and interdisciplinary set of open-access, online journals, promising a paradigm shift from the current review, selection and dissemination processes in academic publishing. All Frontiers journals are driven by researchers for researchers; therefore, they constitute a service to the scholarly community. At the same time, the *Frontiers journal series* operates on a revolutionary invention, the tiered publishing system, initially addressing specific communities of scholars, and gradually climbing up to broader public understanding, thus serving the interests of the lay society, too.

Dedication to quality

Each Frontiers article is a landmark of the highest quality, thanks to genuinely collaborative interactions between authors and review editors, who include some of the world's best academicians. Research must be certified by peers before entering a stream of knowledge that may eventually reach the public - and shape society; therefore, Frontiers only applies the most rigorous and unbiased reviews. Frontiers revolutionizes research publishing by freely delivering the most outstanding research, evaluated with no bias from both the academic and social point of view. By applying the most advanced information technologies, Frontiers is catapulting scholarly publishing into a new generation.

What are Frontiers Research Topics?

Frontiers Research Topics are very popular trademarks of the *Frontiers journals series*: they are collections of at least ten articles, all centered on a particular subject. With their unique mix of varied contributions from Original Research to Review Articles, Frontiers Research Topics unify the most influential researchers, the latest key findings and historical advances in a hot research area.

Find out more on how to host your own Frontiers Research Topic or contribute to one as an author by contacting the Frontiers editorial office: frontiersin.org/about/contact

Insights in brain imaging methods: 2023

Topic editors
Xi-Nian Zuo — Beijing Normal University, China
Federico Giove — Centro Fermi - Museo storico della fisica e Centro studi e ricerche Enrico Fermi, Italy
Vince D. Calhoun — Georgia State University, United States

Citation
Zuo, X.-N., Giove, F., Calhoun, V. D., eds. (2024). *Insights in brain imaging methods: 2023*. Lausanne: Frontiers Media SA. doi: 10.3389/978-2-8325-5521-7

Table of contents

frontiers | Frontiers in Neuroscience

TYPE Editorial
PUBLISHED 23 September 2024
DOI 10.3389/fnins.2024.1488845

OPEN ACCESS

EDITED AND REVIEWED BY
Yuchuan Zhuang,
AbbVie, United States

*CORRESPONDENCE
Federico Giove
✉ federico.giove@uniroma1.it

RECEIVED 30 August 2024
ACCEPTED 09 September 2024
PUBLISHED 23 September 2024

CITATION
Giove F, Zuo X-N and Calhoun VD (2024) Editorial: Insights in brain imaging methods: 2023. *Front. Neurosci.* 18:1488845.
doi: 10.3389/fnins.2024.1488845

Editorial: Insights in brain imaging methods: 2023

Federico Giove[1,2]*, Xi-Nian Zuo[3] and Vince D. Calhoun[4]

[1]MARBILab, Museo storico della fisica e Centro studi e ricerche Enrico Fermi, Rome, Italy, [2]Neuroimaging Laboratory, Fondazione Santa Lucia IRCCS, Rome, Italy, [3]State Key Laboratory of Cognitive Neuroscience and Learning, Beijing Normal University, Beijing, China, [4]Tri-institutional Center for Translational Research in Neuroimaging and Data Science, Georgia State University, Georgia Tech, Emory, Atlanta, GA, United States

KEYWORDS

brain, imaging, neuroscience, MRI, light sheet microscopy, MEG, BCI, EEG

Editorial on the Research Topic
Insights in brain imaging methods: 2023

Brain imaging has revolutionized our understanding of the human brain, enabling the exploration of its structure and function in great detail. This history of enduring success has its roots in the continuous development of methods that merge new technologies and processing approaches. Indeed, funding bodies like the European Commission, the National Institutes of Health, and the Wellcome Trust have repeatedly included advanced neuroimaging and next-generation imaging modalities among their funding priorities to shape the future of neuroscience.

Methodological advances in brain imaging are thus at the forefront of neuroscience progress. New methods in neuroimaging are crucial not only for neuroscience, but also for improving our understanding of how brain structure and function change in response to disease, injury, or therapeutic intervention. Brain imaging is pivotal in identifying biomarkers of neurodegeneration, enabling earlier and more accurate diagnosis and paving the way for more targeted and effective treatments. By providing insight into an individual's brain structure and function, imaging can help tailor treatments to the needs of each patient. Personalized medicine aims to optimize therapeutic outcomes by taking into account individual variability, and brain imaging is an indispensable tool in achieving this goal.

A reliable biomarker of myelin integrity is critical for further developments in the understanding, diagnosis, and treatment of multiple neurological diseases. By combining MRI and histology in mice, Searleman et al. showed that Ultrashort Echo Time (UTE) MRI is sensitive to myelin loss due to its ability to detect very fast relaxation signals.

Structural and functional connectomics based on magnetic resonance imaging (MRI) is a field in constant expansion, where innovations in signal acquisition, processing, and theoretical modeling are equally important. Li et al. focused on the representation of the microstructural connectome. They argued that the conventional reliance on an adjacency matrix hampers statistical and computational efficiency by inflating dimensionality beyond what is needed and showed that a topologically and biologically informed tree representation preserves information and interpretability while drastically reducing dimensionality.

Functional connectivity (FC) was the focus of the study by Hu et al., who investigated its spatiotemporal modulation during naturalistic stimuli. They found that a naturalistic stimulus (watching a movie) modulates the magnitude but does not change the pattern of connectivity compared to resting conditions. Temporal coherence of fluctuations between subjects, as assessed by inter-subject functional connectivity, was weak during the naturalistic stimuli, indicating that brain fluctuations of different subjects are not synchronous under the same naturalistic condition. Overall, the authors reported improved stability of FC metrics under naturalistic stimuli compared to rest, suggesting that the presentation of naturalistic stimuli may be preferable for performing FC studies in neurological and psychiatric patients.

While MRI-based FC has generated substantial new knowledge at the scale of whole-brain connectivity, and single neurons can be effectively studied by electrophysiological methods, it is still a challenge to close the gap at the mesoscale, the scale of neural circuits. Caznok Silveira et al. review the potential, challenges, and limitations of neuroimaging to investigate connectivity at the mesoscale.

Local assessment of cell number and density is a useful tool for the study of CNS diseases in animal models; however, it is prone to technical biases associated with tissue deformation, selection of sampling sites, and mere errors. Tian et al. reported a multimodal approach based on MR histology and light sheet microscopy, to address this problem, and show that their workflow allows accurate regional counting in a mouse model of aging.

At the other extreme of the spatial scale, brain volume and cortical thickness can be assessed by computational techniques leveraging structural MRI images. Del Giovane et al. briefly examined the effectiveness of current approaches for extracting these metrics from brains with abnormal anatomy, such as those seen in idiopathic Normal Pressure Hydrocephalus. They conclude that the task still requires a degree of manual editing that is necessarily associated with inter-rater variability.

While neuroscientists are normally concerned with populations, individual variations can convey information and are certainly crucial for personalizing treatments. Kampel et al. showed that multivariate time-series classification of MEG time-series performed with random convolutional kernel transformation (ROCKET) allows neuronal fingerprinting, i.e., the identification of single subjects with great accuracy on time-series windows as short as 1 s. This performance is promising for personalized medicine and the development of brain-computer interfaces (BCI).

BCI decoding algorithms can be improved by optimizing the extraction of features from EEG signals. Ma et al. introduced a method for extracting network features from EEG traces, based on directed transfer function and graph theory. The authors showed that their method improves performance in the classification and decoding of motor imagery tasks, thus potentially contributing to increased accuracy and reliability of BCI.

Finally, the transition from research to clinical settings requires standardized procedures. Wang et al. described the optimization of a scoring system based on semiquantitative MRI imaging, common in hospitals, designed to assess Wilson's Disease; they showed improved predictive performance over previously available approaches. In another clinically oriented work, Gao et al. investigated the risk of postoperative cerebral hypoperfusion after revascularization surgery for moyamoya disease using pulsed arterial spin labeling combined with time-of-flight angiography. The researchers showed that the risk can be stratified using non-invasive and safe MRI procedures, without the administration of contrast agents.

While certainly not exhaustive, this Research Topic offers an overview of some of the frontier themes in brain imaging methods. Taken together, the studies clearly suggest that multimodal integration, new acquisition and processing techniques, and validation for clinical applications are interplaying features of brain imaging method development.

Author contributions

FG: Writing – original draft. X-NZ: Writing – review & editing. VC: Writing – review & editing.

Funding

The author(s) declare that no financial support was received for the research, authorship, and/or publication of this article.

Conflict of interest

The authors declare that the research was conducted in the absence of any commercial or financial relationships that could be construed as a potential conflict of interest.

The author(s) declared that they were an editorial board member of Frontiers, at the time of submission. This had no impact on the peer review process and the final decision.

Publisher's note

frontiers | Frontiers in Neuroscience

TYPE Original Research
PUBLISHED 15 August 2023
DOI 10.3389/fnins.2023.1186053

A weighted cranial diffusion-weighted imaging scale for Wilson's disease

Shi-jing Wang[1,2†], Hao Geng[3,4†], Si-rui Cheng[5†], Chen-chen Xu[2], Rui-qi Zhang[3,4], Yu Wang[3,4], Tong Wu[1], Bo Li[2], Tao Wang[3], Yong-sheng Han[2], Zeng-hui Ding[3], Yi-ning Sun[3], Xun Wang[1,2], Yong-zhu Han[1,2] and Nan Cheng[1,2*]

[1]Graduate School, Anhui University of Chinese Medicine, Hefei, China, [2]Hospital Affiliated to the Institute of Neurology, Anhui University of Chinese Medicine, Hefei, China, [3]Institute of Intelligent Machines, Hefei Institute of Physical Science, Chinese Academy of Sciences, Hefei, China, [4]Department of Biophysics, University of Science and Technology of China, Hefei, China, [5]Department of Economics, Nankai University, Tainjin, China

OPEN ACCESS

EDITED BY
Federico Giove,
Centro Fermi - Museo Storico della Fisica e Centro Studi e Ricerche Enrico Fermi, Italy

REVIEWED BY
Arastoo Vossough,
Children's Hospital of Philadelphia, United States
Tomasz Litwin,
Institute of Psychiatry and Neurology (IPiN), Poland

*CORRESPONDENCE
Nan Cheng
✉ azychengnan@163.com

†These authors have contributed equally to this work

RECEIVED 14 March 2023
ACCEPTED 31 July 2023
PUBLISHED 15 August 2023

CITATION
Wang S-j, Geng H, Cheng S-r, Xu C-c, Zhang R-q, Wang Y, Wu T, Li B, Wang T, Han Y-s, Ding Z-h, Sun Y-n, Wang X, Han Y-z and Cheng N (2023) A weighted cranial diffusion-weighted imaging scale for Wilson's disease.
Front. Neurosci. 17:1186053.
doi: 10.3389/fnins.2023.1186053

Objectives: Cranial magnetic resonance imaging (MRI) could be a crucial tool for the assessment for neurological symptoms in patients with Wilson's disease (WD). Diffusion-weighted imaging (DWI) hyperintensity reflects the acute brain injuries, which mainly occur in specific brain regions. Therefore, this study aimed to develop a weighted cranial DWI scale for patients with WD, with special focus on specific brain regions.

Materials and methods: In total, 123 patients with WD were enrolled, 118 of whom underwent 1.5 T-MRI on admission. The imaging score was calculated as described previously and depended on the following sequences: one point was acquired when abnormal intensity occurred in the T1, T2, and fluid-attenuation inversion recovery sequences, and two points were acquired when DWI hyperintensity were found. Consensus weighting was conducted based on the symptoms and response to treatment.

Results: Intra-rater agreement were good ($r = 0.855$ [0.798–0.897], $p < 0.0001$). DWI hyperintensity in the putamen was a high-risk factor for deterioration during de-copper therapy (OR = 8.656, $p < 0.05$). The high-risk factors for readmission for intravenous de-copper therapies were DWI hyperintensity in the midbrain (OR = 3.818, $p < 0.05$) and the corpus callosum (OR = 2.654, $p < 0.05$). Both scoring systems had positive correlation with UWDRS scale (original semi-quantitative scoring system, $r = 0.35$, $p < 0.001$; consensus semi-quantitative scoring system, $r = 0.351$, $p < 0.001$.). Compared to the original scoring system, the consensus scoring system had higher correlations with the occurrence of deterioration (OR = 1.052, 95%CI [1.003, 1.0103], $p < 0.05$) and readmission for intravenous de-copper therapy (OR = 1.043, 95%CI [1.001, 1.086], $p < 0.05$).

Conclusion: The predictive performance of the consensus semi-quantitative scoring system for cranial MRI was improved to guide medication, healthcare management, and prognosis prediction in patients with WD. For every point increase in the neuroimaging score, the risk of exacerbations during treatment increased by 5.2%, and the risk of readmission to the hospital within 6 months increased by 4.3%.

KEYWORDS

Wilson disease, rating scores, MRI, neuroimaging, clinical assessment

1. Introduction

Wilson's disease (WD) is an autosomal recessive copper metabolism disorder caused by mutations in the *ATP7B gene* (Członkowska et al., 2018). According to the main symptoms and organs with copper deposits, patients with WD can be divided into hepatic, neurological, and hepatic-neurological subtype (Cheng et al., 2017). Copper-chelating therapy has been used as the main treatment for most patients with WD and is effective in patients with the hepatic subtype, especially in the early-stages of the disease course (Walshe and Yealland, 1993). However, symptom worsening could occur in neurological subtype and hepatic-neurological subtype WD patients during early stage by copper-chelating treatment (Cheng et al., 2014). Currently, this deterioration is predicted through estimation by experienced physicians, instead of reliable biomarkers. Therefore, precise prediction, rather than empirical judgment, of the deterioration in neurological symptoms and prognosis has become a crucial target in recent therapeutic research on WD.

Neurological symptoms are caused by long-term copper accumulation in different brain regions (Masełbas et al., 2010; Hefter et al., 2018). Injuries can be found in putamen, globus pallidum, caudate nucleus, inner capsule, thalamus, midbrain, pons, medulla, cerebellum, cortex, and corpus callosum (Yu et al., 2019). The injury mode can be referred into demyelination, microglial activation, central pontine myelinolysis, and injury of gray/white matter (Dusek et al., 2017). Brain imaging can directly monitor the lesion, presenting as atrophy (Smolinski et al., 2019), white matter hyperintensity, increased magnetic susceptibility (Yang et al., 2015) and diffusion disorders (Favrole et al., 2006). Dusek developed a semi-quantitative MRI scale for patients with WD (Dusek et al., 2020; Rędzia-Ogrodnik et al., 2022). They paid special attention to sequences of T1, T2, Flair and SWI. Acute toxicity scores, chronic damage scores and atrophy scores were determined by the occurrence of T2/FLAIR hyperintensity, T2/T2*/SWI hypointensity and T1, respectively. WD cranial MRI severity was defined by acute injury and chronic damage (including atrophy) simultaneously, semi-quantified (Normal/absent = 0, mild/moderate = 1, severe = 2) to a total score. Intrarater and interrater agreement of the scale were analyzed, and it was verified as a reliable instrument. Meanwhile, the association between clinical and imaging severity proved that it was an effective tool to assess the severity of patients with WD.

DWI hyperintensity showed a higher specificity and clinical predictive value than other sequences. Favrole et al. (2006) found that hyperintense lesions were detected in all symptomatic patients on FLAIR MR images but only in 11 of 13 patients with WD who had typical neurological manifestations on DWI. Additionally, the reduction in diffusion changes was correlated to clinical improvement in patients with WD. Furthermore, lesions intensively occurred in specific brain regions rather than the whole brain among patients with WD. There was a corresponding relationship between different brain region injuries and different symptoms. Thalamic injury, brainstem/cerebellar injury, and corpus callosum injury were associated with a longer disease course, ataxia, and neuropsychiatric symptoms, respectively (Zhong et al., 2019; Zhou et al., 2019). Therefore, DWI hyperintensity in specific brain regions should be taken into crucial consideration as WD cranial MRI severity assessment.

Based on the semi-quantitative MRI scale for patients with WD, we aimed to weighting the specific brain regions according to the DWI hyperintensity and add it to the total WD cranial MRI severity score. Firstly, analysis was conducted to establish a corresponding correlation between injuries in specific brain regions and clinical symptoms, brain regions of interest and weighting coefficients were determined by data calculation and literature analysis. Secondly, weighting diffusion-weighted imaging (DWI) hyperintensity scores were added into WD cranial MRI severity scores. The weighted scores were then analyzed in relation to clinical symptoms, quality of life, and biomarkers. Thirdly, analyzing the relationship between weighted scoring and the worsening of symptoms during treatment, as well as the likelihood of readmission within 6 months or 12 months, to evaluate its clinical predictive value. We hope that this study will further strengthen MRI as an adjunctive examination to evaluate WD and can also become an important marker for predicting the prognosis of WD.

2. Materials and methods

2.1. Participants and general information

This cohort study was performed at the Center of WD, the affiliated hospital of the Institute of Neurology, Anhui University of Chinese Medicine. The cranial imaging analysis was conducted and confirmed by the Hefei Institute of Physical Science, Chinese Academy of Sciences. The study protocol was approved by the Ethics Committee of the Hefei Institutes of Physical Science, Chinese Academy of Sciences (SWYX-Y-2021-08). Written informed consent was obtained from all subjects by the principal researcher after a self-motivated behavior evaluation of the patient's capacity to provide consent. The consent form was signed by the parents of patients under 18 years old.

At baseline, we enrolled 118 inpatients admitted between June 2019 and June 2020 with a diagnosis of WD, as per the Chinese guidelines for the diagnosis and treatment of WD in 2021 (Inherited Metabolic Liver Disease Collaboration Group, Chinese Society of Hepatology, Chinese Medical Association, 2022). WD should be considered in patients with unexplained liver disease, neurological symptoms (especially extrapyramidal symptoms), or psychiatric symptoms. Age of onset cannot be used as a basis for diagnosing or ruling out WD. The recommended diagnostic criteria include: (1) Neurological and/or psychiatric symptoms. (2) Unexplained liver damage. (3) Decreased serum ceruloplasmin and/or elevated 24-h urine copper (strong recommendation, moderate-quality evidence). (4) Positive Kayser-Fleischer (K-F) rings (strong recommendation, moderate-quality evidence). (5) Identification of pathogenic mutations in both chromosomes carrying the ATP7B gene through pedigree segregation and genetic analysis (strong recommendation, moderate-quality evidence). WD can be confirmed when meeting either (1 or 2) plus (3 and 4), or (1 or 2) plus 5. Individuals with criteria 3 plus 4 or 5 but without obvious clinical symptoms are diagnosed as pre-symptomatic individuals. Individuals meeting any two of the first three criteria are diagnosed as "possibly WD, "and further follow-up observation is recommended, with ATP7B gene testing suggested for a definitive diagnosis. The Chinese guidelines for WD emphasize early and lifelong treatment, as well as lifelong monitoring. For patients in the pre-symptomatic stage, zinc preparations can be used for maintenance therapy. Patients already receiving copper-chelating therapy should be monitored for indicators such as complete blood count, liver function, 24-h urine copper, and cranial MRI. The guidelines also provide recommendations for dietary control, including fasting, moderate intake, appropriate consumption, and recommended foods. There are differences in the use of copper-chelating agents between the Chinese guidelines and other guidelines. In China, sodium Dimercaptosulphonate (DMPS), Dimercaptosuccinic acid (DMSA) capsules, zinc gluconate, and traditional Chinese medicine are specifically considered. Among these, DMPS has a higher priority in copper-removing therapy for WD compared to penicillamine. DMSA and zinc gluconate offer alternative options for maintenance therapy and are suitable for patients allergic to penicillamine or with leukopenia. Trientine is not used in China for specific reasons.

Among these, 96 patients had been previously diagnosed with WD (referral patients), while 22 were newly diagnosed. At the time of admission, the Unified Wilson Disease Rating Scale (UWDRS) and cranial MRI examinations were conducted to assess the state of the disease. Patients were evaluated for the presence of any neurologic findings by 2 neurologists (R.W., 5 years of experience; XP.W., >30 years of experience). All patients received Cu-chelating therapy according to the Chinese guidelines for the diagnosis and treatment of WD (Neurogenetics Group and Neurology Branch of Chinese Medical Association, 2021). During the course of treatment, serum copper, ceruloplasmin, and urine copper at 24 h before treatment and the highest urine copper at 24 h during treatment were tested to determine the efficacy of treatment (Figure 1).

2.2. Parameters of magnetic resonance

Philips Achieva 1.5 T MRI scanning equipment was used to scan the images of patients with WD. The scans ranged from the foramen magnum to the upper edge of the corpus callosum. The scan sequences included T1WI, T2WI, FLAIR, and DWI. The scanning parameters were FLAIR, TR/TE = 9,000 ms/140 ms, flip angle 120°, slices thickness 6.5 mm, slices spacing 1.3 mm; DWI (b = 0, 1,000 s/mm^2), single excitation SE-EPI sequence, TR/TE = 2,400 ms/104 ms, FOV 220 mm × 220 mm, matrix 168 × 105, slice thickness 6.5 mm, slice spacing 1.3 mm, number of slices 17 ~ 18 slices.

2.3. Image-scoring method and determination of weight coefficients

The image score evaluations were performed by two radiologists. According to previous studies (Favrole et al., 2006; Sinha et al., 2006), T1, T2, FLAIR, and DWI sequences were selected as reference sequences. The regions of interest included the caudate nucleus, putamen, globus pallidus, internal capsule, thalamus, midbrain, pons, cerebellum, medulla oblongata, cortex, and corpus callosum. T2/FLAIR hyperintensity was scored as 1 point, T1 abnormal signal intensity was scored as 1 point, and DWI hyperintensity was scored as 2 points. Subsequently, we conducted logistic regression analysis, using specific brain region imaging scores as independent variables, and the presence of clinical symptoms and prognostic indicators as dependent variables. Clinical symptoms consisted of dysarthria, dysphagia, gait disturbances, dystonia, muscular hypertonia, and psychiatric disorders. Prognostic indicators included post-treatment deterioration and readmission within 6–12 months. We identified statistically significant data and extracted the corresponding brain regions along with their corresponding odds ratios (OR). Weight coefficients were based on brain regions and corresponding OR mainly, as well as experts' experience, literature reviews and actual application. For example, midbrain lesions are rare and worthless compared to corpus callosum lesions and caudate nucleus lesions. Therefore, the weight assigned to the midbrain region is reduced accordingly.

Finally, the average scores of the two evaluations were calculated. To avoid subjective bias, two researchers independently evaluated the signal abnormality of all images. The specific scoring rules are listed (Table 1). Figures 2A–J shows the injuries to various parts of the brain in the T1, T2, FLAIR, and DWI sequences.

2.4. Statistical analysis

Statistical analyses were performed with R (Version 4.2.1 for Windows, Comprehensive R Archive Network).[1] To determine agreement between two scorers, the intraclass correlation coefficient (ICC) was calculated to determine the inter-rater reliability. A Student's *t*-test of two independent samples was used for normally distributed data, and the Mann–Whitney U test was used for non-normally distributed data. Data were analyzed using the Chi-square test. The Pearson or Spearman correlation test was used for the correlation analysis. The univariate analysis used the logistic regression model selection method, and statistical significance was set at $p < 0.05$.

3. Results

3.1. General characteristics of the patients with WD

The enrolled patients were divided into two groups according to whether they were newly diagnosed. No significant differences ($p > 0.05$) were found in terms of sex, subtype, UWDRS scale, ADL score, highest urine copper level before treatment, serum copper level, ceruloplasmin level, and imaging scores between the newly diagnosed group ($n = 22$) and referral group ($n = 96$). However, the age at onset was higher in the newly diagnosed group than in the referral group ($p < 0.05$). Detailed data are presented in Table 2, Part I.

3.2. Difference in symptoms between newly diagnosed patients and patients referred with WD

The differences in symptoms between patients in the newly diagnosed and referral groups. Compared to the newly diagnosed group, choreoathetosis and torsion spasms were significantly lower in the referral group ($p < 0.05$), whereas no significant differences were found in terms of dysarthria, difficulty swallowing, tremor, gait

---

[1] https://www.r-project.org

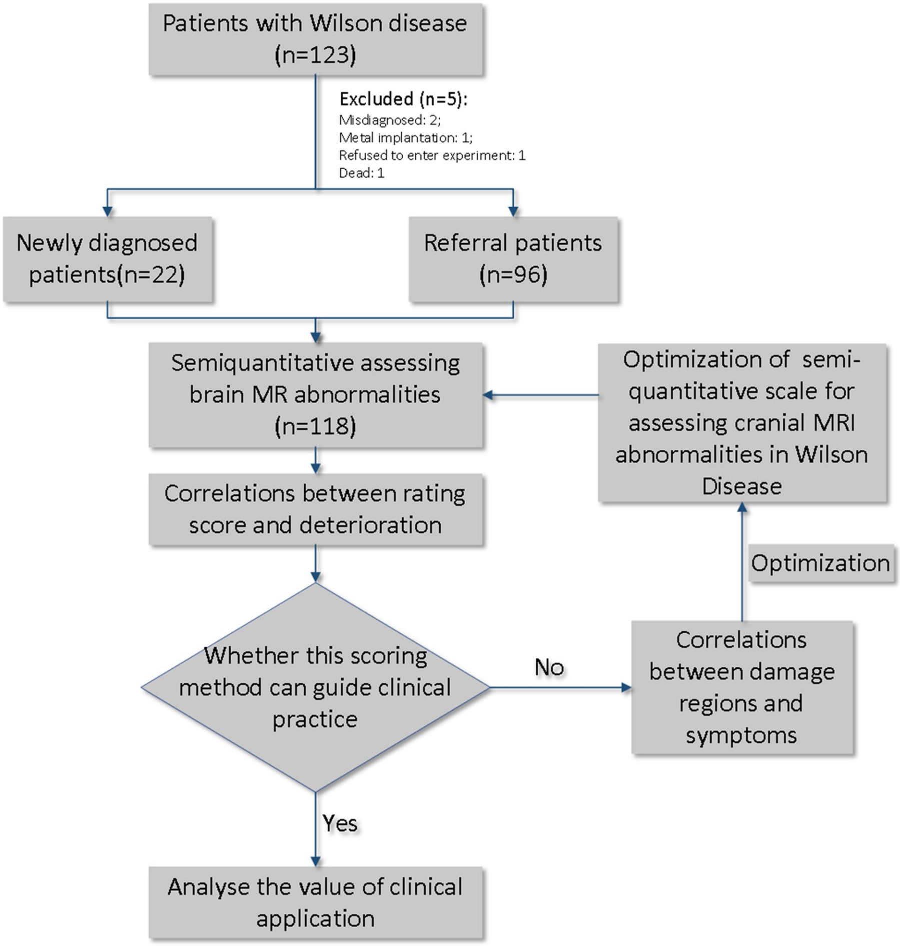

FIGURE 1
General idea and flow chart of this study.

disturbance, salivation, dystonia, bradykinesia and rigidity, ataxia, mental disorders, and epilepsy ($p > 0.05$).

3.3. Analysis of injury sites between newly diagnosed patients and patients referred with WD

Table 2, Part II shows the injury sites of the newly diagnosed and referred patients with WD. The putamen, globus pallidus, caudate nucleus, thalamus, midbrain, pons, and cerebellum are the main damage sites for copper accumulation in patients with WD and brain atrophy. Damage to the cortex and corpus callosum is rare, and medullary damage has only been found in a single patient. There was no significant difference in the common sites between the two groups, as observed on MRI ($p > 0.05$).

3.4. Correlations between the cranial injury site and symptoms

As shown in Figures 2K–N, the correlations between the cranial injury site and clinical symptoms. Putamen injuries were strongly associated with dysarthria (OR = 16.604, 95%CI [4.111, 67.06], $p < 0.001$), dysphagia (OR = 8.554, 95%CI [1.616, 45.283], $p < 0.05$), and dystonia (OR = 4.24, 95%CI [1.129, 15.917], $p < 0.05$). Midbrain injury was strongly associated with dysarthria (OR = 4.012, 95%CI [1.44, 11.176], $p < 0.01$), dysphagia (OR = 3.386, 95%CI [1.197, 9.578], $p < 0.05$), and gait disturbances (OR = 3.7, 95%CI [1.552, 8.822], $p < 0.01$). Pontine injuries were correlated with torsion spasm (OR = 4.239, 95%CI [1.143, 15.726], $p < 0.05$). Thalamic injuries were associated with mental disorders (OR = 2.6, 95%CI [1.124, 5.568], $p < 0.05$).

3.5. Risk prediction of DWI hyperintensity at different sites for deterioration or not during treatment

In this study, we included the DWI sequence as an evaluation index because DWI hyperintensity usually represents acute damage. Therefore, we increased the score weight by up to eight times in the case of DWI hyperintensities. The proportion of hyperintensity in the nucleus, caudate nucleus, thalamus, pons, and cerebellum in the newly diagnosed patient group was significantly higher than in the referral patient group. In contrast, DWI hyperintensity in the globus pallidus, internal capsule, medulla, and cortex in the two groups was rare, and the difference was not statistically significant. Patients in both groups were likely to have DWI hyperintensities in

TABLE 1 Cranial injury score of patients with WD.

Site of injury	T1	T2	FLAIR	DWI
Original				
Putamen	1	1	1	2
Globus pallidus	1	1	1	2
Caudate nucleus head	1	1	1	2
Inner capsule	1	1	1	2
Thalamus	1	1	1	2
Midbrain	1	1	1	2
Pons	1	1	1	2
Medulla oblongata	1	1	1	2
Cerebellum	1	1	1	2
Cortex	1	1	1	2
Corpus callosum	1	1	1	2
Brain atrophy	1			
Total score				
Optimized				
Lentiform nucleus	1	1	1	18
Caudate nucleus head	1	1	1	2
Thalamus	1	1	1	2
Midbrain	1	1	1	4
Pons	1	1	1	2
Cerebellum	1	1	1	2
Corpus callosum	1	1	1	6
Brain atrophy	1			
Score				

Flair, fluid-attenuation inversion recovery; DWI, diffusion weighted imaging. The degree of injury was not taken into account, and points were scored whenever there was damage in a specific area.

the midbrain and corpus callosum, but the difference was not statistically significant.

Therefore, we substituted the putamen, caudate nucleus, thalamus, pons, cerebellum, midbrain, and corpus callosum as independent variables into the logistic regression equation, and OR were calculated using a backward method by taking "whether it was aggravated during treatment," "whether it was readmitted to the hospital within 6 months," and "whether it was readmitted within 1 year" as a dependent variable, respectively. As shown in Figures 2O–Q, putamen injury was strongly associated with deterioration during treatment (OR = 8.656, 95%CI [1.085, 69.043], $p < 0.05$), corpus callosum injury was strongly associated with readmission within 1 year (OR = 2.654, 95%CI [1.003, 7.022], $p < 0.05$), and midbrain injury was strongly associated with readmission within 6 months (OR = 3.818, 95%CI [1.122, 12.999], $p < 0.05$).

3.6. Consensus weighting of the semi-quantitative scoring system for cranial MR in WD

Intrarater agreement (ICC) was good for two scorers, that is for MRI score (0.855 [0.798–0.897], $p < 0.0001$).

According to the results detailed in 3.3 and 3.5, we found that DWI hyperintensities in the lentiform nucleus (putamen and globus pallidus) and midbrain were strongly associated with prognosis and brain atrophy. Therefore, the integral weights of the DWI hyperintensities of the putamen, midbrain, and corpus callosum should be increased to prove the susceptibility of the semi-quantitative scoring system for clinical prediction. Here, we provide an consensus algorithm as presented in Table 1. In this new scoring system, the point weights of the caudate nucleus, thalamus, pons, and cerebellum in the sequences of T1, T2, FLAIR, and DWI remained unchanged compared with the former version (Table 1). The weights of the DWI hyperintensity in the lentiform nucleus, midbrain, and corpus callosum increased to 18, 4, and 6, respectively.

As shown in Figures 3A–J, the original and consensus semi-quantitative scoring systems showed strong correlations between the UWDRS and ADL scores. The positive correlation of UWDRS with the consensus semi-quantitative scoring system ($r = 0.351$, $p < 0.001$) and original semi-quantitative scoring system ($r = 0.35$, $p < 0.001$), while it was both negative correlations to the ADL score (consensus semi-quantitative scoring system, $r = -0.205$, $p < 0.05$; original semi-quantitative scoring system, $r = -0.254$, $p < 0.01$). No significant differences were found between the two systems and other clinical indices (urine copper before treatment, serum copper, and ceruloplasmin).

As shown in Figures 3K,L, we reassessed the predictive performance of the weighted cranial DWI scale. Compared with the original imaging score, the weighted imaging score had a similar result with deterioration during treatment (OR = 1.052, 95%CI [1.003, 1.0103], $p < 0.05$) and readmission within 6 months (OR = 1.043, 95%CI [1.001, 1.086], $p < 0.05$).

4. Discussion

In the early stages of WD treatment, there may be a deterioration of neurological symptoms, which could be associated with copper-related oxidative stress reactions (Ziemssen et al., 2022). However, the current approach to preventing the deterioration of neurological symptoms during treatment is mostly based on physicians' experience, rather than reliable clinical markers (Hou et al., 2022). According to our results, there was no significant difference in terms of gender composition, clinical phenotypes, UWDRS scale scores, cranial MRI imaging scores, 24-h urinary copper, ceruloplasmin, serum copper and ADL scores between newly diagnosed patients and referral patients. This indicated the limited specificity of clinical assessment methods in evaluating the efficacy and prognosis of WD patients, emphasizing the need for more reliable clinical markers (Hou et al., 2022). The imaging scoring system developed by Dusek et al. (2020) can reflect the alleviation of acute cranial brain injury in WD patients as treatment progresses, which indicated that neuroimaging may serve as a potential reliable tool for prognostic prediction. Considering the mild changes in chronic injuries over the short term and the focus trend of damage in the regions of interest, we adjusted the scoring strategy for assessing cranial MRI damage in WD according to former research. Adjustments include increasing of weight coefficient of DWI hyperintensity and specific regions of interest. Subsequently, we verified the clinical value of this scoring system by establishing

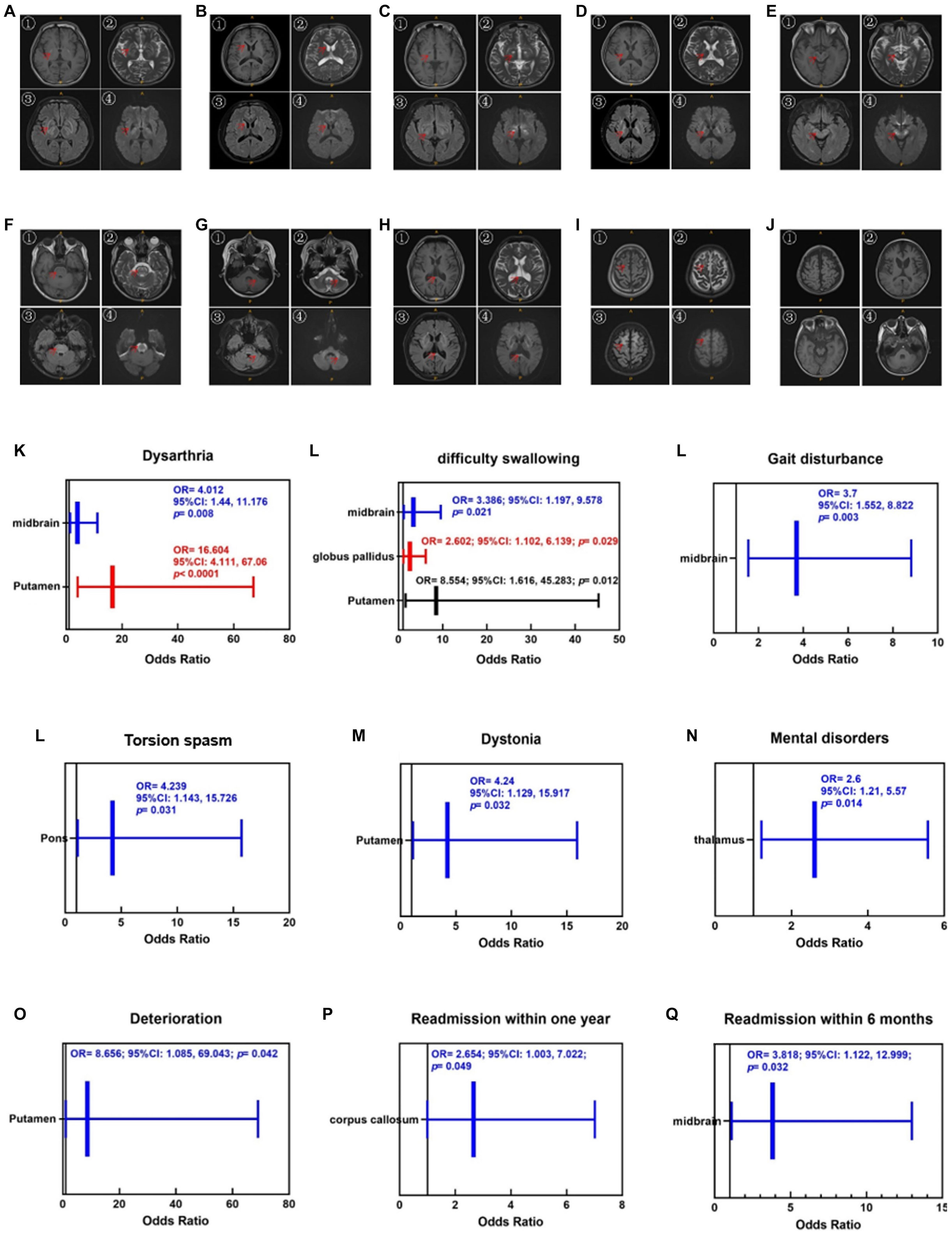

FIGURE 2
Injuries of various parts of the brain in the T1 (①), T2 (②), Flair (③) and DWI (④) sequences. **(A)** Putamen and globus pallidus, **(B)** caudate nucleus, **(C)** thalamus, **(D)** inner capsule, **(E)** midbrain, **(F)** pons, **(G)** cerebellum, **(H)** corpus callosum, **(I)** cortex, **(J)** brain atrophy. The red arrows mark the specific site of the injury. Brain atrophy can only be observed in the T1 sequence. Enlargement of the ventricular system, reduction of brainstem volume, widening of the tricorn and cortical sulcus fissure can be seen when brain atrophy occurs. **(K–N)** Correlations between cranial injury site and symptoms. **(O–Q)** Correlations between cranial injury site and therapeutic regimen.

TABLE 2 General information and injury sites of patient with WD in the newly diagnosed group and the referral group.

	the referral group (n = 96)	the newly diagnosed group (n = 22)	χ^2, Z	p
Sex (male/female)	63/33	14/8	0.031	>0.05
Hepatic subtype/neurologic subtype	10/86	4/18	0.937	0.293
Age of onset	15 (10, 19)	19.91 ± 7.61	−2.37	**0.018**
UWDRS-I	45.5 (36, 60.75)	66.55 ± 47.99	−1.185	0.236
UWDRS-II	6 (4, 7)	5 (5, 8)	−0.708	0.479
UWDRS-III	6.5 (5, 9)	6.5 (5, 8.75)	−0.421	0.674
UWDRS	58 (46.25, 74.75)	82.32 ± 48.48	−1.579	0.114
ADL (able/disabled)	85/11	16/6	3.63	0.087
Urine copper before treatment	194.97 (120.34, 288.37)	274.12 ± 165.32	−1.106	0.269
Highest urine copper	1324.96 (785.45, 2066.23)	1199.73 ± 469.39	−1.258	0.209
Serum copper	2.71 (1.65, 4.05)	2.12 (1.19, 5.32)	−0.308	0.758
ceruloplasmin	45.15 (36.25, 61.23)	47.95 (33.63, 67.45)	−0.373	0.709
Total score of imaging	9.5 (7, 14)	14.32 ± 9.14	−1.741	0.082
Deterioration (yes/no)	38/58	7/15	0.457	0.628
Whether to be readmitted to hospital within 6 months (yes/no)	19/77	9/13	4.41	0.051
Whether to be readmitted to hospital within a year (yes/no)	38/58	16/6	7.922	**0.008**
Putamen (yes/no)	81/11	18/4	0.673	0.476
globus pallidus (yes/no)	38/58	10/12	0.256	0.637
caudate nucleus (yes/no)	26/70	8/14	0.752	0.437
Inner capsule (yes/no)	6/90	1/21	0.099	1
Thalamus (yes/no)	39/57	11/11	0.644	0.478
Midbrain (yes/no)	64/32	17/5	0.98	0.447
Pons (yes/no)	51/45	16/6	2.802	0.103
cerebellum (yes/no)	38/58	10/12	0.256	0.637
medulla (yes/no)	1/95	0/22	0.415	1
cortex (yes/no)	17/79	5/17	0.286	0.556
corpus callosum (yes/no)	17/79	2/20	1.102	0.521
Brain atrophy (yes/no)	86/10	20/2	0.035	1
Putamen DWI hyper-intensity (yes/no)	7/89	6/16	7.289	**0.015**
globus pallidus DWI hyper-intensity (yes/no)	1/95	1/21	1.022	0.339
caudate nucleus DWI hyper-intensity (yes/no)	2/94	3/19	4.429	**0.044**
Inner capsule DWI hyper-intensity (yes/no)	1/95	1/21	1.022	0.339
Thalamus DWI hyper-intensity (yes/no)	5/91	6/16	8.077	**0.005**
Midbrain DWI hyper-intensity (yes/no)	6/90	6/16	8.659	**0.009**
Pons DWI hyper-intensity (yes/no)	2/94	4/18	7.132	**0.011**
Cerebellum DWI hyper-intensity (yes/no)	2/94	4/18	7.132	**0.011**
Medulla DWI hyper-intensity (yes/no)	1/95	0/22	0.415	1
Cortex DWI hyper-intensity (yes/no)	1/95	1/21	1.022	0.339
corpus callosum DWI hyper-intensity (yes/no)	23/73	2/20	2.755	0.156

The significant difference was marked with bold.

the regression relationships between the imaging scores and clinical outcomes. Including deterioration during de-copper therapy and readmission within 6/12 months.

DWI hyperintensity representing acute cranial brain injuries may exhibit greater predictive value and potential for assessing treatment efficacy in the short term, compared to chronic injuries (Chen et al.,

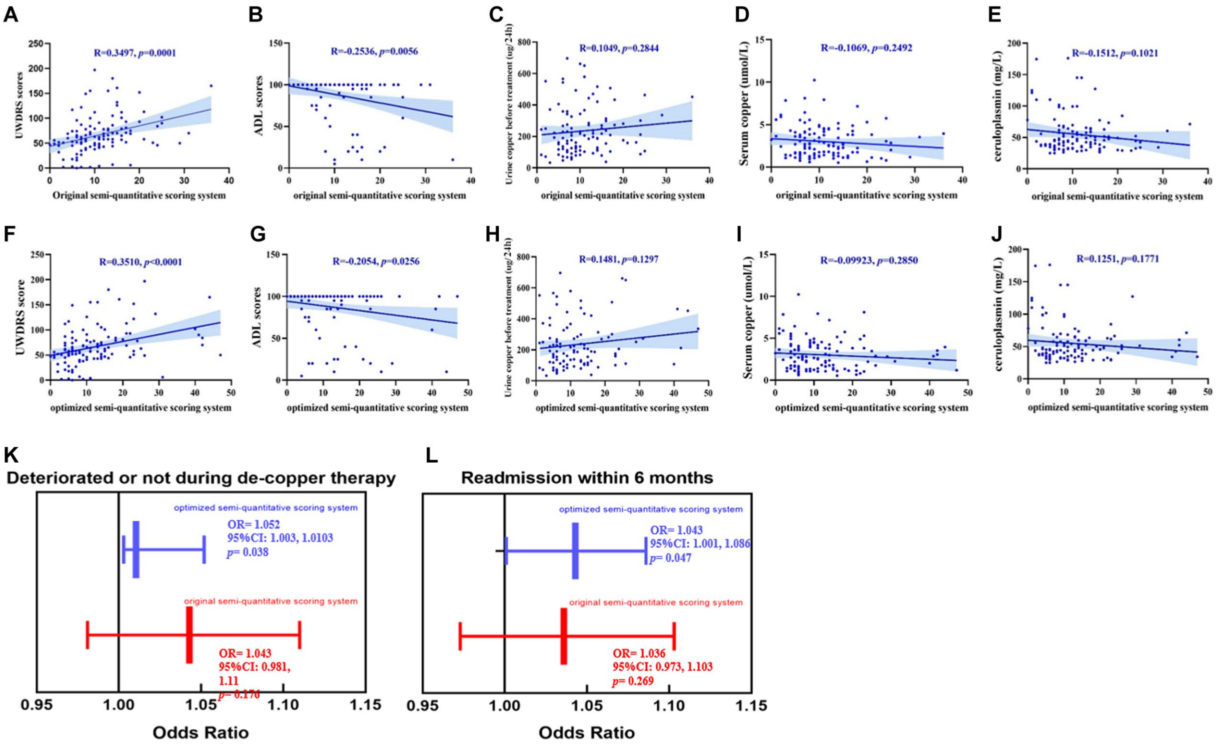

FIGURE 3
(A–J) The promotion of the consensus semi-quantitative scoring system compared to the original semi-quantitative scoring system, both their correlations between the UWDRS score, ADL score and other clinical indexes (urine copper before treatment, serum copper and ceruloplasmin). **(K,L)** The consensus imaging score had a strong correlation between deterioration during treatment [OR = 1.052, 95%CI (1.003, 1.0103), $p < 0.05$] and readmission within 6 months [OR = 1.043, 95%CI (1.001, 1.086), $p < 0.05$]. While no significant correlations had been found between the original imaging score and deterioration during treatment [OR = 1.043, 95%CI (0.981, 1.11), $p > 0.05$] and readmission within 6 months [OR = 1.036, 95%CI (0.973, 1.103), $p > 0.05$].

2017). In this study, no significant differences had been found in the occurrence rates of neurological symptoms related to brain damage, such as dysarthria, dysphagia, tremor, gait disturbances, sialorrhea, dystonia, bradykinesia, muscular rigidity, ataxia, psychiatric disorders, and epilepsy, between newly diagnosed patients and referral patients. These findings suggest that cranial abnormalities in patients with neurologic WD are correlated with their clinical symptoms, age of onset, and disease course (Yu et al., 2019). Previous studies have indicated that common manifestations on cranial MRI lesions of patients with WD include: T1 hypointensity/T2 hyperintensity, T1 hyperintensity and T1/T2 hypointensity, which may be due to the copper accumulation in different disease courses and different brain regions (Li et al., 2019). Sener (2003) found that the restricted water diffusion presenting as DWI hyperintensity/ADC hypointensity is due to cellular inflammatory injury and toxic edema caused by copper deposition among patients with WD (Pulai et al., 2014). In newly diagnosed patients with WD, there is a relatively high proportion of DWI hyperintensity in the caudate nucleus, putamen, thalamus, midbrain, pons, and cerebellum. When considering the apparent diffusion coefficient (ADC) sequence to determine whether DWI hyperintensity represents water diffusion, we found the DWI hyperintensity was caused by T2 shine-through effect in some patients. Therefore, simultaneous presence of DWI hyperintensity and ADC hypointensity was considered as the criterion for abnormal DWI intensity, to exclude the interference of T2 shine-through effect. In conclusion, based on the higher specificity and clinical significance, we have assigned a greater weight to DWI hyperintensity as an important scoring criterion in our assessment.

There is a correlation between different clinical presentations and the location of cranial MRI lesions among patients with WD (Yu et al., 2019). Previously, it was believed that a specific clinical symptom in patients with WD is likely caused by simultaneous damage from different brain regions rather than being directly attributed to the injury of a single brain region (Zhong et al., 2019). In this study, to adjust the weight coefficients, we calculated the OR values of abnormal MRI intensity in different brain regions corresponding to clinical symptoms. Occurrence of putamen injuries promoted the risk of dysarthria, dysphagia and dystonia by 16.604, 8.554 and 4.24 times, respectively. Occurrence of midbrain injuries promoted the risk of dysarthria, dysphagia and gait disturbances by 4.012, 3.386 and 3.7 times, respectively. Occurrence of pontine injuries promoted the risk of torsion spasm by 4.239 times. The occurrence of thalamic injuries promoted the risk of mental disorders by 2.6 times. Additionally, patients with DWI hyperintensity in the putamen were more prone to experiencing deterioration of neurological symptoms during the de-copper treatment. Patients with DWI hyperintensity in the corpus callosum and midbrain may require de-copper therapy within 6/12 months to stabilize the condition.

Sinha et al. (2006) and Selwa et al. (1993) graded quantification criteria for cranial injury in patients with WD, grade was done for the severity of change in signal intensity (deviation from the conventionally accepted signal intensity of a given structure in a particular sequence) and associated atrophy (0 = no abnormality, 1 = change in signal intensity with no atrophy, 2 = change in signal intensity with mild or moderate atrophy, and 3 = change in signal intensity with severe atrophy). MRI changes correlated with the mean NSS, S and E activities of daily living, and Chu staging scores ($p < 0.001$), but did not correlate with the duration of illness. Sinha et al. (2007) investigated the changes in cranial MRI and clinical symptoms in 50 patients with WD, revealing varying degrees of improvement in both MRI and clinical manifestations following treatment. They also found a strong correlation between pre-and post-treatment Neurological Severity Score (NSS) and cranial MRI scores, indicating that both can serve as indicators of treatment effectiveness in WD patients. Their results demonstrate that this method is an effective means of observing treatment response in WD patients. Li (2019) employed the grading method proposed by Sinha et al. (2006) to quantify abnormal signals in WD cranial MRI. This method, based on the T2 sequence, categorizes abnormal signals into hyperintensity and hypointensity and assigns them into four grades based on lesion size: no abnormality = 0 points, mild = 1 point, moderate = 2 points, severe = 3 points. This method can reflect the extent of copper deposition and neural damage in the brains of WD patients. However, it does not provide information regarding the changes and significance of this method during copper chelation therapy. Dusek et al. (2020) developed a semi-quantitative method for assessing abnormalities in WD cranial MRI, which is divided into acute and chronic parts. The acute toxicity scores ranged from 0 to 2 based on the degree of T2/FLAIR hyperintensity in the caudate nucleus, putamen, thalamus, midbrain, and pons. The chronic damage scores were based on the presence of cerebral atrophy and T2/SWI hypointensity. This method demonstrated high consistency and effectiveness in a 24-month follow-up of 37 patients. Changes in MRI scores were primarily driven by changes in the acute and chronic scores. The MRI scores were positively correlated with the UWDRS-III psychiatric scale, indicating that this method can semi-quantitatively reflect the severity of WD. In this study, we explored an improved scoring method for cranial MRI injuries, aiming to assess the extent of brain damage and treatment effectiveness in patients with WD. Based on previous research, we modified the scoring method for WD cranial MRI injuries by incorporating DWI sequences and assigning them higher scores. Eight brain regions were selected as scoring areas, including the caudate nucleus, putamen, thalamus, midbrain, pons, cerebellum, corpus callosum, and cerebral atrophy. We increased the scores for the caudate nucleus, midbrain, and corpus callosum to emphasize their importance based on the therapeutic implications of DWI hyperintensity in different regions. We analyzed the advantages and disadvantages of the two scoring methods and found that the revised scoring system, which includes reselected scoring areas and scores, can be used to evaluate whether WD patients experience deterioration of neurological symptoms during de-copper therapy and whether they require readmission within 6 months to stabilize the copper homeostasis. Our results indicated that for every one-point increase in cranial MRI scores, there is a 5.2% increased risk of deterioration during treatment and a 4.3% increased risk of readmission within 6 months. We believe that this cranial MRI injury scoring method holds significant clinical implications for guiding the management of WD.

Brain injuries in WD primarily involve multiple brain regions, such as the caudate nucleus, putamen, thalamus, midbrain, pons, cerebellum, and corpus callosum, accompanied by varying degrees of cerebral atrophy (Yu et al., 2019). Currently, MRI examination is one of the crucial tools for cranial injuries assessment (Shribman et al., 2022). However, due to significant inter-individual variations in clinical and radiological manifestations of WD, there is a lack of unified standards and methods for its classification and grading. To solve this issue, this study proposed a weighted-multiple-brain-regions-based approach that extracts quantitative features from multimodal images of WD patients. By combining regression models, we have established a cranial imaging scoring system capable of predicting the prognosis of WD patients. This scoring system demonstrates excellent predictive ability and provides a more objective and effective basis for the clinical treatment of WD patients. The scoring system integrates the key injured brain regions, DWI hyperintensity and clinical therapeutic experience to derive a weighted score that reflects neurological symptoms. We conducted correlation analysis between this score and clinical indicators as well as prognostic factors, revealing its effective discrimination ability among patients with different risk levels and significant associations with treatment response and risk of readmission. The method possesses the advantages of objectivity and simplicity, providing a novel tool for prognostic management of WD patients. Our study demonstrates that this imaging scale exhibits favorable predictive performance for the short-term prognosis of WD patients. However, its long-term performance still requires validation. Only 20.33% (24/118) of patients underwent neuroimaging follow-up, and only 37.50% (9/24) of those patients exhibited changes in neuroimaging scores. This suggests that neuroimaging changes may be stable in the short term. Therefore, in future research, it is necessary to include a larger cohort of follow-up and initial visit patients and attempt to construct clinical prediction models for their treatment by incorporating laboratory indicators such as 24-h urinary copper and serum non-ceruloplasmin-bound copper during therapy. This will enable us to more accurately assess the condition and prognosis of WD patients, providing them with consensus individualized treatment plans.

Data availability statement

The raw data supporting the conclusions of this article will be made available by the authors, without undue reservation.

Ethics statement

The studies involving human participants were reviewed and approved by the Ethics Committee of Hefei Institutes of Physical Science, Chinese Academy of Sciences. Written informed consent to participate in this study was provided by the participants' legal guardian/next of kin. Written informed consent was obtained from the individual(s), and minor(s)' legal guardian/next of kin, for the publication of any potentially identifiable images or data included in this article.

Author contributions

S-jW and HG: research project: conception, organization, execution, statistical analysis: design, execution, review, and critique, manuscript preparation: writing the first draft. S-rC: research project: organization, execution, statistical analysis: execution, review, and critique, manuscript preparation: writing the first draft. C-cX and TW: research project: execution, statistical analysis: execution, manuscript preparation: review and critique. YW and BL: research project: organization, statistical analysis: review, and critique, manuscript preparation: review and critique. R-qZ and Y-sH: research project: execution, statistical analysis: review, and critique, manuscript preparation: review and critique. TW, Z-hD, XW, and Y-zH: research project: conception, statistical analysis: review, and critique, manuscript preparation: review and critique. Y-nS and NC: research project: conception, statistical analysis: design, manuscript preparation: review and critique. All authors contributed to the article and approved the submitted version.

Funding

S-jW received funding from the Natural Science Foundation of Anhui Province (grant number: 2208085QH262) and the Anhui Provincial Department of Education (grant number KJ2021A0552). C-cX received funding from the Natural Science Foundation of China (grant number: 81904086). Z-hD received funding from major projects of Anhui Science and Technology (grant number: 202103a07020004). BL received funding from the Natural Science Research Project of the Anhui Educational Committee (grant number: KJ2021A0564).

Acknowledgments

The authors would like to thank all participants and their caregivers for their time and commitment to this research.

Conflict of interest

The authors declare that the research was conducted in the absence of any commercial or financial relationships that could be construed as a potential conflict of interest.

Publisher's note

References

Chen, L., Bentley, P., and Rueckert, D. (2017). Fully automatic acute ischemic lesion segmentation in DWI using convolutional neural networks. *Neuroimage Clin.* 15, 633–643. doi: 10.1016/j.nicl.2017.06.016

Cheng, N., Wang, K., Hu, W., Sun, D., Wang, X., Hu, J., et al. (2014). Wilson disease in the south chinese han population. *Can. J. Neurol. Sci.* 41, 363–367. doi: 10.1017/S0317167100017315

Cheng, N., Wang, H., Wu, W., Yang, R., Liu, L., Han, Y., et al. (2017). Spectrum of ATP7B mutations and genotype-phenotype correlation in large-scale Chinese patients with Wilson disease. *Clin. Genet.* 92, 69–79. doi: 10.1111/cge.12951

Członkowska, A., Litwin, T., Dusek, P., Ferenci, P., Lutsenko, S., Medici, V., et al. (2018). Wilson disease. *Nat. Rev. Dis. Primers.* 4:21. doi: 10.1038/s41572-018-0018-3

Dusek, P., Bahn, E., Litwin, T., Jabłonka-Salach, K., Łuciuk, A., Huelnhagen, T., et al. (2017). Brain iron accumulation in Wilson disease: a post mortem 7 tesla MRI - histopathological study. *Neuropathol. Appl. Neurobiol.* 43, 514–532. doi: 10.1111/nan.12341

Dusek, P., Smolinski, L., Redzia-Ogrodnik, B., Golebiowski, M., Skowronska, M., Poujois, A., et al. (2020). Semiquantitative scale for assessing brain MRI abnormalities in Wilson disease: a validation study. *Mov. Disord.* 35, 994–1001. doi: 10.1002/mds.28018

Favrole, P., Chabriat, H., Guichard, J. P., and Woimant, F. (2006). Clinical correlates of cerebral water diffusion in Wilson disease. *Neurology* 66, 384–389. doi: 10.1212/01.wnl.0000196482.71636.7d

Hefter, H., Tezayak, O., and Rosenthal, D. (2018). Long-term outcome of neurological Wilson's disease. *Parkinsonism Relat. Disord.* 49, 48–53. doi: 10.1016/j.parkreldis.2018.01.007

Hou, H., Chen, D., Liu, J., Feng, L., Zhang, J., Liang, X., et al. (2022). Clinical and genetic analysis in neurological Wilson's disease patients with neurological worsening following Chelator therapy. *Front. Genet.* 13:875694. doi: 10.3389/fgene.2022.875694

Inherited Metabolic Liver Disease Collaboration Group, Chinese Society of Hepatology, Chinese Medical Association (2022). Guidelines for the Diagnosis and Treatment of Hepatolenticular Degeneration (2022nd Edition). *Zhonghua Gan Zang Bing Za Zhi* 30, 9–20. doi: 10.3760/cma.j.cn501113-20211217-00603

Li, A., Zhou, X., and Pu, X. (2019). Relationship between clinical features and abnormal signals tested by quantitative method of brain magnetic resonance imaging in Wilson disease patients. *J. Clin. Med.* 35, 2142–2147. doi: 10.3969/j.issn.1006-5725.2019.13.025

Masełbas, W., Chabik, G., and Członkowska, A. (2010). Persistence with treatment in patients with Wilson disease. *Neurol. Neurochir. Pol.* 44, 260–263. doi: 10.1016/S0028-3843(14)60040-2

Pulai, S., Biswas, A., Roy, A., Guin, D. S., Pandit, A., Gangopadhyay, G., et al. (2014). Clinical features, MRI brain, and MRS abnormalities of drug-naïve neurologic Wilson's disease. *Neurol. India* 62, 153–158. doi: 10.4103/0028-3886.132349

Rędzia-Ogrodnik, B., Członkowska, A., Bembenek, J., Antos, A., Kurkowska-Jastrzębska, I., Skowrońska, M., et al. (2022). Brain magnetic resonance imaging and severity of neurological disease in Wilson's disease - the neuroradiological correlations. *Neurol. Sci.* 43, 4405–4412. doi: 10.1007/s10072-022-06001-2

Selwa, L. M., Vanderzant, C. W., Brunberg, J. A., Brewer, G. J., Drury, I., and Beydoun, A. (1993). Correlation of evoked potential and MRI findings in Wilson's disease. *Neurology* 43, 2059–2064. doi: 10.1212/WNL.43.10.2059

Sener, R. N. (2003). Diffusion MR imaging changes associated with Wilson disease. *AJNR Am. J. Neuroradiol.* 24, 965–967. doi: 10.1034/j.1600-0455.2003.00077.x

Shribman, S., Bocchetta, M., Sudre, C. H., Acosta-Cabronero, J., Burrows, M., Cook, P., et al. (2022). Neuroimaging correlates of brain injury in Wilson's disease: a multimodal, whole-brain MRI study. *Brain* 145, 263–275. doi: 10.1093/brain/awab274

Sinha, S., Taly, A. B., Prashanth, L. K., Ravishankar, S., Arunodaya, G. R., and Vasudev, M. K. (2007). Sequential MRI changes in Wilson's disease with de-coppering therapy: a study of 50 patients. *Br. J. Radiol.* 80, 744–749. doi: 10.1259/bjr/48911350

Sinha, S., Taly, A. B., Ravishankar, S., Prashanth, L. K., Venugopal, K. S., Arunodaya, G. R., et al. (2006). Wilson's disease: cranial MRI observations and clinical correlation. *Neuroradiology* 48, 613–621. doi: 10.1007/s00234-006-0101-4

Smolinski, L., Litwin, T., Redzia-Ogrodnik, B., Dziezyc, K., Kurkowska-Jastrzebska, I., and Czlonkowska, A. (2019). Brain volume is related to neurological impairment and to copper overload in Wilson's disease. *Neurol. Sci.* 40, 2089–2095. doi: 10.1007/s10072-019-03942-z

Walshe, J. M., and Yealland, M. (1993). Chelation treatment of neurological Wilson's disease. *Q. J. Med.* 86, 197–204.

Yang, J., Li, X., Yang, R., Yu, X., Yu, C., Qian, Y., et al. (2015). Susceptibility-weighted imaging manifestations in the brain of Wilson's disease patients. *PLoS One* 10:e0125100. doi: 10.1371/journal.pone.0125100

Yu, X. E., Gao, S., Yang, R. M., and Han, Y. Z. (2019). MR imaging of the brain in neurologic Wilson disease. *AJNR Am. J. Neuroradiol.* 40, 178–183. doi: 10.3174/ajnr.A5936

Zhong, W., Huang, Z., and Tang, X. (2019). A study of brain MRI characteristics and clinical features in 76 cases of Wilson's disease. *J. Clin. Neurosci.* 59, 167–174. doi: 10.1016/j.jocn.2018.10.096

Zhou, Z. H., Wu, Y. F., Cao, J., Hu, J. Y., Han, Y. Z., Hong, M. F., et al. (2019). Characteristics of neurological Wilson's disease with corpus callosum abnormalities. *BMC Neurol.* 19:85. doi: 10.1186/s12883-019-1313-7

Ziemssen, T., Smolinski, L., Członkowska, A., Akgun, K., Antos, A., Bembenek, J., et al. (2022). Serum neurofilament light chain and initial severity of neurological disease predict the early neurological deterioration in Wilson's disease. *Acta Neurol. Belg.* 123, 917–925. doi: 10.1007/s13760-022-02091-z

frontiers | Frontiers in Neuroscience

TYPE Original Research
PUBLISHED 20 September 2023
DOI 10.3389/fnins.2023.1229371

OPEN ACCESS

EDITED BY
Xi-Nian Zuo,
Beijing Normal University, China

REVIEWED BY
Ahmadreza Keihani,
University of Pittsburgh, United States
Chang Wei Tan,
Monash University, Australia

*CORRESPONDENCE
Jürgen Dammers
✉ j.dammers@fz-juelich.de

†These authors have contributed equally to this work

RECEIVED 26 May 2023
ACCEPTED 04 September 2023
PUBLISHED 20 September 2023

CITATION
Kampel N, Kiefer CM, Shah NJ, Neuner I and Dammers J (2023) Neural fingerprinting on MEG time series using MiniRocket.
Front. Neurosci. 17:1229371.
doi: 10.3389/fnins.2023.1229371

Neural fingerprinting on MEG time series using MiniRocket

Nikolas Kampel[1,2,3†], Christian M. Kiefer[1,4†], N. Jon Shah[1,5,6,7], Irene Neuner[1,3,5,8] and Jürgen Dammers[1,2,3]

[1]Institute of Neuroscience and Medicine (INM-4), Forschungszentrum Jülich GmbH, Jülich, Germany, [2]Faculty of Medicine, RWTH Aachen University, Aachen, Germany, [3]Jülich Aachen Research Alliance (JARA) – CSD – Center for Simulation and Data Science, Aachen, Germany, [4]Faculty of Mathematics, Computer Science and Natural Sciences, RWTH Aachen University, Aachen, Germany, [5]Jülich Aachen Research Alliance (JARA) – BRAIN – Translational Medicine, Aachen, Germany, [6]Institute of Neuroscience and Medicine (INM-11), Jülich Aachen Research Alliance (JARA), Forschungszentrum Jülich GmbH, Jülich, Germany, [7]Department of Neurology, University Hospital RWTH Aachen, Aachen, Germany, [8]Department of Psychiatry, Psychotherapy and Psychosomatics, RWTH Aachen University, Aachen, Germany

Neural fingerprinting is the identification of individuals in a cohort based on neuroimaging recordings of brain activity. In magneto- and electroencephalography (M/EEG), it is common practice to use second-order statistical measures, such as correlation or connectivity matrices, when neural fingerprinting is performed. These measures or features typically require coupling between signal channels and often ignore the individual temporal dynamics. In this study, we show that, following recent advances in multivariate time series classification, such as the development of the RandOm Convolutional KErnel Transformation (ROCKET) classifier, it is possible to perform classification directly on short time segments from MEG resting-state recordings with remarkably high classification accuracies. In a cohort of 124 subjects, it was possible to assign windows of time series of 1 s in duration to the correct subject with above 99% accuracy. The achieved accuracies are vastly superior to those of previous methods while simultaneously requiring considerably shorter time segments.

KEYWORDS

neural fingerprinting, resting state, rocket, time series classification, magnetoencephalogra, MEG, machine learning

1. Introduction

Historically, neuroscientists have inferred knowledge about the brain from the population level, and commonalities between individuals were used as the foundation for our understanding of the brain (van Horn et al., 2008). However, it is now known that individual variations may convey important information, and disregarding them as noise may limit our insight into the brain [see (van Horn et al., 2008) for a review]. Placing the individual as the focus of research led to the emergence of the field of neural fingerprinting, i.e., the identification of individuals in a cohort using different neuroimaging modalities such as magnetic resonance imaging (Wachinger et al., 2015; Valizadeh et al., 2018), functional magnetic resonance imaging (Miranda-Dominguez et al., 2014; Finn et al., 2015; Kaufmann et al., 2017; Amico and Goñi, 2018; Bari et al., 2019), functional near-infrared spectroscopy (de Souza Rodrigues et al., 2019), electroencephalography (Rocca et al., 2014; Fraschini et al., 2015; Kong et al., 2019), and magnetoencephalography (MEG) (da Silva Castanheira et al., 2021; Sareen et al., 2021).

The development of neuroimaging techniques has further led to the possibility of using second-order statistical summaries of brain activity, such as functional connectomes, as the basis for neural fingerprinting (Sareen et al., 2021). However, functional connectomes are not necessarily required for neural fingerprinting as neural fingerprinting can be performed directly on the time series from which the connectomes are usually computed. In fact, (multivariate) time series classification ((M)TSC), where unlabeled time series are assigned to one of multiple classes, is an exciting, yet challenging, field of research (Keogh and Kasetty, 2003; Yang and Wu, 2006). For example, many practical applications have emerged for (M)TSC in fields such as biology, medicine, finance, or engineering (Keogh and Kasetty, 2003). Despite these advances, applications have been limited due to the fact that time series classification methods are computationally expensive (Abanda et al., 2019).

Recently, a fast approach for time series classification, known as RandOmConvolutionalKErnelTransform (ROCKET), has been introduced and requires only a fraction of the computational expense of most existing methods (Dempster et al., 2020). Its new variant, called MiniRocket (MINImally RandOm Convolutional KErnel Transform), introduced by the same group, provides similar or better accuracy but is up to 75 times faster compared to ROCKET on larger datasets (Dempster et al., 2021).

Given these capabilities, we sought to reduce the complexity of neural fingerprinting by directly applying the multivariate time series classifier MiniRocket to source time courses from MEG resting-state recordings. Data requirements for training a successful classifier were investigated. Furthermore, it has been suggested that day-to-day variations in the background noise may have a significant impact on the classification results (da Silva Castanheira et al., 2021). Therefore, we conducted experiments to estimate the effect of background noise by incorporating empty-room recordings (i.e., noise recordings taken without a subject being measured) into the training and testing datasets.

Using MiniRocket, it was possible to differentiate between MEG resting-state recordings from 124 subjects with accuracies exceeding 99.5%. A set of parameters providing a good trade-off between accuracy, speed, and amount of available data was investigated. Based on our findings, the impact of background noise on the classification results for fingerprinting appears to be minimal.

2. Methods

2.1. Time series classification

In a similar way to image classification, TSC also requires the input values to be ordered, and it is possible that important information relevant to the classification might be buried in the ordering process (Bagnall et al., 2017). Moreover, in the case of a multivariate time series, discriminatory features might even depend on interactions between the individual time series, and special multivariate classifiers are needed to deal with this added complexity (Ruiz et al., 2021). While it is generally possible to adapt strictly univariate classifiers to the multivariate case, for example, by using an ensemble of separate univariate classifiers for each of the multivariate dimensions, inter-dimensional dependencies are ignored, and information is inevitably lost (Ruiz et al., 2021).

A variety of MTSC methods, which include ensembles of univariate classifiers such as Hierarchical Vote Collective of Transformation-based Ensembles (HIVE-COTE) (Bagnall et al., 2020), dedicated multivariate TSC methods such as RandOm Convolutional KErnel Transformation (ROCKET) (Dempster et al., 2020), MINImally RandOm Convolutional KErnel Transform [MiniRocket, (Dempster et al., 2021)] and deep-learning approaches such as InceptionTime (Ismail Fawaz et al., 2020), were recently reviewed for their performance on openly available TSC datasets (Ruiz et al., 2021). Due to the exceptionally fast training times and state-of-the-art classification accuracy, we elected to use MiniRocket in this paper.

2.1.1. Rocket

The basic principle behind ROCKET is to randomly generate a large number of convolutional kernels, which are then applied to the multivariate time series to obtain transformed features. Finally, a linear classifier, such as logistic regression or ridge regression, is trained on the transformed ROCKET features (Dempster et al., 2020). Since the training complexity is linear in both the length of the time series and the number of training samples, ROCKET is an attractive, scalable algorithm for large datasets (Dempster et al., 2020).

There are five basic parameters that characterize a random convolutional ROCKET kernel: length, l_k and dilation, d, the individual weights, w, a bias term, b, and the use of padding (Ismail Fawaz et al., 2019; Dempster et al., 2020). The convolution, C, of the ROCKET kernel with a univariate time series can be computed by performing a sliding dot product operation over time t across the entire time series:

$$C_t = X_t * w + b = \left(\sum_{j=0}^{l_k - 1} X_{t+(j \times d)} w_j \times w_j \right) + b. \qquad (1)$$

Since patterns in the time series congruent with the kernel will result in large values (Ismail Fawaz et al., 2019; Dempster et al., 2020), basic patterns or shapes can thus be detected. In ROCKET, global max pooling and the proportion of positive values (ppv) pooling are applied separately to the kernel output, providing two features per kernel. By using ppv pooling, ROCKET weights the prevalence of a feature captured by the kernel output over n time samples, t.

$$\mathrm{ppv} = \frac{1}{n} \sum_{i=0}^{n-1} \left[C_i > 0 \right]. \qquad (2)$$

By using different values for the dilation, it is possible to capture patterns at different scales, and it is even possible to capture frequency information with larger dilation values corresponding to smaller frequencies and vice versa (Yu and Koltun, 2016).

ROCKET generates the kernel parameters based on several predefined rules. First, the length of a kernel is selected with uniform probability from the set {7, 9, 11}. Then, the weights are sampled from a normal distribution, $w_j N(0,1)$, and subsequently mean centered, i.e., after all weights have been determined, the mean weight is subtracted. A uniform distribution is used to sample the bias term with $bU(-1,1)$. The dilation is sampled from an exponential scale with $d = [2^x]$ where $xU(0, A)$ and $A = \log_2(l_{\text{input}}{}^{-1}/l_k{}^{-1})$. Finally, a binary decision with equal probability determines whether padding is used, i.e., whether $(l_k - 1)/2$ zeros are added to the beginning and the end of the time series (Dempster et al., 2020).

For multivariate time series, an additional sixth kernel parameter is provided, which determines the particular dimensions a given kernel is applied to Ruiz et al. (2021). The kernels then become matrices with independently generated weights for each dimension, and consequently, the convolution is computed as the sliding dot product between two matrices (Ruiz et al., 2021).

The feature that makes ROCKET special, and distinguishes it from earlier methods using (random) convolutional kernels, is the huge number and variety of kernels (10,000 per default) (Dempster et al., 2020). Furthermore, a key contributor to the ability of ROCKET to detect patterns at different scales and frequencies is its effective use of dilation (Dempster et al., 2020). Yet, the potentially most important aspect of ROCKET's success is that ROCKET computes two features for each kernel: the maximum value (similar to global max pooling) and a novel feature called the proportion of positive values, which provides the classifier with information about the prevalence of a given pattern in the time series (Dempster et al., 2020). Thus, the use of effective features and the combination of a large number of kernels enable ROCKET to distinguish between a multitude of time series patterns for the purpose of classification.

Finally, the ROCKET features are used to train a linear classifier. Logistic regression with stochastic gradient descent was recommended for very large datasets where the number of training examples is significantly higher than the number of features while, for smaller datasets, the authors recommended the use of ridge regression with cross-validation for the regularization parameter (Dempster et al., 2020).

2.1.2. MiniRocket

The major difference between MiniRocket and ROCKET is that it uses a fixed set of convolutional kernels instead of kernels with random hyperparameters. In brief, the kernel length, l_k in MiniRocket is fixed to 9 instead of {7, 9, 11}, and the kernel weights are restricted to either −1 or 2 instead of a weight drawn from a normal distribution between 0 and 1. Moreover, MiniRocket uses fixed padding, and the maximum number of dilation per kernel is restricted to 32 (Dempster et al., 2021). These features allow the method to minimize the number of hyperparameters per kernel, enabling faster computation. Moreover, MiniRocket computes the kernel weights, w and $-w$ and the ppv at the same time by using a trick: with the proportion of negative values being $\text{pnv} = 1 - \text{ppv}$, MiniRocket uses the ppv of the inverted kernel without increasing the number of convolutions, thus doubling the number of kernels applied using a single convolution. In addition, several mathematical optimizations are applied [for details, see (Dempster et al., 2021)] that makes MiniRocket much faster (up to 75 times) compared to ROCKET, while maintaining the same accuracy (Dempster et al., 2021).

2.2. The data

MEG recordings from two different sites (United States and Germany) were used for analysis. The first dataset was obtained from the Human Connectome Project (HCP), while the second dataset was provided by the Institute of Neuroscience and Medicine at Forschungszentrum Jülich (FZJ), Germany. MEG data in the two datasets were recorded at various points in time. For each subject, a minimum of two resting-state measurements and at least one empty-room recording were available. The total number of MEG recordings used was 372 from 124 different subjects.

2.2.1. Dataset HCP

The Human Connectome Project (HCP) offers open access to a dataset consisting of MEG resting-state recordings and anatomical MR scans for 89 subjects acquired at St. Louis University (Van Essen et al., 2012, 2013; Larson-Prior et al., 2013; Hodge et al., 2016). From this dataset, we used recordings from 84 subjects, 44% of whom were female, and the mean age was 28.9 ± 3.6 years. Between two and three resting-state recordings with durations of approximately 6 min were available for each subject. Furthermore, an empty-room measurement of approximately 5 min in duration was available for each subject.

All MEG data were acquired using a whole-head MAGNES 3600 system (4D Neuroimaging, San Diego, CA) with 248 magnetometers and 23 reference channels at a sampling rate of 2034 Hz. ECG and EOG were acquired along with the MEG signals. At the beginning of each MEG recording session, the subject's head shape, together with the positions of the localizer coils, were digitized for the alignment with the anatomical MR scans, which were recorded as T1-weighted volumes with 0.7 mm resolution using a Skyra 3 T scanner (Siemens Healthcare GmbH, Erlangen, Germany).

2.2.2. Dataset FZJ

The FZJ dataset consists of two different MEG resting-state recording sessions. The first one was acquired from 20 male subjects in 2012 and 2013, and the second set was acquired from another set of 20 subjects (55% female) in 2017 and 2018. The mean ages were 26.2+/− 4.3 and 26.6+/− 4.9 years, respectively. While the recordings from 2012 and 2013 had a duration of approximately 3 min, followed by empty room recordings of about 5 min, the recordings from 2017 and 2018 had a duration of 6 min, followed by empty room recordings of between 10 and 15 min. Similar to the HCP data, a whole-head MAGNES 3600 system with 248 magnetometers and 23 reference channels was used; however, the sampling rate was 1017.25 Hz.

Electrocardiography (ECG) and electrooculography (EOG) were recorded using the MAGNES 3600 system along with the MEG measurements. An external BrainAmp ExG system (Brain Products, Gilching, Germany) was used to record ECG and EOG at a sampling rate of 5,000 Hz for the later recordings (2017 and 2018). The subjects' head shapes were digitized prior to the MEG recording sessions for alignment with the anatomical MR scans, which were recorded using a MAGNETOM 3 T scanner (Siemens, Munich, Germany) with MPRAGE (Mugler and Brookeman, 1990).

2.3. Data analysis

Python 3.10 was used for data analysis, with the main packages being MNE-Python v1.3.1 (Gramfort et al., 2013, 2014), Scikit-learn v1.2.2 (Pedregosa et al., 2011), and sktime v0.17.1 (Löning et al., 2019). The source spaces were constructed from the anatomical MR scans based on an octahedral mesh using FreeSurfer (Dale et al., 1999; Fischl et al., 1999).

2.3.1. Pre-processing

The first step in the pre-processing pipeline was to identify MEG channels with strong artifacts. An in-house machine learning algorithm based on density-based spatial clustering of applications with noise (DBSCAN) (Ester et al., 1996), which scans for artifacts both in the time and the frequency domain, was used for this purpose. Channels and time segments with strong artifacts were annotated as 'bad' and were followed by a visual inspection of the automated procedure. Furthermore, all recordings were also visually inspected for segments containing unusually strong artifacts (e.g., muscle artifacts), which were discarded from the analysis. The signals of the annotated bad channels were subsequently replaced by virtual channels using the interpolation method as implemented in (Gramfort et al., 2013, 2014). Table 1 summarizes the duration of the MEG recordings used for each dataset and the recording type (resting-state or empty room data).

Next, the MEG signals were band-pass filtered from 1 to 200 Hz. Environmental and power line noise was removed by subtraction of appropriate weighted reference signals from the band-pass filtered (0.1 to 5 Hz) references signals as described in (Robinson, 1989). Furthermore, power-line noise (50 Hz in Germany and 60 Hz in the United States of America) plus harmonics were isolated in the reference channels using anti-notch filters at these frequencies. The weighted signal from the reference channels was then subtracted from the signal channels to reduce power-line noise.

Finally, ECG and EOG artifacts were removed using independent component analysis (ICA) (Hyvärinen and Oja, 2000; Dammers et al., 2008). Components containing significant contributions of cardiac or ocular activity were removed prior to source localization (Hyvärinen and Oja, 2000; Dammers et al., 2008).

2.3.2. Source localization and extraction of label time courses

The pre-processed, continuous MEG resting-state signals were projected onto the source space using the minimum-norm estimate (MNE) method (Hämäläinen and Ilmoniemi, 1994). The source spaces were then divided into 68 (34 per hemisphere) anatomical regions (labels) based on the Desikan-Killiany Atlas (Desikan et al., 2006). As the frontal pole region is very small in this particular atlas, the number of vertices identified was very small, and no vertices were found in this region for one subject. Therefore, this subject was excluded from the analysis. Following this step, a single representative source time course was extracted for each region as the mean time course of all vertices inside this brain region. Finally, these continuous source time courses were split into time segments of different lengths (hereafter referred to as 'trials').

TABLE 1 Median recording times and its ranges for the type of recording after the removal of bad data segments.

Dataset	Rec. type	T_{median}	T_{max}	T_{min}
FZJ	Empty	460	911	271
FZJ	rs1	220	299	136
FZJ	rs2	231	298	151
HCP	Empty	275	300	171
HCP	rs1	291	300	243
HCP	rs2	293	300	232

Times (T) in seconds.

The same pre-processing and source localization steps were repeated for the empty-room data, with the data being treated as if it were a subject's recording. The empty-room data, which contain environmental noise only, are recorded directly after the MEG recordings. To further investigate whether day-to-day environmental noise variability causes significant differences, all empty-room recordings were also projected onto the same source space of a randomly selected subject. In this way, the influence of the background noise can be minimized, allowing the classifier to use the recordings for fingerprinting decisions.

2.4. Classification

sktime (version 0.17.1) was used to perform the MiniRocket transformation of the MEG trials, and scikit-learn (version 1.2.2) was used to fit a ridge regression classifier to the transformed features.

To evaluate the classification performance, we compute the accuracy (ACC) as the ratio of the number of correctly classified instances to the total number of instances. In relation to neural fingerprinting, we test how accurately the model detects whether two different datasets from the same subject match. In addition to the ACC, the Precision, the Recall, and the F1-Score are computed.

The Precision refers to the proportion of correctly predicted positive instances out of all the instances predicted as positive by the model and is defined by Precision = TP/(TP + FP), with TP and FP being the True Positive and False Positives, respectively. A high precision value indicates that the model has a low rate of false positives. Recall (a.k.a. Sensitivity) is defined by Recall = TP/(TP + FN), with FN being the False Negatives, and measures the proportion of actual positive instances that are correctly identified by the model. Higher Recall indicates that the model is better at identifying all relevant positive instances in the dataset. The F1-Score is defined by F1-Score = 2 * (Precision * Recall)/(Precision + Recall). Thus, the F1-Score provides a balance between Precision and Recall and ranges from 0 to 1, where 1 represents perfect precision and recall, and 0 indicates poor performance. We report the macro-average F1-Score, Precision, and Recall for each class independently and then take the average across all classes to ensure that the performance of each class (the subject) is given equal importance.

To evaluate the overall performance of the model, we employed a leave-one-out method (LOOM) at the subject level (Schlögl and Supp, 2006). Specifically, each subject was left out of the training and test sets once. This results in a total of 124 mean scores (e.g., accuracy) for each of the two training and test variants, for which the overall mean and standard deviation are computed. In this way, the stability of the model performance and the influence of data from individuals can be evaluated by computing the variance of the performance metrics.

2.4.1. Resting-state neural fingerprinting

To investigate the performance of the classifier with respect to identifying a specific subject within the cohort, time series originating from the first resting-state recording (rs1) were used for training, while time series originating from the second resting-state recording (rs2) were used for testing. This order was then reversed to determine a broader estimate of the classifier's performance.

The continuous source time course of each brain region was used for a *z*-scored normalization. A random but fixed subset of trials was sampled from each recording to ensure balanced datasets across subjects. To gauge the variance expected due to the random nature of the method, we repeated the procedure ten times using random selections of trials and kernel initializations. The classifier's dependence on several parameters was tested by means of varying the number of trials used per subject in the training set, the trial duration, and the number of ROCKET kernels used.

2.4.2. Empty-room noise

To assess the impact of the day-to-day variations in the background noise with respect to the classification performance, we performed a control experiment with identical settings but with no subject in the scanner. These so-called empty room recordings were performed directly after the subject recording and were labeled with the same ID as the subject. In other words, the environmental noise data is used to have a third control condition to evaluate the model. With the empty-room noise data as a third set of recordings (rs1, rs2, empty), we performed the training and the testing of the model for all possible combinations. Each experiment was repeated ten times with a random selection of trials as well as different random kernel initializations. The mean accuracy was computed for each combination.

3. Results

3.1. Resting-state neural fingerprinting and its dependency on parameters

The classification of two MEG datasets recorded from the same subjects on the same day revealed remarkably high accuracy scores of about 99% using MiniRocket. The impact of important parameters on the classification accuracy was tested by varying the number of kernels, the number of trials, and the trial duration. While investigating the impact of one parameter, all other parameters were fixed as follows (unless stated otherwise): the number of kernels was set to 3,500, the number of trials to 15, and its duration to 1.5 s.

Figure 1 shows the dependency of the accuracy scores on the number of kernels used in MiniRocket. The figure shows a sharp increase in accuracy between 100 and 500 kernels, with scores already above 96% for 500 kernels. For the number of kernels ranging from 1,000 to 5,000, there was a relatively marginal increase in accuracy, which only ranged from about 98.9 to 99.5%. All results, including the upper and lower range, can be found in Table 2.

To estimate the impact of the number of time segments used on the classification result, the number of trials was gradually increased until no further change in accuracy was observed. Figure 2 shows the dependence of accuracy scores on the number of training trials. The figure shows that when five or more trials are used, classification accuracies of 98% and above can be achieved. Only a marginal increase in accuracy, ranging from about 99.3 to 99.6%, was achieved from 10 to 30 trials (Table 2).

The dependency of the accuracy scores on the trial duration is shown in Figure 3. For segment durations ranging from 0.1 s to 0.5 s, there is a sharp increase in accuracy, while for durations of 1 s in length, scores above 99.4% could already be achieved. Only a marginal increase in accuracy, from 99.5 to 99.6%, was achieved for durations ranging from 2.0 s to 5.0 s. A summary of all results and combinations is shown in Table 2.

The MiniRocket classification accuracy scores obtained through the LOOM method for neural fingerprinting based on resting-state data are as follows: The average accuracy score after cross-validation for training on rs1 and testing on rs2 was 99.15% ± 0.078%. Similarly, the mean Recall and Precision were found to be 99.15% ± 0.078 and 98.72% ± 0.425%, respectively, and the F1-Score was 98.80% ± 0.124% (Table 3). For training on rs2 and testing on rs1, the average accuracy score was found to be slightly larger with 99.96% ± 0.036%, as compared to the accuracy of 99.15% for training on rs1 and testing on rs2. This tendency was also observed in the other three metrics (cf. Table 3). Since the probability of obtaining a match for a single subject out of 124 subjects is 1/124, which is about 0.0081, the chance level in our experiment is approximately 0.81%. The difference in accuracy

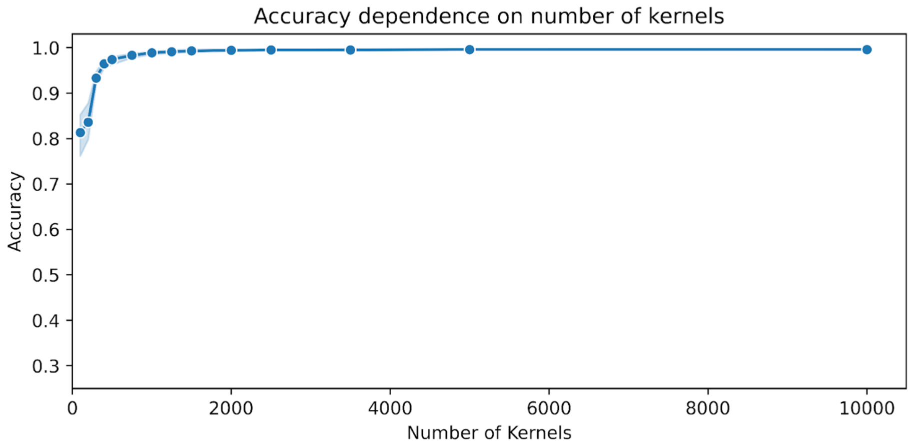

FIGURE 1
Dependence of the accuracy scores on the number of MiniRocket kernels. The classifier was trained on 15 time segments with a duration of 1.5 s per segment. The blue shaded area indicates the upper and lower range of the classification accuracy between the 10 repetitions with a random selection of time segments and a random initialization of kernels.

TABLE 2 MiniRocket accuracy scores dependent on several parameters.

Dependence on number of kernels (15 training trials, 1.5 s duration)			
Number of kernels	Mean accuracy	Min accuracy	Max accuracy
100	81.32	76.16	85.27
200	83.6	79.78	87.8
300	93.33	91.96	94.73
400	96.45	95.51	97.34
500	97.37	96.26	98.01
750	98.32	97.74	98.71
1,000	98.87	98.52	99.06
1,250	99.11	98.79	99.52
1,500	99.3	98.98	99.6
2000	99.42	99.22	99.6
2,500	99.49	99.3	99.57
3,500	99.51	99.3	99.7
5,000	99.57	99.49	99.65
10,000	99.59	99.49	99.65

Dependence number of trials (3,500 kernels, trial duration 1.5)			
Number of trials	Mean accuracy	Min accuracy	Max accuracy
1	63.63	56.45	70.16
2	90.18	86.29	93.15
3	96.36	94.76	97.58
4	97.97	97.48	98.29
5	98.63	98.31	98.87
6	98.97	98.66	99.26
7	99.11	98.85	99.37
8	99.22	98.94	99.5
9	99.31	99.06	99.55
10	99.35	99.15	99.52
12	99.45	99.13	99.56
15	99.51	99.3	99.7
20	99.57	99.54	99.6
25	99.58	99.56	99.61

Dependence on trail duration (3,500 kernels, 15 training trails)			
Trail duration	Mean accuracy	Min accuracy	Max accuracy
0.1	29.56	26.02	31.77
0.2	71.15	67.66	73.76
0.3	89.64	88.12	91.64
0.4	95.67	95.22	96.26
0.5	97.88	97.58	98.28
0.6	98.58	98.2	99.03
0.7	99.01	98.79	99.33
0.8	99.2	98.87	99.46
0.9	99.28	99.11	99.52
1.0	99.37	99.09	99.6
1.25	99.5	99.33	99.57
1.5	99.51	99.3	99.7
2.0	99.55	99.33	99.65
2.5	99.58	99.49	99.62
3.0	99.6	99.57	99.62
3.5	99.6	99.57	99.68
4.0	99.6	99.54	99.68
4.5	99.61	99.57	99.7
5.0	99.6	99.57	99.68

between the two classification tests were found to be significant, but with a change in score around the chance level (0.80–1.24%).

3.2. Influence of empty-room noise

Ten random trials were sampled per subject and per set with a trial duration of 1.5 s and 3,500 kernels. Whenever data originated from the same recordings, the continuous signal for each subject was split into two parts, and the trials for training and testing were sampled from the first and second half of the recording, respectively.

Figure 4 shows the dependence of the MiniRocket classifier accuracy scores on different combinations of training and test sets. The results show that accuracies above 99.3% were achieved for all combinations of training and testing on resting-state data (rs1 vs. rs2 and rs2 vs. rs1). For resting-state recordings evaluated against the empty room recordings from the same day, the accuracies were close to the chance level, as depicted in Figure 4. In the case of empty vs. empty room recordings, the classifier achieved a low accuracy of 7.9%.

4. Discussion

There are many promising applications of multivariate time series classifications (MTSC) in medicine and neuroscience, including in the diagnosis of medical conditions, personalized treatment planning, and the development of brain-computer interfaces (BCIs). With this study, we have shown that it is possible to perform neural fingerprinting directly on MEG time series without performing feature engineering. This is, to the best of our knowledge, the first time that neural fingerprinting has been achieved based on magnetic field changes in single trials of MEG time series recordings without the need for a feature-based analysis. Furthermore, the MiniRocket approach used in the study required fewer data (shorter trials) for successful classification and also improved accuracy. For example, previous MEG

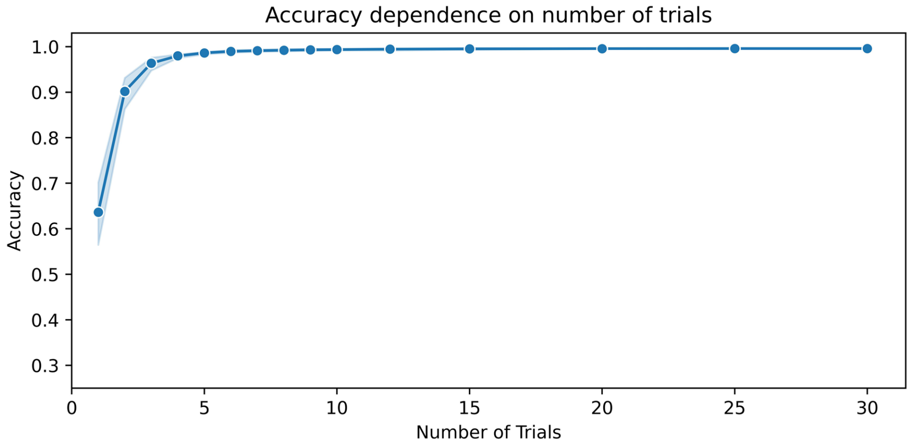

FIGURE 2
Dependence of the accuracy scores on the number of training segments. The number of kernels for the MiniRocket classifier was set to 3,500. The duration of the time segments was set to 1.5 s. The blue shaded area indicates the upper and lower range of the classification accuracy between the 10 repetitions with a random selection of time segments and a random initialization of kernels.

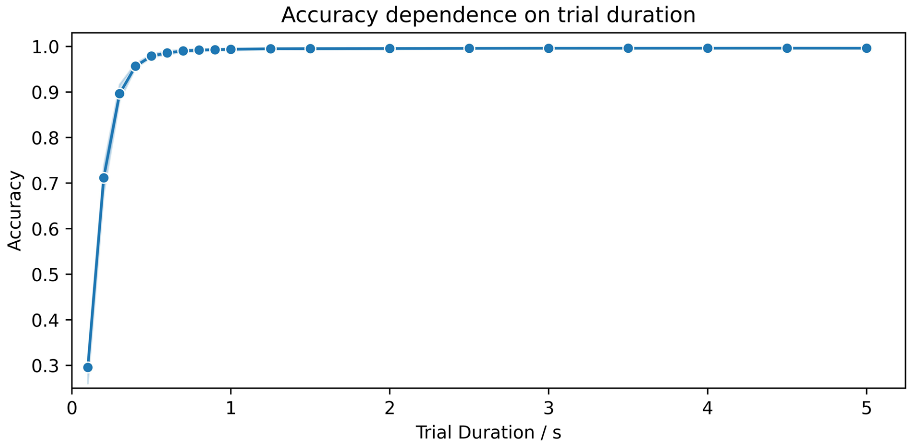

FIGURE 3
Dependence of the accuracy scores on the duration of the time segments. The number of kernels for the MiniRocket classifier was set to 3,500 and trained on 15 time segments. The duration of segments varied from 0.1 to 5 s. The blue shaded area indicates the upper and lower range of the classification accuracy between the 10 repetitions with a random selection of time segments and a random initialization of kernels.

TABLE 3 Loom-based performance scores for two classification tests with the number of kernels set to 3,500, the number of trials to 15, and its duration to 1.5 s.

Metric	rs1 – rs2	rs2 – rs1
Accuracy	99.15 ± 0.0779	99.96 ± 0.0364
Precision	98.72 ± 0.4250	99.96 ± 0.0338
Recall	99.15 ± 0.0779	99.96 ± 0.0364
F1-Score	98.80 ± 0.1238	99.96 ± 0.0364

publications reached MEG resting-state classification accuracies with trial lengths of 30 s in healthy controls of about 94.9–96.2% (da Silva Castanheira et al., 2021), and 94.5–98.2% at trial lengths of 8 s (Sareen et al., 2021). In contrast, MiniRocket analysis with 3,500 kernels achieved a classification accuracy of over 99% when training the model on as little as 15 s of data and testing it on 1 s time segments. These results demonstrate that substantially fewer data are needed for accurate classification in comparison with previous approaches that use MEG data in combination with connectivity measures (Demuru et al., 2017; da Silva Castanheira et al., 2021; Sareen et al., 2021) or data from electroencephalography (EEG) using EEG power spectra (Kong et al., 2019; Demuru and Fraschini, 2020).

In our parameter investigation, we aimed to explore the minimum input data requirements while maintaining computational efficiency. Our tests on trial duration suggested that a minimum of 0.9 s and 15 trials were sufficient to achieve accuracies above 99%. In terms of the number of trials, we found that training a MiniRocket classifier with 3,500 kernels requires at least nine trials of 1.5 s length to achieve accuracies above 99%. During our exploration of the number of kernels, we observed that increasing the number of kernels led to improved results in the low data regime, at the expense of

FIGURE 4
Dependence of the accuracy scores of the MiniRocket classifier on different combinations of training and test sets. Since rest1, rest2, and empty were all recorded on the same day, it is possible to isolate the contribution of the daily background noise to the classification outcomes. The number of kernels for the MiniRocket classifier was set to 3,500. For both the training and test set, 10 time segments of 1.5 s were sampled from each of the subjects.

computational demand. We were surprised to find that accuracies saturated at a relatively low number of 3,500 kernels using a fixed set of 15 trials of 1.5 s duration, resulting in accuracies above 99.3% (Table 2).

Interestingly, we observed a small but significant difference in all metrics when we reversed the order of training and evaluation set using the LOOM method. Specifically, the accuracies were 99.96% when training on rs1 and testing on rs2, whereas they fell to 99.15% when the order was reversed (Table 3). This difference in accuracy of 0.81% is about chance level and may be due to a single subject only. In principle, we did not expect the accuracies to be identical as the two measurements will not be identical in practice. The subject's condition, such as mood and fatigue, is very likely to have an influence on the matching performance. Moreover, another source contributing to this difference may be due to a slight reduction in data quality over long recording sessions, possibly caused by increased subject movement due to fatigue or the execution of tasks before the second resting-state session. These findings raise the possibility that prioritizing training on datasets with higher complexity and diversity could be more crucial than employing the most complex data exclusively at the time of testing. However, in future work, it would be very interesting to investigate the model performance in a cohort of subjects where the temporal distance between rs1 and rs2 is increased by means of hours, days, weeks, and months.

In summary, these results are a proof of concept that subject differentiation can, in principle, be achieved directly from MEG brain recordings as short as 1 s to achieve high accuracies of about 99% using MiniRocket. This would greatly simplify current procedures as the technique does not require the selection of the best-performing feature for the classification model – as is the case when using functional connectomes (da Silva Castanheira et al., 2021; Sareen et al., 2021), for which the best-performing method needs to be determined. The high classification accuracy and the need for only relatively short segments of single trials data make MiniRocket a promising candidate for BCI research and motivate further research into the application of MiniRocket to MEG recordings.

4.1. Limitations

It has been suggested that day-to-day variations in the background noise during the recording may contribute significantly to the classification (da Silva Castanheira et al., 2021). We investigated this possibility by training the classifier on the subject's recording and testing on corresponding empty-room data, which were recorded soon after the experiment. While our study shows that training the classifier on empty-room data and applying it to the subject's resting-state data or vice versa did not result in the correct identification of individuals, and accuracies achieved on the cross-over of resting-state measurements and empty-room measurements were approximately at chance level, our findings suggest that the background noise may have a minor influence on the fingerprinting classification results. Notably, our analysis shows that matching empty room signals could be identified with an accuracy of approximately 8%.

To further investigate the classification performance and limitations on neural fingerprinting, we plan to implement a longitudinal study design to investigate the stability and performance of the classifier over time. Moreover, given that the subject is the class to be identified in this approach, we cannot split the data into training and test sets by subjects for the typical generalization purposes, which is a limitation of the method and is similar to a fingerprint analysis in criminal investigations, where a match can only be found if the suspect's fingerprints are already in the database.

Data availability statement

The original contributions presented in the study are included in the article/supplementary material, further inquiries can be directed to the corresponding author.

Ethics statement

The studies involving humans were approved by the ethical committee of the RWTH Aachen University, Aachen, under the code EK 249/22. The studies were conducted in accordance with the local legislation and institutional requirements. The participants provided their written informed consent to participate in this study.

Author contributions

NK and CK contributed equally to the conception and design of the study and to the data analysis. CK wrote the original draft. NS, IN, and JD supervised the study and acquired funding. All authors contributed to the article and approved the submitted version.

Funding

Funded by the Deutsche Forschungsgemeinschaft (DFG, German Research Foundation) – 491111487, by the HBP SGA3 – Human Brain Project Specific Grant Agreement 3 (2020-04-01–2023-03-31), Helmholtz Metadata Collaboration (HMC), by the Deutsche Forschungsgemeinschaft (DFG, German Research Foundation) – 368482240/GRK2416, and by the Joint Lab "Supercomputing and Modeling for the Human Brain.

Acknowledgments

The authors would like to thank Claire Rick for proofreading the manuscript. This study is part of the doctoral thesis (Dr. rer. medic.) of Nikolas Kampel at the Medical Faculty of the RWTH Aachen University, Germany.

Conflict of interest

The authors declare that the research was conducted in the absence of any commercial or financial relationships that could be construed as a potential conflict of interest.

Publisher's note

References

Abanda, A., Mori, U., and Lozano, J. A. (2019). A review on distance based time series classification. *Data Min. Knowl. Disc.* 33, 378–412. doi: 10.1007/s10618-018-0596-4

Amico, E., and Goñi, J. (2018). The quest for identifiability in human functional connectomes. *Sci. Rep.* 8:8254. doi: 10.1038/s41598-018-25089-1

Bagnall, A., Flynn, M., Large, J., Lines, J., and Middlehurst, M. (2020). On the usage and performance of the hierarchical vote collective of transformation-based ensembles version 1.0 (HIVE-COTE v1.0). Lecture Notes in Computer Science (including subseries Lecture Notes in Artificial Intelligence and Lecture Notes in Bioinformatics) 12588 LNAI, 3–18

Bagnall, A., Lines, J., Bostrom, A., Large, J., Keogh, E., et al. (2017). The great time series classification bake off: a review and experimental evaluation of recent algorithmic advances. *Data Min. Knowl. Disc.* 31, 606–660. doi: 10.1007/s10618-016-0483-9

Bari, S., Amico, E., Vike, N., Talavage, T. M., and Goñi, J. (2019). Uncovering multi-site identifiability based on resting-state functional connectomes. *NeuroImage* 202:115967. doi: 10.1016/j.neuroimage.2019.06.045

da Silva Castanheira, J., Orozco Perez, H. D., Misic, B., and Baillet, S. (2021). Brief segments of neurophysiological activity enable individual differentiation. *Nat. Commun.* 12:5713. doi: 10.1038/s41467-021-25895-8

Dale, A. M., Fischl, B., and Sereno, M. I. (1999). Cortical surface-based analysis: I Segmentation and surface reconstruction. *NeuroImage* 9, 179–194. doi: 10.1006/nimg.1998.0395

Dammers, J., Schiek, M., Boers, F., Silex, C., Zvyagintsev, M., Pietrzyk, U., et al. (2008). Integration of amplitude and phase statistics for complete artifact removal in independent components of neuromagnetic recordings. *IEEE Trans. Biomed. Eng.* 55, 2353–2362. doi: 10.1109/TBME.2008.926677

de Souza Rodrigues, J., Ribeiro, F. L., Sato, J. R., Mesquita, R. C., and Júnior, C. E. B. (2019). Identifying individuals using fNIRS-based cortical connectomes. *Biomed. Opt. Express* 10, 2889–2897. doi: 10.1364/boe.10.002889

Dempster, A., Petitjean, F., and Webb, G. I. (2020). ROCKET: exceptionally fast and accurate time series classification using random convolutional kernels. *Data Min. Knowl. Disc.* 34, 1454–1495. doi: 10.1007/s10618-020-00701-z

Dempster, A., Schmidt, D. F., and Webb, G. I. (2021). MiniRocket: a very fast (almost) deterministic transform for time series classification. Proceedings of the ACM SIGKDD International Conference on Knowledge Discovery and Data Mining (ACM), 248–257

Demuru, M., and Fraschini, M. (2020). EEG fingerprinting: subject-specific signature based on the aperiodic component of power spectrum. *Comput. Biol. Med.* 120:103748. doi: 10.1016/j.compbiomed.2020.103748

Demuru, M., Gouw, A. A., Hillebrand, A., Stam, C. J., van Dijk, B. W., Scheltens, P., et al. (2017). Functional and effective whole brain connectivity using magnetoencephalography to identify monozygotic twin pairs. *Sci. Rep.* 7:9685. doi: 10.1038/s41598-017-10235-y

Desikan, R. S., Ségonne, F., Fischl, B., Quinn, B. T., Dickerson, B. C., Blacker, D., et al. (2006). An automated labeling system for subdividing the human cerebral cortex on MRI scans into gyral based regions of interest. *NeuroImage* 31, 968–980. doi: 10.1016/j.neuroimage.2006.01.021

Ester, M., Kriegel, H.-P., Sander, J., and Xu, X. (1996). A density-based algorithm for discovering clusters in large spatial databases with noise. *KDD* 96, 226–231. https://dl.acm.org/doi/proceedings/10.5555/3001460

Finn, E. S., Shen, X., Scheinost, D., Rosenberg, M. D., Huang, J., Chun, M. M., et al. (2015). Functional connectome fingerprinting: identifying individuals using patterns of brain connectivity. *Nat. Neurosci.* 18, 1664–1671. doi: 10.1038/nn.4135

Fischl, B., Sereno, M. I., Tootell, R. B. H., and Dale, A. M. (1999). High-resolution inter subject averaging and a coordinate system for the cortical surface. *Hum. Brain Mapp.* 8, 272–284. doi: 10.1002/(SICI)1097-0193(1999)8:4<272::AID-HBM10>3.0.CO;2-4

Fraschini, M., Hillebrand, A., Demuru, M., Didaci, L., and Marcialis, G. L. (2015). An EEG-based biometric system using eigenvector centrality in resting state brain networks. *IEEE Signal Process Lett.* 22, 666–670. doi: 10.1109/LSP.2014.2367091

Gramfort, A., Luessi, M., Larson, E., Engemann, D. A., Strohmeier, D., Brodbeck, C., et al. (2013). MEG and EEG data analysis with MNE-python. *Front. Neurosci.* 7:267. doi: 10.3389/fnins.2013.00267

Gramfort, A., Luessi, M., Larson, E., Engemann, D. A., Strohmeier, D., Brodbeck, C., et al. (2014). MNE software for processing MEG and EEG data. *NeuroImage* 86, 446–460. doi: 10.1016/j.neuroimage.2013.10.027

Hämäläinen, M. S., and Ilmoniemi, R. J. (1994). Interpreting magnetic fields of the brain: minimum norm estimates. *Med. Biol. Eng. Comput.* 32, 35–42. doi: 10.1007/BF02512476

Hodge, M. R., Horton, W., Brown, T., Herrick, R., Olsen, T., Hileman, M. E., et al. (2016). ConnectomeDB-sharing human brain connectivity data. *NeuroImage* 124, 1102–1107. doi: 10.1016/j.neuroimage.2015.04.046

Hyvärinen, A., and Oja, E. (2000). Independent component analysis: algorithms and applications. *Neural Networks Off. J. Int. Neur. Netw. Soc.* 13, 411–430. doi: 10.1016/S0893-6080(00)00026-5

Ismail Fawaz, H., Forestier, G., Weber, J., Idoumghar, L., and Muller, P.-A. (2019). Deep learning for time series classification: a review. *Data Min. Knowl. Disc.* 33, 917–963. doi: 10.1007/s10618-019-00619-1

Ismail Fawaz, H., Lucas, B., Forestier, G., Pelletier, C., Schmidt, D. F., Weber, J., et al. (2020). InceptionTime: finding AlexNet for time series classification. *Data Min. Knowl. Disc.* 34, 1936–1962. doi: 10.1007/S10618-020-00710-Y

Kaufmann, T., Alnæs, D., Doan, N. T., Brandt, C. L., Andreassen, O. A., and Westlye, L. T. (2017). Delayed stabilization and individualization in connectome development are related to psychiatric disorders. *Nat. Neurosci.* 20, 513–515. doi: 10.1038/nn.4511

Keogh, E., and Kasetty, S. (2003). On the need for time series data Mining benchmarks: a survey and empirical demonstration. *Data Min. Knowl. Disc.* 7, 349–371. doi: 10.1023/A:1024988512476

Kong, W., Wang, L., Xu, S., Babiloni, F., and Chen, H. (2019). EEG fingerprints: phase synchronization of EEG signals as biomarker for subject identification. *IEEE Access* 7, 121165–121173. doi: 10.1109/ACCESS.2019.2931624

Larson-Prior, L. J., Oostenveld, R., Della Penna, S., Michalareas, G., Prior, F., Babajani-Feremi, A., et al. (2013). Adding dynamics to the human connectome project with MEG. *NeuroImage* 80, 190–201. doi: 10.1016/j.neuroimage.2013.05.056

Löning, M., Bagnall, A., Ganesh, S., Kazakov, V., Lines, J., and Király, F. J. (2019). Sktime: a unified Interface for machine learning with time series. 33rd conference on neural information processing systems, Vancouver, Canada.

Miranda-Dominguez, O., Mills, B. D., Carpenter, S. D., Grant, K. A., Kroenke, C. D., Nigg, J. T., et al. (2014). Connectotyping: model based fingerprinting of the functional connectome. *PLoS One* 9:e111048. doi: 10.1371/journal.pone.0111048

Mugler, J. P., and Brookeman, J. R. (1990). Three-dimensional magnetization-prepared rapid gradient-echo imaging (3D MP RAGE). *Magn. Reson. Med.* 15, 152–157. doi: 10.1002/mrm.1910150117

Pedregosa, F., Varoquaux, G., Gramfort, A., Michel, V., Thirion, B., Grisel, O., et al. (2011). Scikit-learn: machine learning in python. *J. Mach. Learn. Res.* 12, 2825–2830.

Robinson, S. E. (1989). Environmental noise cancellation for biomagnetic measurements, *Advances in Biomagnetism*, (Ed.) S. Williamsonet al. Boston, MA: Springer US, 721–724

Rocca, D. L., Campisi, P., Vegso, B., Cserti, P., Kozmann, G., Babiloni, F., et al. (2014). Human brain distinctiveness based on EEG spectral coherence connectivity. *IEEE Trans. Biomed. Eng.* 61, 2406–2412. doi: 10.1109/TBME.2014.2317881

Ruiz, A. P., Flynn, M., Large, J., Middlehurst, M., and Bagnall, A. (2021). The great multivariate time series classification bake off: a review and experimental evaluation of recent algorithmic advances. *Data Min. Knowl. Disc.* 35, 401–449. doi: 10.1007/s10618-020-00727-3

Sareen, E., Zahar, S., Ville, D. V. D., Gupta, A., Griffa, A., and Amico, E. (2021). Exploring MEG brain fingerprints: evaluation, pitfalls, and interpretations. *NeuroImage* 240:118331. doi: 10.1016/j.neuroimage.2021.118331

Schlögl, A., and Supp, G. (2006). Analyzing event-related EEG data with multivariate autoregressive parameters. *Prog. Brain Res.*, 159:135–147. doi: 10.1016/S0079-6123(06)59009-0

Valizadeh, S. A., Liem, F., Mérillat, S., Hänggi, J., and Jäncke, L. (2018). Identification of individual subjects on the basis of their brain anatomical features. *Sci. Rep.* 8, 5611–5619. doi: 10.1038/s41598-018-23696-6

Van Essen, D. C., Smith, S. M., Barch, D. M., Behrens, T. E. J., Yacoub, E., and Ugurbil, K. (2013). The WU-Minn human connectome project: an overview. *NeuroImage* 80, 62–79. doi: 10.1016/j.neuroimage.2013.05.041

Van Essen, D. C., Ugurbil, K., Auerbach, E., Barch, D., Behrens, T. E. J., Bucholz, R., et al. (2012). The human connectome project: a data acquisition perspective. *NeuroImage* 62, 2222–2231. doi: 10.1016/j.neuroimage.2012.02.018

van Horn, J. D., Grafton, S. T., and Miller, M. B. (2008). Individual variability in brain activity: a nuisance or an opportunity? *Brain Imaging Behav.* 2, 327–334. doi: 10.1007/s11682-008-9049-9

Wachinger, C., Golland, P., Kremen, W., Fischl, B., and Reuter, M. (2015). BrainPrint: a discriminative characterization of brain morphology. *NeuroImage* 109, 232–248. doi: 10.1016/j.neuroimage.2015.01.032

Welch, B. L. (1947). The generalisation of student's problems when several different population variances are involved. *Biometrika* 34, 28–35. doi: 10.1093/biomet/34.1-2.28

Yang, Q., and Wu, X. (2006). 10 CHALLENGING PROBLEMS IN DATA MINING RESEARCH. *Int. J. Inf. Technol. Decision Making* 5, 597–604. doi: 10.1142/S0219622006002258

Yu, F., and Koltun, V. (2016). Multi-scale context aggregation by dilated convolutions. 4th International Conference on Learning Representations.

frontiers | Frontiers in Neuroscience

TYPE Original Research
PUBLISHED 27 September 2023
DOI 10.3389/fnins.2023.1223226

OPEN ACCESS

EDITED BY
Federico Giove,
Centro Fermi - Museo Storico della Fisica e Centro Studi e Ricerche Enrico Fermi, Italy

REVIEWED BY
Ryan John Cubero,
Institute of Science and Technology Austria (IST Austria), Austria
Jason Stein,
University of North Carolina at Chapel Hill, United States

*CORRESPONDENCE
Leonard E. White
✉ len.white@duke.edu

RECEIVED 15 May 2023
ACCEPTED 04 September 2023
PUBLISHED 27 September 2023

CITATION
Tian Y, Johnson GA, Williams RW and White LE (2023) A rapid workflow for neuron counting in combined light sheet microscopy and magnetic resonance histology. *Front. Neurosci.* 17:1223226.
doi: 10.3389/fnins.2023.1223226

A rapid workflow for neuron counting in combined light sheet microscopy and magnetic resonance histology

Yuqi Tian[1], G. Allan Johnson[1], Robert W. Williams[2] and Leonard E. White[3]*

[1]Duke Center for In Vivo Microscopy, Department of Radiology, Duke University, Durham, NC, United States, [2]Department of Genetics, Genomics and Informatics, The University of Tennessee Health Science Center, Memphis, TN, United States, [3]Department of Neurology, Duke University, Durham, NC, United States

Information on regional variation in cell numbers and densities in the CNS provides critical insight into structure, function, and the progression of CNS diseases. However, variability can be real or a consequence of methods that do not account for technical biases, including morphologic deformations, errors in the application of cell type labels and boundaries of regions, errors of counting rules and sampling sites. We address these issues in a mouse model by introducing a workflow that consists of the following steps: 1. Magnetic resonance histology (MRH) to establish the size, shape, and regional morphology of the mouse brain *in situ*. 2. Light-sheet microscopy (LSM) to selectively label neurons or other cells in the entire brain without sectioning artifacts. 3. Register LSM volumes to MRH volumes to correct for dissection errors and both global and regional deformations. 4. Implement stereological protocols for automated sampling and counting of cells in 3D LSM volumes. This workflow can analyze the cell densities of one brain region in less than 1 min and is highly replicable in cortical and subcortical gray matter regions and structures throughout the brain. This method demonstrates the advantage of not requiring an extensive amount of training data, achieving a F1 score of approximately 0.9 with just 20 training nuclei. We report deformation-corrected neuron (NeuN) counts and neuronal density in 13 representative regions in 5 C57BL/6J cases and 2 BXD strains. The data represent the variability among specimens for the same brain region and across regions within the specimen. Neuronal densities estimated with our workflow are within the range of values in previous classical stereological studies. We demonstrate the application of our workflow to a mouse model of aging. This workflow improves the accuracy of neuron counting and the assessment of neuronal density on a region-by-region basis, with broad applications for studies of how genetics, environment, and development across the lifespan impact cell numbers in the CNS.

KEYWORDS

neuron density, light sheet microscopy, mouse brain, neurologic image analysis, neuron counting method

1. Introduction

Accurate counts of neurons are essential metrics for understanding the structure and function of the brain (Bonthius et al., 2004; Herculano-Houzel and Lent, 2005). This is particularly important for pre-clinical studies of human disease, as it provides a necessary starting point for assessing neurodegenerative changes on a regional basis (Price et al., 2001; Rosen and Williams, 2001; Bandeira et al., 2009). In addition to absolute counts, measuring neuron density can provide important insights into the structural complexity of local circuits. The distribution of neurons in the mouse brain on a region-by-region basis is also crucial for understanding variation between individuals and strains. The density of neurons can reflect the distinctive cytoarchitecture of brain regions, including laminar organization, size and shape of constituent neurons, and the volume and composition of associated neuropil (Wree et al., 1982; Spocter et al., 2012; Kasthuri et al., 2015). Furthermore, assessing neuronal densities in targeted brain regions under varying conditions may reveal impacts that change the composition of neuropil with or without associated loss (or gain) of neuronal cell bodies (Amunts et al., 1996; Selemon and Goldman-Rakic, 1999). The heterogeneity of neuronal density within a given region can provide insights into the complexity, developmental history, and functional diversity of the region (Peters et al., 1991). Establishing such datasets enables pre-clinical studies of the impact of genetics, environment, and development across the lifespan on brain structure.

To investigate cells numbers and densities in CNS, researchers have developed various quantitative methods, including several stereological approaches (Williams and Rakic, 1988; West, 1999; von Bartheld, 2002; Schmitz and Hof, 2005; Deniz et al., 2018) and approaches that first homogenize brain tissue and dissociate brain cells (Herculano-Houzel and Lent, 2005; Collins et al., 2010; Young et al., 2012). Stereology is a quantitative method for estimating the three-dimensional characteristics of biological structures using two-dimensional histological sections or images and systematic random sampling within delineated brain regions. In traditional approaches to stereology, the specimen is preserved by means of chemical fixation, the brain is removed from skull, sectioned into thin slices (usually 5–50 μm thick), and stained with specific dyes to highlight different cell types. The sections are then viewed under a microscope, and measurements are taken to estimate the cell numbers within delineated brain regions. Both 3D counting and the optical fractionation are alternatives to traditional stereological methods introduced by Abercrombie (1946, reviewed in Rosen and Williams, 2001) that is design-based in its approach to sampling a volume of tissue, counting targeted objects (e.g., neurons), and generating statistics that assess the precision of the counts (West, 1999). These methods are considered unbiased, but still can suffer from bias due to differential z-axis shrinkage and variable penetration of stains. By providing a less biased estimate of structural parameters, these modern stereological methods have contributed significantly to our understanding of many biological systems. However, there are some limitations. Stereological methods require extensive preparation of tissue and the use of microtomes to produce thin tissue sections. This can introduce damaging artifacts, lost sections, and distortions, even in the hands of experts. The results are sensitive to a range of factors, including the choice of chemical fixation, the post-fixation treatment of the specimens, the specific histological protocols used, and the specific features of the design-based approach to sampling and counting. Thus, it has be difficult to determine the accuracy of the measurements obtained in tissue that was subject to such deformation and the range of operational variables employed. Finally, stereological analysis can be a laborious and time-consuming process (Bonthius et al., 2004). When multiple brain regions are analyzed, the time and effort required can increase significantly, and the manual aspect of the process can introduce additional sources of variability.

In contrast, the isotropic fractionator (IF) involves homogenizing a small tissue sample from a region of interest—or the entire brain — and processing it into a uniform suspension of cells. The cells are then stained with a dye and placed into a special counting chamber, where the number of cells in a known volume is counted under a microscope (Herculano-Houzel and Lent, 2005), or by the flow cytometry (Collins et al., 2010; Young et al., 2012). The total number of cells in the brain region can then be estimated by extrapolating the cell density from the counting chamber to the reported or measured volume of the entire brain region. The downsides to isotropic fractionator are similar to stereology. One limitation is that both IF and stereology use the brain which is taken out of the skull and processed, introducing swelling and/or shrinkage, which can affect the accuracy of volume estimation.

Light sheet microscopy (LSM) has emerged as a powerful tool for 3D visualization of targeted populations of cells in intact, cleared tissue samples using fluorescent immunocytochemistry. Recent advances in tissue clearing (Ueda et al., 2020) have enabled the capture of high-quality, countable images in the whole-brain using LSM (Hillman et al., 2019). These intact 3D volumes can then be used for accurate counting of neurons and assessing neuronal densities, providing a more comprehensive and representative view of the brain region of interest. Typically, the whole brain images are registered to a standard reference atlas, such as the Waxholm Space Atlas (WHS) (Johnson et al., 2010) or the Allen Brain Atlas (ABA) (Wang et al., 2020). The combination of the digital images and the standard reference atlas facilitates the segmentation of regions and correction of altered brain morphology, allowing for comparison of neuron numbers and density within and across studies.

Researchers have employed this approach of registering LSM to WHS or ABA atlases in a number of recent studies (Susaki et al., 2014; Menegas et al., 2015; Renier et al., 2016; Zhang et al., 2017; Krupa et al., 2021). Susaki et al. (2014) mapped LSM to WHS space but did not proceed with cytometric quantitative analysis. The remaining studies mapped the LSM images to ABA space for analysis. ClearMap, as described by Renier et al. (2016), utilizes a peak detection algorithm with a threshold determined by comparing manual and machine counting, which may not yield optimal results when applied to complex and heterogeneous neuron distributions. Zhang et al. (2017) employed L1 minimization (Lasso), a machine learning regression method, to detect neurons in the whole brain. However, this method assumes sparsity of objects and a linear relationship between input features and output variables, with all features equally important, which may not hold true in the case of heterogeneous neuron distributions. Krupa et al. (2021) used a 3D Unet for cell detection, but these deep learning methods require large inputs and considerable training time compared to other machine learning methods. Menegas et al. (2015) utilized Ilastics[1] to segment cells in eight brain regions, with separate training for each region.

Registration of LSM images obtained from mouse brains to ABA space for correcting deformation and quantitatively segmenting brain

---

[1] https://www.ilastik.org

TABLE 1 Test specimens for neuron counting.

Specimen ID	Sex	Strain/Age
191209	M	C57BL/6J/90 d
200302	M	C57BL/6J/90 d
200316	F	C57BL/6J/90 d
200826	M	C57BL/6J/92 d
210823	M	C57BL/6J/93 d
190108	M	BXD89/111 d
200803	M	BXD89/687 d

structures and regions has one fundamental deficiency. The ABA atlas was generated from multiple specimens that were imaged after the brains were removed from the skulls (Wang et al., 2020). The lack of skull support and the effects of processing will deform the brain. Furthermore, ABA assembled their atlas from 1,600 animals, which were registered into a volume that does not conform to the size and morphology of the *in situ* mouse brain—as we demonstrate in this work.

We present a novel approach that is highly reproducible and allows efficient counting across the whole brain. Our method utilizes magnetic resonance histology (MRH), an extension of MRI to microscopic resolution of fixed tissue specimens (Johnson et al., 1993). MRH images are acquired with the brain inside the skull, resulting in a representation that more closely approximates the size and morphology of the *in vivo* brain (Johnson et al., 2023), as compared to reconstructions from histological methods that require cranial dissection, serial sectioning of the brain, and chemical treatment of thin brain sections. As a result, MRH images can serve as the "gold standard" for correcting *ex situ* brain morphology. Our workflow offers a powerful combination of morphological correction based on MRH, machine learning-based neuron classification, and post-processing. It provides accurate and detailed neuron counts and calculations of neuronal density, which can be readily derived from different brain regions and specimens. Our method features a large, well-defined field of view in 3D, which allows for a comprehensive analysis of an entire subvolume under study. Moreover, our workflow applies the principles of optical fractionation to systematically sample and count neuron numbers in 3D volumes, which reduces the computational costs and represents a novel digital approach not previously explored.

2. Materials and methods

2.1. Specimens

Two groups of animals were used to test the methods (see Table 1). The first group included 5 C57BL/6J mice (4 male and 1 female) that were sacrificed at 90 ± 3 days to test the consistency of the counts and provide measures that could be related to existing literature. A second experiment with BXD89 mice included two male specimens at 111 and 687 days to test the sensitivity of the method to changes in neuronal density arising from aging. The mice were obtained from independent litters. The BXD strains are a set of well-characterized recombinant inbred mouse strains, making them a valuable tool for systems genetics studies (Ashbrook et al., 2021).

2.2. MRH, label map and LSM scanning

All animal procedures were carried out in accordance with guidelines approved by the Duke Institutional Animal Care and Use Committee. Specimens were perfusion-fixed using an active staining method as previously described (Johnson et al., 2019). Briefly, warm saline was perfused through a catheter in the left ventricle to exsanguinate, followed by ~5 min of perfusion (50 mL) of a mixture of 10% buffered formalin and 10% Prohance (Gadoteridol) to reduce the spin lattice relaxation time (T1) of the tissue for accelerated scanning. MRH scanning was performed on a 9.4 T vertical bore magnet with a Resonance Research, Inc., gradient coil yielding peak gradients up to 2,500 mT/m, controlled by an Agilent console running VnmrJ 4.0. The MRH scanning was performed using a Stesjkal Tanner spin echo sequence with b values of 3,000 s/mm^2 and 108 angular samples spaced uniformly on the unit sphere. Compressed sensing (Lustig et al., 2007) was used with a compression factor of 8X (Wang et al., 2018), resulting in a large (252 GB) 4D volume with isotropic resolution of 15 μm (Johnson et al., 2023).

The label map in this study is based on a modified version of the Common Coordinate Framework (CCFv3) (Johnson et al., 2023) from ABA (Wang et al., 2020). The CCFv3 atlas includes 461 carefully curated regions of interest (ROIs). Our workflow relies on an initial mapping of labels from our canonical MRH atlas of a 90-day male C57BL/6J mouse to the MRH of the specimen under study using a pipeline built around Advanced Normalization Tools (ANTs) (Avants et al., 2011; Anderson et al., 2019). Many of the CCFv3 ROIs are less than 1 mm^3, including numerous subdivisions of cortical areas (laminae) and subcortical structures (subnuclei) that are of limited value within the present scope of our analyses. Accordingly, we reduced the label set to 360 ROI (180 per hemisphere) gray matter and white matter structures. This modified atlas, which we refer to as the reduced CCFv3 (r1CCFv3), consolidates these smaller subregions in CCFv3. The r1CCFv3 provides a label set that registers to the MRH volumes reproducibly enabling precise neuron counting within a large number of structures. The details of this registration process are described in Johnson et al. (2023).

Following the MRH scans, the brains were carefully removed from the skulls. Paraformaldehyde-fixed samples were preserved with using SHIELD reagents (LifeCanvas Technologies) using the manufacturer's instructions (Park et al., 2019). Samples were delipidated using Clear+ delipidation reagents. Following delipidation samples were labeled using eFLASH technology which integrates stochastic electrotransport (Kim et al., 2015) and SWITCH (Murray et al., 2015). The samples were then washed in PBS for 7-8 h before overnight fixation in 4% paraformaldehyde followed by incubation in secondary labeling buffer at 37°C with two refreshes over the course of 7–8 h before secondary labeling in the SmartLabel device. For each brain, 10 μg of rabbit anti-Iba1 (Cell Signaling Technologies 17198S*) primary antibody, 10 μg mouse anti-NeuN (Encor MCA-1B7), 6 μg rabbit anti-NeuN (Cell Signaling Technologies 24307S*), or 20 μg mouse anti-MBP (Encor MCA-7G7). Secondary antibodies were used at a 2:1 Secondary:Primary molar ratio. After immunolabeling, samples were incubated in 50% EasyIndex (RI = 1.52, LifeCanvas Technologies) overnight at 37°C followed by 1 d incubation in 100% EasyIndex for refractive index matching. After index matching the samples were imaged using a SmartSPIM axially-swept light sheet microscope using a 3.6x objective (0.2 NA) (LifeCanvas Technologies, Cambridge, MA). The processing streams for MRH and LSM are depicted in Figure 1A.

2.3. Automated neuron counting

2.3.1. Overview of the algorithm

To address the significant distortion introduced during skull removal and chemical processing in the preparation of LSM samples, the LSM images are first registered to the MRH volumes of the same specimen (Figure 1B; Tian et al., 2023). Section 3.1, accompanied by Figure 2, provides a detailed explanation of the impact of correcting the morphology and extraction of the cytometric statistics. We examine the effects of the preprocessing steps on the neuron density measurements, providing insights into the importance of these steps for accurate data analysis.

The workflow is visualized in Figure 1C. After warping the LSM and label map to the MRH space, the user selects a region for analysis by inputting the corresponding label from the label map into Fiji. This generates a surface defining the region of the selected label, as well as a group of subvolumes within the surface. These subvolumes are distributed in a uniform but random manner, which improves the accuracy of neuron counting and facilitates analysis of the heterogeneity of neuron distribution throughout the selected region. Please note that subvolumes located on boundaries and containing broken tissues will be automatically excluded by screening the label value of the subvolume. For each subvolume (Figure 1C), we apply a lightly supervised algorithm called random forest neuron segmentation, which utilizes an ensemble of decision trees to generalize the projection between graphical features and labels. This algorithm is commonly used in image processing tasks and requires only a small amount of training data to perform well (Pavlov, 2000). Prior to segmentation, the random forest classifier is pre-trained using training data consisting of binary signatures, where neurons are labeled as 1 and non-neurons as 0, as well as feature vectors extracted from various visual characteristics of the image, such as texture, shape, and size. The training process optimizes the relationship between graphical features of an image and the assigned neuron labels. The labeling example can be seen in Supplementary Figure S1. In general, labeling approximately 20 neurons with both the cell body and background enables the algorithm to learn the essential features of neurons, resulting in a commendable F1 score (Supplementary Section S2) of around 0.9, as illustrated in Supplementary Figure S2. After the random forest segmentation is applied to each subvolume, the workflow will perform post-processing on the objects classified as neurons. This post-processing uses 3D watershed (showcased in Supplementary Figure S3) and volume filters to further isolate the neurons as discrete objects. The final count of the neurons in each subvolume is generated based on these refined objects. The density is calculated by averaging densities obtained from subvolumes, and the standard deviation of the density provides insight into the variability of the neuron distribution within the region.

2.3.2. Big data environment

Whole brain LSM images are large – typically ~300 GB. To enable efficient, interactive development and execution of the workflow we have assembled a hardware/software environment suited for these large data. The pipeline has been implemented on two high performance Dell servers: Dell E5-2400, NVIDIA Tesla V100 GPU and a Dell E52670, NVIDIA V100 GPU. Each server has 1.5 TB of memory.

Several software packages have been integrated into the big data environment. Imaris[2] is a commercial software package designed for interactive 3D/4D viewing of large microscopy data sets. It accommodates simultaneous visualization of multiple light sheet volumes using a hierarchical data format. Imaris has been developed to allow memory sharing with external packages. One of these is Fiji,[3] a distribution of Image J that has been developed for applications such as that envisioned here through the extensive use of plugins. One crucial plugin for our work is BigDataViewer (Pietzsch et al., 2015), an open source solution for accommodating large volumes in Fiji and supporting plugins for post processing. This includes LabKit (Arzt et al., 2022) a user friendly Fiji plugin for microscopy segmentation using the random forest algorithm.

2.3.3. Compiled algorithms

To improve the accuracy and efficiency of neuron counting, we developed two pipelines for different purposes: one for visualized validation and the other for production use. The initial pipeline (available on GitHub[4]) provides visualization of classification and segmentation performance. This algorithm is built on the coding interface of the image rendering software, Imaris.[5] The procedures, from applying classifiers to obtaining statistics, are executed in the GUI of Imaris. Although the workflow cannot be fully automated through the Imaris coding interface, it can be automated through recording applications such as OS Automator.[6] The second algorithm (available on GitHub[7]) provides an automated workflow constructed using Python and macros. This method utilizes Fiji macro GUIs to automate segmentation, 3D watershed, and region counting plugins. The watershed uses morphological erosion to identify the center of each object, followed by calculating a distance map from the object center points to the object edges. The resulting topological map is then filled with imaginary water, and dams are built at locations where two watersheds meet to separate them. The region counting method assigns unique labels to each unconnected component to facilitate subsequent counting. The plugin used for constructing the random forest model is Labkit.[8] The watershed method and the 3D connected region counting method in the first algorithm are available in Imaris. The 3D watershed and 3D connected region counting method in the second algorithm are the Fiji/binary/watershed function and from the open-source plugin MorphoLibj.[9]

---

[2] https://imaris.oxinst.com

[3] https://fiji.sc/

[4] https://github.com/YuqiTianCIVM/NeuronCounting/blob/main/Algor_forVisualization.py

[5] https://imaris.oxinst.com

[6] https://support.apple.com/guide/automator/intro-to-automator-aut6e8156d85/mac

[7] https://github.com/YuqiTianCIVM/NeuronCounting/blob/main/MainAlgor.py

[8] https://imagej.net/plugins/labkit/

[9] http://imagej.net/MorphoLibJ

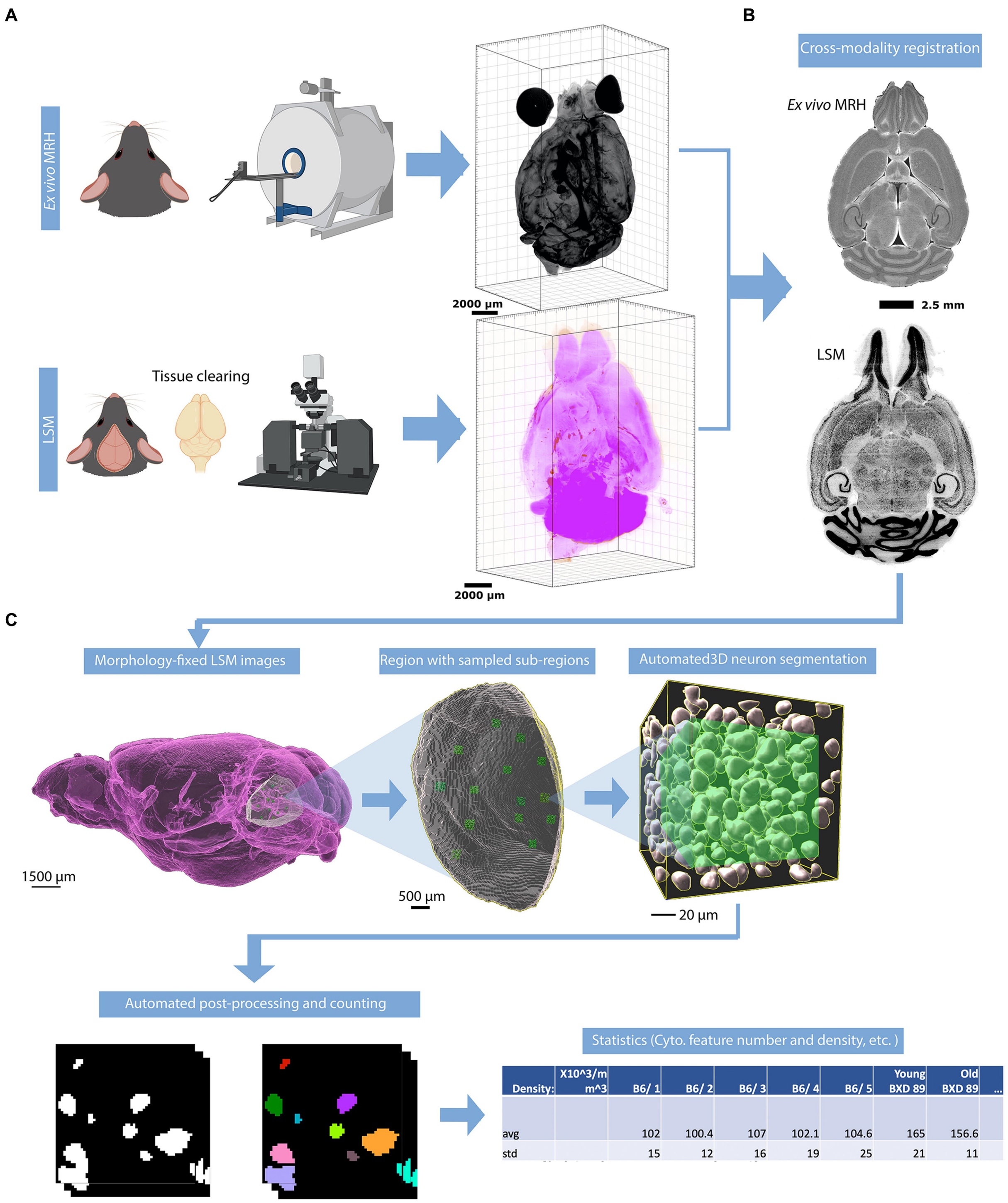

Density:	X10^3/mm^3	B6/ 1	B6/ 2	B6/ 3	B6/ 4	B6/ 5	Young BXD 89	Old BXD 89	...
avg		102	100.4	107	102.1	104.6	165	156.6	
std		15	12	16	19	25	21	11	

FIGURE 1
Overview of the workflow for assessing the density of neurons. **(A)** The mouse brain is imaged using two modalities: MRH imaging while the brain is in the skull, followed by LSM after the brain is removed from the skull and subjected to tissue clearing. **(B)** The LSM data are pre-processed by registering to MRH correcting the deformation in brain morphology. **(C)** The automated workflow locates the region with the label from r1CCFv3 and generates random subvolumes within that region to sample, applying the design-based principles of optical fractionation. Neurons in each subvolume are identified via a random forest algorithm followed by 3D watershed and volume filters and counted.

2.3.3.1. Imaris pipeline for visualization

The user identifies the structure to be analyzed and loads the surface defining that structure. A Python script generates a collection of 3D subregions that are randomly placed within the volume of the structure defined by the surface. Each counting subregion is a 100 µm × 100 µm × 100 µm cube. To avoid oversampling or undersampling in different regions and to accurately capture the heterogeneity, we analyzed 15 subvolumes per brain region while keeping the number of subvolumes consistent across regions to facilitate statistical analysis. The user selects "Labkit" in the Fuji extension. The GUI displays the subregion's volume, and the user either imports a pre-trained classifier or starts labeling neurons and background with binary labels. Supplementary Figure S1 shows representative images of the training process. Once a classifier has been trained, it can be saved for future use in other ROI or other specimens, with some limitations discussed below. The classification is then sent to Imaris. Imaris applies thresholding to the binary labels and generates individual surfaces based on the results. The watershed algorithm uses seed points to split touching surfaces. After approximating the size of neurons through visualization, the volume filter is applied, and the count is generated.

2.3.3.2. Fiji pipeline for high throughput

A Python script generates sub-regions inside the surface of the structure being analyzed and saves these subvolumes as individual TIFF files. The same Python script creates and executes a FIJI macro that reads the TIFF files in batches, applies the pre-trained random forest classifier, and performs 3D watershed. Components in the resulting image are labeled with different colors using the FIJI function "connected components labeling" and saved as a TIFF file. A second Python script reads these TIFF files in batches, applies volume filters, and generate counts of the components. The details of the volume filters are provided in Supplementary Section S6.

2.4. Data availability statement

Original datasets are available in a repository. The access will be granted upon request.

3. Results

3.1. Visualization of morphology correction

Figure 2 displays the comparison between images from an uncorrected and deformation-corrected whole brain light sheet volume. Much of the existing literature for stereology has employed optical light microscopy and confocal microscopy with higher resolution and smaller field of view than that in the whole brain LSM images. However, the deformation, which is dependent on the fixation and staining method, is likely to be similar to that presented in Figures 2A,C,E. The compensation of this deformation is usually done through the application of an isotropic correction factor, but this factor may be insufficient to fully address the nonuniform

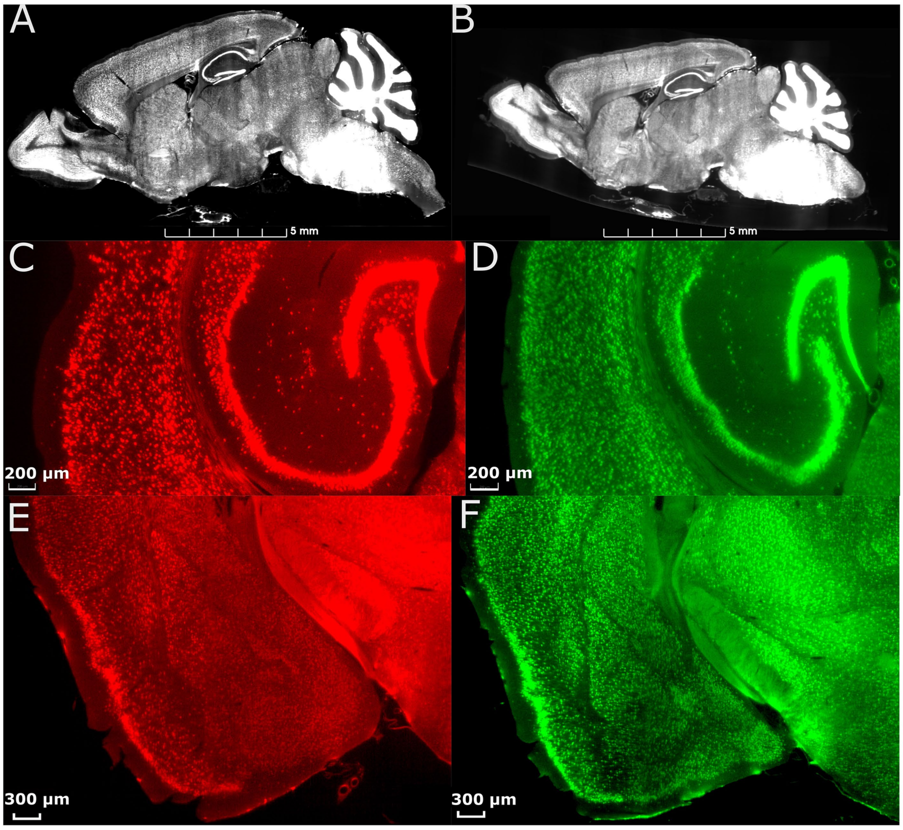

FIGURE 2
Effect of morphology correction on light-sheet datasets. **(A)** A single slice from a whole-brain LSM before correction. **(B)** The same slice as in **(A)** after correction using MRH. Magnified axial views of auditory areas and hippocampus before **(C)** and after **(D)** correction, and coronal views of the anterior temporal and posterior diencephalic region (showing the amygdaloid complex) before **(E)** and after **(F)** correction. The specimen is the same on both sides, and the colormap is used to illustrate the contrast between before and after correction.

deformation arising from tissue processing. Figure 2B shows the LSM image with morphology correction by MRH, which significantly reduces the irregular distortion present in the raw LSM images. The magnified views of the posterior cerebrum (showing the auditory cortex and hippocampus (Figure 2D) and LGN (Figure 2F)) illustrate the benefits of the morphology correction method in improving the quality of imaging data and segmentation label maps, compared to Figures 2C,E. Supplementary Figure S4 illustrates the differences in neuron density between raw LSM and deformation corrected LSM for 6 brain regions. The smallest percent difference (calculated as the difference between raw and corrected density over the corrected density), observed in the primary visual cortex, is 7%, while the largest, observed in the subiculum, is 64%. These results demonstrate that deformation is not uniform throughout the brain.

Figures 3A,C,E displays the label-map CCFv3. Data for the ABA were obtained by averaging 2-photon microscopy images of 1,600 animals. The distortions from tissue handling are not consistent across all 1,600 animals. Wang et al. (2020) report variability in the volume of the regions in their atlas ranging from 6 to 80% so tissue handling introduces variation. Figures 3B,D,F displays the r1CCFv3 labels with morphology correction by MRH. The resulting corrected label map provides more accurate representation of brain regions (Figure 3).

3.2. Comparison of machine counting and human counting

To assess the accuracy and precision of our workflow, we chose five brain regions with cell densities we determined would be countable: Dorsal part of the lateral geniculate complex (LGd), Auditory area (AUD), retrosplenial area (RSP), orbital area (Orb), and subicular region (SUBR). We created 15–20 3D subvolumes for sampling within these regions with dimensions of 1,000 μm × 1,000 μm × 12 μm (556 × 556 × 3 voxels) for visualization in Figures 4A,B, and 100 μm × 100 μm × 100 μm (56 × 56 × 25 voxels) for routine implementation of the workflow. The random forest classifier, trained on a random sub volume in the auditory cortex of a specimen not involved in the experiment, was applied automatically to identify the objects to be included. We randomly selected 10–15 subvolumes within the same datasets, and an experienced researcher manually counted the neurons within them by labeling neurons in subvolumes across 3–5 specimens. We compared the results of both methods and found that both manual counting and the machine had overall performance that was comparable (Figures 4A,B). One consideration to note is that during the manual labeling process, the researcher was involved in selecting the subvolumes, which introduced potential bias. Although efforts were made to minimize bias and select subregions randomly, there may have been a tendency to choose subregions with visually distinguishable neurons, leading to an uneven distribution. That means the manual classification has a tendency to underestimatesthe heterogenieoty of the neuron distribution. However, in the subsequent machine classifier analysis, subvolumes were automatically generated without bias. As a result, the machine counts in this panel exhibit greater variability in comparison. A statistical comparison is shown in Figure 4D.

Supplementary Table S2 presents a comparison between the proposed method and other cell counting software solutions.

3.3. Neuron counting in C57BL/6J mouse brain

We demonstrated the use of the pipeline in counting neurons in 13 different brain regions across 7 specimens. We choose representative regions to demonstrate the capability of our workflow in neocortex, hippocampus, amygdala, thalamus, and brainstem. These regions include (1) neocortex: orbital area (Orb), auditory area (AUD), retrosplenial area (RSP), primary visual area (VISp); (2) hippocampal region: entorhinal area (ENT), subicular region (SUBR), field CA1 (CA1), field CA3 (CA3); (3) amygdala: basolateral amygdalar nucleus (BLA); (4) thalamus: dorsal part of the lateral geniculate complex (LGd), and the entire thalamus (Th); (5) brainstem: facial motor nucleus (VII), principal sensory nucleus of the trigeminal (PSV). Initial measurements were performed on 5, 90-day old male C57BL/6J specimens. The results show that neuron density in some regions (LGd, AUD, RSP, Orb) is quite consistent across specimens, and much more variable while there is a high standard deviation in others (PSV, VISp, TH, BLA), as indicated by the relatively high standard deviation of the means (Figure 5). Supplementary Figure S5 and Supplementary Table S1 present the comparison between the neuron density obtained from our workflow and previous studies.

To assess the variability of our measurements, we calculated the coefficient of variation (CV) for the density and number of neurons in several brain regions across different specimens (Supplementary Table S3). The CV for neuron density ranged from 0.062 in CA1 to 0.333 in VII, with an average of 0.139. The CV for neuron number ranged from 0.06 in CA1 to 0.44 in PSV, with an average of 0.17. These results indicate that there is considerable variation in neuron density and number across individual animals, even within the same brain region. Notably, the regions with the highest CV for neuron density and number were VII (0.333) and PSV (0.44), respectively. This is likely to be induced by the small sizes of these regions. The higher coefficient of variation for small regions may be due to minor displacements between the placement of individual delineations from the labelmap and the actual neuroanatomical structures, as discerned in LSM, especially for brainstem regions where deformation was significant. Conversely, the regions with the lowest CV for neuron density and number were CA1 (0.062), RSP (0.073), AUD (0.076), Orb (0.092), CA3 (0.091), and SUBR (0.097), respectively. These findings underscore the importance of accounting for inter-individual variability when analyzing neuronal parameters and highlight the need for careful consideration of sample size and statistical power in studies of brain structure.

3.4. Illustration of aging effects on the neuron density and number

Figure 6 presents a comparison between one young (111 day) and one old (687 day) BXD89 specimen to demonstrate the application of our workflow to a different strain and its potential to be used to examine the impact of aging on neuron density. It is important to note that only two animals are being assessed in this Figure and the standard deviation thus reflects the heterogeneity of neuron distribution within each brain region, which was obtained by analyzing mean neuronal counts within the subvolumes. Our analysis

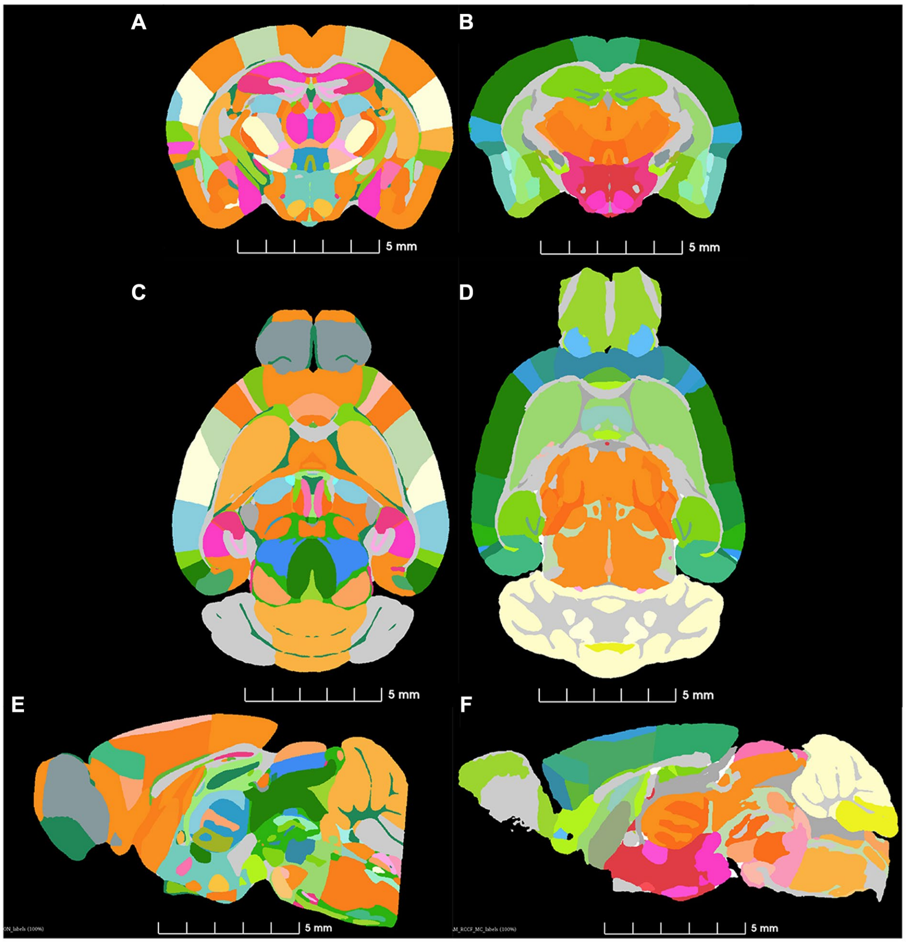

FIGURE 3
Comparison of similar levels from the ABA **(A,C,E)** and a single specimen imaged by MRH. **(B,D,F)** The colormaps are different because the ABA atlas is shown with the full complement of 461 (CCFv3) labels and the MRH is shown with the reduced (r1CCFv3) labels in which some ROI have been combined.

revealed that in certain regions, such as the orbital area (Orb), the observed decrease in neuron density was primarily due to a reduction in the total number of neurons, while in other regions such as the entorhinal area (ENT) and basolateral amygdala (BLA), the observed decrease in density was largely attributable to regional enlargement of the brain during aging. These findings underscore regional variation and the complexity of the aging process and highlight the need for careful consideration of volume and cellular number when studying brain development across the lifespan.

4. Discussion

We present a workflow that corrects the deformation introduced by the chemical treatment of brain tissue for LSM and uses an automated algorithm for neuron segmentation and counting through machine learning and post-processing. To improve the accuracy of the results, we use the MRH of the same specimen as a reference for LSM image morphology, as MRH provides in-skull images of the brain that closely approximate the compartmental configuration and accurate size of the living brain. Our method offers a reliable means of acquiring neuron number and density and requires less human labor and subjective judgment than previous methods. The method exhibits high flexibility, as it requires a much lower amount of pre-training data and demonstrates efficient computational time and performance compared to deep learning methods, as depicted in Supplementary Figure S6. It is also much easier to replicate across multiple brain regions and specimens. By correcting raw images and conducting region segmentation, our method provides improved estimates over previous counting methods. Furthermore, by incorporating the principles of optical fractionation, our workflow provides an unbiased sampling method with equal probability to sample for each section with a relatively low sampling ratio (Supplementary Table S4), resulting in reduced computational costs and representing a novel digital approach that has not been explored before.

To validate the method, we used the workflow to analyze 13 regions in different divisions of 5 C57BL/6 J specimens. The results, as shown in Figure 5, demonstrate the variability in neuron density across regions within the same animal and across animals for the same regions. In the Supplementary materials, we conducted a systematic search of the literature providing neuron counts of the same regions for comparison with our method. As our method produces regional neuron density as its direct output, we assessed the accuracy of our results in terms of density. For most cortical regions, our findings were consistent with those of previous studies or fell within the range of previously reported results. However, in some regions, e.g., LGd, PSV, VISp, TH, and BLA, our results showed a higher neuron density than what was reported in earlier studies. This is likely due to our utilization of the morphology-corrected space for calculating neuron density. This space closely approximates the volume and morphology of the brain confined within the skull, which may have contributed to the observed differences in density measurements. In certain regions where our density measurements were markedly different from those reported in previous studies, such as the facial motor nucleus, we manually counted the sub-regions to validate the neuron distribution. Our findings indicated that the neuron distribution in this region was indeed sparse, with a density measurement about six times lower than that reported in the Blue Brain Map (BBM) (Ero et al., 2018). We hypothesize that this discrepancy may be due to differences in data quality or acquisition methods between studies. BBM estimated neuron counts using a transfer function and Monte Carlo method applied to the ABA Nissl atlas. The authors only used whole-brain values from literature, such as the total number of cells and neurons in the mouse brain, to constrain their estimates of cell densities in each brain region. Further investigation is required to elucidate the causes of the observed discrepancy. Nonetheless, our method, which directly measures regional neuron density, provides a reliable alternative to indirect methods such as those used by BBM, and can contribute to a more accurate appreciation of brain structure.

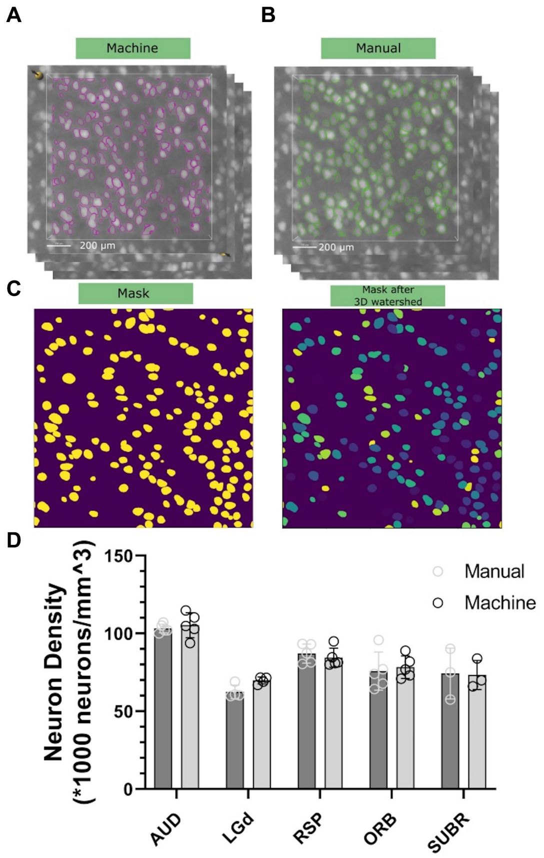

FIGURE 4
Comparison of neuron density between the machine workflow **(A)** and manual counting **(B)**. Note that both the labeling will go through watershed illustrated in **(C)** to ensure the connected surfaces are separated. Standard deviation is shown in **(D)**, representing statistical variations across five different 90-day C57BL/6J specimens.

Our method has two limitations. In those regions in which the cell density is so high that the resolution of the LSM we acquired is not sufficient to differentiate countable cells (e.g., dentate gyrus, granule cell layer of cerebellar cortex), the random forest classifier and watershed algorithms will fail, and hence the performance hinges on the volume filter, which approximates the neuron count by partitioning the volumes of nested neurons based on the average neuron size (Supplementary Section S7). A second limitation is that performance is dependent on the quality of the raw data. In cases where the tissue preparation and scanning are suboptimal, the method will not function properly. Although the data provided by LifeCanvas, which we used for our study, are generally of high quality, there are occasionally regions with poor image quality (as shown in Supplementary Figure S7), which

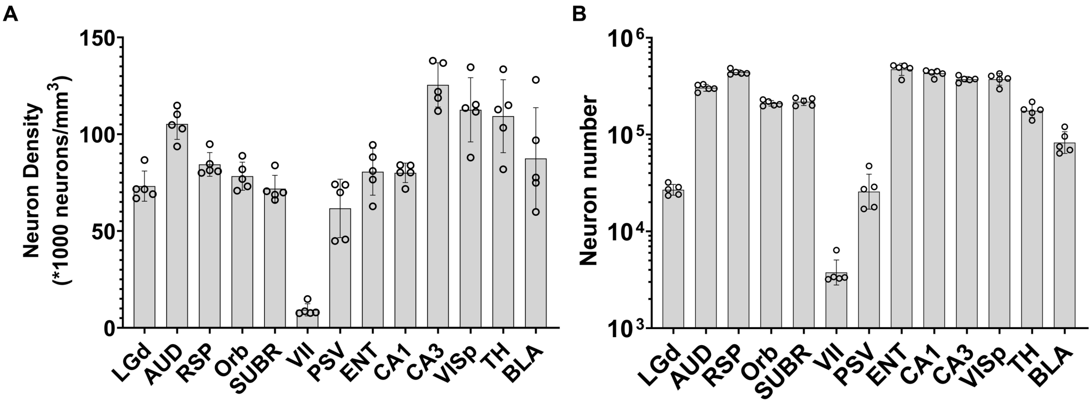

FIGURE 5
Demonstration of the variation of neuron density **(A)** and neuron number **(B)** across brain regions, as well as variations across specimens. Error bars are standard deviations of the means. The dots indicate neuron counts from individual specimens. Region: LGd: Dorsal lateral geniculate nucleus, AUD: auditory area, RSP: retrosplenial area, Orb: orbital area, SUBR: subiculum, VII: facial motor cortex, PSV: trigeminal, ENT: entorhinal area, CA1: field CA1, CA3: field CA3, VISp: primary cortex, TH: thalamus, BLA: Basolateral amygdala.

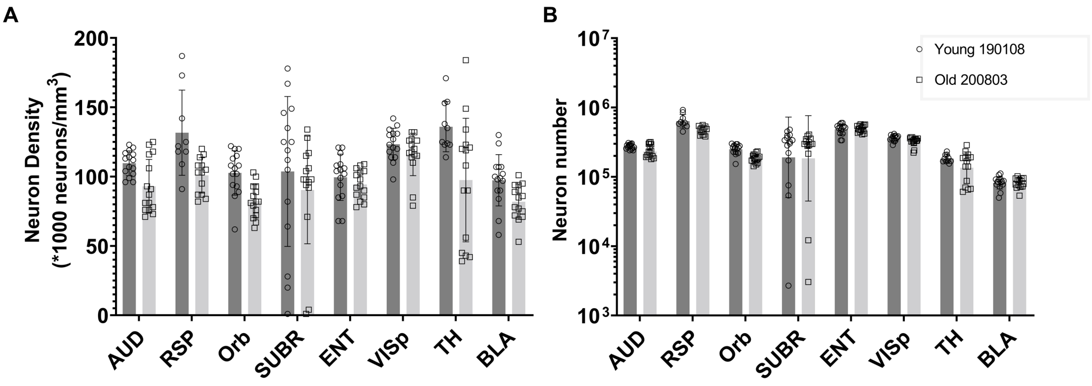

FIGURE 6
Comparison of the neuron density **(A)** and number **(B)** in multiple brain regions of a young and an old BXD89 mouse, demonstrating the application of the workflow to a study of the impact of aging on neuronal populations in a different strain. The error bars in this figure represent the standard deviation of neuron distribution within each region, obtained from subvolumes.

can limit the method's reliability. Advanced imaging techniques such as expansion microscopy, as demonstrated by Wassie et al. (2019) or acquisition with higher power objectives will address resolution questions and are likely to produce reliable and accurate counts of neurons using our workflow.

The application of stereology to counting cells has a venerable history. As acquisition methods have improved the methods to count cells have been adapted to the newer data. The advent of tissue clearing and volume light sheet imaging yield opportunities for significant improvement in precision and accuracy. This is particularly important in our studies of the mouse brain as we seek apply this workflow to quantitative studies of the mophological and cytological impacts of neurodegeneration and aging. Correction for tissue changes, use of a more accurate label set, and automation described in this work will provide crucial tools in quantitative neuropathology.

Data availability statement

The datasets presented in this study can be found in online repositories. The names of the repository/repositories and accession number(s) can be found in the article/Supplementary material.

Ethics statement

The animal study was approved by Duke Institutional Animal Care and Use Committee. The study was conducted in accordance with the local legislation and institutional requirements.

Author contributions

YT: Designed and coded the workflow, conducted the evaluation, and wrote the manuscript. GJ: Conceived the project, guided YT, and contributed to manuscript writing. RW: Offered valuable expertise and guidance in stereology. LW: Provided valuable expertise and guidance into neuron density, neuroscience, and strategy. GJ and RW: Provided funding and contributed to manuscript writing. All authors participated in manuscript revisions, reviewed, and approved the final submission.

Funding

This work was supported by National Institute of Aging R01AG070913 to GJ and RW.

Acknowledgments

We are grateful to James J. Cook for technical support and assistance in software development. We are grateful to Tatiana Johnson for assistance in editing the manuscript.

Conflict of interest

The authors declare that the research was conducted in the absence of any commercial or financial relationships that could be construed as a potential conflict of interest.

Publisher's note

Supplementary material

The Supplementary material for this article can be found online at: https://www.frontiersin.org/articles/10.3389/fnins.2023.1223226/full#supplementary-material

References

Abercrombie, M. (1946). Estimation of nuclear population from microtome sections. *Anat. Rec.* 80, 191–202. doi: 10.1002/ar.1090940210

Amunts, K., Schlaug, G., Schleicher, A., Steinmetz, H., Dabringhaus, A., Roland, P. E., et al. (1996). Asymmetry in the human motor cortex and handedness. *NeuroImage* 4, 216–222. doi: 10.1006/nimg.1996.0073

Anderson, R. J., Cook, J. J., Delpratt, N., Nouls, J. C., Gu, B., McNamara, J. O., et al. (2019). Small animal multivariate brain analysis (SAMBA) – a high throughput pipeline with a validation framework. *Neuroinformatics* 17, 451–472. doi: 10.1007/s12021-018-9410-0

Arzt, M., Jr, D., Schmied, C., Pietzsch, T., Schmidt, D., Tomancak, P., et al. (2022). LABKIT: labeling and segmentation toolkit for big image data. *Front. Comput. Sci* 4:4. doi: 10.3389/fcomp.2022.777728

Ashbrook, D. G., Arends, D., Prins, P., Mulligan, M. K., Roy, S., Williams, E. G., et al. (2021). A platform for experimental precision medicine: the extended BXD mouse family. *Cell Syst* 12, 235–247.e9. doi: 10.1016/j.cels.2020.12.002

Avants, B. B., Tustison, N. J., Wu, J., Cook, P. A., and Gee, J. C. (2011). An open source multivariate framework for n-tissue segmentation with evaluation on public data. *Neuroinformatics* 9, 381–400. doi: 10.1007/s12021-011-9109-y

Bandeira, F., Lent, R., and Herculano-Houzel, S. (2009). Changing numbers of neuronal and non-neuronal cells underlie postnatal brain growth in the rat. *Proc. Natl. Acad. Sci. U. S. A.* 106, 14108–14113. doi: 10.1073/pnas.0804650106

Bonthius, D. J., McKim, R., Koele, L., Harb, H., Karacay, B., Mahoney, J., et al. (2004). Use of frozen sections to determine neuronal number in the murine hippocampus and neocortex using the optical disector and optical fractionator. *Brain Res. Brain Res. Protoc.* 14, 45–57. doi: 10.1016/j.brainresprot.2004.09.003

Collins, C. E., Young, N. A., Flaherty, D. K., Airey, D. C., and Kaas, J. H. (2010). A rapid and reliable method of counting neurons and other cells in brain tissue: a comparison of flow cytometry and manual counting methods. *Front. Neuroanat.* 4:5. doi: 10.3389/neuro.05.005.2010

Deniz, O. G., Altun, G., Kaplan, A. A., Yurt, K. K., von Bartheld, C. S., and Kaplan, S. (2018). A concise review of optical, physical and isotropic fractionator techniques in neuroscience studies, including recent developments. *J. Neurosci. Methods* 310, 45–53. doi: 10.1016/j.jneumeth.2018.07.012

Ero, C., Gewaltig, M. O., Keller, D., and Markram, H. (2018). A cell atlas for the mouse brain. *Front. Neuroinform.* 12:84. doi: 10.3389/fninf.2018.00084

Herculano-Houzel, S., and Lent, R. (2005). Isotropic fractionator: a simple, rapid method for the quantification of total cell and neuron numbers in the brain. *J. Neurosci.* 25, 2518–2521. doi: 10.1523/JNEUROSCI.4526-04.2005

Hillman, E. M. C., Voleti, V., Li, W., and Yu, H. (2019). Light-sheet microscopy in neuroscience. *Annu. Rev. Neurosci.* 42, 295–313. doi: 10.1146/annurev-neuro-070918-050357

Johnson, G. A., Badea, A., Brandenburg, J., Cofer, G., Fubara, B., Liu, S., et al. (2010). Waxholm space: an image-based reference for coordinating mouse brain research. *NeuroImage* 53, 365–372. doi: 10.1016/j.neuroimage.2010.06.067

Johnson, G. A., Benveniste, H., Black, R. D., Hedlund, L. W., Maronpot, R. R., and Smith, B. R. (1993). Histology by magnetic resonance microscopy. *Magn. Reson. Q.* 9, 1–30.

Johnson, G. A., Tian, Y., Ashbrook, D. G., Cofer, G. P., Cook, J. J., Gee, J. C., et al. (2023). Merged magnetic resonance and light sheet microscopy of the whole mouse brain. *Proc. Natl. Acad. Sci. U. S. A.* 120:e2218617120. doi: 10.1073/pnas.2218617120

Johnson, G. A., Wang, N., Anderson, R. J., Chen, M., Cofer, G. P., Gee, J. C., et al. (2019). Whole mouse brain connectomics. *J. Comp. Neurol.* 527, 2146–2157. doi: 10.1002/cne.24560

Kasthuri, N., Hayworth, K. J., Berger, D. R., Schalek, R. L., Conchello, J. A., Knowles-Barley, S., et al. (2015). Saturated reconstruction of a volume of neocortex. *Cells* 162, 648–661. doi: 10.1016/j.cell.2015.06.054

Kim, S. Y., Cho, J. H., Murray, E., Bakh, N., Choi, H., Ohn, K., et al. (2015). Stochastic electrotransport selectively enhances the transport of highly electromobile molecules. *Proc. Natl. Acad. Sci. U. S. A.* 112, E6274–E6283. doi: 10.1073/pnas.1510133112

Krupa, O., Fragola, G., Hadden-Ford, E., Mory, J. T., Liu, T., Humphrey, Z., et al. (2021). NuMorph: tools for cortical cellular phenotyping in tissue-cleared whole-brain images. *Cell Rep.* 37:109802. doi: 10.1016/j.celrep.2021.109802

Lustig, M., Donoho, D., and Pauly, J. M. (2007). Sparse MRI: the application of compressed sensing for rapid MR imaging. *Magn. Reson. Med.* 58, 1182–1195. doi: 10.1002/mrm.21391

Menegas, W., Bergan, J. F., Ogawa, S. K., Isogai, Y., Umadevi Venkataraju, K., Osten, P., et al. (2015). Dopamine neurons projecting to the posterior striatum form an anatomically distinct subclass. *elife* 4:e10032. doi: 10.7554/eLife.10032

Murray, E., Cho, J. H., Goodwin, D., Ku, T., Swaney, J., Kim, S. Y., et al. (2015). Simple, scalable proteomic imaging for high-dimensional profiling of intact systems. *Cells* 163, 1500–1514. doi: 10.1016/j.cell.2015.11.025

Park, Y. G., Sohn, C. H., Chen, R., McCue, M., Yun, D. H., Drummond, G. T., et al. (2019). Protection of tissue physicochemical properties using polyfunctional crosslinkers. *Nat. Biotechnol.* 37:73-+. doi: 10.1038/nbt.4281

Pavlov, Y. L. (2000). *Random forests*. Utrecht, Boston, VSP

Peters, A., Josephson, K., and Vincent, S. L. (1991). Effects of aging on the neuroglial cells and pericytes within area 17 of the rhesus-monkey cerebral-cortex. *Anat. Rec.* 229, 384–398. doi: 10.1002/ar.1092290311

Pietzsch, T., Saalfeld, S., Preibisch, S., and Tomancak, P. (2015). BigDataViewer: visualization and processing for large image data sets. *Nat. Methods* 12, 481–483. doi: 10.1038/nmeth.3392

Price, J. L., Ko, A. I., Wade, M. J., Tsou, S. K., McKeel, D. W., and Morris, J. C. (2001). Neuron number in the entorhinal cortex and CA1 in preclinical Alzheimer disease. *Arch. Neurol.* 58, 1395–1402. doi: 10.1001/archneur.58.9.1395

Renier, N., Adams, E. L., Kirst, C., Wu, Z., Azevedo, R., Kohl, J., et al. (2016). Mapping of brain activity by automated volume analysis of immediate early genes. *Cells* 165, 1789–1802. doi: 10.1016/j.cell.2016.05.007

Rosen, G. D., and Williams, R. W. (2001). Complex trait analysis of the mouse striatum: independent QTLs modulate volume and neuron number. *BMC Neurosci.* 2:5. doi: 10.1186/1471-2202-2-5

Schmitz, C., and Hof, P. R. (2005). Design-based stereology in neuroscience. *Neuroscience* 130, 813–831. doi: 10.1016/j.neuroscience.2004.08.050

Selemon, L. D., and Goldman-Rakic, P. S. (1999). The reduced neuropil hypothesis: a circuit based model of schizophrenia. *Biol. Psychiatry* 45, 17–25. doi: 10.1016/S0006-3223(98)00281-9

Spocter, M. A., Hopkins, W. D., Barks, S. K., Bianchi, S., Hehmeyer, A. E., Anderson, S. M., et al. (2012). Neuropil distribution in the cerebral cortex differs between humans and chimpanzees. *J. Comp. Neurol.* 520, 2917–2929. doi: 10.1002/cne.23074

Susaki, E. A., Tainaka, K., Perrin, D., Kishino, F., Tawara, T., Watanabe, T. M., et al. (2014). Whole-brain imaging with single-cell resolution using chemical cocktails and computational analysis. *Cells* 157, 726–739. doi: 10.1016/j.cell.2014.03.042

Tian, Y., Cook, J. J., and Johnson, G. A. (2023). Restoring morphology of light sheet microscopy data based on magnetic resonance histology. *Front. Neurosci.* 16:1011895. doi: 10.3389/fnins.2022.1011895

Ueda, H. R., Ertürk, A., Chung, K., Gradinaru, V., Chédotal, A., Tomancak, P., et al. (2020). Tissue clearing and its applications in neuroscience. *Nat. Rev. Neurosci.* 21, 61–79. doi: 10.1038/s41583-019-0250-1

von Bartheld, C. (2002). Counting particles in tissue sections: choices of methods and importance of calibration to minimize biases. *Histol. Histopathol.* 17, 639–648. doi: 10.14670/HH-17.639

Wang, N., Anderson, R. J., Badea, A., Cofer, G., Dibb, R., Qi, Y., et al. (2018). Whole mouse brain structural connectomics using magnetic resonance histology. *Brain Struct. Funct.* 223, 4323–4335. doi: 10.1007/s00429-018-1750-x

Wang, Q., Ding, S. L., Li, Y., Royall, J., Feng, D., Lesnar, P., et al. (2020). The Allen mouse brain common coordinate framework: a 3D reference atlas. *Cells* 181, 936–953.e20. doi: 10.1016/j.cell.2020.04.007

Wassie, A. T., Zhao, Y., and Boyden, E. S. (2019). Expansion microscopy: principles and uses in biological research. *Nat. Methods* 16, 33–41. doi: 10.1038/s41592-018-0219-4

West, M. J. (1999). Stereological methods for estimating the total number of neurons and synapses: issues of precision and bias. *Trends Neurosci.* 22, 51–61. doi: 10.1016/S0166-2236(98)01362-9

Williams, R. W., and Rakic, P. (1988). Three-dimensional counting: an accurate and direct method to estimate numbers of cells in sectioned material. *J. Comp. Neurol.* 278, 344–352. doi: 10.1002/cne.902780305

Wree, A., Schleicher, A., and Zilles, K. (1982). Estimation of volume fractions in nervous tissue with an image analyzer. *J. Neurosci. Methods* 6, 29–43. doi: 10.1016/0165-0270(82)90014-0

Young, N. A., Flaherty, D. K., Airey, D. C., Varlan, P., Aworunse, F., Kaas, J. H., et al. (2012). Use of flow cytometry for high-throughput cell population estimates in brain tissue. *Front. Neuroanat.* 6:27. doi: 10.3389/fnana.2012.00027

Zhang, C., Yan, C., Ren, M., Li, A., Quan, T., Gong, H., et al. (2017). A platform for stereological quantitative analysis of the brain-wide distribution of type-specific neurons. *Sci. Rep.* 7:14334. doi: 10.1038/s41598-017-14699-w

frontiers | Frontiers in Neuroscience

TYPE Methods
PUBLISHED 13 October 2023
DOI 10.3389/fnins.2023.1200373

EDITED BY
Xi-Nian Zuo,
Beijing Normal University, China

REVIEWED BY
Liang Ma,
University of Chinese Academy of Sciences, China
Kun Meng,
Brown University, United States
Shuo Chen,
University of Maryland, United States

*CORRESPONDENCE
Didong Li
✉ didongli@unc.edu

†These authors have contributed equally to this work and share first authorship

RECEIVED 04 April 2023
ACCEPTED 05 September 2023
PUBLISHED 13 October 2023

CITATION
Li D, Nguyen P, Zhang Z and Dunson D (2023) Tree representations of brain structural connectivity via persistent homology. *Front. Neurosci.* 17:1200373.
doi: 10.3389/fnins.2023.1200373

Tree representations of brain structural connectivity via persistent homology

Didong Li[1]*†, Phuc Nguyen[2]†, Zhengwu Zhang[3] and David Dunson[2]

[1]Department of Biostatistics, University of North Carolina at Chapel Hill, Chapel Hill, NC, United States, [2]Department of Statistical Science, Duke University, Durham, NC, United States, [3]Department of Statistics and Operations Research, University of North Carolina at Chapel Hill, Chapel Hill, NC, United States

The brain structural connectome is generated by a collection of white matter fiber bundles constructed from diffusion weighted MRI (dMRI), acting as highways for neural activity. There has been abundant interest in studying how the structural connectome varies across individuals in relation to their traits, ranging from age and gender to neuropsychiatric outcomes. After applying tractography to dMRI to get white matter fiber bundles, a key question is how to represent the brain connectome to facilitate statistical analyses relating connectomes to traits. The current standard divides the brain into regions of interest (ROIs), and then relies on an *adjacency matrix* (AM) representation. Each cell in the AM is a measure of connectivity, e.g., number of fiber curves, between a pair of ROIs. Although the AM representation is intuitive, a disadvantage is the high-dimensionality due to the large number of cells in the matrix. This article proposes a simpler tree representation of the brain connectome, which is motivated by ideas in computational topology and takes topological and biological information on the cortical surface into consideration. We demonstrate that our tree representation preserves useful information and interpretability, while reducing dimensionality to improve statistical and computational efficiency. Applications to data from the Human Connectome Project (HCP) are considered and code is provided for reproducing our analyses.

KEYWORDS

adjacency matrix, brain connectome, persistent homology, structural connectivity, tree

1. Introduction

The human brain structural connectome, defined as the white matter fiber tracts connecting different brain regions, plays a central role in understanding how brain structure impacts human function and behavior (Park and Friston, 2013). Recent advances in neuroimaging methods have led to increasing collection of high quality functional and structural connectome data in humans. There are multiple large datasets available containing 1,000s of connectomes, including the Human Connectome Project (HCP) and the UK Biobank (Essen et al., 2012; Bycroft et al., 2018). We can now better relate variations in the connectomes between individuals to phenotypic traits (Wang et al., 2012; Hong et al., 2019; Roy et al., 2019). However, the large amount of data also creates the need for informative and efficient representations of the brain and its structural connectome (Galletta et al., 2017; Zhang et al., 2018; Jeurissen et al., 2019; Pizarro et al., 2019; Sotiropoulos and Zalesky, 2019). The main focus of this article is a novel and efficient representation of the processed connectome data as an alternative to the adjacency matrix (AM) as input to statistical analyses.

Diffusion magnetic resonance imaging (dMRI) uses diffusion-driven displacement of water molecules in the brain to map the organization and orientation of white fiber tracts on a microscopic scale (Bihan, 2003). Applying tractography to the dMRI data, we can construct a "tractogram" of 3D trajectories of white fiber tracts (Jeurissen et al., 2019). It is challenging to analyze the tractogram directly because (1) the number of fiber trajectories is extremely large; (2) the tractogram contains geometric structure; and (3) alignment of individual tracts between subjects remains difficult (Zhang et al., 2019). Because of these challenges, it is common to parcellate the brain into anatomical regions of interest (ROIs; Desikan et al., 2006; Destrieux et al., 2010; Wang et al., 2010), and then extract fiber bundles connecting ROIs. We can then represent the brain structural connectome as a weighted network in the form of an AM, a p by p symmetric matrix, with i, j-th entry equal to the number of fiber curves connecting region i and region j, where p is the total number of regions in the parcellation.

Statistical analyses of structural connectomes are typically based on this AM representation, which characterizes the connectome on a fixed scale depending on the resolution of ROIs. However, research has shown that brain networks fundamentally organize as multi-scale and hierarchical entities (Bassett and Siebenhühner, 2013). Some research has attempted to analyze community structures in functional and structural brain networks across resolutions (Betzel and Bassett, 2017); however, these works are limited to community detection. Brain atlases have anatomically meaningful hierarchies but only one level can be captured by the AM representation. If the lowest level in the atlas hierarchy with the greatest number of ROIs is used, this creates a very high-dimensional representation of the brain. The number of pairs of ROIs often exceeds the number of connectomes in the dataset. This presents statistical and computational challenges, with analyses often having low power and a lack of interpretability (Cremers et al., 2017; Poldrack et al., 2017).

For instance, to infer relationships between the connectome and a trait of interest, it is common to conduct hypothesis tests for association between each edge (connection strength between a pair of ROIs) and the trait (Fornito et al., 2016; Gou et al., 2018; Wang et al., 2019; Lee and Son, 2021). As the number of edges is very large, such tests will tend to produce a large number of type I errors without multiple testing adjustment. If a Bonferroni adjustment is used, then the power for detecting associations between particular edges and traits will be very low. A common alternative is to control for false discovery rate, for example via the Benjamini-Hochberg approach (Genovese et al., 2002). However, such corrections cannot solve the inevitable increase in testing errors that occur with more ROIs. An alternative is to take into account the network structure of the data in the statistical analysis (see, for example Leek and Storey, 2008; Fornito et al., 2016; Alberton et al., 2020). Such approaches can potentially improve power to detect differences while controlling type I errors through appropriate borrowing of information across the edges or relaxation of the independence assumption, but statistical and computational problems arise as the number of ROIs increases. Finally, it is common to vectorize the lower-triangular portion of the brain AM and then apply regression or classification methods designed for high-dimensional features (e.g., by penalizing using the ridge or lasso penalties).

To make the problems more concrete, note that a symmetric $p \times p$ connectome AM has $\frac{(p-1)p}{2}$ pairs of brain ROIs. For the popular Desikan-Killiany parcellation (Desikan et al., 2006) with $p = 68$, $\frac{(p-1)p}{2} = 2,278$. A number of other common atlases have many more than $p = 68$ brain regions, leading to a much larger number of edges. Even if one is relying on data from a large cohort, such as the UK Biobank, the sample size (number of subjects) is still much smaller than the connectivity features, leading to statistical efficiency problems without reducing the dimensionality greatly from $q = \frac{(p-1)p}{2}$. Dimensionality reduction methods, such as Principal Components Analysis (PCA), tensor decomposition, or non-negative matrix factorization, can be a remedy for studying relationships between the connectome and traits (Yourganov et al., 2014; Smith et al., 2015; Zhang et al., 2019; Patel et al., 2020). But, they may lack interpretability and fail to detect important relationships when the first few principal components are not biologically meaningful or predictive of traits.

In this paper, we propose a new representation of the brain connectome that is inspired by ideas in computational topology, a field focused on developing computational tools for investigating topological and geometric structure in complex data (Carlsson, 2009; Edelsbrunner and Harer, 2010). A common technique in computational topology is *persistent homology*, which investigates geometry/topology of the data by assessing how features of the data come and go at different scales of representation. Related ideas have been used successfully in studying brain vascular networks (Bendich et al., 2016), hippocampal spatial maps (Dabaghian et al., 2012), dynamical neuroimaging spatiotemporal representations (Lee et al., 2011; Geniesse et al., 2019), neural data decoding (Rybakken et al., 2019), and so on (Sizemore et al., 2019). We propose a fundamentally different framework, which incorporates an anatomically meaningful hierarchy of brain regions within a persistent homology approach to produce a new tree representation of the brain structural connectome. This representation reduces dimensionality substantially relative to the AM approach, leading to statistical and computational advantages, while enhancing interpretability. After showing our construction and providing mathematical and biological justification, we contrast the new representation with AM representations in analyses of data from the Human Connectome Project (HCP).

2. Method

2.1. Tree construction

There is a rich literature defining a wide variety of parcellations of the brain into regions of interest (ROIs) that are motivated by a combination of biological and statistical justifications (Desikan et al., 2006; Destrieux et al., 2010; Klein and Tourville, 2012). The ROIs should ideally be chosen based on biological function and to avoid inappropriately merging biologically and structurally distinct regions of the brain. Also, it is important to not sub-divide the brain into regions that are so small that (a) it may be difficult to align the data for different subjects and (b) the number of ROIs is so large that the statistical and computational problems mentioned in the introduction are exacerbated. Based on such considerations, the Desikan-Killiany (DK) atlas is particularly popular, breaking the brain into $p = 68$ ROIs (Desikan et al., 2006).

A parcellation such as DK is typically used to construct an AM representation of the structural connectome at a single level of resolution. However, we instead propose to introduce a multi-resolution tree in which we start with the entire cortical surface of the brain as the root node, and then divide into the right and left hemisphere to produce two children of the root node. We further sub-divide the two hemispheres into large sub-regions, then divide these sub-regions into smaller regions. We continue this sub-division until obtaining the regions of DK (or another target atlas) as the leaf nodes in the tree. In doing this, we note that there is substantial flexibility in defining the tree structure; we need not choose a binary tree and can choose the regions at each level of the tree based on biological function considerations to the extent possible. Finally, we summarize the connectivity information at different resolutions in the weights of the tree nodes.

In this article, we focus primarily on the following tree construction based on the DK atlas for illustration, while hoping that this work motivates additional work using careful statistical and biological thinking to choose the regions at each layer of the tree. The DK parcellation is informed by standard neuroanatomical conventions, previous works on brain parcellations, conversations with expert scientists in neuroscience, and anatomic information on local folds and grooves of the brain (Desikan et al., 2006). We use the Freesurfer software to obtain the DK parcellation for each individual brain, and DK parcellation divides each hemisphere into 34 regions that can be organized hierarchically (Desikan et al., 2006). Specifically, each hemisphere has six regions: frontal lobe, parietal lobe, occipital lobe, cingulate cortex, temporal lobe, and insula. All of these regions, except the insula, have multiple sub-regions, many of which are further sub-divided in the DK atlas. The full hierarchy can be found in Appendix 1.1 (Supplementary material). We calculate the weight of each node as the sum of all connections between its immediate children. For instance, the weight at the root node will equal the sum of all the inter-hemisphere connections. The weight of the left hemisphere node will equal the sum of all connections among the left temporal lobe, frontal lobe, parietal lobe, occipital lobe, cingulate cortex, and insula. The weight of the left temporal lobe is the sum of all connections between regions within the temporal medial aspect and lateral aspect. We continue this calculation for all nodes that have children. The weights of a leaf node will be all connections within that region, or equivalently, the diagonal element at that region's index on the AM representation.

To rephrase the tree construction in math notations, let $A = A_1^1$ be the whole brain, A_1^2 be the left hemisphere, A_2^2 be the right hemisphere, and A_i^l be the i-th region at level l, where $l = 1, \cdots, L$ and $i = 1, \cdots, N_l$. For example, in DK, $L = 5$, $N_1 = 1$, $N_2 = 2$, $N_3 = 12, N_4 = 44, N_5 = 32$ (Appendix 1.1 in Supplementary material). Define the weight of region A_i^l, denoted by H_i^l, as $H_i^l :=$ number of fibers connecting any two children of A_i^l for all $l = 1, 2, \cdots, L$ and $i = 1, \cdots, N_l$. For example, for DK-based tree, H_1^2 is the number of fibers connecting children of left hemisphere, that is, fibers between temporal lobe, cingulate cortex, occipital lobe, parietal lobe, and frontal lobe. Similarly, H_1^3 is the number of fibers connecting children of temporal lobe, that is, fibers between medial aspect and lateral aspect.

Figure 1 provides an illustration of the DK-based tree structure and the connections summarized at each node. Often the connections within the leaf nodes are not estimated in the AM representation (i.e., the diagonal elements of an AM are set to zero), thus, they have weights zero and are omitted from the figure. We also introduce a more compact visualization of the tree based on circle chord plots. Figure 2 shows the steps in our pipeline to construct a brain tree. The final output circle plot displays bundles of white matter tracts as overlapping chords scaled inversely proportional to the level of the tree they belong to and color-coded by the node they belong to.

2.2. A persistent homology interpretation

Persistent homology is a method for computing topological features of a space at different resolutions. As quantitative features of noisy data, persistent homology is less sensitive to the choice of coordinate and metric and robust to noise (Carlsson, 2009). The key construction in persistent homology is the filtration, a multi-scale structure similar to the brain network. As a result, we can interpret the above defined H_k^l as corank of the persistent homology. As a rigorous definition of persistent homology is highly technical, we present a simple version and leave the rigorous version and the proof to the Appendix in Supplementary material. For relevant background in topology (see Hatcher, 2002; Munkres, 2016).

Theorem 1. *H_k^l is the corank of the persistent homology.*

Theorem 1 provides a topological interpretation of H_k^l, and partially explains why the tree $T = (A, H)$ is a powerful representation of the brain network. It states that H_k^l, our proposed summary statistic, is the corank of the persistent homology. In simpler terms, this means that our statistic measures the "holes" or loops in the structure of the brain network that persist across different levels of partition. These holes can be thought of as stable features of the network, in that they remain even when we change our perspective or level of detail. As we increase the resolution (i.e., when we move from looking at large-scale structures to focusing on smaller-scale details), some holes may "close up" (disappear), while others continue to exist. These persistent holes can inform us about the topological structure of the brain network. Thus, H_k^l, by capturing these persistent features, provides a summary statistic that is less sensitive to changes in perspective and robust against noise.

We consider the tree $T = (A, H)$ to be a powerful representation because it captures not just the connections between different regions of the brain (as the adjacency matrix A does), but also the persistent homological features (captured by H_k^l). This allows us to include topological information, like the persistence of holes at different scales, which can potentially capture complex structural information about the brain network that a simple adjacency matrix might miss. In effect, $T = (A, H)$ provides us with a richer, more nuanced view of the brain network, thus making it a powerful representation for brain connectivity analysis.

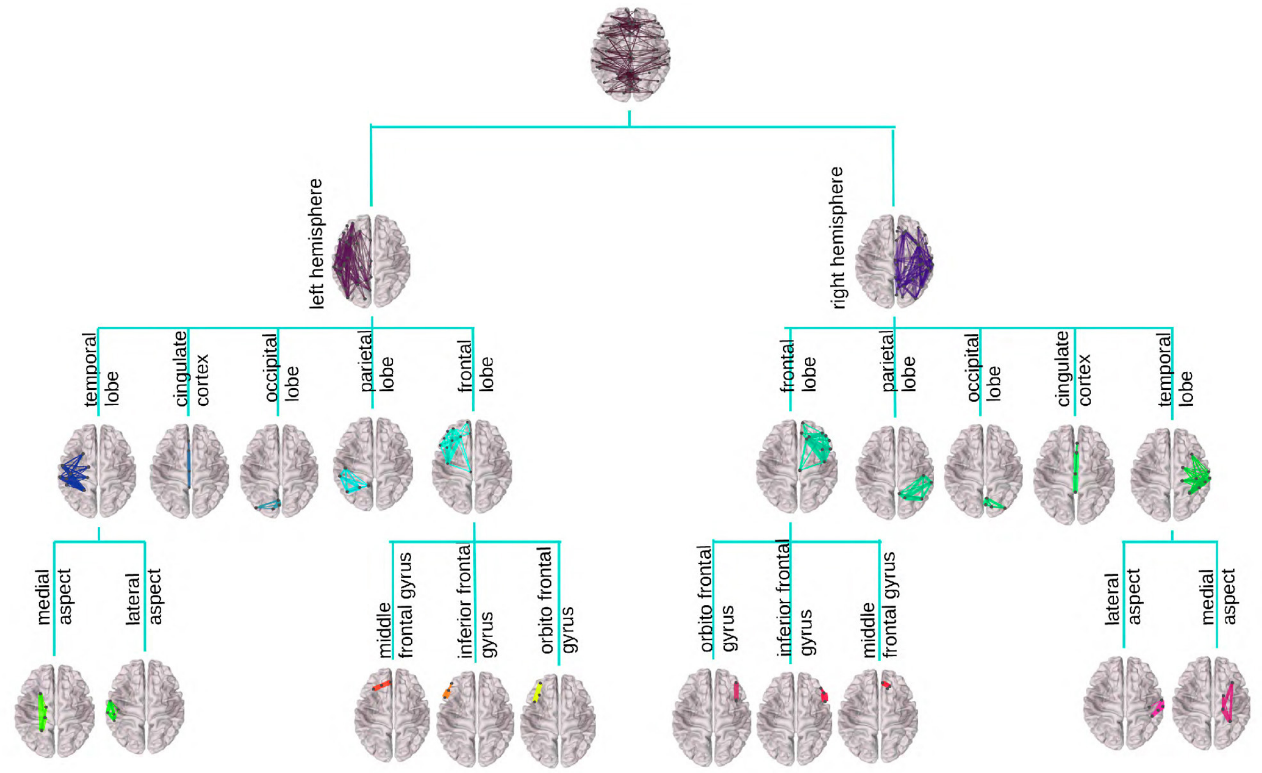

FIGURE 1
Visualization of the DK tree structure and connections summarized at each node on the brain image. Leaves, including the insula, have no internal connections and are omitted for readability. Individual brains were created using the `brainconn` R package (Orchard et al., 2021).

3. Results

3.1. Data description

We investigate our tree representation's ability to preserve information from the AM representation while improving interpretability in analyses relating brain structures to behavioral traits. We use neuroimaging data and scores on various behavioral assessments from the HCP (Glasser et al., 2013, 2016). The HCP collects high-quality diffusion MRI (dMRI) and structural MRI (sMRI) data, characterizing brain connectivity of 1,200 healthy adults, and enables comparison between brain circuits, behavior and genetics at the individual subject level (Essen et al., 2012). We use data from the 2017 release accessed through ConnectomeDB. Details on data acquisition and preprocessing pipeline of dMRI and sMRI data in the HCP can be found in Essen et al. (2012) and Glasser et al. (2013, 2016). To produce connectome data from raw dMRI/sMRI data, we use the reproducible probabilistic tractography algorithm in Girard et al. (2014) to construct tractography data for each subject, the DK atlas (Desikan et al., 2006) to define the brain parcellation, and the preprocessing pipeline in Zhang et al. (2018) to extract weighted matrices of connections. More details of these steps can be found in Zhang et al. (2019). In the extracted data matrices, each connection is described by a scalar number. The HCP data include scores for many behavioral traits related to cognition, motor skills, substance use, sensories, emotions, personalities, and many others. Details can be found at https://wiki.humanconnectome.org/display/PublicData/HCP-YA+Data+Dictionary-+Updated+for+the+1200+Subject+Release. The final data set consists of $n = 1,065$ brain connectomes and 175 traits. We construct the tree representations of the connectomes based on the construction described in Section 2.1.

We conduct purely visual exploratory comparisons of the tree and AM representation in Figure 3. Figure 3A shows how four example brain connectomes are visualized differently under two representations. We see that different nodes in the tree representation correspond to different pixel patterns in the AM representation. Figure 3B shows the percent difference in brain connections between the top and bottom ten percent of scores in four cognitive tasks. The percent difference in the AM representation of a trait is calculated as $\frac{C^{AM}_{top}-C^{AM}_{bottom}}{C^{AM}_{bottom}}$, where C^{AM}_{top} is the average AM of people who score in the top 10% of that trait, and C^{AM}_{bottom} is the average AM of people who score in the bottom 10%. Similarly, the percent difference in the tree representation of a trait is calculated as $\frac{C^{tree}_{top}-C^{tree}_{bottom}}{C^{tree}_{bottom}}$, where C^{tree}_{top} is the average tree of people who score in the top 10% of that trait, and C^{tree}_{bottom} is the average tree of people who score in the bottom 10%. Figure 3B shows the visualization of the tree representation as a more effective exploratory analysis tool to find regions of the brain with large percentage change between the top and bottom scores. On the other

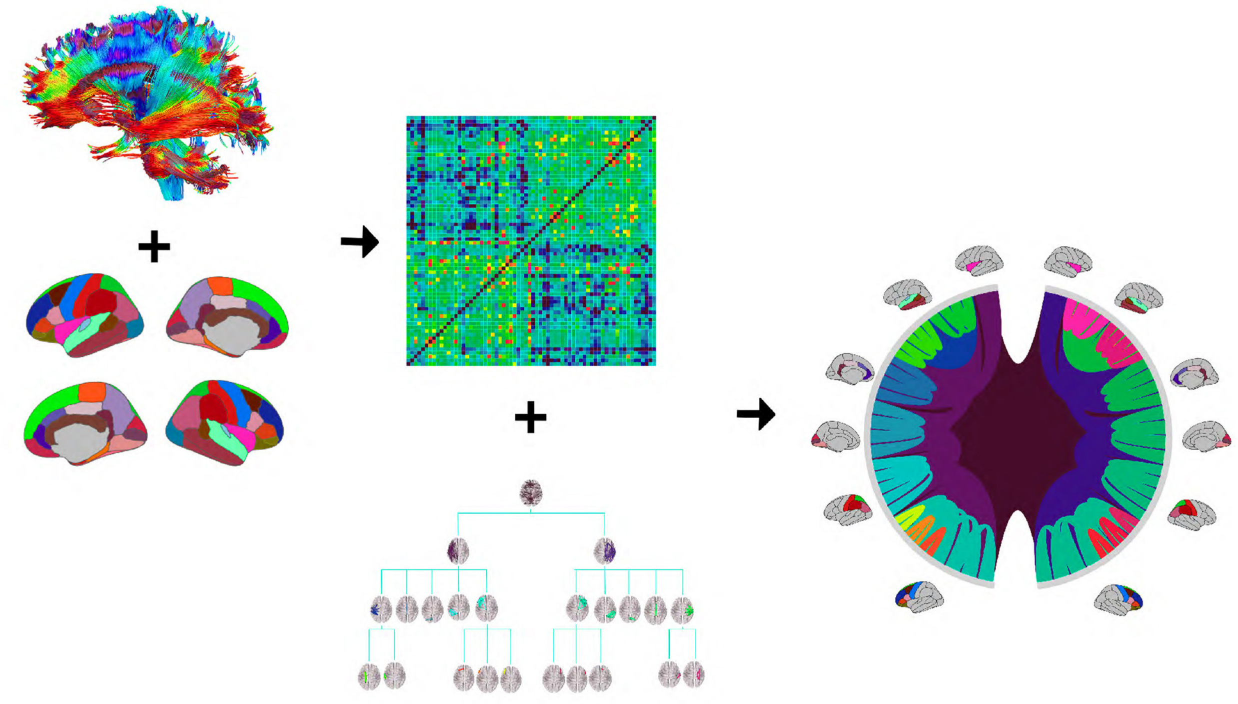

FIGURE 2
The tree construction pipeline: first, tractography and Desikan-Killiany (DK) protocol are used to estimate an adjacency matrix; then, the adjacency matrix and a hierarchy based on the DK protocol are combined to produce the tree representation. We introduce a compact circle chord plot that shows the tree representation of white matter fiber tracts connecting brain regions from the DK protocol. Connections are color-coded by the node they belong to, the same color codes as in Figure 1, and scaled inversely proportional to the level they belong to in the tree.

hand, the AM, being a much higher dimensional representation, can capture connection-specific associations, especially negative ones that get washed out at the brain-region level.

To quantitatively compare the strengths and weaknesses of the AM and tree-based representations of the brain connectome in the next subsections, we use a simple two-step approach: first vectorizing the connectome data, and then applying a regression method. Since a connectome matrix is symmetric, we only vectorize the upper triangular part, resulting in a 2,278-dimensional vector for each matrix. We also remove pairs of ROIs that show no variability in connectivity across subjects, reducing the vectorized matrices to 2,202 dimensions. Self-edges are not recorded in the connectome matrices, so the leaves in the tree representation have zero weights. As a result, we remove the leaf nodes, leaving the vectorized trees to be 23-dimensional instead of 91-dimensional.

To apply regression algorithms, we first reduce the dimension of the adjacency matrix to $K \ll 2,202$ by selecting the top principal components (PCs). We observed that the regression MSEs of commonly used algorithms including linear regression, decision trees, support vector machines (SVM), boosting, Gaussian process (GP) regression, etc., did not decrease when we increased the number of PCs, and Zhang et al. (2019) also observed that the regression performance is robust for $K = 20$–60. As a result, we keep the first $K = 23$ PCs to match the dimension of the tree for a fair comparison. We refer to the data from the vectorized trees as D_{tree} and that from principal components of the vectorized matrices as D_{PCA}.

3.2. Canonical correlation analysis

Human brain connectivity has been shown to be capable of explaining significant variation in a variety of human traits. Specifically, data on functional and structural connectivity have been used to form latent variables that are positively correlated with desirable, positive traits (i.e., high scores on fluid intelligence or oral reading comprehension) while also being negatively correlated with undesirable traits (i.e., low sleep quality, frequent use of tobacco, or cannabis; Smith et al., 2015; Tian et al., 2020). In this first analysis, we compare how strongly latent variables inferred from the two representations are associated with the perceived desirability of traits. We choose to work with a subset of 45 traits that have been shown to strongly associate with brain connectome variations, including cognitive traits, tobacco/drug use, income, years of education, and negative and positive emotions (Smith et al., 2015; Zhang et al., 2019). We include only traits with continuous values to simplify the analyses. The full list of variables used can be found in the Appendix (Supplementary material). We will use a statistical method called canonical correlation analysis (CCA), which finds linear combinations of the predictors that are most

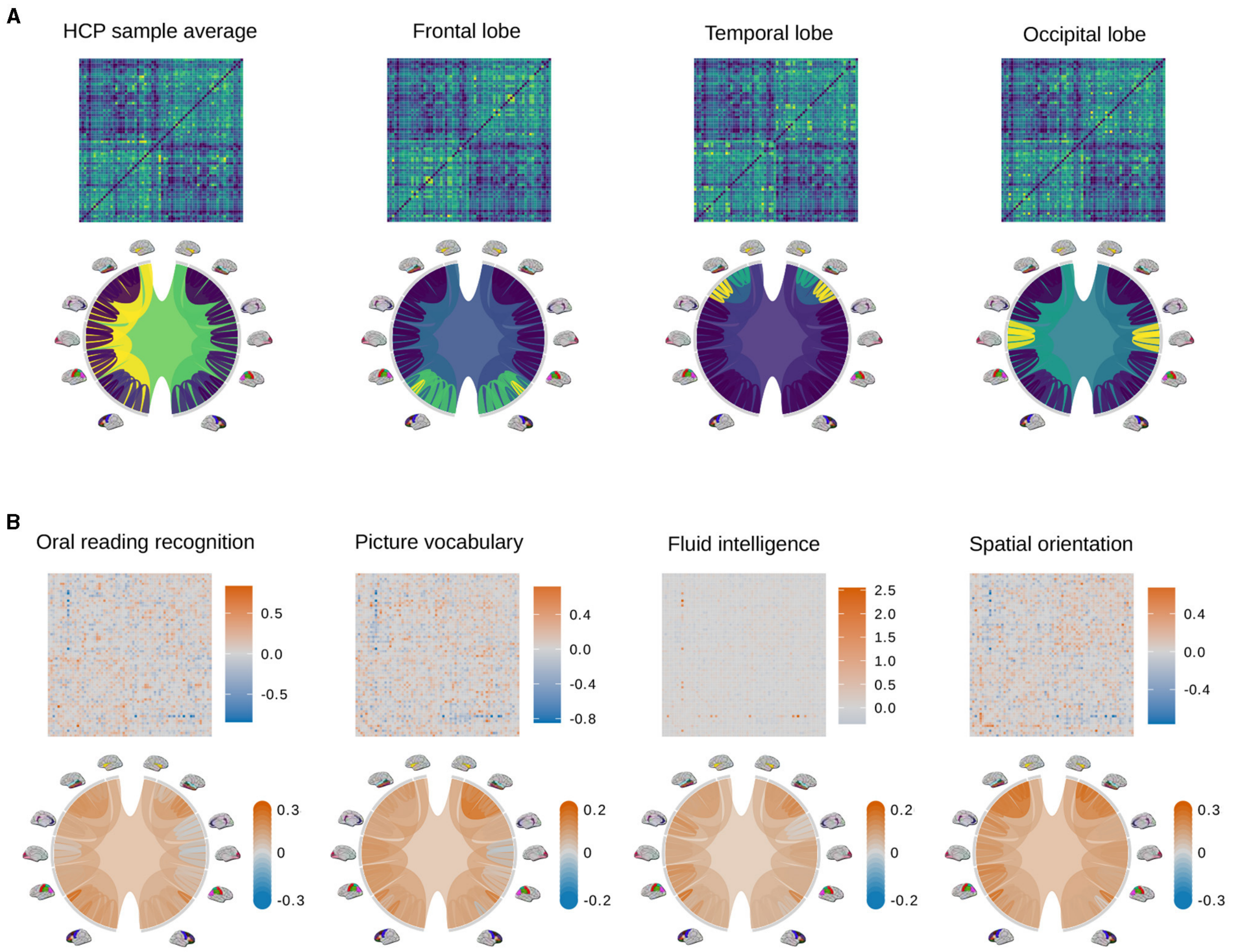

FIGURE 3
Examples of adjacency matrices and corresponding tree representations of brain connectomes. **(A)** The sample average from the HCP data (left most) and its modifications so that different regions of the brain (i.e., the frontal lobe, temporal lobe, and occipital lobe) have denser connections. Because these modifications are unrealistic and only meant to better distinguish how connections are visualized differently in the AM and tree representations, color scales are omitted. Values in the adjacency matrices are normalized for visual clarity. **(B)** Percent difference in brain connections between the top and bottom ten percent of scores in four cognitive tasks.

correlated with some other linear combinations of the outcomes. In our case, the predictors are principal components of the vectorized AM or features of the vectorized trees, and the outcomes are scores measured on 45 traits. Mathematically, let $X \in \mathbb{R}^{n\times p}$ be the feature matrix ($n = 1,065, p = 23$), and $Y \in \mathbb{R}^{n\times q}$ be the outcome matrix ($q = 39$ with some traits being removed due to extensive missing values, see the next paragraph for more details). Additionally, let $\boldsymbol{a}_k \in \mathbb{R}^p$ and $\boldsymbol{b}_k \in \mathbb{R}^q$, $k = 1, ..., \min(p, q)$ be pairs of linear transformation of the data. We refer to $(\boldsymbol{r}_k, \boldsymbol{s}_k) = (X\boldsymbol{a}_k, Y\boldsymbol{b}_k)$ as the feature and outcome canonical variates or the k^{th} pair of canonical variates. CCA aims to learn $\boldsymbol{a}_k, \boldsymbol{b}_k$ such that $(\boldsymbol{a}_k, \boldsymbol{b}_k) = \text{argmax}_{\boldsymbol{a}_k,\boldsymbol{b}_k} \text{corr}(\boldsymbol{r}_k, \boldsymbol{s}_k)$, so the linear transformations maximize the correlation between components of the canonical variates pair. Pairs of canonical variates are also constrained to be orthogonal, that is, $\boldsymbol{r}_k^T \boldsymbol{r}_h = 0$ and $\boldsymbol{s}_k^T \boldsymbol{s}_h = 0$ for $k \neq h$.

Since this analysis considers all traits simultaneously, we remove traits with extensive missing values (i.e., more than 10% of all observations) and are left with 39 traits. We then normalize D_{tree}, D_{PCA}, and these 39 trait scores, and fill in missing values with the feature's mean. We fit two CCAs using D_{tree} and D_{PCA} separately, and use the Wilks's lambda test to check that the first canonical variate pair, which has the largest co-variation, is significant at the 5% level in each model. We hand-label the traits as desirable or not desirable based on previous research (Smith et al., 2015; Tian et al., 2020). Figure 4 plots the correlation of the trait scores with the first feature canonical variate and color-codes traits by desirability. Traits with smaller fonts have smaller contributions to the linear combination that makes up the first outcome canonical variate. It shows that desirable traits tend to be more highly negatively correlated with the first feature canonical variate compared to the undesirable traits, which tend to be weakly correlated. This is most clear with traits with strong signal such as fluid intelligence and spatial orientation. With the same number of features, the tree representation produces a canonical variate that can separate traits into groups of the same desirability slightly better than the principal components of the AM can.

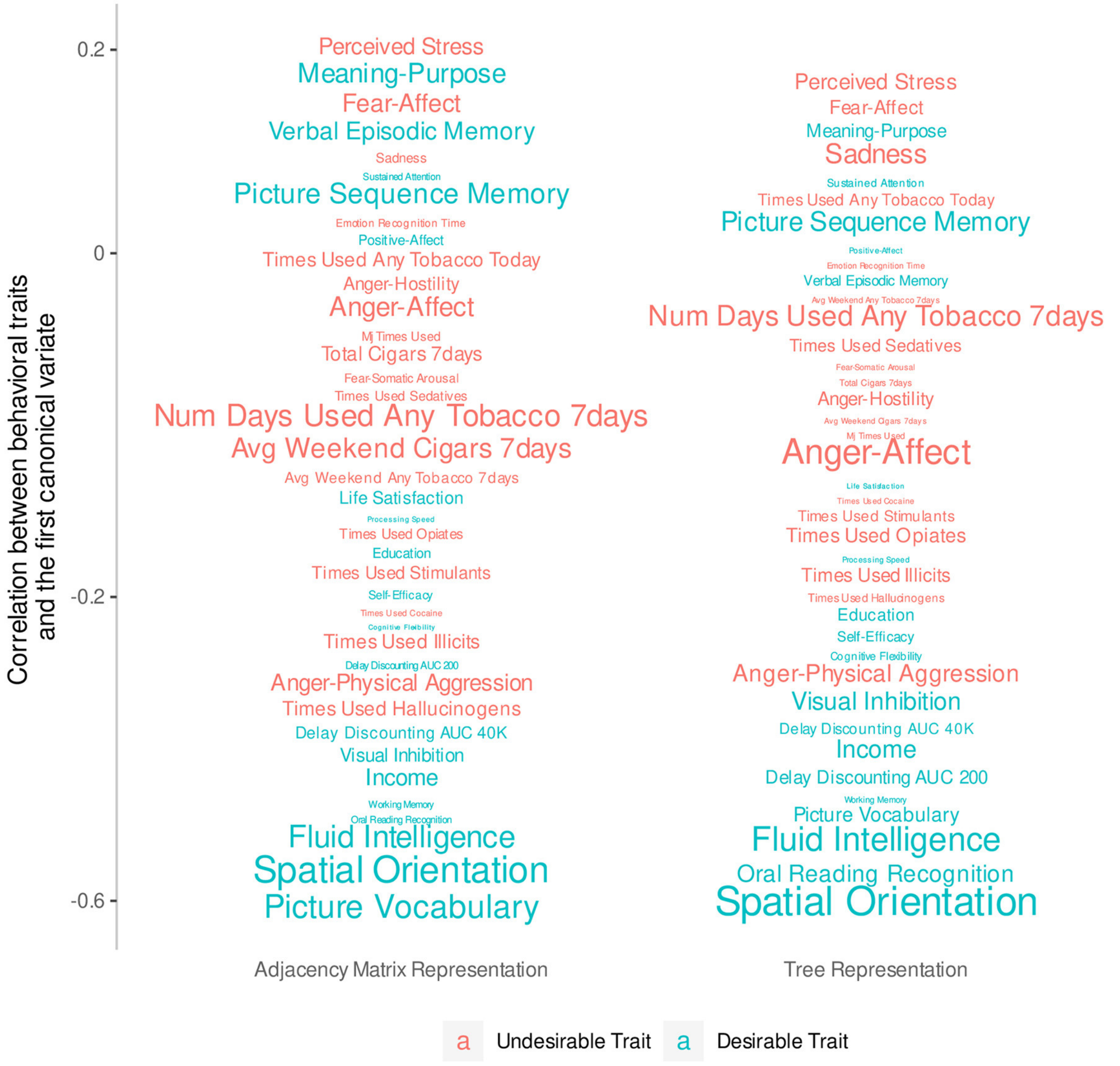

FIGURE 4
Correlations between behavioral traits and the first canonical variate extracted from 23 principal components of the AM compared to the 23 non-leaf nodes of the tree representation. The y-axis has been transformed so that traits do not overlap. The font size of each trait indicates the magnitude of the coefficients of a linear combination that defines the first canonical variate.

3.3. Prediction

Additionally, we consider the performance of these representations in predictive tasks. We hypothesize that if the tree representation preserves important information from the AM representation, they will provide comparable performance in predicting trait scores. Since in Section 3.2, cognitive traits generally have the largest correlations with the first feature canonical variate, we will examine cognitive traits in more details in this section. Specifically, we include all 45 cognitive traits in the HCP data, including different metrics of the same trait. We fit a baseline model that returns the sample mean and 19 popular machine learning models (including linear regression, decision tree, SVM, ensemble trees, GP regression, and their variants) to the D_{tree} and D_{PCA} data. To evaluate predictive performance, we consider two scale-free metrics: (1) correlations between predictions and true outcomes and (2) the percentage of improvement in test MSE compared to the baseline predictor. We calculate these metrics using five-fold cross validation repeated 10 times. Figures 5, 6 shows the cross-validated predictive performance for two representative regression algorithms: linear regression and GP regression. Linear regression represents a simple, interpretable, and widely used algorithm, while GP regression is a flexible algorithm that has the best overall performance among the 19 algorithms we studied. For each algorithm and each trait, the x-axis is the performance of the AM representation while the y-axis is that of the tree representation. Points above the diagonal line $y = x$ indicate better performance by the tree representation, while points below the line indicate better performance by the AM representation.

Overall, the performance of both representations seems similar. However, for most traits, even when considering the

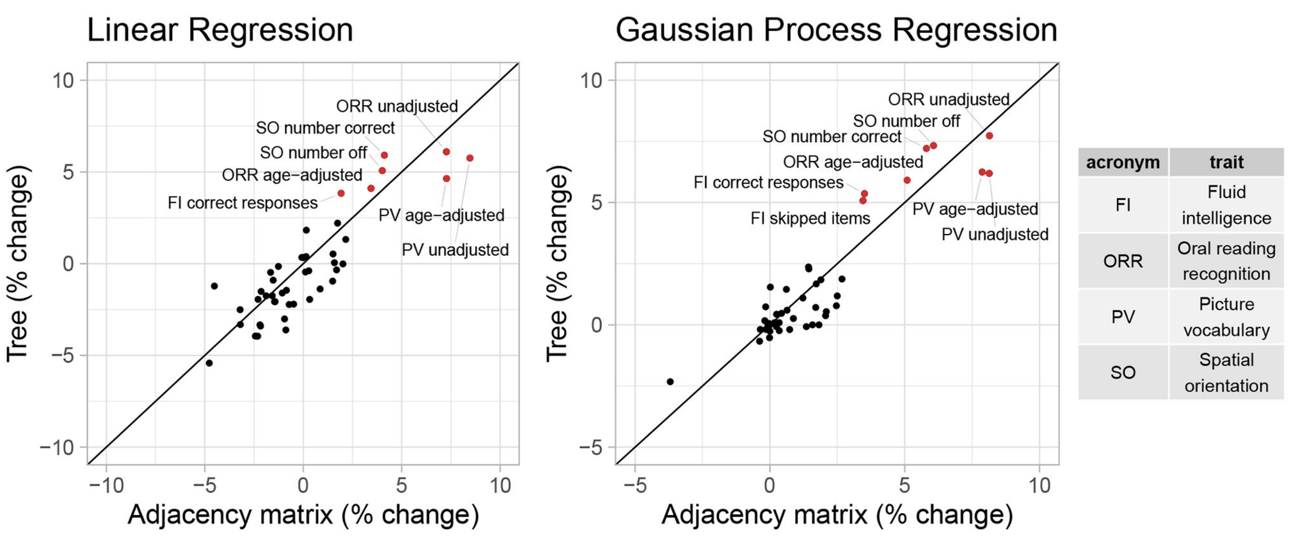

FIGURE 5
Percentage of change in MSE compared to baseline of linear regression and GP regression using tree and AM representation in predicting 45 cognitive traits.

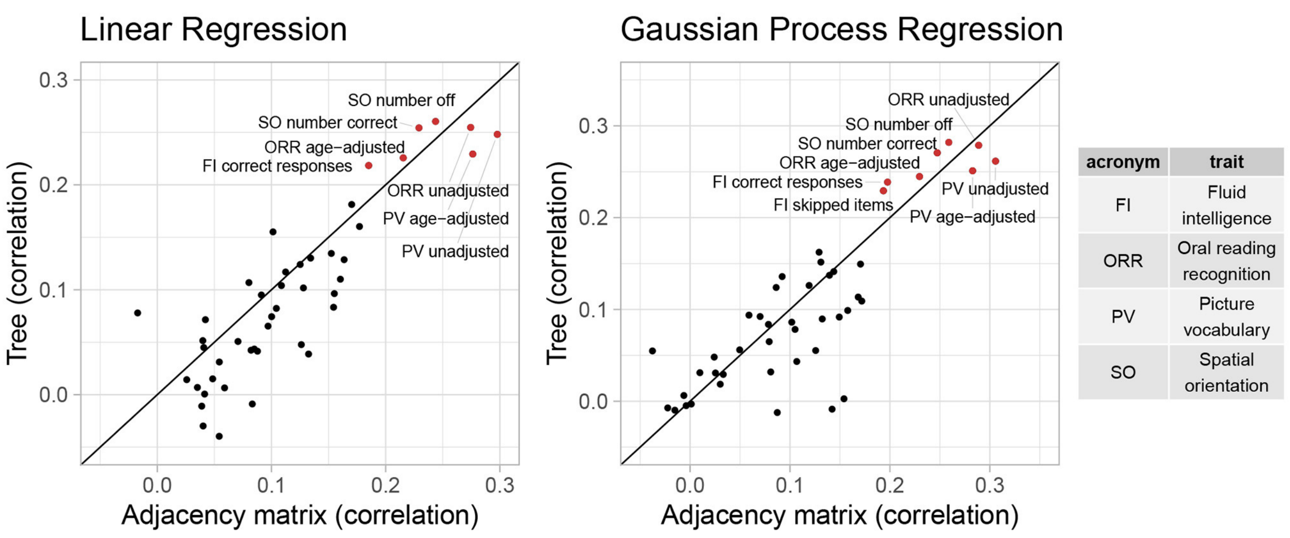

FIGURE 6
Correlation between predictions and observed outcomes of linear regression and GP regression using tree and AM representation in predicting 45 cognitive traits.

GP regression with best overall performance, the correlation is smaller than 0.2, and the improvement in test MSE is <3%. This suggests that the vectorized brain connectivity might not be relevant to predicting most of these traits. If we focus on traits with large correlations or improvement in MSE, the tree representation has better performance in terms of both correlation and improvement in MSE for five out of eight traits with correlations >0.2. These traits include fluid intelligence, picture vocabulary, spatial orientation, and oral reading recognition, which also have the largest correlations with the canonical variate in Section 3.2.

3.4. Interpretability of regression

Finally, we compare interpretability of the two representations. Scientists are often interested in identifying structures in the connectomes that are associated with traits to answer questions such as which kind of connections might be damaged by routine use of drugs or which might be responsible for enhanced working memory. Therefore, we compare interpretability, in terms of biologically meaningful inference, of regression results using the two representations. We focus on spatial orientation (number correct), picture vocabulary (age-adjusted), fluid intelligence (correct responses), oral reading recognition (age-adjusted), and working memory (age-adjusted) because these traits show strong associations with the connectomes in the CCA and prediction tasks.

We fit a separate linear regression with Bayesian model selection on D_{tree} and D_{PCA} to infer associations between brain connectomes and the traits mentioned above. Bayesian model selection accounts for uncertainty in the model selection process by posterior probabilities for the different possible models. The regression coefficients are averaged across all models, weighted by estimated model posterior probabilities. For feature selection, we define important features as those with posterior inclusion probabilities of more than 0.75. For models using D_{tree}, we simply interpret posterior means and credible intervals of the estimated effects of important features directly. Figures 7, 8 (left column) show tree features whose colors are based on their estimated coefficients, and opacity are based on their posterior inclusion probabilities.

For the models using D_{PCA}, after selecting important principal components, we can calculate a regression coefficient for each brain connection from the regression coefficients of these important principal components. Let X be an $n \times p$ matrix of vectorized brain connections whose columns have been standardized. Recall that PCA is based on the singular-value decomposition of the data matrix $X = UDV^T$, where $VV^T = I$, $U^TU = I$ and D is a diagonal matrix of p non-negative singular values, sorted in decreasing order. The jth principal axis is the jth eigenvector or the jth column of V, and the jth principal component is the jth column of UD. With K PCs, we get a rank-K approximation of $X \approx U_K D_K V_K^T$ where M_K contains the first K columns of matrix M. Applying the approximation to the linear model $Y = X\boldsymbol{\beta} + \boldsymbol{\epsilon} \approx U_K D_K \boldsymbol{\theta} + \boldsymbol{\epsilon}$, we get $V_K^T \boldsymbol{\beta} \approx \boldsymbol{\theta}$, where $\boldsymbol{\theta}$ is a K-vector of regression coefficients of the principal components. There are multiple generalized inverses $\hat{\boldsymbol{\beta}} = V_K \boldsymbol{\theta} + \mathbf{b}$ for $\mathbf{b}$ such that $V_K^T \mathbf{b} = \mathbf{0}$. We will use $\mathbf{b} = \mathbf{0}$ to get the standard least-norm inverse $\hat{\boldsymbol{\beta}} = V_K \boldsymbol{\theta}$ as estimates of the regression coefficient for the original brain connections (Bernardo et al., 2003). We interpret the results based on 50 connections with the largest coefficient magnitude. Figures 7, 8 (right column) show these connections colored by their estimated coefficients.

The tree-based model finds no structure statistically significant (with posterior inclusion probability >0.75) in predicting enhanced working memory. This is consistent with previous sections showing weak signals for associations between working memory and brain connectomes. The matrix-based model finds some cross-hemispheric connections between temporal lobes positively correlated with enhanced memory, which is supported by prior research (Eriksson et al., 2015). However, it also finds many right hemispheric connections negatively correlated with these scores, which contradicts some prior findings (Poldrack and Gabrieli, 1998). For oral reading recognition, the models find cross-hemispheric and left-hemispheric connections important in both the tree and adjacency matrix representations. This is consistent with prior research that showed better reading ability associated with more cross-hemispheric connections between frontal lobes (Zhang et al., 2019) and with increased fractional anisotropy in some left hemispheric fiber tracts (Yeatman et al., 2012). The matrix-based model additionally finds many connections across all regions in the right hemisphere to be important, among which the insula, frontal opercular, and lateral temporal lobe have previously been found to correlate with this score (Kristanto et al., 2020). On the other hand, the tree-based model found increased connectivity in the right occipital lobe to negatively correlate with higher scores. While healthy adults typically have larger left occipital lobar volume, research has found associations between developmental stuttering and phonological dyslexia with rightward occipital asymmetry or no occipital asymmetry (Foundas et al., 2003; Zadina et al., 2006), which is consistent with our tree-based model's result. For fluid intelligence, the tree-based model finds connections within the left hemisphere and between hemispheres to be important. The matrix-based model finds within-hemisphere connections, especially those involving the frontal lobes, to be important. The fluid intelligence score serves as proxy for "general intelligence" (Raven, 2000; Gershon et al., 2014), which relies on many sub-networks distributed across the brain (Dubois et al., 2018). For the vocabulary task, the tree-based model finds connections within the left hemisphere, while the matrix-based model finds connections within both hemispheres, to be important. Both results support existing findings that interpreting meanings of words activates many regions across the brain (Huth et al., 2016). Finally, in the spatial orientation task, the tree-based model finds cross-hemispheric connections to be important and positively correlated with better scores, while the matrix-based model does for connections between regions within each hemisphere (Figure 8, bottom). Both are somewhat similar to prior research that found decreased cross-hemispheric and right hemispheric connectivity to be associated with impaired spatial recognition of stroke patients (Ptak et al., 2020). Overall, we observe that the results from the tree representation are easier to interpret because of the inherent low-dimensional and biologically meaningful structure. The results from the AM representation tend to be noisier, and more likely to involve negative correlations between connectivity and better performance in cognitive tasks. Potentially, the representations may better encode different kinds of information that are both important.

4. Discussion

We propose a novel and efficient tree representation based on persistent homology for the brain network. Through analyses of the HCP data, we show that the tree representation preserves information from the AM representation that relates brain structures to traits while being much simpler to interpret. Simultaneously, it reduces the computational cost and complexity of the analysis because of its inherent lower dimension. We believe the advantages of the tree representation will be more evident on small brain imaging data sets.

Our new representation opens doors to new mathematical and statistical methods to analyze brain connectomes; in particular, taking into account the tree structure of the data. Topological data analysis (TDA) uses notions of shapes and connectivity to find structure in data, and persistent homology is one of the most well-known TDA methods (Wasserman, 2017). TDA has been used successfully in studying brain networks (Saggar et al., 2018; Gracia-Tabuenca et al., 2020), but we provide a fundamentally different approach. Our analyses of the connectome trees in this paper are simplistic. We treat tree nodes as independent and

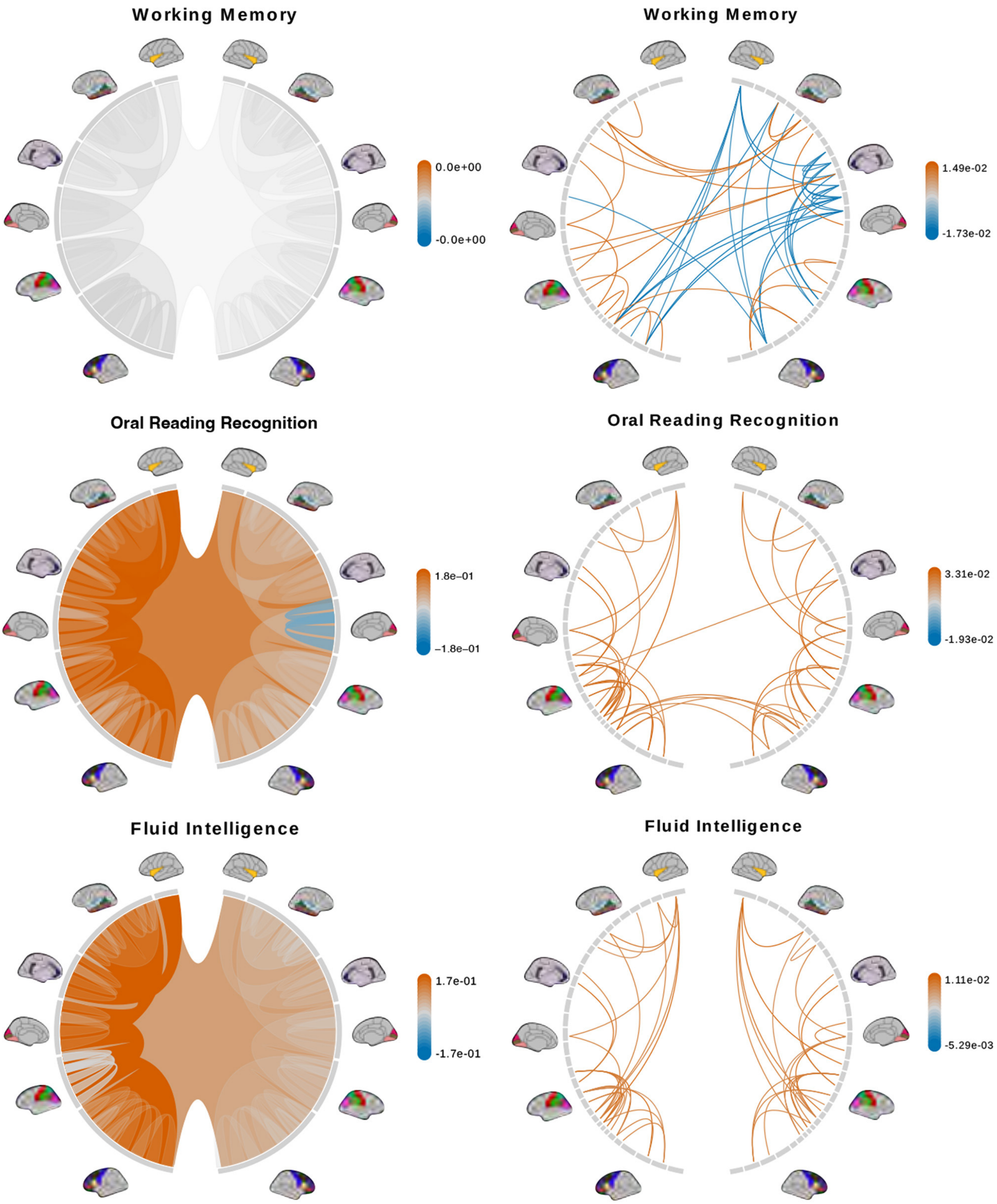

FIGURE 7
Brain connectome structures significantly associated with each trait inferred using the tree representation **(left)** and principal components of the AM representation **(right)**. Colors represent the sign and magnitude of significant (i.e., posterior inclusion probability >0.75) regression coefficients. For tree-based results, the opacity also represents the posterior inclusion probability to improve the visibility of bundles of connections with larger effects.

non-interacting. Future work should consider the tree structure to enforce dependence between the nodes, and hence, between their effects on behavioral traits. The tree structure may also be exploited to model interactions between connectome structures across different scales. For instance, Bayesian treed models are flexible, nonparametric methods that have found widespread and

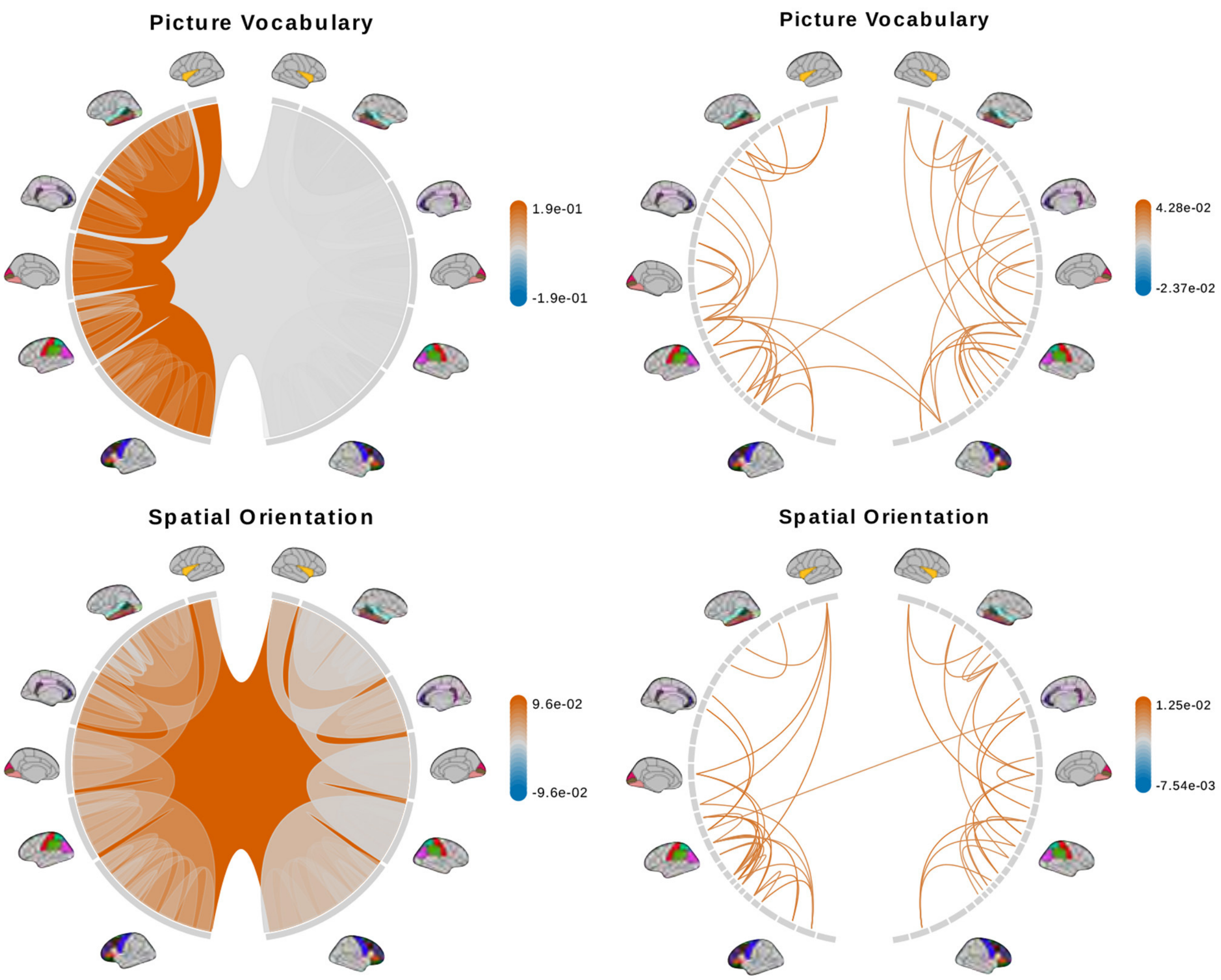

FIGURE 8
(Continue) Brain connectome structures significantly associated with each trait inferred using the tree representation **(left)** and principal components of the AM representation **(right)**. Colors represent the sign and magnitude of significant (i.e., posterior inclusion probability >0.75) regression coefficients. For tree-based results, the opacity also represents the posterior inclusion probability to improve the visibility of bundles of connections with larger effects.

successful applications in many domains (Linero, 2017). Existing treed models might prove unwieldy to fit and interpret on AM-based brain networks but their modifications may fit the nature of our tree representation well.

Data availability statement

Publicly available datasets were analyzed in this study. This data can be found at: https://github.com/phuchonguyen/brain-topology; https://wiki.humanconnectome.org/display/PublicData/How+to+Access+Data+on+ConnectomeDB.

Author contributions

DL, PN, ZZ, and DD designed the method, analyzed the results, and edited the manuscript. DL and PN implemented the method, conducted data analysis, and wrote the manuscript. All authors contributed to the article and approved the submitted version.

Funding

DL was supported by NIH/NCATS award UL1 TR002489, NIH/NHLBI award R01 HL149683, and NIH/NIEHS award P30 ES010126. PN and DD were supported by NIH award R01ES035625. ZZ was supported by NIH award R01 MH118927.

Conflict of interest

The authors declare that the research was conducted in the absence of any commercial or financial relationships that could be construed as a potential conflict of interest.

Publisher's note

All claims expressed in this article are solely those of the authors and do not necessarily represent those of

Supplementary material

The Supplementary Material for this article can be found online at: https://www.frontiersin.org/articles/10.3389/fnins.2023.1200373/full#supplementary-material

References

Alberton, B. A., Nichols, T. E., Gamba, H. R., and Winkler, A. M. (2020). Multiple testing correction over contrasts for brain imaging. *NeuroImage* 216, 116760. doi: 10.1016/j.neuroimage.2020.116760

Bassett, D. S., and Siebenhühner, F. (2013). Multiscale network organization in the human brain. *Multisc. Analysis Nonlin. Dyn.* 179–204. doi: 10.1002/9783527671632.CH07

Bendich, P., Marron, J. S., Miller, E., Pieloch, A., and Skwerer, S. (2016). Persistent homology analysis of brain artery trees. *Ann. Appl. Stat.* 10, 198. doi: 10.1214/15-AOAS886

Bernardo, J., Bayarri, M., Berger, J., Dawid, A., Heckerman, D., Smith, A., et al. (2003). Bayesian factor regression models in the "large p, small n" paradigm. *Bayesian Statist.* 7, 733–742.

Betzel, R. F., and Bassett, D. S. (2017). Multi-scale brain networks. *NeuroImage* 160, 73–83. doi: 10.1016/j.neuroimage.2016.11.006

Bihan, D. L. (2003). Looking into the functional architecture of the brain with diffusion MRI. *Nat. Rev. Neurosci.* 4, 469–480. doi: 10.1038/nrn1119

Bycroft, C., Freeman, C., Petkova, D., Band, G., Elliott, L. T., Sharp, K., et al. (2018). The UK Biobank resource with deep phenotyping and genomic data. *Nature* 562, 203–209. doi: 10.1038/s41586-018-0579-z

Carlsson, G. (2009). Topology and data. *Bull. Am. Math. Soc.* 46, 255–308. doi: 10.1090/S0273-0979-09-01249-X

Cremers, H. R., Wager, T. D., and Yarkoni, T. (2017). The relation between statistical power and inference in fMRI. *PLoS ONE* 12, e0184923. doi: 10.1371/journal.pone.0184923

Dabaghian, Y., Mémoli, F., Frank, L., and Carlsson, G. (2012). *A Topological Paradigm for Hippocampal Spatial Map Formation Using Persistent Homology*. San Francisco, CA: Public Library of Science. doi: 10.1371/journal.pcbi.1002581

Desikan, R. S., Ségonne, F., Fischl, B., Quinn, B. T., Dickerson, B. C., Blacker, D., et al. (2006). An automated labeling system for subdividing the human cerebral cortex on MRI scans into gyral based regions of interest. *NeuroImage* 31, 968–980. doi: 10.1016/j.neuroimage.2006.01.021

Destrieux, C., Fischl, B., Dale, A., and Halgren, E. (2010). Automatic parcellation of human cortical gyri and sulci using standard anatomical nomenclature. *NeuroImage* 53, 1–15. doi: 10.1016/j.neuroimage.2010.06.010

Dubois, J., Galdi, P., Paul, L. K., and Adolphs, R. (2018). A distributed brain network predicts general intelligence from resting-state human neuroimaging data. *Philos. Trans. R. Soc. B Biol. Sci.* 373, 20170284. doi: 10.1098/rstb.2017.0284

Edelsbrunner, H., and Harer, J. (2010). *Computational Topology: An Introduction*. Providence, Rhode Island: American Mathematical Society.

Eriksson, J., Vogel, E., Lansner, A., Bergstrm, F., and Nyberg, L. (2015). Neurocognitive architecture of working memory. *Neuron* 88, 33–46. doi: 10.1016/j.neuron.2015.09.020

Essen, D. C. V., Ugurbil, K., Auerbach, E., Barch, D., Behrens, T. E. J., Bucholz, R., et al. (2012). The human connectome project: a data acquisition perspective. *NeuroImage* 62, 2222–2231. doi: 10.1016/j.neuroimage.2012.02.018

Fornito, A., Zalesky, A., and Bullmore, E. (2016). *Fundamentals of Brain Network Analysis*. San Diego, CA: Academic press.

Foundas, A., Corey, D., Angeles, V., Bollich, A., Crabtree-Hartman, E., and Heilman, K. (2003). Atypical cerebral laterality in adults with persistent developmental stuttering. *Neurology* 61, 1378–1385. doi: 10.1212/01.WNL.0000094320.44334.86

Galletta, A., Celesti, A., Tusa, F., Fazio, M., Bramanti, P., and Villari, M. (2017). "Big mri data dissemination and retrieval in a multi-cloud hospital storage system" in *Proceedings of the 2017 International Conference on Digital Health* (London), 162–166.

Geniesse, C., Sporns, O., Petri, G., and Saggar, M. (2019). Generating dynamical neuroimaging spatiotemporal representations (DyNeuSR) using topological data analysis. *Netw. Neurosci.* 3, 763–778. doi: 10.1162/netn_a_00093

Genovese, C. R., Lazar, N. A., and Nichols, T. (2002). Thresholding of statistical maps in functional neuroimaging using the false discovery rate. *NeuroImage* 15, 870–878. doi: 10.1006/nimg.2001.1037

Gershon, R. C., Cook, K. F., Mungas, D., Manly, J. J., Slotkin, J., Beaumont, J. L., et al. (2014). Language measures of the NIH toolbox cognition battery. *J. Int. Neuropsychol. Soc.* 20, 642–651. doi: 10.1017/S1355617714000411

Girard, G., Whittingstall, K., Deriche, R., and Descoteaux, M. (2014). Towards quantitative connectivity analysis: reducing tractography biases. *NeuroImage* 98, 266–278. doi: 10.1016/j.neuroimage.2014.04.074

Glasser, M. F., Smith, S. M., Marcus, D. S., Andersson, J. L. R., Auerbach, E. J., Behrens, T. E. J., et al. (2016). The Human Connectome Project's neuroimaging approach. *Nat. Neurosci.* 19, 1175–1187. doi: 10.1038/nn.4361

Glasser, M. F., Sotiropoulos, S. N., Wilson, J. A., Coalson, T. S., Fischl, B., Andersson, J. L., et al. (2013). The minimal preprocessing pipelines for the human connectome project. *NeuroImage* 80, 105–124. doi: 10.1016/j.neuroimage.2013.04.127

Gou, L., Zhang, W., Li, C., Shi, X., Zhou, Z., Zhong, W., et al. (2018). Structural brain network alteration and its correlation with structural impairments in patients with depression in *de novo* and drug-naıve Parkinson's disease. *Front. Neurol.* 9, 608. doi: 10.3389/fneur.2018.00608

Gracia-Tabuenca, Z., Díaz-Patiño, J. C., Arelio, I., and Alcauter, S. (2020). Topological data analysis reveals robust alterations in the whole-brain and frontal lobe functional connectomes in attentiondeficit/hyperactivity disorder. *eNeuro* 7. doi: 10.1523/ENEURO.0543-19.2020

Hatcher, A. (2002). *Algebraic Topology*. Cambridge, UK: Cambridge University Press.

Hong, S.-J., Vos de Wael, R., Bethlehem, R. A., Lariviere, S., Paquola, C., Valk, S. L., et al. (2019). Atypical functional connectome hierarchy in autism. *Nat. Commun.* 10, 1–13. doi: 10.1038/s41467-019-08944-1

Huth, A. G., De Heer, W. A., Griffiths, T. L., Theunissen, F. E., and Gallant, J. L. (2016). Natural speech reveals the semantic maps that tile human cerebral cortex. *Nature* 532, 453–458. doi: 10.1038/nature17637

Jeurissen, B., Descoteaux, M., Mori, S., and Leemans, A. (2019). Diffusion MRI fiber tractography of the brain. *NMR Biomed.* 32, e3785. doi: 10.1002/nbm.3785

Klein, A., and Tourville, J. (2012). 101 labeled brain images and a consistent human cortical labeling protocol. *Front. Neurosci.* 6, 171. doi: 10.3389/fnins.2012.00171

Kristanto, D., Liu, M., Liu, X., Sommer, W., and Zhou, C. (2020). Predicting reading ability from brain anatomy and function: from areas to connections. *NeuroImage* 218, 116966. doi: 10.1016/j.neuroimage.2020.116966

Lee, D., and Son, T. (2021). Structural connectivity differs between males and females in the brain object manipulation network. *PLoS ONE* 16, e0253273. doi: 10.1371/journal.pone.0253273

Lee, H., Chung, M. K., Kang, H., Kim, B.-N., and Lee, D. S. (2011). "Discriminative persistent homology of brain networks" in *2011 IEEE International Symposium on Biomedical Imaging: From Nano to Macro* (IEEE), 841–844.

Leek, J. T., and Storey, J. D. (2008). A general framework for multiple testing dependence. *Proc. Natl. Acad. Sci. U.S.A.* 105, 18718–18723. doi: 10.1073/pnas.0808709105

Linero, A. (2017). A review of tree-based Bayesian methods. *CSAM* 24, 543–559. doi: 10.29220/CSAM.2017.24.6.543

Munkres, J. R. (2016). *Topology*. New York City, NY: Pearson Education.

Orchard, E. R., Ward, P. G., Chopra, S., Storey, E., Egan, G. F., and Jamadar, S. D. (2021). Neuroprotective effects of motherhood on brain function in late life: a resting-state fMRI study. *Cereb. Cortex* 31, 1270–1283. doi: 10.1093/cercor/bhaa293

Park, H.-J., and Friston, K. (2013). Structural and functional brain networks: from connections to cognition. *Science* 342, 1238411. doi: 10.1126/science.1238411

Patel, R., Steele, C. J., Chen, A. G., Patel, S., Devenyi, G. A., Germann, J., et al. (2020). Investigating microstructural variation in the human hippocampus using non-negative matrix factorization. *NeuroImage* 207, 116348. doi: 10.1016/j.neuroimage.2019.116348

Pizarro, R., Assemlal, H.-E., Nigris, D. D., Elliott, C., Antel, S., Arnold, D., et al. (2019). Algorithms to automatically identify the brain MRI contrast: implications for managing large databases. *Neuroinformatics* 17, 115–130. doi: 10.1007/s12021-018-9387-8

Poldrack, R. A., Baker, C. I., Durnez, J., Gorgolewski, K. J., Matthews, P. M., Munafò, M. R., et al. (2017). Scanning the horizon: towards transparent and reproducible neuroimaging research. *Nat. Rev. Neurosci.* 18, 115–126. doi: 10.1038/nrn.2016.167

Poldrack, R. A., and Gabrieli, J. D. (1998). Memory and the brain: what's right and what's left? *Cell* 93, 1091–1093. doi: 10.1016/S0092-8674(00)81451-8

Ptak, R., Bourgeois, A., Cavelti, S., Doganci, N., Schnider, A., and Iannotti, G. R. (2020). Discrete patterns of cross-hemispheric functional connectivity underlie impairments of spatial cognition after stroke. *J. Neurosci.* 40, 6638–6648. doi: 10.1523/JNEUROSCI.0625-20.2020

Raven, J. (2000). The Raven's progressive matrices: change and stability over culture and time. *Cogn. Psychol.* 41, 1–48. doi: 10.1006/cogp.1999.0735

Roy, H. A., Griffiths, D. J., Aziz, T. Z., Green, A. L., and Menke, R. A. L. (2019). Investigation of urinary storage symptoms in Parkinson's disease utilizing structural MRI techniques. *Neurourol. Urodyn.* 38, 1168–1175. doi: 10.1002/nau.23976

Rybakken, E., Baas, N., and Dunn, B. (2019). Decoding of neural data using cohomological feature extraction. *Neural Comput.* 31, 68–93. doi: 10.1162/neco_a_01150

Saggar, M., Sporns, O., Gonzalez-Castillo, J., Bandettini, P. A., Carlsson, G., Glover, G., et al. (2018). Towards a new approach to reveal dynamical organization of the brain using topological data analysis. *Nat. Commun.* 9, 1399. doi: 10.1038/s41467-018-03664-4

Sizemore, A. E., Phillips-Cremins, J. E., Ghrist, R., and Bassett, D. S. (2019). The importance of the whole: topological data analysis for the network neuroscientist. *Netw. Neurosci.* 3, 656–673. doi: 10.1162/netn_a_00073

Smith, S., Nichols, T., Vidaurre, D., Winkler, A., Behrens, T., Glasser, M., et al. (2015). A positive-negative mode of population covariation links brain connectivity, demographics and behavior. *Nat. Neurosci.* 18, 1565–1567. doi: 10.1038/nn.4125

Sotiropoulos, S. N., and Zalesky, A. (2019). Building connectomes using diffusion MRI: why, how and but. *NMR Biomed.* 32, e3752. doi: 10.1002/nbm.3752

Tian, Y., Margulies, D. S., Breakspear, M., and Zalesky, A. (2020). Topographic organization of the human subcortex unveiled with functional connectivity gradients. *Nat. Neurosci.* 23, 1421–1432. doi: 10.1038/s41593-020-00711-6

Wang, J., Zuo, X., Dai, Z., Xia, M., Zhao, Z., Zhao, X., et al. (2012). Disrupted functional brain connectome in individuals at risk for Alzheimer's disease. *Biol. Psychiatry* 73, 471–481. doi: 10.1016/j.biopsych.2012.03.026

Wang, J., Zuo, X., and He, Y. (2010). Graph-based network analysis of resting-state functional MRI. *Front. Syst. Neurosci.* 4, 16. doi: 10.3389/fnsys.2010.00016

Wang, L., Zhang, Z., and Dunson, D. (2019). Symmetric bilinear regression for signal subgraph estimation. *IEEE Trans. Signal Process.* 67, 1929–1940. doi: 10.1109/TSP.2019.2899818

Wasserman, L. (2017). Topological data analysis. *Annu. Rev. Stat. Appl.* 5, 501–532. doi: 10.1146/annurev-statistics-031017-100045

Yeatman, J. D., Dougherty, R. F., Ben-Shachar, M., and Wandell, B. A. (2012). Development of white matter and reading skills. *Proc. Natl. Acad. Sci. U.S.A.* 109, E3045–E3053. doi: 10.1073/pnas.1206792109

Yourganov, G., Schmah, T., Churchill, N. W., Berman, M. G., Grady, C. L., and Strother, S. C. (2014). Pattern classification of fMRI data: applications for analysis of spatially distributed cortical networks. *NeuroImage* 96, 117–132. doi: 10.1016/j.neuroimage.2014.03.074

Zadina, J. N., Corey, D. M., Casbergue, R. M., Lemen, L. C., Rouse, J. C., Knaus, T. A., et al. (2006). Lobar asymmetries in subtypes of dyslexic and control subjects. *J. Child Neurol.* 21, 922–931. doi: 10.1177/08830738060210110201

Zhang, Z., Allen, G. I., Zhu, H., and Dunson, D. (2019). Tensor network factorizations: relationships between brain structural connectomes and traits. *NeuroImage* 197, 330–343. doi: 10.1016/j.neuroimage.2019.04.027

Zhang, Z., Descoteaux, M., Zhang, J., Girard, G., Chamberland, M., Dunson, D., et al. (2018). Mapping population-based structural connectomes. *NeuroImage* 172, 130–145. doi: 10.1016/j.neuroimage.2017.12.064

frontiers | Frontiers in Neuroscience

TYPE Original Research
PUBLISHED 19 October 2023
DOI 10.3389/fnins.2023.1274038

OPEN ACCESS

EDITED BY
Xi-Nian Zuo,
Beijing Normal University, China

REVIEWED BY
Pan Wang,
University of Electronic Science and Technology of China, China
Akio Koizumi,
Kyoto University, Japan

*CORRESPONDENCE
Feng Gao
✉ gaofenga1@126.com

†These authors have contributed equally to this work

RECEIVED 07 August 2023
ACCEPTED 02 October 2023
PUBLISHED 19 October 2023

CITATION
Gao F, Cong J, Duan Y, Zhao W, Zhu Z, Zheng Y, Jin L, Ji M and Li M (2023) Screening of postoperative cerebral hyperperfusion syndrome in moyamoya disease: a three-dimensional pulsed arterial-spin labeling magnetic resonance imaging approach. *Front. Neurosci.* 17:1274038. doi: 10.3389/fnins.2023.1274038

Screening of postoperative cerebral hyperperfusion syndrome in moyamoya disease: a three-dimensional pulsed arterial-spin labeling magnetic resonance imaging approach

Feng Gao[1*†], Jianhua Cong[2†], Yu Duan[3], Wei Zhao[4], Zhenfang Zhu[1], Yu Zheng[5], Liang Jin[1], Ming Ji[1] and Ming Li[1]

[1]Department of Radiology, Huadong Hospital Fudan University, Shanghai, China, [2]Department of Medical Centre, Huadong Hospital Fudan University, Shanghai, China, [3]Department of Neurosurgery, Huadong Hospital Fudan University, Shanghai, China, [4]Department of Radiology, Second Xiangya Hospital, Central South University, Changsha, China, [5]Department of Magnetic Resonance, Lanzhou University Second Hospital, Lanzhou, China

Introduction: Moyamoya disease (MMD) is associated with a risk of postoperative cerebral hyperperfusion syndrome (CHS) after revascularization surgery. This study aimed to explore the feasibility of using three-dimensional pulsed arterial spin labeling (3D PASL) and phase contrast (PC) magnetic resonance imaging (MRI) for predicting CHS occurrence in patients with MMD before revascularization surgery.

Methods: Overall, 191 adult patients (207 hemispheres) with MMD who underwent combined revascularization surgery were included in this study. Preoperative 3D PASL-MRI and PC-MRI were performed before surgery. The PASL-MRI data were analyzed using SPM12. Patient clinical information, average flow, and preoperative cerebral blood flow (CBF) were compared between the non-CHS and CHS groups.

Results: Among the patients, 45 (21.74%) developed CHS after revascularization surgery. No significant differences were noted in age, sex, clinical symptoms, hypertension, diabetes, surgical side, or history of revascularization surgery between the non-CHS and CHS groups. However, the average flow in the superficial temporal artery was significantly lower in the CHS group than in the non-CHS group ($p < 0.05$). Furthermore, 11 clusters of preoperative CBF values were significantly greater in the CHS group than in the non-CHS group [$p < 0.05$, false discovery rate (FDR) corrected]. A significant correlation was also observed between the preoperative time-to-flight MR angiography (MRA) scores and CBF values in patients with MMD ($p < 0.05$).

Conclusion: Compare patients with lower preoperative CBF and higher preoperative average flow in the STA, patients with higher preoperative CBF and lower preoperative average flow in the STA are more likely to develop postoperative CHS Preoperative PASL-MRI and PC-MRI examinations may help to screen patients at high risk of developing CHS after revascularization surgery.

KEYWORDS

moyamoya disease, arterial spin labeling, magnetic resonance imaging, surgery, phase contrast MRI, cerebral hyperperfusion syndrome

1. Introduction

Moyamoya disease (MMD) is a chronic, occlusive cerebrovascular disease of unknown etiology. It is characterized by steno-occlusive changes in the terminal part of the internal carotid artery and an abnormal development of vascular network (moyamoya vessels) at the base of the brain (Research Committee on the Pathology and Treatment of Spontaneous Occlusion of the Circle of Willis, and Health Labour Sciences Research Grant for Research on Measures for Infractable Diseases, 2012). The symptoms of MMD primarily result from two major causes: brain ischemia (transient ischemic attacks, stroke, and seizures) and the compensatory response to ischemia. These include the common symptom of headache, which may be due to dilated transdural collaterals, and another symptom of hemorrhage, which is caused by fragile moyamoya vessels (Scott and Smith, 2009).

MMD often presents at younger ages, and its progressive characteristics can lead to irreversible brain damage due to prolonged brain hypoperfusion and multiple cerebral infarction/hemorrhagic events, resulting in severe disability and a poor prognosis (Fung et al., 2005). Revascularization surgery, including indirect, direct, and combined procedures, is recommended to improve cerebral perfusion, reduce the incidence of cerebrovascular events, and prevent neurocognitive decline (Zhang et al., 2020). Indirect procedures in combination with direct bypass offer the advantages of both direct and indirect bypass and are recommended for patients with MMD (Esposito et al., 2018). However, it should be noted that the superficial temporal artery-middle cerebral artery (STA-MCA) bypass provides only a limited blood supply (Kazumata et al., 2014).

Patients with MMD are more likely to experience postoperative cerebral hyperperfusion syndrome (CHS), compared to patients with other atherosclerotic diseases (Fujimura et al., 2011). Postoperative CHS can cause transient neurological symptoms, including permanent neurological defects, as intracranial vasculature pressure increases, which may elicit intracranial hemorrhage and even hematogenous cerebral edema (Park et al., 2018). Multiple studies recommend maintaining low perioperative blood pressure to reduce the risk of postoperative CHS (Hayashi et al., 2012). However, lowering blood pressure can also result in cerebral hypoperfusion and an increased risk of cerebral infarction after surgery (Hayashi et al., 2012). Some studies suggest induction of hypertension and hypervolemia during the perioperative period to prevent neurologic complications (Li et al., 2022). The identification of high-risk patients for developing postoperative CHS before surgery is crucial. Implementing appropriate treatment during the perioperative period is essential in preventing postoperative CHS and avoid adverse events at the same time, this may improve the overall prognosis of these patients (Østergaard et al., 2014).

Various imaging modalities can evaluate cerebral perfusion status. Computed tomography and single-photon emission computed tomography are radiation-based techniques, while magnetic resonance imaging (MRI) is a nonradiative alternative. MRI techniques include perfusion imaging, dynamic susceptibility contrast, and arterial spin labeling (ASL). ASL-MRI is magnetically labeled by the radiofrequency (RF) pulse protons of arterial blood flowing into the brain as an endogenous tracer (Zaharchuk et al., 2009). The cerebral blood flow (CBF) of brain tissues is quantified by estimating the labeled arterial blood water (Goetti et al., 2013). Studies have shown that even patients with normal renal function may have chronic gadolinium deposition in brain tissue after repeated intravenous injections of gadolinium-based contrast agents (McDonald et al., 2015). The ASL sequence presents a viable alternative for gadolinium-based contrast perfusion imaging. ASL permits repeated examinations without the risk of contrast leakage or residuals, and its clinical utility spans from ischemic stroke to arteriovenous malformations. ASL also has the potential to measure CBF patterns in patients with MMD (Federau et al., 2017). In addition, quantitative phase-contrast MR imaging (PC-MRI) can measure blood flow in a specified vessel without the need of contrast agent.

Patients with MMD, who are typically young, require regular MR examinations throughout their lifetime. This renders ASL sequences and quantitative PC-MRI highly suitable those patients. This study aimed to identify potential risk factors for postoperative CHS in adult patients with MMD who underwent surgical revascularization using three-dimensional (3D) pulsed arterial spin labeling (PASL)-MRI and PC-MRI were employed. We anticipate that the findings of this study contribute to the advancement of personalized medicine, implementation of appropriate treatment during the perioperative period, and improved patient care in Moyamoya disease.

2. Materials and methods

2.1. Clinical data and participants

This study was approved by the Ethics Committee of HuaDong Hospital (approval no. 2018030). All examinations in current study are in accordance with relevant regulations and guidelines. All patients in current study provided written informed consent.

From August 2018 to September 2022, a total of 191 adult patients with MMD (mean age, 43.80 ± 11.29 years; range, 18–65 years; female, 102; male, 89) were included in this study. A small subset (16/191) of these participants underwent bilateral revascularization surgery. Finally, 207 hemispheres were included in this study. Digital subtraction angiography (DSA) was used to diagnose MMD (Fukui, 1997). The inclusion criteria were as follows: (i) patients aged ≥18 years; (ii) those with no contraindication to MR examination; and (iii) those who underwent combined revascularization surgery [encephalo-duro-myo-synangiosis (EDMS) combines STA-MCA bypass]. The exclusion criteria were as follows: (i) patients with any other neurosurgical disease and (ii) those who underwent only STA-MCA bypass or EDMS surgery. The enrolment flowchart is shown in Figure 1. In this study, the preoperative and postoperative blood pressure and blood glucose will be carefully monitored for patients with hypertension and diabetes (blood glucose is controlled

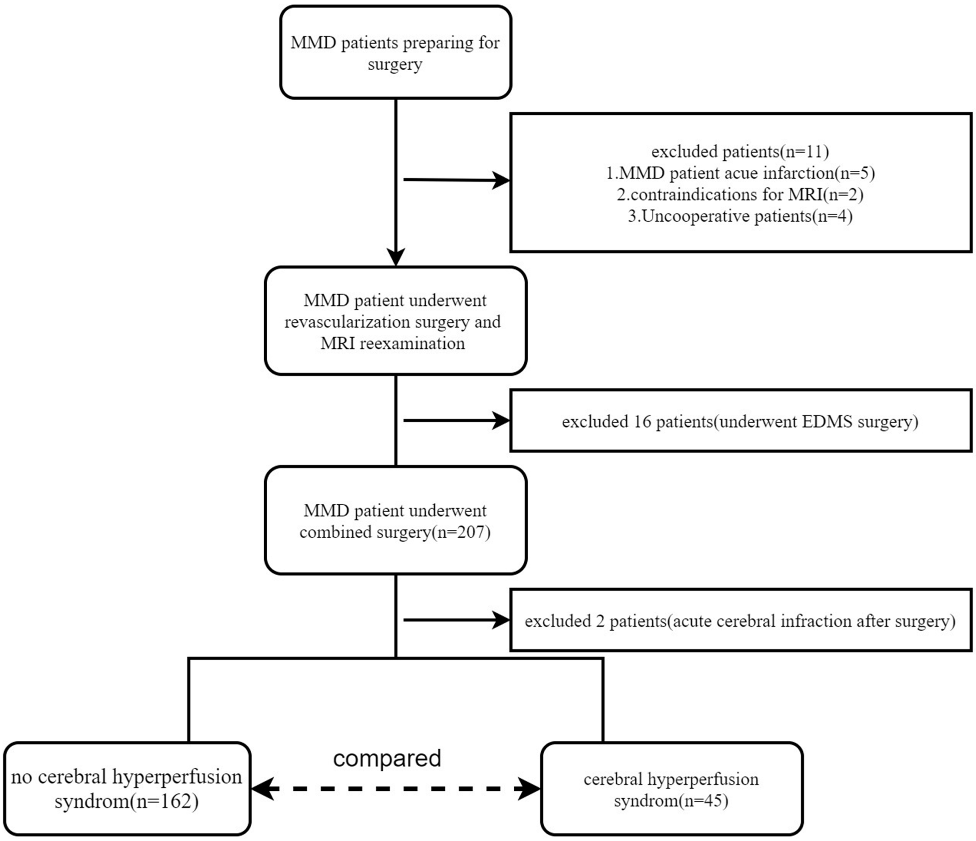

FIGURE 1
Flowchart describing the patient inclusion process.

TABLE 1 MRI scanning sequences and parameters.

	TR/TE (ms)	Thickness (mm)	Flip angle (°)	Intersection gap	TA	FOV (cm^2)	Matrix	*b* value
T1WI	230/2.46	5	70	30%	25 s	22 × 22	256 × 192	/
T2WI	5000/117	5	90	30%	54 s	22 × 22	384 × 281	/
FLAIR	8000/85	5	140	20%	1 min 36 s	22 × 22	256 × 162	/
DWI	1300/62	5	192	30%	30 s	24 × 24	192 × 192	0,1,000
T1-MPRAGE	2300/2.32	0.9	8	50%	5 min 22 s	26 × 26	256 × 256	/
TOF-MRA	21/3.43	1	18	−18.75%	5 min 13 s	22 × 22	320 × 180	/
PC-MRI (pre-scan)	84.6/4.86	6	20	20%	19 s	34 × 34	192 × 68	/
PC-MRI	73.08/7.54	4	10	20%	5 min 29 s	18 × 18	336 × 336	/

TR, time of repetition; TE, time of echo; FOV, field of view; TA, time of acquisition; FLAIR, fluid-attenuated inversion-recovery sequence; DWI, diffusion-weighted imaging; T1-MPRAGE, T1 magnetization prepared rapid acquisition gradient echo; TOF-MRA, time-to-flight MR angiography; PC-MRI, phase-contrast MRI.

within the range of 7–9 mmol/L; systolic blood pressure is controlled within the range of 120–130 mmHg).

2.2. MRI examination protocol

All MRI examinations were performed using a 3-T machine (Siemens Prisma; Siemens Medical Solutions) with a 32-channel head–neck coil. Preoperative MRI examinations were conducted within 1 week before surgery.

The parameters for 3D PASL acquisition were as follows: label time: 700 ms; post-labeling delay time: 1,290 ms; inversion time: 1,990 ms; field of view (FOV): 192 × 192; voxel size: 3 × 3 × 3 mm; slice thickness: 3 mm with a 1.5 mm gap; time to echo (TE): 16.18 ms; repetition time (TR): 4,600 ms; axial slices: 40; number of excitations: 4; and time of acquisition (TA): 296 s. The other MRI sequence parameters are listed in Table 1.

The 3D-time-of-flight (TOF) MR angiography (MRA) sequence, from the top of the skull to the common carotid artery, was located using the T1- MPRAGE sequence. The TOF-MRA sequence is reconstructed by maximum intensity projection (MIP), and it was used to locate the PC MRI sequence. The detailed procedure for measuring the average flow in the internal carotid artery (ICA), basilar artery (BA), and superficial temporal artery (STA) is consistent with a previous study (Gao et al., 2019).

2.3. MRI data Preprocessing

The 3D PASL data were analyzed using SPM12 software [1] and the ASL toolbox[2] (Wang et al., 2008). In this study, CBF was quantitatively assessed at the whole-cerebral voxel level, using an individual's T1-MPRAGE anatomical scan as a reference. The detailed procedure for ASL image analysis has been previously described (Huang et al., 2022). CBF map values were reported in absolute units (mL/100 g/min).

The MIP images of the MRA sequence were used to assess the MRA scores of the intracranial arteries. Two senior neuroradiologists with more than 10 years of experience evaluated the MRA scores following previously reported criteria (Houkin et al., 2005). The total MRA scores ranged from 0 to 20.

2.4. Diagnosis of CHS, grouping, and analysis

In this study, postoperative symptomatic CHS was diagnosed if patients experienced severe headaches, seizures, or new neurological deficits developed after surgery, and brain CT images or/and diffusion magnetic resonance images shows neither definite hematomas nor definite acute infarctions (van Mook et al., 2005; Iwata et al., 2014). The diagnosis of postoperative symptomatic CHS was made by a senior neurosurgeon who was blinded to the study. Based on the presence or absence of CHS, the patients were divided into CHS and non-CHS groups. The preoperative CBF status and average flow in the ICA, STA, and BA were compared between the two groups.

2.5. Statistical analyses

An independent t-test was used to compare the age and average flow in the ICA, STA, and BA between the CHS and non-CHS groups. The average flows of the target blood vessel were separately measured for the left and right sides, and the data from both sides were averaged. The Chi-squared test was used to compare categorical variables, such as sex, clinical symptoms, diabetes, hypertension, surgical side, and history of revascularization surgery between the CHS and non-CHS groups. Statistical analyses were conducted using the Statistical Package for the Social Sciences (version 24.0; IBM SPSS) and an automated anatomical labeling atlas (AAL) template (Ashburner, 2007).

The CBF maps were statistically analyzed using second-level statistical procedures implemented in SPM12, based on a generalized linear model. The preoperative CBF in the CHS and non-CHS groups was compared using a two-sample *t*-test. Only CBF of cerebral was selected for analysis, as MMD rarely affects the cerebellum. Sex and age were included as covariates in the regression analysis. The correlation between preoperative CBF and MRA scores was analyzed using multiple regression and regression of the z-transformed correlation coefficients. A statistically significant difference was considered at $p < 0.05$ after false discovery rate (FDR) correction.

The xjview toolbox[3] was used to visualize CBF clusters. Clusters with significant differences and correlations are displayed in pseudo-colors on a calibrated standard brain map. The voxel sizes of the peak intensities and also their Montreal Neurological Institute coordinates are listed.

3. Results

In this study, 45 of 207 patients with MMD (21.74%) developed symptomatic CHS after surgery. The main symptoms of CHS included speech impairment (15 cases), severe headache (12 cases), decreased muscle strength (upper limbs in 3 cases and lower limbs in 5 cases), persistent vomiting (4 cases), dysphagia (3 cases), seizures (2 cases), and face and eye pain (1 case). These symptoms typically appeared within 1–9 days (3.87 ± 1.87 days) after surgery and improved before the patients were discharged from our hospital.

No significant differences were noted in age, sex, clinical symptoms, hypertension, diabetes, surgical side, or history of revascularization surgery between the two groups (Table 2). The average preoperative flows in the ICA and BA were not significantly different between the two groups (Table 2). However, before surgery, the average STA flow was significantly lower in the CHS group than in the non-CHS group ($p < 0.05$; Table 2). The ROC curve of the average flow of STA in predicting postoperative CHS is shown in Figure 2, and the area under curve (AUC) was 0.67. The two-sample t-test showed the significant differences in preoperative CBF status between the two groups. Specifically, 11 clusters of preoperative CBF were significantly higher in the CHS group than in the non-CHS group. These clusters were mainly located in the following brain areas: right inferior temporal gyrus (Temporal_Inf_R), left gyrus rectus (Rectus_L), right lenticular nucleus, putamen (Putamen_R), right olfactory cortex (Olfactory_R), right precuneus (Precumeus_R), right hippocampus (Hippocampus_R), right middle temporal gyrus (Temporal_Mid_R), left calcarine fissure and surrounding cortex (Calcarine_L), right superior temporal gyrus (Temporal_Sup_R) (Table 3; Figure 3).

Spearman's correlation coefficients were calculated to evaluate the relationship between the preoperative CBF values and MRA scores of intracranial arteries in patients with MMD. The results revealed a significant correlation between preoperative MRA scores and CBF values in patients with MMD ($p < 0.05$). The brain areas related to

---

[1] http://www.fil.ion.ucl.ac.uk/spm

[2] http://cfn.upenn.edu/zewang/ASLtbs.php

[3] http://www.Alivelearn.p/xjview

MRA scores in the CHS group are shown in Table 4 and Figure 4. Negative correlations were observed between MRA scores and the following preoperative brain areas: the bilateral superior temporal gyri (Temporal_Sup_R,L), right superior frontal gyri, medial (Frontal_Sup_Medial_R), right middle temporal gyri (Temporal_Mid_R), right inferior occipital gyri (Occipital_Inf_R), right middle occipital gyri (Occipital_Mid_R), and right superior parietal gyri (Parietal_Sup_R). On the other hand, positive correlations were identified between the MRA scores and the following preoperative brain areas: the bilateral posterior cingulate gyrus (Cingulum_Post_R,L), left parahippocampal gyrus (ParaHippocampal_L), left hippocampus (Hippocampal_L), left olfactory cortex (Olfactory_L), left lenticular nucleus, putamen (Putamen_L), and left thalamus (Thalamus_L).

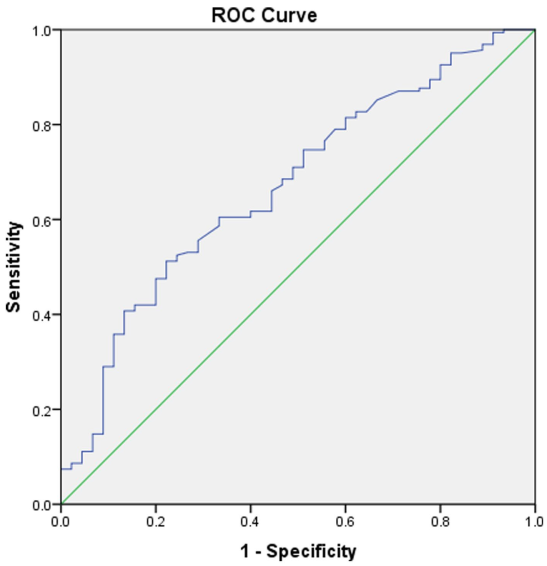

FIGURE 2
Received operating characteristic (ROC) curve of the average flow of STA in predicting postoperative CHS. The area under the curve (AUC) is 0.67.

4. Discussion

In this study, 3D PASL sequences were used to evaluate cerebral perfusion in patients with MMD. The results indicate that the preoperative 3D PASL-CBF in certain brain areas was significantly higher in the CHS group than in the non-CHS group. There was a significant correlation between the preoperative MRA and CBF values in patients with MMD. The utilization of 3D PASL sequences and PC MRI may help to identify patients with MMD who are at a higher risk of accruing postoperative symptomatic CHS.

The development of new pathological vessels in MMD is caused by chronic brain hypoperfusion and ischemia. These new compensatory vessels are pathological vessels. The cerebrovascular reactivity and autonomic regulation are impaired. Consequently, after

TABLE 2 Clinical information of MMD patients (207 brain hemispheres).

	CHS	Non-CHS		*p*
No. of patients (%)	45 (21.74%)	162 (78.26%)		
Age	40.47 ± 13.82	44.04 ± 10.59	$t = -1.61$	0.113
Gender			$\chi^2 = 0.281$	0.596
Male	22	72		
Female	23	90		
Hypertension	29	89	$\chi^2 = 1.299$	0.254
Diabetes	21	72	$\chi^2 = 0.385$	0.535
Clinical symptom			$\chi^2 = 0.443$	0.801
Ischemia	26	85		
Hemorrhage	15	59		
Nonspecific	4	18		
Surgery side			$\chi^2 = 0.238$	0.626
Left	24	93		
Right	21	69		
Revascularization surgery history			$\chi^2 = 2.748$	0.097
No	45	114		
Yes	10	48		
Average flow (mL/s)				
Superficial temporal artery	0.24 ± 0.19	0.37 ± 0.29	$t = -3.552$	0.010
Internal carotid artery	2.17 ± 1.69	2.37 ± 1.92	$t = -0.657$	0.512
Basilar artery	1.28 ± 1.17	1.57 ± 1.33	$t = -1.312$	0.191

CHS, cerebral hyperperfusion syndrome; non-CHS, non-cerebral hyperperfusion syndrome.

TABLE 3 Comparison of the preoperative cerebral blood flow between CHS and non-CHS groups.

Cluster	Brain region	Cluster size	Peak MNI coordinates(x, y, z)	Peak intensity	T value	p FDR-corr
1	Temporal_Inf_R	518	54, −38, −28	6.176	6.18	0.000
2	Rectus_L	167	−6, 20, −26	4.398	4.40	0.005
3	Putamen_R	42	16, 8, −8	3.999	4.00	0.011
4	Olfactory_R	123	2, 16, −6	4.282	4.28	0.006
5	Precumeus_R	691	12, −46, 6	5.745	5.74	0.000
6	Hippocampus_R	81	32, −30, −4	4.321	4.32	0.006
7	Putamen_R	638	28, −12, 12	5.034	5.03	0.001
8	Temporal_Mid_R	71	58, −60, 6	4.525	4.53	0.004
9	Calcarine_L	28	−14, −60, 10	3.496	3.50	0.028
10	Temporal_Sup_R	51	56, −46, 14	3.710	3.71	0.019
11	Temporal_Mid_R	26	44, −66, 22	4.059	4.06	0.010

CHS, cerebral hyperperfusion syndrome; non-CHS, non-cerebral hyperperfusion syndrome.

TABLE 4 Correlation between the preoperative CBF values and MRA scores of intracranial arteries in the CHS group.

Cluster	Brain region	Cluster size	Peak MNI coordinates(x, y, z)	Peak intensity	T value	p FDR-corr
Negative						
1	Frontal_Sup_Medial_R	81,668	12, 44, 32	10.291	10.29	0.000
2	Temporal_Mid_R	504	70, −34, 0	4.499	3.68	0.001
3	Occipital_Inf_R	174	36, −88, −12	3.542	3.54	0.001
4	Occipital_Mid_R	33	36, −96, 8	3.420	3.42	0.001
5	Temporal_Sup_R	64	50, −30, 6	2.375	2.37	0.019
6	Temporal_Sup_L	147	−44, −36, 14	3.056	3.06	0.003
7	Parietal_Sup_R	39	36, −74, 50	2.962	2.96	0.004
Positive						
1	ParaHippocampal_L	107	−16, 2, −18	−5.948	5.95	0.000
2	Hippocampal_L	50	−22, −20, −12	−4.602	4.60	0.002
3	Olfactory_L	34	0, 6, −8	−5.660	5.66	0.000
4	Putamen_L	345	−22, −6, 10	−6.202	6.20	0.000
5	Cingulum_Post_L	27	−4, −38, 10	−5.689	5.69	0.000
6	Cingulum_Post_R	85	4, −38, 12	−6.687	6.69	0.000
7	Thalamus_L	40	−2, −18, 16	−5.204	5.20	0.000

CHS, cerebral hyperperfusion syndrome; non-CHS, non-cerebral hyperperfusion syndrome; MRA, time-to-flight MR angiography.

successful revascularization surgery, these vessels are unable to control the increased cerebral blood flow, leading to the occurrence of symptomatic CHS (Hayashi et al., 2012). In this study, the incidence of postoperative CHS was found to be 21.74% (45/207), which is consistent with previous studies (Fujimura et al., 2011, 2012). The reduced cerebral metabolism and downregulation of cortical neurotransmitter receptor function by CHS can lead to cerebral function impaired (Shimada et al., 2018). During the perioperative period, it is crucial to take reasonable preventive measures for high-risk patients who may come up with CHS after surgery.

Further, no significant differences were observed in age, sex, clinical symptoms, hypertension, diabetes, surgical side, or history of revascularization surgery between the two groups. Although symptoms related to ischemia are the most common clinical manifestation of MMD, 10.63% (22/207) of the patients were asymptomatic which is consistent with previous studies, that 1.5% ~ 17.8% of patients with MMD are asymptomatic (Baba et al., 2008). Current study showed that hemorrhage-onset symptoms were observed in approximately 35.75% (74/207) of the patients. Among patients with postoperative CHS, 57.78% (26/45) and 33.33% (15/45) presented with ischemic- and hemorrhage-onset symptoms, respectively. Whether patients with hemorrhagic- or ischemia-onset symptoms more often come up with postoperative CHS remains controversial (Fujimura et al., 2009; Hayashi et al., 2010). Different study populations, preoperative management, and surgical procedures may have contributed to this discrepancy.

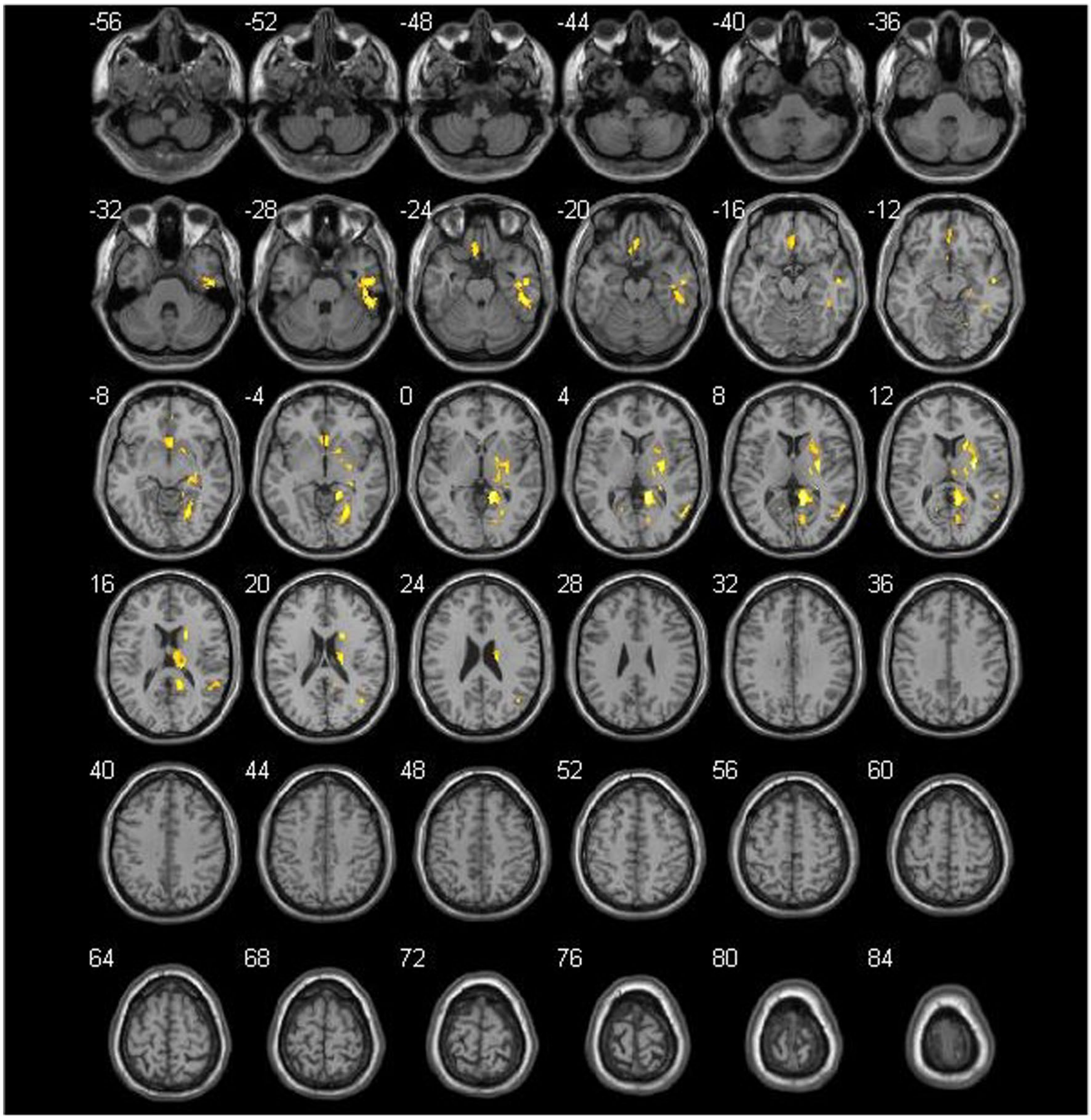

FIGURE 3
Comparison of the preoperative cerebral blood flow between cerebral hyperperfusion syndrome (CHS) and non-CHS groups. Significant regions are (false discovery rate corrected $p < 0.05$) illustrated in warm colors for increased values. Significant differences are revealed in the following brain regions: right inferior temporal gyrus (Temporal_Inf_R), left gyrus rectus (Rectus_L), right lenticular nucleus, putamen (Putamen_R), right olfactory cortex (Olfactory_R), right precuneus (Precumeus_R), right hippocampus (Hippocampus_R), right middle temporal gyrus (Temporal_Mid_R), left calcarine fissure and surrounding cortex (Calcarine_L), right superior temporal gyrus (Temporal_Sup_R).

Previous studies have demonstrated that symptomatic CHS can be diagnosed based on specific postoperative clinical symptoms (van Mook et al., 2005; Iwata et al., 2014). In the present study, the most prevalent clinical symptoms of CHS were headache and speech impairment, which was consistent with previous study (Egashira et al., 2017).

PC MRI was used to calculate preoperative blood flow in the ICA, BA, and STA. The target vessels for bypass surgery were MCA (branch of ICA) and STA (branch of the external carotid artery). This study showed that the average flow in the ICA and BA had not significantly different between the two groups. However, the preoperative average STA flow was significantly lower in the CHS than in the non-CHS group ($p < 0.05$). Cerebral reconstruction surgery artificially lowers blood pressure and increases blood flow in the distal STA. Patients with lower vessel flow before surgery may experience a more substantial increase in blood flow volume after surgery. The average STA flow increases significantly after cerebrovascular reconstruction surgery, which greatly affects the blood supply to the brain tissue. This may be the reason why patients with a lower average STA flow before surgery were more likely to develop symptomatic CHS after reconstruction surgery.

The preoperative CBF status measured by PASL was compared between the non-CHS and CHS groups. The importance of ASL sequence has been well-validated in studies on ischemic brain diseases (Soman et al., 2020). In patients with MMD, extensive collateral circulation may cause vascular territory boundaries to shift. In this

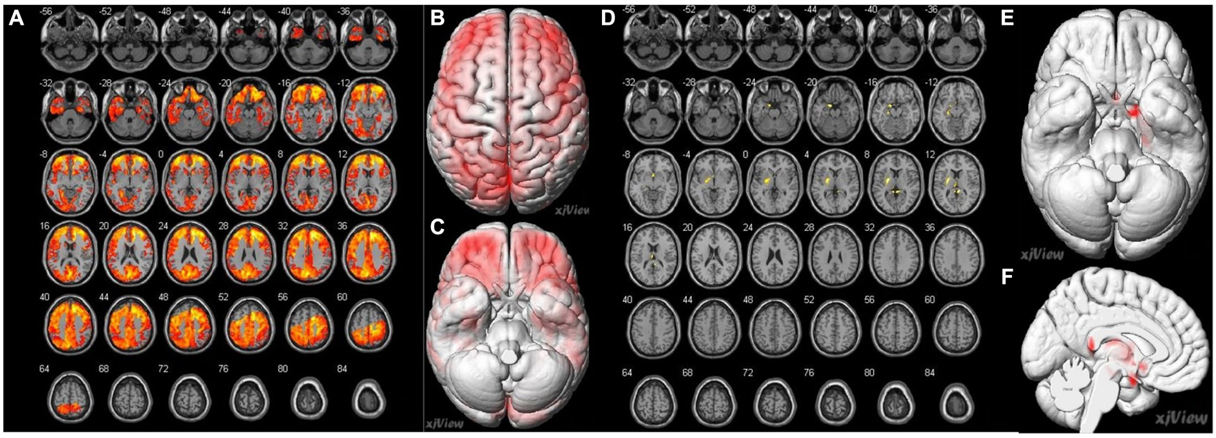

FIGURE 4
Correlation of preoperative cerebral blood flow (CBF) between brain regions and preoperative MRA sores in patients with MMD. **(A–C)** A negative correlation (false discovery rate corrected p < 0.05) is identified between MRA scores and the following preoperative brain area: bilateral superior temporal gyrus (Temporal_Sup_R, L), right superior frontal gyrus, medial (Frontal_Sup_Medial_R), right middle temporal gyrus (Temporal_Mid_R), right inferior occipital gyrus (Occipital_Inf_R), right middle occipital gyrus (Occipital_Mid_R), right superior parietal gyrus (Parietal_Sup_R). **(D–F)** Positive correlations (false discovery rate corrected p < 0.05) were identified between the MRA scores and the following preoperative brain areas: the bilateral posterior cingulate gyrus (Cingulum_Post_R, L), left parahippocampal gyrus (ParaHippocampal_L), left hippocampus (Hippocampal_L), left olfactory cortex (Olfactory_L), left lenticular nucleus, putamen (Putamen_L), and left thalamus (Thalamus_L).

study, CBF was assessed quantitatively based on the whole-cerebral voxel level but not on a specific cerebral artery-supplied brain region. This method of measurement can aid in direct analysis of the original data, while simultaneously avoiding the effects of malacia or chronic hemorrhagic foci.

The results of the current study indicate that preoperative 3D PASL-CBF was higher in the CHS group than in the non-CHS group in some brain areas of the frontal lobe, temporal lobe, limbic lobe, lentiform nucleus, and white matter, which are typically supplied by the ICA and MCA (Table 3; Figure 3). The PCA is rarely involved in MMD. In this study, 29.95% (62/207) of the patients showed PCA involvement (27 cases with unilateral and 35 cases with bilateral PCA involvement). The ischemic status of MMD is different from other internal carotid artery stenosis caused by atherosclerotic disease. In MMD, as the recipient's vessels are relatively small, postoperative CHS is not only caused by an increase in postoperative bypass flow but may also be caused by vasodilation due to long-term chronic ischemia (Chen and Tu, 2022). In MMD, stenosis of the ICA and its terminal branches may lead to the development of moyamoya vessels and compensatory vasodilation, which may extend the time to peak and mean transmission time, while CBF is increased as a compensatory mechanism. In this study, preoperative CBF was also higher in the CHS group than in the non-CHS group, indicating that the collateral circulation status before surgery was slightly better in the CHS group.

Impaired cerebral autoregulation is related to postoperative cerebral hyperperfusion, which is mediated by endothelial dysfunction. After surgery, cerebral vascular reactivity cannot respond appropriately to the increased blood flow as it is impaired and requires several days to adapt to the new state (Bernstein et al., 1984). A new vascular pathway was established after revascularization surgery, which may have a high priority. This means the blood flow pattern was reversed after revascularization surgery, led to hyperperfusion in the operation area and manifested as hypoperfusion remote from the site of anastomosis (Bao et al., 2022). The clinical symptoms improved after several days of the revascularization surgery.

Our study showed a negative correlation between preoperative MRA scores and CBF values in some brain regions, especially in the temporal and frontal lobes ($p < 0.05$; Table 4; Figure 4). This observation is consistent with previous ASL reports stating that with the severity of intracranial arterial steno-occlusions, the CBF value decreases (Noguchi et al., 2013). Our study also showed that a small part of the brain region exhibited a positive correlation between preoperative MRA scores and CBF values, especially in the limbic lobe of the left cerebral cortex ($p < 0.05$, Table 4; Figure 4). A previous study showed that the dominant language functional area is the left hemisphere and the functional areas are sensitive to CBF changes; therefore, it required higher CBF stability (Lu et al., 2019). In addition, impaired cerebrovascular reactivity is more evident in the left hemisphere (Mukerji et al., 2015). Therefore, when the blood supply to the brain is insufficient, moyamoya vessels may preferentially supply blood to the dominant brain areas. However, as the sample size in this study was limited, this result requires further verification.

In the current study, non-invasive 3D PASL sequences and PC-MRI were used to access cerebral perfusion and blood flow in patients with MMD. The results indicate that the sequences may help to identify patients with MMD at a higher risk of developing postoperative symptomatic CHS. CBF in this study was assessed quantitatively based on the whole-cerebral voxel level, as this method avoids the effects of malacia or chronic hemorrhagic foci, which are often seen in patients with MMD. This measurement method also increases the reliability of this study.

Our study has few limitations. First, it did not include a comparison with other traditional methods for measuring cerebral perfusion status. Previous studies have compared the ability of ASL-MRI to assess hemodynamic status using nuclear medicine methods (Yun et al., 2016). The results of ASL perfusion MRI can be influenced by moyamoya vessels, which may lead to an underestimation of CBF values (Zaharchuk et al., 2011). However, recent studies have suggested that the overestimation effects on the calculated CBF using single post-label delay ASL can be negligible in patients with MMD (Fahlström et al., 2020). A validation study that compares it with other methods and re-evaluates it will be conducted in the future. Second, symptomatic CHS was diagnosed mainly based on the clinical features of patients (van Mook et al., 2005). However, these clinical features are not unique to patients with postoperative CHS. Furthermore, a comparison of postoperative CBF with preoperative CBF status will be conducted in future studies to further investigate changes in CBF. In this study we considered the possible influence of diabetes and hypertension for the results, but education and medication may affect the results. The data of this study was small, especially the CHS group. We will increase the number of cases in future study to further validate the results.

To further enhance our understanding and improve clinical practice, future research should focus on conducting comparative analyses between ASL-MRI and traditional methods, exploring the impact of collateral moyamoya vessels on ASL perfusion MRI results, refining diagnostic criteria for postoperative symptomatic CHS, and evaluating changes in cerebral perfusion by comparing postoperative CBF with preoperative CBF status. Addressing these aspects can contribute to advancing our knowledge and application of ASL-MRI in assessing cerebral perfusion and optimizing patient management in moyamoya disease.

5. Conclusion

Patients with higher preoperative PASL-CBF and lower preoperative average STA flow were more likely to develop postoperative symptomatic CHS, compared with those with lower preoperative PASL-CBF and higher preoperative average STA flow. Preoperative 3D PASL sequencing and PC MRI may assist in identifying patients at high risk of developing postoperative CHS before surgery and in determining the most suitable treatment strategy during the perioperative period.

Data availability statement

The raw data supporting the conclusions of this article will be made available by the authors, without undue reservation.

Ethics statement

The studies involving humans were approved by The ethic committee of Huadong hospital. The studies were conducted in accordance with the local legislation and institutional requirements. Written informed consent for participation in this study was provided by the participants' legal guardians/next of kin. Written informed consent was obtained from the individual(s) for the publication of any potentially identifiable images or data included in this article.

Author contributions

FG: Conceptualization, Investigation, Methodology, Project administration, Software, Supervision, Visualization, Writing – original draft. YD: Validation, Visualization, Writing – original draft, Formal analysis, Investigation, Methodology, Resources. WZ: Conceptualization, Formal analysis, Investigation, Methodology, Project administration, Resources, Supervision, Validation, Visualization, Writing – review & editing. ZZ: Data curation, Formal analysis, Investigation, Methodology, Visualization, Writing – review & editing. YZ: Data curation, Investigation, Methodology, Software, Validation, Visualization, Writing – original draft. LJ: Conceptualization, Funding acquisition, Investigation, Methodology, Project administration, Resources, Writing – review & editing. MJ: Investigation, Methodology, Validation, Visualization, Writing – review & editing. ML: Funding acquisition, Investigation, Methodology, Project administration, Resources, Supervision, Validation, Visualization, Writing – review & editing. JC: Investigation, Software, Validation, Writing – review & editing.

Funding

The author(s) declare financial support was received for the research, authorship, and/or publication of this article. This study was funded by the National Natural Science Foundation of China (grant number 61976238), Science and Technology Planning Project of Shanghai Science and Technology Commission (grant number 22Y11910700), Science and Technology Planning Project of Shanghai Science and Technology Commission (grant number 20Y11902900), Shanghai "Rising Stars of Medical Talent" Youth Development Program "Outstanding Youth Medical Talents" (grant number SHWJRS [2021]-99), and National key research and development program (grant number 2022YFF1203301). Leading Talent Program (LJRC2202) of Huadong Hospital, and Excellent Academic Leaders of Shanghai (2022XD042).

Conflict of interest

The authors declare that the research was conducted in the absence of any commercial or financial relationships that could be construed as a potential conflict of interest.

Publisher's note

References

Ashburner, J. (2007). A fast diffeomorphic image registration algorithm. *NeuroImage* 38, 95–113. doi: 10.1016/j.neuroimage.2007.07.007

Baba, T., Houkin, K., and Kuroda, S. (2008). Novel epidemiological features of Moyamoya disease. *J. Neurol. Neurosurg. Psychiatry* 79, 900–904. doi: 10.1136/jnnp.2007.130666

Bao, Y., Yu, F., Wei, L., Zhu, W., Wang, L., Ding, H., et al. (2022). Association between cognitive decline and altered cerebral perfusion in adults with Moyamoya disease after revascularization. *Cerebrovasc. Dis.* 51, 764–773. doi: 10.1159/000524240

Bernstein, M., Fleming, J. F., and Deck, J. H. (1984). Cerebral hyperperfusion after carotid endarterectomy: a cause of cerebral hemorrhage. *Neurosurgery* 15, 50–56. doi: 10.1227/00006123-198407000-00010

Chen, J. Y., and Tu, X. K. (2022). Research progress on postoperative transient neurological dysfunction in pediatric and adult patients with Moyamoya disease after revascularization surgery. *Clin. Neurol. Neurosurg.* 217:107254. doi: 10.1016/j.clineuro.2022.107254

Egashira, Y., Yamauchi, K., Enomoto, Y., Nakayama, N., Yoshimura, S., and Iwama, T. (2017). Disruption of cortical arterial network is associated with the severity of transient neurologic events after direct bypass surgery in adult Moyamoya disease. *World Neurosurg.* 100, 311–315. doi: 10.1016/j.wneu.2017.01.039

Esposito, G., Sebok, M., Amin-Hanjani, S., and Regli, L. (2018). Cerebral bypass surgery: level of evidence and grade of recommendation. *Acta Neurochir. Suppl.* 129, 73–77. doi: 10.1007/978-3-319-73739-3_10

Fahlström, M., Lewén, A., Enblad, P., Larsson, E. M., and Wikström, J. (2020). High intravascular signal arterial transit time artifacts have negligible effects on cerebral blood flow and cerebrovascular reserve capacity measurement using single postlabel delay arterial spin-labeling in patients with Moyamoya disease. *AJNR Am. J. Neuroradiol.* 41, 430–436. doi: 10.3174/ajnr.A6411

Federau, C., Christensen, S., Zun, Z., Park, S. W., Ni, W., Moseley, M., et al. (2017). Cerebral blood flow, transit time, and apparent diffusion coefficient in Moyamoya disease before and after acetazolamide. *Neuroradiology* 59, 5–12. doi: 10.1007/s00234-016-1766-y

Fujimura, M., Inoue, T., Shimizu, H., Saito, A., Mugikura, S., and Tominaga, T. (2012). Efficacy of prophylactic blood pressure lowering according to a standardized postoperative management protocol to prevent symptomatic cerebral hyperperfusion after direct revascularization surgery for Moyamoya disease. *Cerebrovasc. Dis.* 33, 436–445. doi: 10.1159/000336765

Fujimura, M., Mugikura, S., Kaneta, T., Shimizu, H., and Tominaga, T. (2009). Incidence and risk factors for symptomatic cerebral hyperperfusion after superficial temporal artery-middle cerebral artery anastomosis in patients with Moyamoya disease. *Surg. Neurol.* 71, 442–447. doi: 10.1016/j.surneu.2008.02.031

Fujimura, M., Shimizu, H., Inoue, T., Mugikura, S., Saito, A., and Tominaga, T. (2011). Significance of focal cerebral hyperperfusion as a cause of transient neurologic deterioration after extracranial-intracranial bypass for Moyamoya disease: comparative study with non-moyamoya patients using n-isopropyl-p-[(123)i]iodoamphetamine single-photon emission computed tomography. *Neurosurgery* 68:957–64; discussion 964-965. doi: 10.1227/NEU.0b013e318208f1da

Fukui, M. (1997). Guidelines for the diagnosis and treatment of spontaneous occlusion of the circle of Willis ("moyamoya" disease). Research committee on spontaneous occlusion of the circle of Willis (Moyamoya disease) of the ministry of health and welfare, Japan. *Clin. Neurol. Neurosurg.* 99 Suppl 2, S238–S240. doi: 10.1016/S0303-8467(97)00082-6

Fung, L. W., Thompson, D., and Ganesan, V. (2005). Revascularisation surgery for paediatric moyamoya: a review of the literature. *Childs Nerv. Syst.* 21, 358–364. doi: 10.1007/s00381-004-1118-9

Gao, F., Zhao, W., Zheng, Y., Li, S., Lin, G., Ji, M., et al. (2019). Phase-contrast magnetic resonance imaging analysis of cerebral hyperperfusion syndrome after surgery in adult patients with Moyamoya disease. *World Neurosurg.* 129, e48–e55. doi: 10.1016/j.wneu.2019.04.191

Goetti, R., O'Gorman, R., Khan, N., Kellenberger, C. J., and Scheer, I. (2013). Arterial spin labelling mri for assessment of cerebral perfusion in children with Moyamoya disease: comparison with dynamic susceptibility contrast mri. *Neuroradiology* 55, 639–647. doi: 10.1007/s00234-013-1155-8

Hayashi, K., Horie, N., Suyama, K., and Nagata, I. (2012). Incidence and clinical features of symptomatic cerebral hyperperfusion syndrome after vascular reconstruction. *World Neurosurg.* 78, 447–454. doi: 10.1016/j.wneu.2011.10.041

Hayashi, T., Shirane, R., Fujimura, M., and Tominaga, T. (2010). Postoperative neurological deterioration in pediatric Moyamoya disease: watershed shift and hyperperfusion. *J. Neurosurg. Pediatr.* 6, 73–81. doi: 10.3171/2010.4.PEDS09478

Houkin, K., Nakayama, N., Kuroda, S., Nonaka, T., Shonai, T., and Yoshimoto, T. (2005). Novel magnetic resonance angiography stage grading for Moyamoya disease. *Cerebrovasc. Dis.* 20, 347–354. doi: 10.1159/000087935

Huang, W., Fang, X., Li, S., Mao, R., Ye, C., Liu, W., et al. (2022). Shunt surgery efficacy is correlated with baseline cerebrum perfusion in idiopathic normal pressure hydrocephalus: a 3d pulsed arterial-spin labeling study. *Front. Aging Neurosci.* 14:797803. doi: 10.3389/fnagi.2022.797803

Iwata, T., Mori, T., Miyazaki, Y., Tanno, Y., Kasakura, S., and Aoyagi, Y. (2014). Global oxygen extraction fraction by blood sampling to anticipate cerebral hyperperfusion phenomenon after carotid artery stenting. *Neurosurgery* 75:546–51; discussion 551. doi: 10.1227/NEU.0000000000000485

Kazumata, K., Ito, M., Tokairin, K., Ito, Y., Houkin, K., Nakayama, N., et al. (2014). The frequency of postoperative stroke in Moyamoya disease following combined revascularization: a single-university series and systematic review. *J. Neurosurg.* 121, 432–440. doi: 10.3171/2014.1.JNS13946

Li, Y., Wang, A. R., and Steinberg, G. K. (2022). Safety and efficacy of induced hypertension and hypervolemia in preventing neurologic complications after combined direct and indirect bypass in hemorrhagic-onset Moyamoya disease. *World Neurosurg.* 160, e381–e387. doi: 10.1016/j.wneu.2022.01.017

Lu, J., Zhao, Y., Ma, L., Chen, Y., Li, M., Chen, X., et al. (2019). Predictors and clinical features of transient neurological events after combined bypass revascularization for Moyamoya disease. *Clin. Neurol. Neurosurg.* 186:105505. doi: 10.1016/j.clineuro.2019.105505

McDonald, R. J., McDonald, J. S., Kallmes, D. F., Jentoft, M. E., Murray, D. L., Thielen, K. R., et al. (2015). Intracranial gadolinium deposition after contrast-enhanced mr imaging. *Radiology* 275, 772–782. doi: 10.1148/radiol.15150025

Mukerji, N., Cook, D. J., and Steinberg, G. K. (2015). Is local hypoperfusion the reason for transient neurological deficits after sta-mca bypass for Moyamoya disease? *J. Neurosurg.* 122, 90–94. doi: 10.3171/2014.8.JNS132413

Noguchi, T., Kawashima, M., Nishihara, M., Hirai, T., Matsushima, T., and Irie, H. (2013). Arterial spin-labeling mr imaging in Moyamoya disease compared with clinical assessments and other mr imaging findings. *Eur. J. Radiol.* 82, e840–e847. doi: 10.1016/j.ejrad.2013.08.040

Østergaard, L., Engedal, T. S., Aamand, R., Mikkelsen, R., Iversen, N. K., Anzabi, M., et al. (2014). Capillary transit time heterogeneity and flow-metabolism coupling after traumatic brain injury. *J. Cereb. Blood Flow Metab.* 34, 1585–1598. doi: 10.1038/jcbfm.2014.131

Park, W., Park, E. S., Lee, S., Park, J. C., Chung, J., Lee, J. M., et al. (2018). Intracranial hemorrhage after superficial temporal artery-middle cerebral artery direct anastomosis for adults with Moyamoya disease. *World Neurosurg.* 119, e774–e782. doi: 10.1016/j.wneu.2018.07.266

Research Committee on the Pathology and Treatment of Spontaneous Occlusion of the Circle of Willis, and Health Labour Sciences Research Grant for Research on Measures for Infractable Diseases (2012). Guidelines for diagnosis and treatment of moyamoya disease (spontaneous occlusion of the circle of Willis). *Neurol. Med. Chir.* 52, 245–266. doi: 10.2176/nmc.52.245

Scott, R. M., and Smith, E. R. (2009). Moyamoya disease and Moyamoya syndrome. *N. Engl. J. Med.* 360, 1226–1237. doi: 10.1056/NEJMra0804622

Shimada, Y., Kojima, D., Yoshida, J., Kobayashi, M., Yoshida, K., Fujiwara, S., et al. (2018). Transient symptomatic downregulation of cortical neurotransmitter receptor function due to cerebral hyperperfusion after arterial bypass surgery for a patient with ischemic Moyamoya disease. *Neurol. Med. Chir.* 58, 481–484. doi: 10.2176/nmc.cr.2018-0143

Soman, S., Dai, W., Dong, L., Hitchner, E., Lee, K., Baughman, B. D., et al. (2020). Identifying cardiovascular risk factors that impact cerebrovascular reactivity: an asl mri study. *J. Magn. Reson. Imaging* 51, 734–747. doi: 10.1002/jmri.26862

van Mook, W. N., Rennenberg, R. J., Schurink, G. W., van Oostenbrugge, R. J., Mess, W. H., Hofman, P. A., et al. (2005). Cerebral hyperperfusion syndrome. *Lancet Neurol.* 4, 877–888. doi: 10.1016/S1474-4422(05)70251-9

Wang, Z., Aguirre, G. K., Rao, H., Wang, J., Fernández-Seara, M. A., Childress, A. R., et al. (2008). Empirical optimization of asl data analysis using an asl data processing toolbox: ASLtbx. *Magn. Reson. Imaging* 26, 261–269. doi: 10.1016/j.mri.2007.07.003

Yun, T. J., Paeng, J. C., Sohn, C. H., Kim, J. E., Kang, H. S., Yoon, B. W., et al. (2016). Monitoring cerebrovascular reactivity through the use of arterial spin labeling in patients with Moyamoya disease. *Radiology* 278, 205–213. doi: 10.1148/radiol.2015141865

Zaharchuk, G., Bammer, R., Straka, M., Shankaranarayan, A., Alsop, D. C., Fischbein, N. J., et al. (2009). Arterial spin-label imaging in patients with normal bolus perfusion-weighted mr imaging findings: pilot identification of the borderzone sign. *Radiology* 252, 797–807. doi: 10.1148/radiol.2523082018

Zaharchuk, G., Do, H. M., Marks, M. P., Rosenberg, J., Moseley, M. E., and Steinberg, G. K. (2011). Arterial spin-labeling mri can identify the presence and intensity of collateral perfusion in patients with Moyamoya disease. *Stroke* 42, 2485–2491. doi: 10.1161/STROKEAHA.111.616466

Zhang, M., Tang, J., Liu, N., Xue, Y., Ren, X., and Fu, J. (2020). Postoperative functional outcomes and prognostic factors in two types of adult moyamoya diseases. *J. Stroke Cerebrovasc. Dis.* 29:104846. doi: 10.1016/j.jstrokecerebrovasdis.2020.104846

frontiers | Frontiers in Neuroscience

TYPE Original Research
PUBLISHED 09 November 2023
DOI 10.3389/fnins.2023.1248610

EDITED BY
Xi-Nian Zuo,
Beijing Normal University, China

REVIEWED BY
Peng Gao,
Beijing Normal University, China
Zhaohua Ding,
Vanderbilt University, United States
Thomas Bolton,
Advanced Telecommunications Research
Institute International (ATR), Japan

*CORRESPONDENCE
Pan Wang
✉ wpjoepan@163.com
Bharat B. Biswal
✉ bbiswal@gmail.com

RECEIVED 27 June 2023
ACCEPTED 25 October 2023
PUBLISHED 09 November 2023

CITATION
Hu P, Wang P, Zhao R, Yang H and Biswal BB (2023) Characterizing the spatiotemporal features of functional connectivity across the white matter and gray matter during the naturalistic condition. *Front. Neurosci.* 17:1248610. doi: 10.3389/fnins.2023.1248610

Characterizing the spatiotemporal features of functional connectivity across the white matter and gray matter during the naturalistic condition

Peng Hu[1], Pan Wang[1]*, Rong Zhao[1], Hang Yang[1,2] and Bharat B. Biswal[1,3]*

[1]MOE Key Laboratory for Neuroinformation, The Clinical Hospital of Chengdu Brain Science Institute, Center for Information in Medicine, School of Life Science and Technology, University of Electronic Science and Technology of China, Chengdu, China, [2]Chinese Institute for Brain Research, Beijing, China, [3]Department of Biomedical Engineering, New Jersey Institute of Technology, Newark, NJ, United States

Introduction: The naturalistic stimuli due to its ease of operability has attracted many researchers in recent years. However, the influence of the naturalistic stimuli for whole-brain functions compared with the resting state is still unclear.

Methods: In this study, we clustered gray matter (GM) and white matter (WM) masks both at the ROI- and network-levels. Functional connectivity (FC) and inter-subject functional connectivity (ISFC) were calculated in GM, WM, and between GM and WM under the movie-watching and the resting-state conditions. Furthermore, intra-class correlation coefficients (ICC) of FC and ISFC were estimated on different runs of fMRI data to denote the reliability of them during the two conditions. In addition, static and dynamic connectivity indices were calculated with Pearson correlation coefficient to demonstrate the associations between the movie-watching and the resting-state.

Results: As the results, we found that the movie-watching significantly affected FC in whole-brain compared with the resting-state, but ISFC did not show significant connectivity induced by the naturalistic condition. ICC of FC and ISFC was generally higher during movie-watching compared with the resting-state, demonstrating that naturalistic stimuli could promote the reliability of connectivity. The associations between static and dynamic ISFC were weakly negative correlations in the naturalistic stimuli while there is no correlation between them under resting-state condition.

Discussion: Our findings confirmed that compared to resting-state condition, the connectivity indices under the naturalistic stimuli were more reliable and stable to investigate the normal functional activities of the human brain, and might promote the applications of FC in the cerebral dysfunction in various mental disorders.

KEYWORDS

functional connectivity, inter-subject functional connectivity, intra-class correlation coefficient, naturalistic condition, white matter

1. Introduction

Functional connectivity (FC) was proposed as a measure to characterize the temporal synchronization between different brain regions (Aertsen et al., 1989; Friston et al., 1993). Biswal and colleagues found that primary motor network existed during the resting-state by performing FC, suggesting that the human brain has also functional pattern even though subjects did not perform a specific task (Biswal et al., 1995). Additional intrinsic function networks have also been extracted from resting-state fMRI (rsfMRI) adopting the FC measure, such as the auditory network (Cordes et al., 2000), visual network (Lowe et al., 1998), and default mode network (Greicius et al., 2003). Furthermore, FC under rsfMRI has been associated with demographic and cognitive measures, such as age (Dosenbach et al., 2010), gender (Zhang et al., 2016, 2018b), and fluid intelligence (Finn et al., 2015). FC during rsfMRI has also provided an impetus to the field of brain disorders, such as autism (Plitta et al., 2015), schizophrenia (Yang et al., 2018), Alzheimer (Dennis and Thompson, 2014), and depression (Villa et al., 2020). These studies have established that FC measures have many important applications in characterizing the human brain's functional activities.

Since static FC (sFC) did not consider the dynamic of signal changes in time, researchers further investigate the dynamic fluctuation of FC (Chang et al., 2009). Dynamic FC (dFC) also have important applications in recognizing relationship between the behavioral/clinical measures and brain functional activities such as the attention scores (Fong et al., 2019), brain maturity (Qin et al., 2015) and cognitive vulnerabilities unmasked by a stressor like sleep restriction (Patanaik et al., 2018). Moreover, combining dFC and sFC features numerically improves predictions over either model alone (Fong et al., 2019). dFC hold promise to provide fundamental information for the neurodegenerative diseases, including Alzheimer's disease (Jones et al., 2012; Córdova-Palomera et al., 2017; Jie et al., 2018), Parkinson's disease (Madhyastha et al., 2015; Kim et al., 2017; Liu et al., 2018), and dementia with Lewy bodies (Lowther et al., 2014; Peraza et al., 2014). The aforementioned studies suggested that the dFC is as important as the sFC for understanding the functional activity of the human brain and psychiatric disorders.

Accumulating naturalistic stimuli studies including watching the movie and listening to the story have attracted the interest of many researchers as a compromise between rsfMRI and task-evoked fMRI (tfMRI). Compared with rsfMRI, naturalistic condition improves the similarity between subjects as they are experiencing the same stimuli (Hasson et al., 2004; Nastase et al., 2019). With continuous presentation of sound and visual information, naturalistic scanning is closer to the real life environment (Chen G. et al., 2020). Furthermore, previous studies demonstrated that the naturalistic paradigm was better than the resting-state for controlling the head motion, especially for children (Vanderwal et al., 2015, 2019; Greene et al., 2018). Movie-watching paradigm also has been shown to improve participant arousal levels (Vanderwal et al., 2017). Compared with tfMRI, naturalistic condition is easier to perform particularly for children, elders, and clinical populations (Vanderwal et al., 2015; Huijbers et al., 2017).

As both movie-watching and resting-state had no specific task when subjects were scanned, the naturalistic paradigm is more similar to rsfMRI than tfMRI, resulting in the universality of FC patterns that are especially associated with the resting-state. Finn and Bandettini demonstrated that compared to the resting-state condition, FC during the naturalistic viewing (i.e., movie watching) gave more accurate prediction of trait-like phenotypes in the domains of both cognition and emotion (Finn and Bandettini, 2021). A widespread FC pattern was identified that it could predict whether individuals are watching a movie or resting (Sanchez-Alonso et al., 2021). To uncover differences between two states, Lynch and colleagues calculated the FC differences between them, and suggested that the naturalistic condition showed weaker FC than the resting-state after correction (Lynch et al., 2018). However, only 10 subjects were used in this study and the length of the movie clip was less than 6 min, suggesting that their findings need to be evaluated in a large group of subjects. In another study, the FC reliability of brain networks was significantly improved during natural viewing conditions over resting-state conditions, with an average increase of almost 50% across various connectivity measures (Wang et al., 2017).

The dFC measure has recently been used in the naturalistic stimuli as a method of detecting the neuro-information (Sastry et al., 2022). For clinical populations involving body dysmorphic disorder (BDD), Wong and colleagues uncovered that the naturalistic viewing could affect dynamic connectivity when symptoms of BDD were triggered (Wong et al., 2021). Previous studies have shown that although dFC values exhibited weaker reliability than sFC during the resting-state and in the naturalistic viewing condition, the reliability of dFC could be significantly improved in the naturalistic viewing (Zhang et al., 2018a, 2021; Wang et al., 2021).

A basic question in neuroscience is how synchronous different subjects' brains are under the real-world. To answer this question, the naturalistic condition such as movie have been used to simulate the real-world stimuli. Inter-subject correlation (ISC) and inter-subject functional connectivity (ISFC) have been performed to evaluate the synchronization between subjects. Hasson and colleagues calculated ISC during natural vision and found that similarities for visual, auditory, and their association cortices were significantly improved (Hasson et al., 2004). Furthermore, dynamic ISC was proposed to explore the consistent dynamic connectivity between different subjects in widespread brain regions (Di and Biswal, 2020). As an extension of ISC, Simony and colleagues introduced ISFC that was calculated between the time series in one ROI of one subject and the average time series in all ROIs of all subjects. ISFC could be used to evaluate stimuli-evoked correlations, because non-neuronal artificial signals are not correlated between different subjects (Simony et al., 2016). Moreover, ISFC could be calculated with another way. Specifically, the correlation was evaluated between the time series of one ROI of one subject and all ROIs' time series across other subjects. The approach of correlating each subject with every other subject (rather than correlating each subject's data with all other subjects' data average) preserves the variability from individual subjects (Cantlon and Li, 2013). The authors found that primary sensory cortices appeared to have strong ISFC consistence (Ren et al., 2017). Furthermore, ISFC was proved as an effective measure to evaluate specific brain disorder, such as attention deficit hyperactivity disorder (ADHD; Tang et al., 2019), and had benefit to discover the influence of negative family environments for children's psychological wellbeing (Su et al., 2022). The joint model (ISFC + FC) yield the highest predictive accuracy and significantly predicted individuals' social cognitive abilities. The model also proved the hypothesize that ISFC and FC provide distinct and complementary information about individual differences in social cognition (Xie and Redcay, 2022). ISFC has ability to explore the importance of feed-back connections in action prediction (Cerliani et al., 2022). Dynamic ISFC (dISFC) was able to isolate effects of the naturalistic condition and to capture the temporal information of brain activity (Bolton et al., 2019). Furthermore, dISFC could be used to detect the functional brain configurations, which autism spectrum disorder and typical development subjects continuously adjusted based on movie cues under the naturalistic stimulation (Bolton et al., 2020). The effect of naturalistic stimuli for FC and ISFC compared with rsfMRI has not been systematically addressed.

White matter (WM) is a dense structure that connects to different gray matter (GM) areas and occupies almost half of human brain (Teo et al., 1997; Zhang and Sejnowski, 2000; Arai and Lo, 2009; Harris and Attwell, 2012). Although the WM plays an important role in the human brain, the functional properties of WM were rarely analyzed and frequently ignored in fMRI. Recent studies have suggested that WM shows blood oxygen level-dependent (BOLD) signal fluctuations similar to those of GM (Peer et al., 2017; Jiang et al., 2019; Ji F. et al., 2019; Ji G. J. et al., 2019). Peer and colleagues found that the signals of WM could be organized with FC to generate symmetrical WM functional networks and the replication was proved in an independent group (Peer et al., 2017; Wang et al., 2021). Furthermore, by evaluating the reliability of sFC and dFC in GM and WM, Wang and colleagues found that the reliability of sFC was higher than that of dFC, applying to both WM and GM (Wang et al., 2021). Moreover, WM functional signals could be used to explain neurological diseases, such as schizophrenia (Jiang et al., 2019; Fan et al., 2020), Parkinson's disease (Ji G. J. et al., 2019), and Alzheimer's disease (Ji F. et al., 2019). However, the influence of naturalistic condition for WM functional signals remains unclear.

In this study, we aim to investigate the influence of the naturalistic paradigm on the whole-brain FC compared with the resting state. We have mainly focused on the following three topics: (1) Compared with the resting-state, the differences of naturalistic paradigm for different connectivity in whole-brain (sFC, dFC, sISFC and dISFC in GM, WM, and between GM-WM); (2) Evaluating the reliability of different connectivity in the naturalistic and the resting-state conditions; (3) Associations between the naturalistic stimuli and the resting-state conditions, and associations between them for different connectivity measures. Specifically, we clustered GM templates with 200 ROIs and 8 functional networks and adopted similar processing steps to obtain WM templates with 200 ROIs and 9 functional networks. sFC, dFC, sISFC, and dISFC were calculated for both movie-watching and resting-state at ROI- and network-levels. To compare sFC and dFC between the naturalistic and resting-state conditions, we calculated paired-T test to show significant changes between two states. The subject-wise bootstrapping (SWB) was performed to show the significant sISFC and dISFC induced by naturalistic viewing. ICC was performed to demonstrate the reliability of FC and ISFC. Heat maps were calculated to denote associations between two conditions and between static and dynamic properties.

2. Materials and methods

2.1. Human connectome project data

This study used data from the WU-Minn 7-Tesla Human Connectome Project (HCP). This is a widely used open-access dataset.[1] Using the 7-Tesla scanner a total of 184 subjects were scanned. Eight subjects had incomplete data and were therefore excluded from this study. We also removed four subjects with missing rest or movie images. Therefore, a total of 172 subjects could be used in this study. Briefly, in this study, four sessions were scanned across two or three different days. A number of imaging sequences including movie-watching and resting-state data was performed. Specifically, session1 included MOVIE1, MOVIE2, and REST1; session2 included REST2; session3 included REST3; and session4 included MOVIE3, MOVIE4, and REST4. The REST and MOVIE runs were collected using the same gradient-echo-planar imaging (EPI) sequence with the following parameters: repetition time (TR) = 1,000 ms, echo time (TE) = 22.2 ms, flip angle = 45 deg., field of view (FOV) = 208 × 208 mm, matrix = 130 × 130, spatial resolution = 1.6 mm^3, number of slices = 85, multiband factor = 5, image acceleration factor = 2, partial fourier sampling = 7/8, echo spacing = 0.64 ms, bandwidth = 1,924 Hz/Px. The parameters of T1 series were as following: TR = 2,400 ms, TE = 2.14 ms, TI = 1,000 ms, flip angle = 8 deg., FOV = 224 × 224 mm, voxel size = 0.7 mm isotropic, BW = 210 Hz/Px, iPAT = 2, acquisition time = 7 min and 40 s. The direction of phase encoding alternated between posterior-to-anterior (REST1, REST2, MOVIE2, MOVIE3) and anterior-to-posterior (REST3, REST4, MOVIE1, MOVIE4). Frames (TRs, second) per run for REST = 900; frames of MOVIE1 = 921; frames of MOVIE2 = 918; frames of MOVIE3 = 915; frames of MOVIE4 = 901.

Detailed information about the Movie paradigm has been described elsewhere and therefore only briefly described here (Finn and Bandettini, 2021). The MOVIE runs contained several rest and movie clips. There was a rest clip before and after movie clips. The detailed MOVIE clips' time points were described in Table 1.

2.2. The preprocessing steps of fMRI dataset

The preprocessing steps of fMRI data were performed using custom built MATLAB scripts and the Data Processing Assistant for Resting-State fMRI (DPARSF; Chao-Gan and Yu-Feng, 2010)[2] and Statistical Parametric Mapping (SPM12).[3] REST and MOVIE data sets were analyzed using the same preprocessing steps. The first 20 time points were discarded as the first clip of MOVE data was a 20s rest clip, and to minimize the T1 relaxation. Head motion was corrected using rigid body translation and rotation. T1-weighted anatomic images were co-registrated with functional images, then segmented to GM, WM, and CSF by using the DARTEL algorithm. Linear drift was detrended. CSF signal as covariates were regressed from functional images. Head motion was also regressed based on Friston 24-parameter model (6 head motion parameters, 6 head motion parameters one time point before, and the 12 corresponding squared items; Friston et al., 1996). To further reduce the influence of head motion, we performed scrubbing regressors by motion "spikes," which was defined by the frame-wise displacement (FD) > 1 mm and used

---

[1] http://humanconnectomeproject.org

[2] http://rfmri.org/DPARSF

[3] http://www.fil.ion.ucl.ac.uk/spm

TABLE 1 The information about movie runs.

Run	Clip	Start TP	End TP	Duration	Run	Clip	Start TP	End TP	Duration
MOVIE1	1	21	264	244	MOVIE3	1	21	201	181
	2	285	506	222		2	222	406	185
	3	527	714	188		3	427	630	204
	4	735	798	64		4	651	792	142
	5	819	901	83		5	813	895	83
MOVIE2	1	21	247	227	MOVIE4	1	21	253	233
	2	268	526	259		2	274	503	230
	3	547	795	249		3	524	778	255
	4	816	898	83		4	799	881	83

Here are the start time point, end time point, and duration of movie clips for all four movie runs. TP, time point.

TABLE 2 The description of concatenate MOVIE and REST runs.

Series	Concatenate runs	Time points
MOVIE Day1	MOVIE1 + MOVIE2	801 + 818 = 1,619
MOVIE Day2	MOVIE3 + MOVIE4	795 + 801 = 1,596
REST Day1	REST1 + REST2	880 + 880 = 1,760
REST Day2	REST3 + REST4	880 + 880 = 1,760

MOVIE1 and MOVIE2 were concatenated as MOVIE Day1; MOVIE3 and MOVIE4 were concatenated as MOVIE Day2; REST1 and REST2 were concatenated as REST Day1; REST3 and REST4 were concatenated as REST Day2.

by previous WM BOLD signals studies demonstrating highly reliable FC both in GM and WM (Power et al., 2012; Peer et al., 2017; Jiang et al., 2019; Wang et al., 2020, 2021). Previous studies demonstrated that the head motion scrubbing did not affect correlation coefficients and could effectively reduce the influence of head motion (Power et al., 2012; Satterthwaite et al., 2013). A temporal filter with range from 0.01 to 0.1 Hz was performed to reduce the non-neuronal contribution to blood oxygen level dependent fluctuations. The functional images were smoothed separately within GM and WM using MATLAB scripts to avoid the confusion between GM and WM signals. Normalization was performed to transform the smoothed functional images to standard Montreal Neurological Institute (MNI) space with $3 \times 3 \times 3\,\text{mm}^3$.

After preprocessing the data sets using the steps described above, the resting state clips (4 or 5) were removed from the MOVIE runs. The remaining time points of MOVIE runs were as follows: MOVIE1 = 801 (244 + 222 + 188 + 64 + 83, second); MOVIE2 = 818 (227 + 259 + 249 + 83, second); MOVIE3 = 795 (181 + 185 + 204 + 142 + 83, second); and MOVIE4 = 801 (233 + 230 + 255 + 83, second; Table 1). MOVIE1 and MOVIE2 were concatenated as MOVIE Day1 (time points = 801 + 818 = 1,619, second); MOVIE3 and MOVIE4 were concatenated as MOVIE Day2 (time points = 795 + 801 = 1,596, second); REST1 and REST2 were concatenated as REST Day1 (time points = 880 + 880 = 1,760, second); REST3 and REST4 were concatenated as REST Day2 (time points = 880 + 880 = 1,760, second; Table 2). The advantage of concatenation was to increase signal length to improve signal-noise ratio. Furthermore, except the last movie clip, all other movie clips are different, so it is hard to average MOVIE runs. Though some subjects were not scanned in 2 days but in 3 days, we still separate them in Day1 and Day2 as shown above.

2.3. Creation of group-level masks and functional networks

Group-level structural GM and WM masks were calculated separately by MATLAB scripts. First, spatially normalized GM maps or WM maps were averaged from all subjects (Figure 1A, step 1). Then, the subcortical and cerebellum were removed based on the Harvard-Oxford atlas and Buckner atlas. Only values greater than 0.6 were identified as WM. The voxels were recognized as GM if they were not WM and their values were higher than 0.2. If less than 80% of them from all subjects was not a number based on obtained GM and WM masks, the voxels were removed.

Since the brain function is based on the cooperation of many regions whose voxels may be adjacent in space, normalized cut spectral clustering (NCUT) was determined to generate ROIs by its spatial constraint (Craddock et al., 2012). Because WM had no functional template and we wanted to keep the processing steps similar between GM and WM, we clustered functional templates with 200 ROIs as Craddock and colleagues recommended for GM and WM by using preprocessed REST1 images. As the processing steps to perform clustering for GM and WM were similar, we have only described it for the WM clustering. Voxel-level signals were extracted from REST1 fMRI data using the group-level WM mask (Figure 1A, steps 2, 3). Then, functional template with 200 ROIs was obtained based on NCUT by using voxel-level signals (Figure 1A, step 4). To detect FC on a larger scale compared with ROI-level, we also clustered network-level functional templates for both GM and WM. Similar to the processing for extracting voxel-wise signals, we got ROI-level signals from REST1 images by averaging all voxel time series in the ROIs based on the above template (Figure 1A, steps 5, 6). sFC matrices were calculated by the Pearson correlation coefficient of ROI-level signals (Figure 1A, step 7). We transformed sFC matrices from r to z by using the Fisher's z transform. They were then averaged to generate the group-level z matrix. The group-level matrix was converted back to r (Figure 1A, step 8). Then, the group-level connectivity matrix was as input of K-means analysis to cluster functional networks from 2 to 20. Based on the elbow criterion of the cluster validity index that was calculated by the ratio between within-cluster to between-cluster distance and the distance was decided by Squared Euclidean distance (Allen et al., 2014). We iterated 100 times to evaluate the relationships between the number of functional networks and the elbow criterion. By drawing the relationship curve figures, 8 GM functional networks

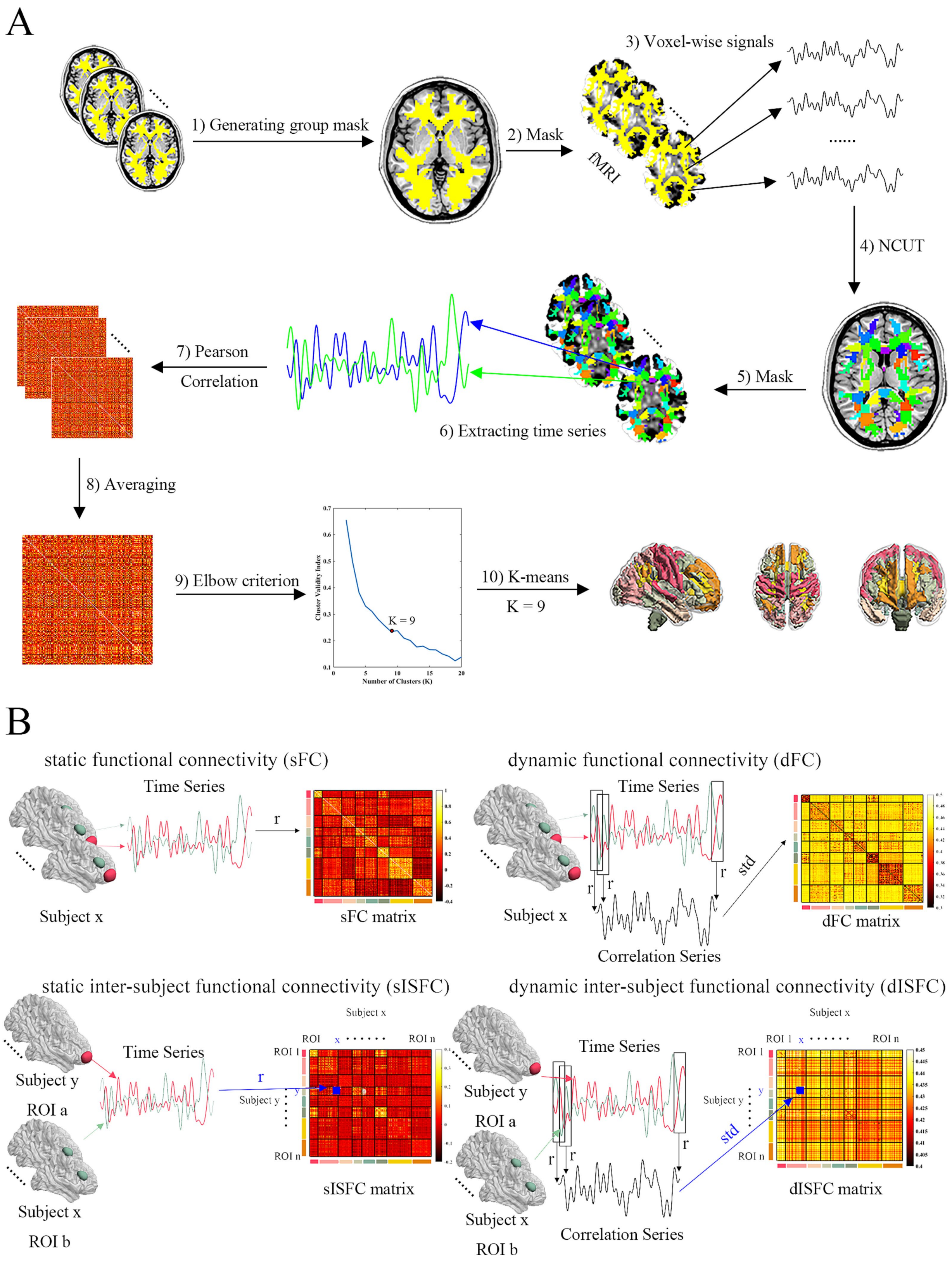

FIGURE 1
Schema of clustering functional networks and FC measures analysis. **(A)** ROI-level and network-level functional templates were clustered based on normalized cut spectral clustering (NCUT) and K-means in WM. The processing steps were: (1) Group WM mask was generated based on all subjects' WM masks. (2) All fMRI data were masked by the group WM mask. (3) Voxels-wise signals were extracted from masked fMRI data. (4) 200 ROIs functional template was clustered by NCUT using voxel-wise signals. (5) All fMRI data were masked by ROI-level template. (6) ROI-level signals were extracted from fMRI data after being masked. (7) Every subject's FC matrices were calculated by Pearson correlation coefficient. (8) These matrices

(Continued)

FIGURE 1 (Continued)

were transformed to z matrices based on Fisher's z. And they were averaged as group z matrix. Then group FC matrix was converted back from group z matrix. (9) Elbow criterion was used to decide the number of clusters (networks). The cluster validity index was the ratio between within-cluster to between-cluster distance. 9 clusters were determined as the results shown. (10) 9 WM networks were clustered by K-means. **(B)** FC methods. sFC was calculated by Pearson correlation coefficient. dFC was calculated by slice window method. Standard deviation was determined as dFC index. sISFC matrix was calculated based on Pearson correlation coefficient between ROI a and ROI b from different subjects. sISFC-z matrix was calculated by Fisher's z transform. Group sISFC-z value between ROI a and ROI b was calculated by averaging upper triangular (UT) and lower triangular (LT) of the sISFC-z matrix. Group sISFC value was transformed back from z to r. dISFC was calculated using the slice window method between ROI a and ROI b from different subjects. dISFC index was also the standard deviation. UT and LT of dISFC matrix were averaged as the group dISFC value between ROI a and ROI b.

and 9 WM functional networks were finally determined because they have more clear "turning point" than other network numbers (Figure 1A, steps 9, 10; Supplementary Figure S1). Because the serial numbers of ROIs in a network were not continuous, we reorganized ROIs based on the networks of GM or WM.

2.4. Static FC and static inter-subject FC

Voxel-wise time series were averaged in the ROIs to generate ROI time series for each subject. sFC matrices for all ROI pairs across all subjects were calculated by using Pearson correlation coefficients in MOVIE and REST images (Figure 1B). Fisher' z transform was performed on all subjects' sFC matrices and above transformed matrices were averaged as the group-level sFC matrix. The z values of group-level sFC matrix were transformed back to r for more intuitive exhibiting the degree of correlation.

Similar to sFC, the static inter-subject FC (sISFC) was calculated by the Pearson correlation coefficient based on ROI signals. The difference was that sFC was evaluated in the same subject but the sISFC was calculated between different subjects. Since the matrices of sISFC were not symmetrical for each ROI pair and the diagonal values were calculated in the same subject, we averaged each matrix of sISFC excluding the diagonal elements. Specifically, the sISFC between {Subject x – ROI a} and {Subject y – ROI b} is different from the sISFC between {Subject x – ROI b} and {Subject y – ROI a}. Even though both presented the sISFC between ROI a and ROI b. Therefore, we first performed the Fisher's z analysis to transform r to z values for the ROI a and ROI b sISFC matrix generating sISFC-z matrices. Then, upper angular and lower angular values within the sISFC-z matrix were averaged as the z value of these two ROIs, which meant that the z transformed sISFC matrix was averaged except for its diagonal because the diagonal values were the (intra-subject) sFC. After averaging, the z values were transformed back to r values as the group-level sISFC to show correlation level (Figure 1B). We performed the same steps above for all ROIs to obtain the group-level sISFC matrix.

2.5. Dynamic FC and dynamic inter-subject FC

Sliding window analysis has been commonly used to estimate the dynamic FC (dFC; Hutchison et al., 2013; Di and Biswal, 2020; Zhang et al., 2021). Previous studies have indicated higher reliability when the sliding window size was around 30 s in calculating dFC (Hutchison et al., 2013; Allen et al., 2014; Leonardi and Van De Ville, 2015). Therefore, the current study used a sliding window size of 30 time points (30 s), and a time step of 1 time point (1 s). ROI time series were extracted from all subjects by averaging all voxels time series in the ROI from the same subject. Pearson correlation analysis was performed on each sliding window between different ROI time series. Thus, there were a series of correlation coefficients across each pair of ROIs. We calculated the standard deviation of these correlation coefficient series to generate a dFC matrix for each subject (Figure 1B). Group-level dFC was calculated by averaging all subjects' dFC matrices.

Dynamic inter-subject FC (dISFC) was also computed to detect the dynamic property across different subjects. ROI signals were extracted by averaging all voxels signals in the same ROIs. dISFC was then calculated using different subjects' ROI signals based on the sliding window with the same parameters described in dFC. As with sISFC, the matrices of dISFC were not symmetric. Therefore, we averaged the upper angular and lower angular of all ROI pairs dISFC matrices as the values of the group-level dISFC matrix (Figure 1B).

2.6. Movie-watching vs. resting-state conditions

To estimate the sFC and dFC differences between the movie-watching and the resting-state conditions, MOVIE vs. REST matrices were calculated by subtracting REST matrices from the corresponding MOVIE matrices. The pair-T test was performed on pairs of ROI or network between the resting-state and the movie conditions to determine which ROIs or networks had significant differences between two conditions. For any pair of ROIs, there were 172 (number of subjects) correlation coefficients. Thus, the inputs of pair-T test were the vector of 172 sFC or dFC in the naturalistic condition and the vector of 172 sFC or dFC in the resting-state condition for each pair of ROIs. Fisher's z transform was performed on the correlation coefficients of sFC before statistics. The above resulting matrices were shown as reverted z to r. Bonferroni correction was performed to estimate the significant differences with $p < 0.05/n$ (n was the number of ROI-pairs or network-pairs).

2.7. Movie-evoked FC

An earlier study demonstrated that FC of the movie-watching contained the intrinsic FC in addition to the movie-evoked FC (Lynch et al., 2018). To demonstrate the influence of movie contents, we performed the statistic method of subject-wise bootstrapping (SWB). It has been shown that when using SWB, the false positive rate was the lowest compared with other nonparametric approaches (i.e., element-wise bootstrapping, subject-wise permutation, and element-wise permutation) and student's *t*-test (Chen et al., 2016). Another reason for not using the student's t-test is that most of the ISFC values are dependent, violating the principle of independence needed for *t*-test.

We also performed SWB for ISFC. Since the ISC is calculated between pairs of subjects in the same ROI or network, it results in a symmetrical ISC matrix. Thus, Chen and colleagues had only focused on the lower triangles. However, when the ISFC was calculated using different ROIs, the matrix of ISFC was not symmetrical. In other words, ISFC contains ISC (Simony et al., 2016). To solve the asymmetrical matrix of ISFC, we calculated centrality-based measure on both the lower and upper triangles of ISFC matrices without using the diagonal elements of the matrices. Instead of the mean, we performed median as the chosen centrality measure of ISFC to prevent the back-and-forth transformation processing. For example, if using mean value, we should first performed the Fisher's z transform for correlation coefficients, then average above z values, and further converted the z values back to correlation coefficients (r). Another reason is that the median is less sensitive to biases than the mean when data are not represent normal Gaussian distribution (Chen et al., 2016). The median of the lower and upper triangles of the ISFC matrix was calculated as the statistical parameter from all subjects of each ROI or network. Specifically, SWB was performed as following: (1) The median value of the ISFC matrix was calculated as the raw median value. (2) ISFC values were selected randomly to raw ISFC matrix size as bootstrapping ISFC matrix, then the bootstrapping median value was calculated based on this bootstrapping ISFC matrix. (3) If the bootstrapping median value was higher (lower) than raw median value, the number increases by one. (4) Bootstrapping was performed using 5,000 repetitions from step (2) to step (3). Then *p*-value was calculated based on the number divided by 5,000. (5) Multiple comparison correction was performed by Bonferroni ($p < 0.05/n$). (6) All these steps were performed for each ROI or network within GM, WM, and GM-WM. Only the ROI (or network) pairs that passed the multiple comparison correlation were shown.

2.8. Reliability

To estimate the reliability of results, the intraclass correlation coefficient (ICC) was performed on the FC or ISFC between Day1 and Day2 (Müller and Büttner, 1994). Specifically, ICC was computed as:

$$ICC = \frac{BMS - WMS}{BMS + (k-1)WMS} \quad (1)$$

where BMS is the between-subjects mean squared variance, WMS is the within-subjects mean squared variance, and k is the repetition number of scans for each participant (k = 2). The reliability of FC and ISFC were calculated as follows: (1) sFC was calculated for all ROI pairs across all subjects separate on Day1 and Day2, resulting in 172 (number of subjects) correlation coefficients for each ROI pair on Day1 or Day2. For each pair of ROIs, both Day1 and Day2 have the vectors of length 172. sFC ICC matrix was calculated based on the vectors between Day1 and Day2 across all ROI pairs. For dFC ICC, we used standard deviation to calculate ICC. Finally, sFC ICC and dFC ICC in GM, WM, and GM-WM were estimated based on these steps above within network- and ROI-levels. (2) For sISFC, we first calculated Pearson correlation coefficients between subjects for each ROI pairs, resulting in the sISFC matrix for each pair of ROIs. The lower and upper triangles of sISFC matrix (excluding diagonal elements) were reshaped to a vector (length is $172 \times 172 - 172 = 29{,}412$). After arranging the vectors for both Day1 and Day2, sISFC ICC was calculated using the vectors of Day1 and Day2 for each pair of ROIs. Similar to dFC ICC, we analyzed the dISFC ICC using its standard deviation. These processing steps were performed in GM, WM, and GM-WM at the network- and ROI-levels separately.

After calculating the ICC, permutation analysis of ICC was performed between the movie-watching and the resting-state. The raw difference was calculated by mean ICC value of movie-watching subtracting mean ICC value of resting-state. The permutation was iterated with 5,000 times. In each iteration, ICC matrices between two conditions were shuffled, then separated to two matrices. The random difference was calculated by minus between mean values of these two matrices. The count was added when the raw difference was lower than the random difference. The p value was calculated by the count dividing by the iteration number.

3. Results

3.1. Clustering GM and WM functional networks

We performed the elbow criterion of the cluster validity index to estimate the numbers of functional networks in GM and WM. We found that the optimal numbers of functional networks in GM and WM were 8 and 9, respectively. These functional networks within GM were: lateral visual network (LVN), limbic network (LIMB), frontoparietal network (FPN), dorsal attention network (DAN), ventral attention network (VAN), medial visual network (MVN), sensorimotor network (SMN), and default mode network (DMN). These results have been labeled and shown in Figure 2. The primary networks contained LVN, MVN, and SMN. The high-level networks contained LIMB, FPN, DAN, VAN, and DMN. The functional networks in WM were: sensorimotor network (SMN-WM), occipital network (ON-WM), superior temporal network (STN-WM), anterior corona radiata network (ACRN-WM), posterior corona radiata network (PCRN-WM), inferior corticospinal network (ICN-WM), deep network (DN-WM), orbitofrontal network (OFN-WM), frontoparietal network (FPN-WM; Figure 2). The superficial layers contained SMN-, ON-, STN-, OFN-, and FPN-WMs. The middle layers contained ACRN- and PCRN-WMs. The deep layer contained DN-WM. The ICN-WM across superficial and middle layers.

To compare between the results of clustering and traditional networks, we decided the Yeo7 GM networks as the traditional GM networks and the Peer12 WM networks as the traditional WM networks. The Dice Coefficient was determined as the similarity algorithm. As the result shown, somatomotor (Sensorimotor), dorsal attention, ventral attention, limbic, frontoparietal, and default mode networks indicated the high connection between the Yeo's networks and our networks. The visual network of Yeo was separate to two networks, which were lateral visual network and medial visual network. For WM networks, some of our WM networks integrated

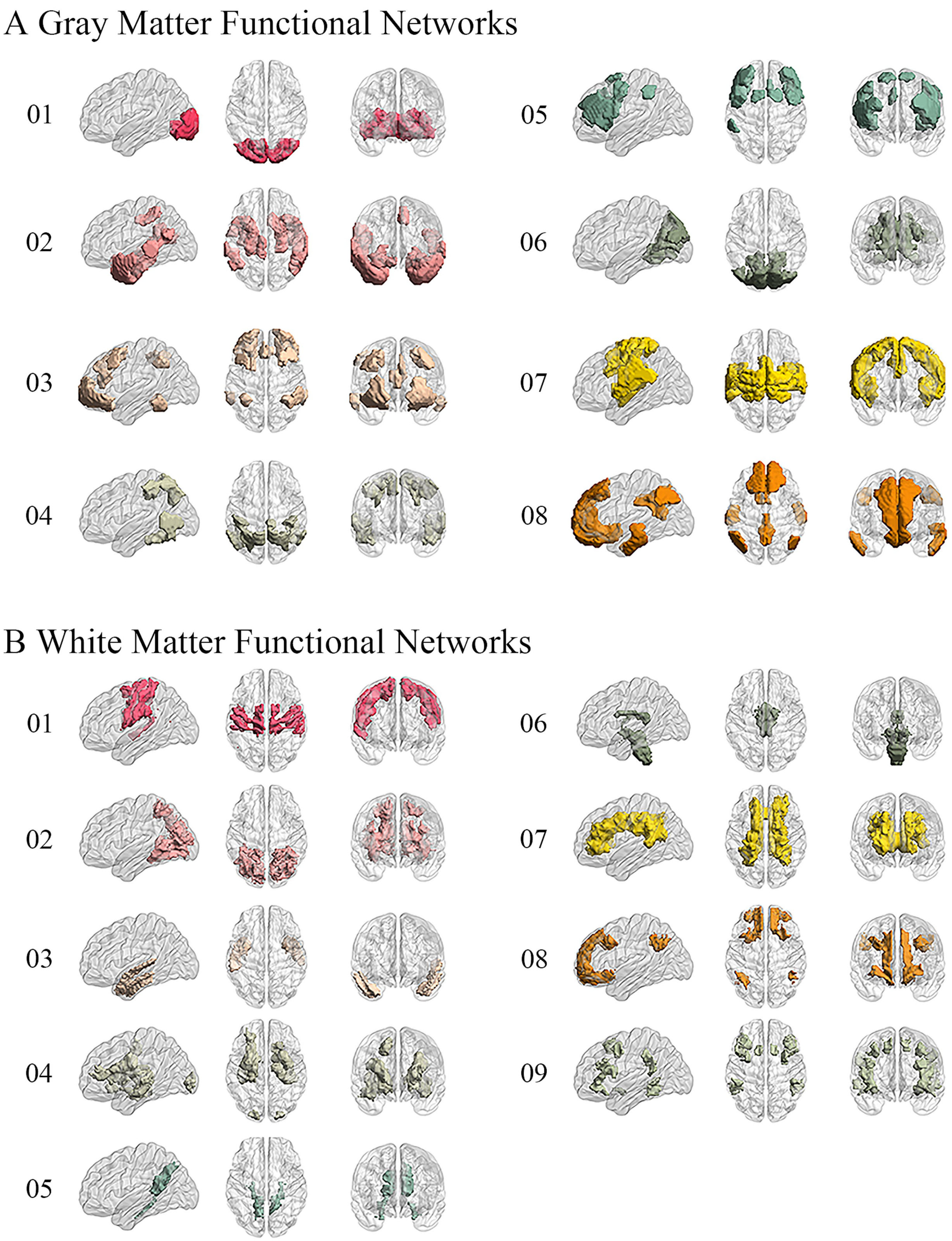

FIGURE 2
Obtaining 8 GM and 9 WM functional networks. **(A)** GM networks: 01. Lateral visual network (LVN); 02. Limbic network (LIMB); 03. Frontoparietal network (FPN); 04. Dorsal attention network (DAN); 05. Ventral attention network (VAN); 06. Medial visual network (MVN); 07. Sensorimotor network (SMN); 08. Default mode network (DMN). **(B)** WM networks: 01. Sensorimotor network in WM (SMN-WM); 02. Occipital network in WM (ON-WM); 03. Superior temporal network in WM (STN-WM); 04. Anterior corona radiata network in WM (ACRN-WM); 05. Posterior corona radiata network in WM (PCRN-WM); 06. Inferior corticospinal network in WM (ICN-WM); 07. Deep network in WM (DN-WM); 08. Orbitofrontal network in WM (OFN-WM); 09. Frontoparietal network in WM (FPN-WM).

Peer's WM networks. To be specific, sensorimotor network contained semsorimotor superficial white-matter system and dorsal frontoparietal tracts; occipital network contained visual superficial white-matter system and inferior longitudinal fasciculus system; superior temporal network was similar to uncinate and middle temporal lobe tracts; anterior corona radiata network was similar to ventral frontoparietal tracts; posterior corona radiata network was similar to cingulum and associated tracts; inferior corticospinal network contained inferior corticospinal tract and posterior cerebellar tracts; deep network contained superior longitudinal fasciculus system; orbitofrontal network was similar to forceps minor system; frontoparietal network was similar to ventral frontoparietal tracts (Supplementary Figure S2).

3.2. FC and ISFC in GM

At the ROI-level and network-level analyses of GM regions, the resting-state and the movie-watching had similar functional patterns of sFC (Figures 3A,C). sFC demonstrated higher FC strengths within intra-networks than them within inter-networks (Figure 3A). We analyzed the differences of sFC between movie and rest conditions, and found the positive and negative values both existed in the difference matrix of sFC (Figure 3B). To better discuss the FC within networks, we calculated number of elements, number of passed correction elements, number of positive elements, number of negative elements, and mean values within networks. More than half of the elements relating to LVN, MVN, and SMN passed significance based on Bonferroni correction. The above three networks had different performances of sFC during the resting-state and the movie-watching. All significant ROI pairs relating to LVN had higher sFC values in the naturalistic viewing, indicating the movie-watching heightened sFC relating to LVN. On the contrary, for significant ROI pairs in the SMN, the movie-watching condition showed weaker sFC than that during the resting-state. For MVN, most ROI pairs exhibited enhanced sFC, but 19% of ROIs showed negative values. The averaged sFC values within the various networks ranged between −0.077 and 0.07 (Table 3). For the sFC Movie vs. Rest matrix at the network-level, primary networks had different performances. Specifically, in the movie-watching, sFC between LVN and MVN was higher than that in the resting state. But the sFC between MVN and SMN was stronger under the resting-state than under the naturalistic condition. The conditions had no significant difference between LVN and SMN. Between primary and high-level networks, sFC values between LVN and LIMV and between LVN and DAN were improved by the movie stimuli. However, sFC values were lower in the movie-watching condition than in the resting-state between LVN and FPN, between LVN and VAN, as well as between SMN and DAN. For the high-level networks, sFC between VAN and DMN was higher in the movie condition than that during the resting-state. However, sFC became weaker under the movie stimuli between LIMB and FPN, between FPN and DAN, as well as between DAN and VAN (Figure 3D).

The dFC patterns were similar in general between the resting-sate and the movie-watching at the ROI-level and network-level (Figures 3A,C). dFC showed weaker connectivity fluctuations in intra-networks than those in inter-networks (Figure 3A). We analyzed the differences of dFC between Movie and Rest conditions, and the positive and negative values were found in the difference matrix of dFC (Figure 3B). The top 3 GM networks were LVN, MVN, and DAN, which had most elements that passed multiple correction. Specifically, 30% of ROIs in the LVN have passed correction. It was found that all of them were weaker under the movie-watching than those in the resting-state. 27% of ROIs in the MVN demonstrated the significance. 75% of these ROIs' values were positive and 25% of them were negative. 18% of elements in the DAN have passed the correction. 17% of them were positive and 83% of them were negative. The range of averaged dFC values was from −0.017 to 0.01 (Table 3). As the dFC Movie vs. Rest matrix at the network-level, dFC between LVN and MVN became lower in movie-watching than in the resting-state. But dFC between MVN and SMN was higher in the naturalistic condition than that in the resting-state. Between primary and high-level networks, dFC showed lower values under the movie-watching than them in the resting-state between LVN and DAN as well as between DAN and MVN. Within high-level networks, dFC values were lower in the movie condition than them during the resting-state between FPN and VAN. But, the movie stimuli improved dFC values between LIMB and FPN, between DAN and VAN, and between LIMB and DMN (Figure 3D).

We did not find the specific functional pattern of sISFC and dISFC in the resting-state at the ROI-level. Under the movie-watching condition, compared to other functional networks, the sISFC values relating to LVN and MVN exhibited enhancement. However, dISFC did not show clear functional patterns (Figure 3A). At the network-level, compared with the naturalistic condition, the resting-state did not show the clear sISFC and dISFC patterns. sISFC values of LVN, MVN, as well as between LVN and MVN were improved by the movie-watching condition. Compared with LVN, the enhancements of dISFC in MVN and between LVN and MVN were more evident (Figure 3C).

3.3. FC and ISFC in WM

As shown in the sFC matrices at the ROI-level and network-level, the movie-watching did not modify the functional patterns compared with the resting-state (Figures 4A,C). About the Movie vs. Rest matrix of sFC, the naturalistic condition increased FC within some networks, but the opposite situation also existed in some networks (Figure 4B). Specifically, about 30% of the ROIs passed the multiple comparison correction in the SMN-WM, and most (99%) of these ROIs were negative values. 33% of ROIs demonstrated significance within ON-WM, and 77% of them were positive values (Table 4). As the sFC Movie vs. Rest matrix at the network-level, sFC values between SMN- and ON-WMs and between STN- and OFN-WMs were lower in the naturalistic condition than them in the resting-state within the superficial layer. However, sFC between STN- and FPN-WMs was higher in the movie-watching than that during the resting-state within the superficial layer. As the WM network crosses superficial and middle layers, ICN-WM showed high sFC values with superficial networks, including SMN-, STN-, and FPN-WMs. As layers between superficial and middle, the sFC between STN- and PCRN-WMs was weak in the naturalistic condition. However, the sFC values between STN- and ACRN-WMs, and between PCRN- and FPN-WMs became strong from the resting-state to the movie condition. For layers between superficial and deep, the sFC between ON- and DN-WMs was lower in the movie-watching while sFC values between SMN- and

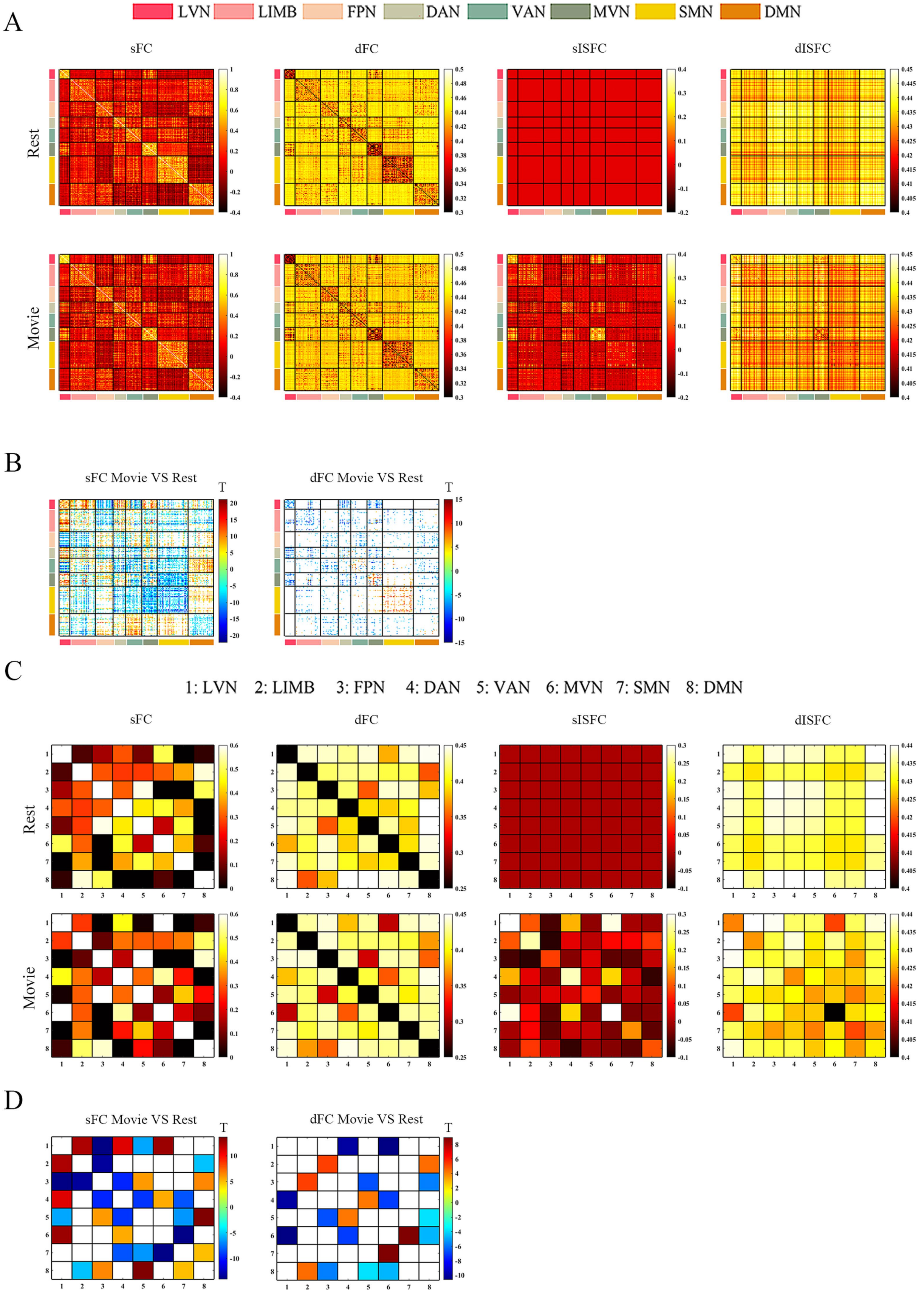

FIGURE 3
ROI- and network-levels FC and ISFC matrices in GM. **(A)** ROI-level sFC, dFC, sISFC, and dISFC matrices were calculated separately in the resting-state and the movie-watching. **(B)** sFC and dFC Movie vs. Rest matrices were calculated by subtracting REST matrices from the corresponding MOVIE

(Continued)

FIGURE 3 (Continued)
matrices. They were performed the pair-T test and were corrected by Bonferroni. ROIs that did not pass the Bonferroni were set blank. **(C)** Networks-level sFC, dFC, sISFC, and dISFC matrices were calculated separately in the resting-state and the movie-watching. **(D)** The processing steps within network-level sFC and dFC Movie vs. Rest matrices were similar to ROI-level. LVN, Lateral visual network; LIMB, Limbic network; FPN, Frontoparietal network; DAN, Dorsal attention network; VAN, Ventral attention network; MVN, Medial visual network; SMN, Sensorimotor network; DMN, Default mode network.

TABLE 3 sFC and dFC in GM networks.

Networks	NoE	NoPE (NoPE/NoE)		NoP (NoP/NoPE)		NoN (NoN/NoPE)		Mean	
		sFC	dFC	sFC	dFC	sFC	dFC	sFC	dFC
LVN	225	138 (61%)	68 (30%)	138 (100%)	0 (0%)	0 (0%)	68 (100%)	0.070	−0.017
LIMB	1,089	300 (28%)	120 (11%)	166 (55%)	0 (0%)	134 (45%)	120 (100%)	0.004	−0.009
FPN	529	134 (25%)	70 (13%)	116 (87%)	0 (0%)	18 (13%)	70 (100%)	0.027	−0.011
DAN	256	72 (28%)	46 (18%)	30 (42%)	8 (17%)	42 (58%)	38 (83%)	−0.014	−0.007
VAN	441	196 (44%)	50 (11%)	14 (7%)	34 (68%)	182 (93%)	16 (32%)	−0.051	0.001
MVN	400	210 (53%)	106 (27%)	40 (19%)	80 (75%)	170 (81%)	26 (25%)	−0.051	0.010
SMN	1,600	798 (50%)	242 (15%)	0 (0%)	240 (99%)	798 (100%)	2 (1%)	−0.077	0.010
DMN	1,024	292 (29%)	24 (2%)	4 (1%)	10 (42%)	288 (99%)	14 (58%)	−0.046	0

NoE, number of elements; NoPE, number of passed correction elements; NoP, number of positive elements from correction elements; NoN, number of negative elements from correction elements. LVN, lateral visual network in GM; LIMB, limbic network in GM; FPN, frontoparietal network in GM; DAN, dorsal attention network in GM; VAN, ventral attention network in GM; MVN, medial visual network in GM; SMN, sensorimotor network in GM; DMN, default mode network in GM.

DN-WMs, and between DN- and OFN-WMs were higher in the movie-stimuli than them during the resting-state. The sFC between ACRN- and PCRN-WMs was improved by the movie-watching in the middle layer. Between middle and deep layers, the sFC between PCRN- and DN-WMs was higher in the movie condition than that during the resting-state (Figure 4D).

The dFC patterns under the movie-watching condition were similar to the corresponding values in the resting-state at the ROI-level and network-level (Figures 4A,C). For the dFC Movie vs. Rest matrix at the ROI-level, 22% of ROIs in the ON-WM demonstrated the significance and 83% of them were negative. Only a small fraction of elements (4%) passed multiple comparison correction in the SMN-WM (Table 4). For the dFC Movie vs. Rest matrix at the network-level, dFC between STN- and FPN-WMs of the superficial layers was lower during the movie-watching than that in the resting-state. But dFC values between SMN- and ON-WMs, and between STN- and OFN-WMs were higher in the movie-stimuli than them during the resting-state. Between superficial and middle layers, dFC between STN- and ACRN-WMs became low from the resting-state to the movie-watching. For layers between middle and deep, the dFC also got low in the movie condition compared with the resting-state between PCRN- and DN-WMs (Figure 4D).

For ISFC matrices at the ROI-level, only the sISFC matrix of the movie-watching demonstrated distinct functional patterns. The sISFC patterns of ON- and STN-WMs were found to be distinct during the movie watching (Figure 4A). For sISFC and dISFC matrices at the network-level, the resting-state did not show clear patterns. The movie stimuli have improved sISFC values of the ON- and STN-WMs. Compared with sISFC matrix, only the ON-WM showed a relatively stable signal due to its low dISFC value during the movie-watching. On the other hand, inter-networks connectivity had relatively fewer sISFC and higher dISFC values compared with the intra-networks (Figure 4C).

3.4. FC and ISFC in GM-WM

Like GM and WM, the resting-state and the movie-watching had similar sFC patterns at the ROI-level and the network-level (Figures 5A,C). Unlike GM or WM in which intra-network FC values were talked at the ROI-level, we calculated Pearson correlation coefficients between GM and WM networks both in the resting-state and during the movie-watching. In general, the correspondence between GM and WM functional networks were similar, and the only difference was that the GM network corresponding to the PCRN-WM became the MVN under movie-watching condition from DMN during the resting-state. However, as the absolute difference of correlation coefficients between MVN-PCRN (GM-WM networks) and DMN-PCRN was less than 0.01, GM network could be thought as the DMN corresponding to the PCRN-WM (Supplementary Tables S1, S2). For the matrix of sFC Movie vs. Rest at the ROI-level, 40% of elements in SMN-SMN and MVN-ON passed correction. 99% of SMN-SMN values were negative. 47% of MVN-ON values were positive and 53% of them were negative. 32% of elements in LVN-ACRN, DMN-PCRN, and LVN-DN have demonstrated significance. 77% of LVN-ACRN values were positive. 100% of DMN-PCRN and 95% of LVN-DN values were negative (Table 5). Under the movie-watching condition, the sFC matrix showed stronger connectivity for MVN-ON and SMN-SMN. However, we also observed weaker connectivity between GM-WM networks including the LVN-DN, LVN-ICN, VAN-FPN, and DMN-PCRN in the movie condition. LVN-ACRN, LIMB-STN, and DMN-OFN did not show significant differences between the resting-state and the naturalistic conditions (Figure 5D).

dFC of the resting-state and movie-watching performed similar functional patterns at the ROI-level and the network-level (Figures 5A,C). As dFC Movie vs. Rest matrices at the ROI-level, MVN-ON demonstrated most correction elements. Still, only 20%

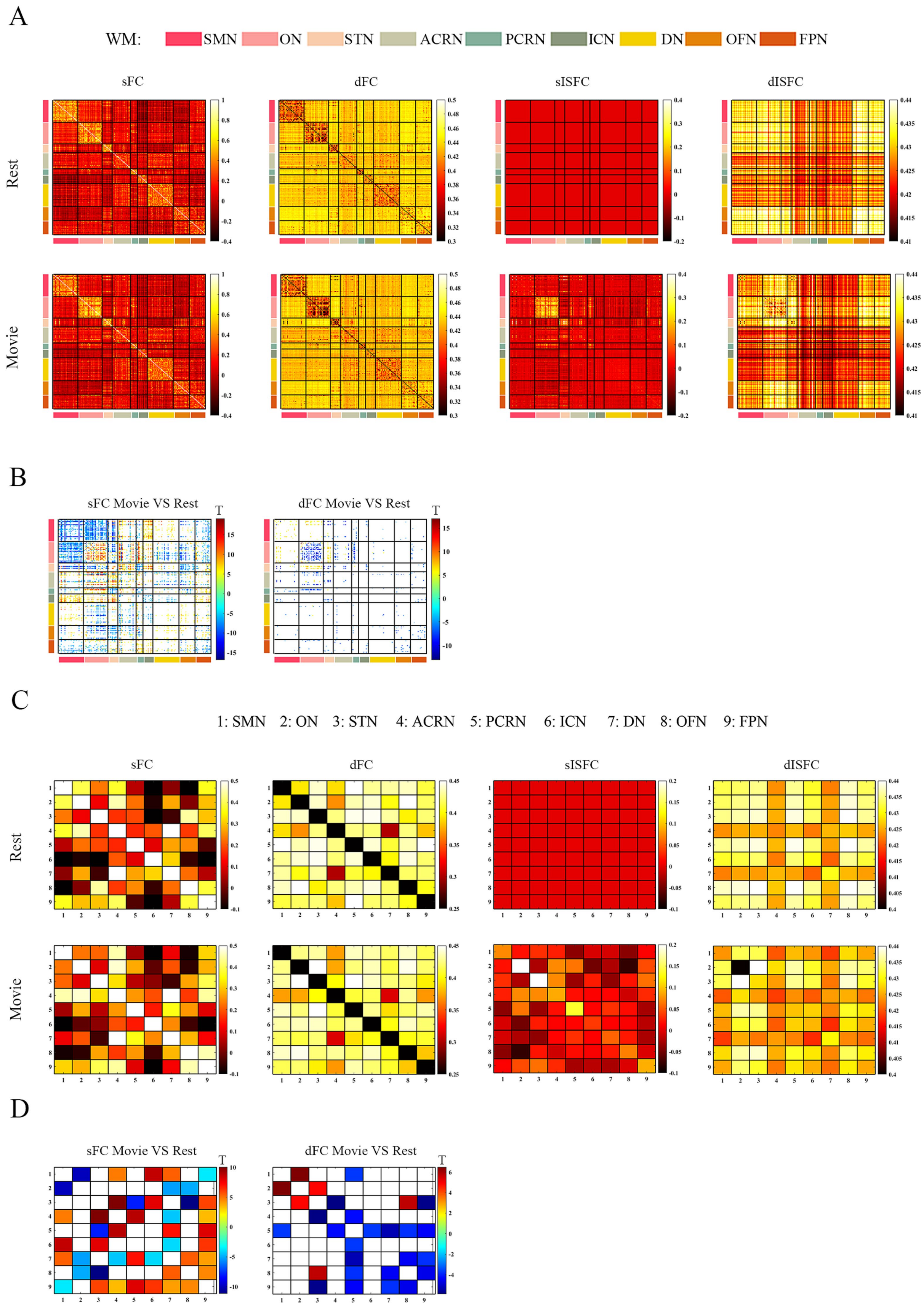

FIGURE 4

ROI- and network-levels FC and ISFC matrices in WM. **(A)** ROI-level sFC, dFC, sISFC, and dISFC matrices were calculated separately in the resting-state and the movie-watching. **(B)** sFC and dFC Movie vs. Rest matrices were calculated by subtracting REST matrices from the corresponding MOVIE

(Continued)

FIGURE 4 (Continued)
matrices. They were performed the pair-T test and were corrected by Bonferroni. ROIs that did not pass the Bonferroni were set blank. **(C)** Networks-level sFC, dFC, sISFC, and dISFC matrices were calculated separately in the resting-state and the movie-watching. **(D)** The processing steps within Network-level sFC and dFC Movie vs. Rest matrices were similar to ROI-level. SMN, Sensorimotor network; ON, Occipital network; STN, Superior temporal network; ACRN, Anterior corona radiata network; PCRN, Posterior corona radiata network; ICN, Inferior corticospinal network; DN, Deep network; OFN, Orbitofrontal network; FPN, Frontoparietal network.

TABLE 4 sFC and dFC in WM networks.

Networks	NoE	NoPE (NoPE/NoE)		NoP (NoP/NoPE)		NoN (NoN/NoPE)		Mean	
		sFC	dFC	sFC	dFC	sFC	dFC	sFC	dFC
SMN-WM	1,156	352 (30%)	42 (4%)	2 (1%)	40 (95%)	350 (99%)	2 (5%)	−0.067	0.005
ON-WM	1,024	342 (33%)	224 (22%)	262 (77%)	38 (17%)	80 (23%)	186 (83%)	0.028	−0.008
STN-WM	169	16 (9%)	6 (4%)	14 (88%)	0 (0%)	2 (12%)	6 (100%)	0.016	−0.007
ACRN-WM	576	102 (18%)	2 (0.4%)	68 (67%)	0 (0%)	34 (33%)	2 (100%)	0.010	−0.004
PCRN-WM	81	12 (15%)	0 (0%)	0 (0%)	0	12 (100%)	0	−0.034	−0.002
ICN-WM	169	26 (15%)	0 (0%)	0 (0%)	0	26 (100%)	0	−0.055	0.001
DN-WM	1,156	20 (2%)	2 (0.2%)	18 (90%)	0 (0%)	2 (10%)	2 (100%)	−0.001	−0.002
OFN-WM	441	22 (5%)	12 (3%)	14 (64%)	0 (0%)	8 (36%)	12 (100%)	0.010	−0.008
FPN-WM	400	52 (13%)	2 (0.5%)	2 (4%)	0 (0%)	50 (96%)	2 (100%)	−0.022	−0.003

NoE, number of elements; NoPE, number of passed correction elements; NoP, number of positive elements from correction elements; NoN, number of negative elements from correction elements; SMN-WM, sensorimotor network in WM; ON-WM, occipital network in WM; STN-WM, superior temporal network in WM; ACRN-WM, anterior corona radiata network in WM; PCRN-WM, posterior corona radiata network in WM; ICN-WM, inferior corticospinal network in WM; DN-WM, deep network in WM; OFN-WM, orbitofrontal network in WM; FPN-WM, frontoparietal network in WM.

of elements passed multiple comparison correction. 40% of their values were positive and 60% of their values were negative. There were too few elements left after correction for other networks between GM and WM (Table 5). For the matrix of dFC Movie vs. Rest at the network-level, MVN-ON, LVN-ACRN, LVN-DN, DMN-OFN and VAN-FPN exhibited similar connectivity patterns with the sFC results. For other networks between GM and WM, dFC of SMN-SMN was higher while LIMB-STN performed weaker dFC value under the naturalistic viewing than them during the resting-state. Furthermore, LVN-ICN and DMN-PCRN did not show significant differences between the resting-state and the movie condition (Figure 5D).

For four matrices of ISFC at the ROI-level, only sISFC matrix in the movie condition showed functional patterns. sISFC values in LVN-ON and MVN-ON were stronger than other networks (Figure 5A). At the network-level, sISFC and dISFC did not denote any clear functional patterns in the resting-state. sISFC values of LVN-ON, DAN-ON, MVN-ON and LIMB-STN were improved by the naturalistic stimuli. For dISFC in movie-watching, only MVN-ON performed weaker signal fluctuation compared with the resting-state (Figure 5C).

3.5. Movie-evoked FC

The subject-wise bootstrapping (SWB) was performed to detect the significant activation induced by the movie stimuli. However, we did not observe any ROI or network that exhibited the significant activation in both sISFC and dISFC. We also repeated the analysis steps in the Day2 data and the results were similar to Day1. Though the movie-watching did enhance ISFC of the visual networks for both GM and WM, as the matrices have shown in Figure 5, the improvements were not strong enough to pass the nonparametric approach.

3.6. Reliability analysis

In general, the intraclass correlation coefficients (ICCs) in the movie-watching were higher than them during the resting-state in GM, WM, and GM-WM. In detail, sFC and sISFC values in the resting-state were low, and their ICCs were poor. sISFC and dISFC values of visual networks denoted relatively high reliability including the LVN, MVN, and ON-WM than other networks. sISFC and dISFC values between visual networks of GM and WM have also shown strong reliability. These results about visual networks performed similarly at the ROI-level and network-level.

Compared with the resting state condition, the sISFC ICC of SMN at network-level under the movie-watching showed relative improvement. At the ROI-level, the sISFC ICC of SMN was smaller than the corresponding value obtained at the network-level. The sISFC ICC of DAN exhibited a similar result between ROI- and network-levels under the movie-watching condition. The network-level dFC ICCs between FPN and VAN and between LIMB and DMN were relatively high, and their ROI-level results had a similar result (Figure 6).

For WM, the sISFC ICCs within STN-WM, between ON- and ACRN-WMs, and between STN- and FPN-WMs were high in the movie-watching. As the dFC, the ICCs between SMN- and ACRN-WMs and between OFN- and FPN-WMs showed the high values under the movie condition. The dISFC ICC denoted high value between ON- and DN-WMs in the movie stimuli (Figure 7).

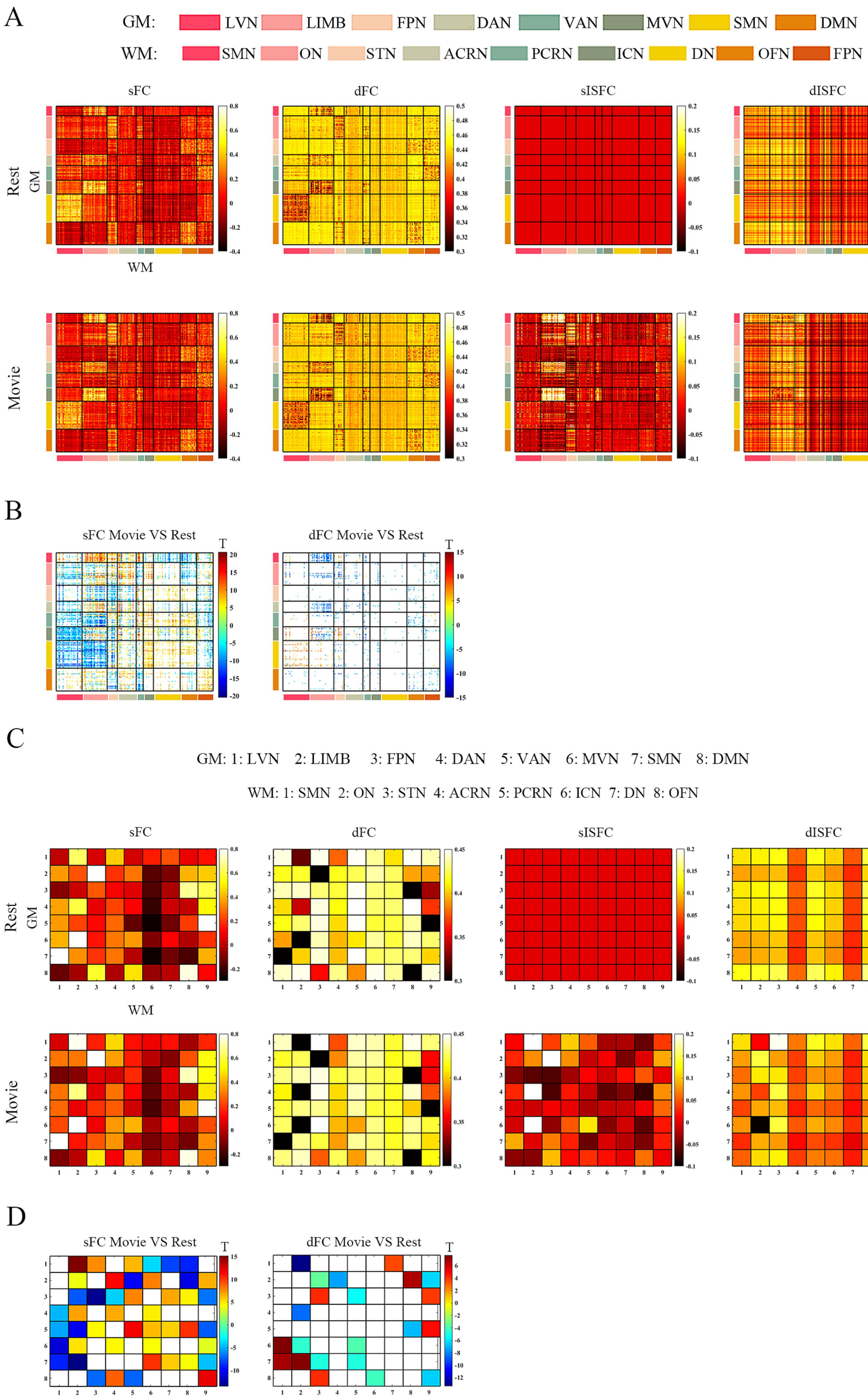

FIGURE 5

ROI- and network-levels FC and ISFC matrices between GM and WM. **(A)** ROI-level sFC, dFC, sISFC, and dISFC matrices were calculated separately in the resting-state and the movie-watching. **(B)** sFC and dFC Movie vs. Rest matrices were calculated by subtracting REST matrices from the

(Continued)

FIGURE 5 (Continued)
corresponding MOVIE matrices. They were performed the pair-T test and were corrected by Bonferroni. ROIs that did not pass the Bonferroni were set blank. **(C)** Networks-level sFC, dFC, sISFC, and dISFC matrices were calculated separately in the resting-state and the movie-watching. **(D)** The processing steps within Network-level sFC and dFC Movie vs. Rest matrices were similar to ROI-level. GM: LVN, Lateral visual network; LIMB, Limbic network; FPN, Frontoparietal network; DAN, Dorsal attention network; VAN, Ventral attention network; MVN, Medial visual network; SMN, Sensorimotor network; DMN, Default mode network. WM: SMN, Sensorimotor network; ON, Occipital network; STN, Superior temporal network; ACRN, Anterior corona radiata network; PCRN, Posterior corona radiata network; ICN, Inferior corticospinal network; DN, Deep network; OFN, Orbitofrontal network; FPN, Frontoparietal network.

TABLE 5 sFC and dFC between GM and WM networks.

Networks (GM-WM)	NoE	NoPE (NoPE/NoE)		NoP (NoP/NoPE)		NoN (NoN/NoPE)		Mean	
		sFC	dFC	sFC	dFC	sFC	dFC	sFC	dFC
SMN-SMN	1,360	546 (40%)	128 (9%)	8 (1%)	117 (91%)	538 (99%)	11 (9%)	−0.014	−0.004
MVN-ON	640	259 (40%)	129 (20%)	121 (47%)	51 (40%)	138 (53%)	78 (60%)	−0.006	−0.005
LIMB-STN	429	117 (27%)	47 (11%)	65 (56%)	7 (15%)	52 (44%)	40 (85%)	−0.027	−0.004
LVN-ACRN	360	115 (32%)	14 (4%)	88 (77%)	5 (36%)	27 (23%)	9 (64%)	0.009	−0.006
DMN-PCRN	288	93 (32%)	9 (3%)	0 (0%)	2 (22%)	93 (100%)	7 (78%)	0.045	−0.008
LVN-ICN	195	26 (13%)	0 (0%)	8 (31%)	0	18 (69%)	0	0.033	−0.006
LVN-DN	510	165 (32%)	0 (0%)	9 (5%)	0	156 (95%)	0	0.038	−0.006
DMN-OFN	672	72 (11%)	26 (4%)	24 (33%)	0 (0%)	48 (67%)	26 (100%)	−0.007	−0.006
VAN-FPN	420	117 (28%)	10 (2%)	10 (9%)	7 (70%)	107 (91%)	3 (30%)	0.051	−0.009

NoE, number of elements; NoPE, number of passed correction elements; NoP, number of positive elements from correction elements; NoN, number of negative elements from correction elements; SMN-SMN, sensorimotor network in GM and sensorimotor network in WM; MVN-ON, medial visual network in GM and occipital network in WM; LIMB-STN, limbic network in GM and superior temporal network in WM; LVN-ACRN, lateral visual network in GM and anterior corona radiata network in WM; DMN-PCRN, default mode network in GM and posterior corona radiata network in WM; LVN-ICN, lateral visual network in GM and inferior corticospinal network in WM; LVN-DN, lateral visual network in GM and deep network in WM; DMN-OFN, default mode network in GM and orbitofrontal network in WM; VAN-FPN, ventral attention network in GM and frontoparietal network in WM.

For GM-WM, ROI-level sISFC ICC in DAN-ON was higher under the movie-watching than that during the resting-state. Generally, the sISFC reliability of GM-WM networks was enhanced by the naturalistic condition in network-level, especially in SMN-SMN, DAN-ON, LIMB-STN, LVN-ACRN, SMN-STN, MVN-PCRN, LIMB-FPN, and DAN-FPN. The dFC values of DMN-PCRN and FPN-FPN exhibited higher reliability than others in the resting-state. dISFC ICC of LVN-DN performed relatively high reliability under the movie-watching compared with the resting-state and other networks (Figure 8).

Permutation analysis was performed between the movie-watching ICC matrix and the resting-state ICC matrix to evaluate the reliability differences between two conditions. As the result shown, most of FC and ISFC indicated $p < 0.0001$. The biggest p value was in network-level GM dFC ICC matrices between the movie-watching and the resting-state, which was around with 0.01 (Supplementary Table S3).

3.7. Association between movie-watching and resting-state

We calculated the heat maps to estimate the associations between the resting-state and the movie-watching using both static and dynamic connectivity indices. Positive correlations for sFC were observed between the movie-watching and the resting-state in GM, WM, and GM-WM. Moreover, dFC also showed a degree of positive correlation between the movie condition and the resting-state. For sISFC and dISFC associations between naturalistic condition and resting-state, there were no correlations in GM, WM, and GM-WM (Figure 9).

Associations between sFC and dFC in the resting-state and the movie-watching showed negative correlations in GM, WM, and GM-WM. In addition, we did not observe any correlations between sISFC and dISFC under the resting-state, but a relatively negative correlation was observed between sISFC and dISFC in the movie-watching (Figure 10).

4. Discussion

The current study compared the spatiotemporal characteristics of whole-brain FC between the naturalistic and the resting-state conditions. We found that the naturalistic stimuli not only improved sFC within and between networks compared with the resting-state, but lower sFC values also existed in some networks during the movie-watching. dFC values demonstrated opposite in general. The movie-watching did not change the FC patterns compared with the resting-state. sISFC was enhanced by the naturalistic condition, but the movie-watching had limited effect on dISFC, especially for ROI-level. The naturalistic paradigm improved the reliabilities of sFC, dFC, sISFC, and dISFC. Moreover, sFC and dFC showed positive correlations between the two conditions. sISFC and dISFC had negative correlation under the naturalistic viewing, but they demonstrated no correlation during the resting-state.

We found the high consistency patterns between the resting-state and movie-watching conditions similar to previous studies about the rfMRI and tfMRI (Cole et al., 2014; Krienen et al., 2014; Gratton et al.,

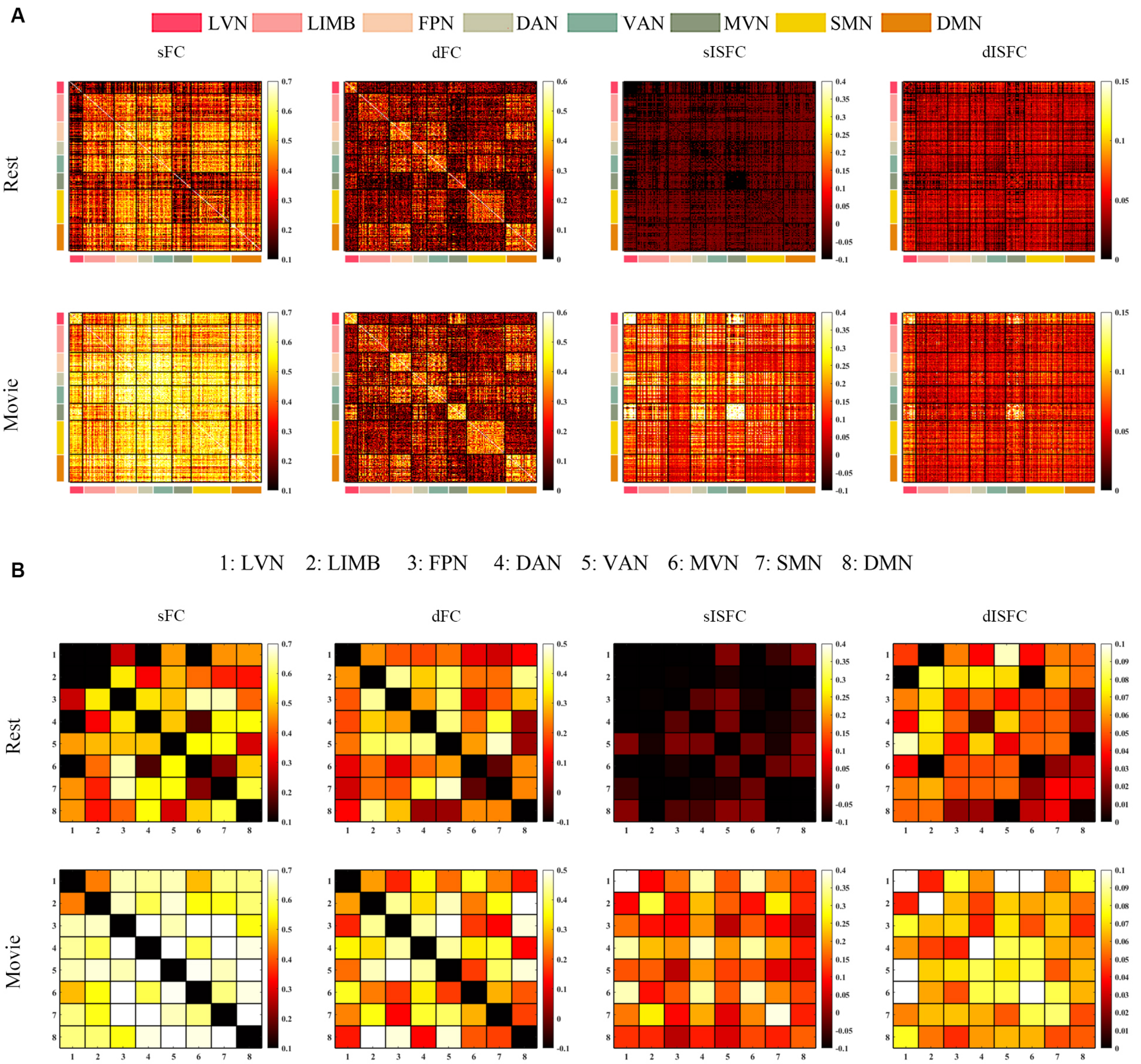

FIGURE 6
The ICC analysis of FC and ISFC in GM. **(A)** ROI-level sFC, dFC, sISFC, and dISFC ICC matrices were calculated separately in the resting-state and movie-watching. **(B)** Network-level sFC, dFC, sISFC, and dISFC ICC matrices were calculated in the resting-state and the movie-watching separately. LVN, Lateral visual network. LIMB, Limbic network; FPN, Frontoparietal network; DAN, Dorsal attention network; VAN, Ventral attention network; MVN, Medial visual network; SMN, Sensorimotor network; DMN, Default mode network.

2016). They suggested that the patterns of the functional networks were relatively stable, and the tasks or naturalistic condition only influenced the strength of FC. Lynch and colleagues denoted that all of the significant connectivity differences were stronger under the resting-state than that under the movie-watching, particularly for visual networks (Lynch et al., 2018). However, several weaker connections were observed in the current study under the resting-state than them during the naturalistic condition. Further, the increase and decrease in connectivity occurred in both primary and high-level GM networks, and superficial, middle, and deep WM layers. This denotes the influence of the naturalistic viewing for connectivity is not dependent on the traditional classifications of primary and high-level networks in GM and layers in WM, but the effect of the movie-watching for FC relates to the whole-brain. The explanations could be that: (1) The naturalistic condition contains a wealth of information, which induced different effect for different functional networks. (2) Functional networks might affect each other (Demirci et al., 2009). Tian and colleagues found considerable resemblance among movie-watching FC based on different movies (Tian et al., 2021), suggesting that the type of movie has limited impact on FC.

The higher ISFC under the naturalistic viewing was found to be associated with visual networks. Specifically, sISFC of LVN, MVN, ON-WM, and MVN-ON was improved during the movie-watching, demonstrating that ON-WM may show more similarly visual function to MVN than LVN. We found the sISFC within STN-WM was improved during the naturalistic viewing as STN-WM could be consider as the hub for the distributed brain network in complex stimuli (Jefferys et al., 2012; Lahnakoski et al., 2012). The movie-watching condition reduced dISFC values of MVN, ON-WM, and MVN-ON at the network-level. But for other networks at the

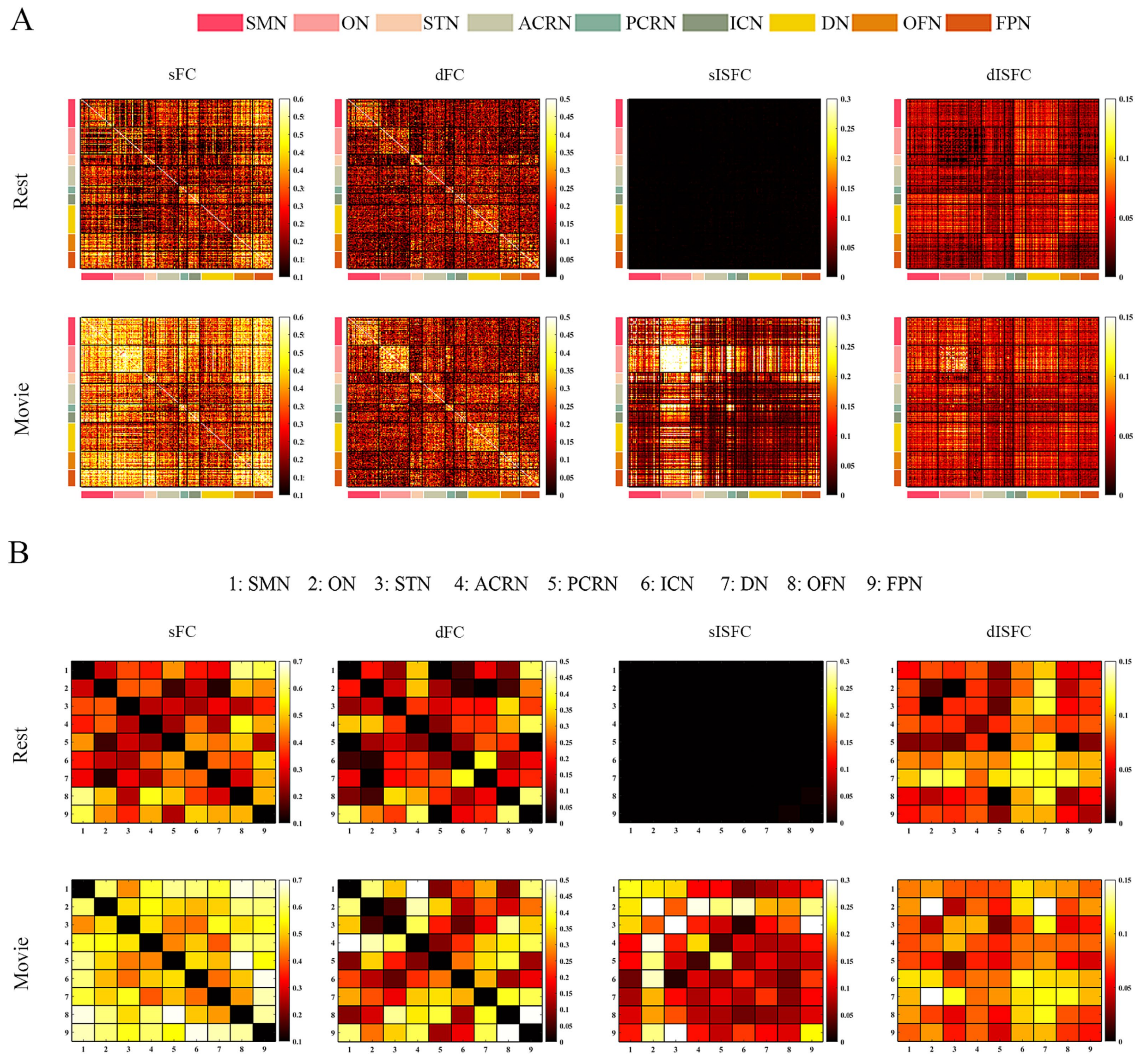

FIGURE 7
The ICC analysis of FC and ISFC in WM. **(A)** ROI-level sFC, dFC, sISFC, and dISFC ICC matrices were calculated separately in the resting-state and movie-watching. **(B)** Network-level sFC, dFC, sISFC, and dISFC ICC matrices were calculated in the resting-state and the movie-watching separately. SMN, Sensorimotor network; ON, Occipital network; STN, Superior temporal network; ACRN, Anterior corona radiata network; PCRN, Posterior corona radiata network; ICN, Inferior corticospinal network; DN, Deep network; OFN, Orbitofrontal network; FPN, Frontoparietal network.

network-level and all networks at the ROI-level, the naturalistic viewing performed limited effect about dISFC.

As the number of time points in MOVIE DAY1 and MOVIE DAY2 are different, we balanced the number of time points between them by extracting the first 1,596 time points of MOVIE DAY1, and compared the difference matrix of FC and ISFC. The results showed that there was limit change of FC and ISFC after the balance in the whole-brain (Supplementary Figures S3–S5).

The reliability of FC and ISFC was evaluated by ICC. In general, ICC values of the movie-watching were higher than them of the resting-state, denoting that the naturalistic viewing could improve the reliability of FC and ISFC. In addition, previous studies have demonstrated that ICCs of sFC were stronger than that of dFC within whole-brain under the resting-state (Wang et al., 2021). In our study, we also found that the reliability of sFC was higher than that of dFC under the naturalistic condition. Further reliability analysis showed the low reliability corresponding to sISFC and dISFC under the resting-state, denoting that ISFC may not be suitable for the resting-state due to the huge variance between subjects in the resting-state. The reason may be that subjects may have different thoughts under the rest scanning inducing the high signal fluctuation between subjects. Therefore, ISFC values were lower in the resting-state than those under the movie-watching. Though ISFC maps showed relative reliability in the naturalistic condition, ISFC ICC values were weaker than FC ICC values under the naturalistic viewing. The reason may be that FC is affected by more noise than ISFC, as ISFC could isolate the noise (Simony et al., 2016).

Chen and colleagues suggested nonparametric approaches and parametric methods for ISC (Chen et al., 2016, 2017; Chen G. et al., 2020). As these statistical approaches were designed for

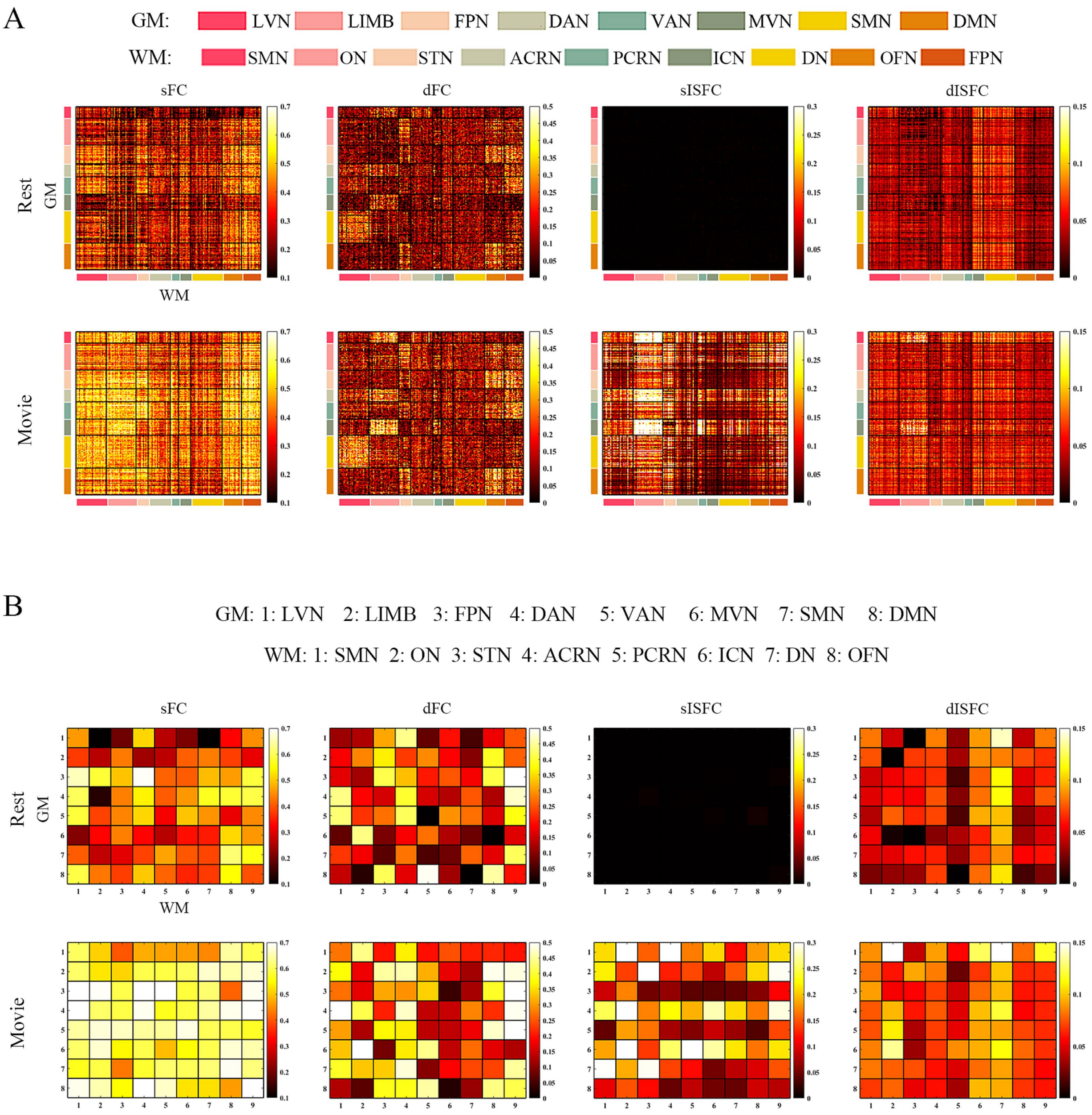

FIGURE 8
The ICC analysis of FC and ISFC between GM and WM. **(A)** ROI-level sFC, dFC, sISFC, and dISFC ICC matrices were calculated separately in the resting-state and movie-watching. **(B)** Network-level sFC, dFC, sISFC, and dISFC ICC matrices were calculated in the resting-state and the movie-watching separately. GM: LVN, Lateral visual network; LIMB, Limbic network; FPN, Frontoparietal network; DAN, Dorsal attention network; VAN, Ventral attention network; MVN, Medial visual network; SMN, Sensorimotor network; DMN, Default mode network; WM: SMN, Sensorimotor network; ON, Occipital network; STN, Superior temporal network; ACRN, Anterior corona radiata network; PCRN, Posterior corona radiata network; ICN, Inferior corticospinal network; DN, Deep network; OFN, Orbitofrontal network; FPN, Frontoparietal network.

ISC and nonparametric approaches were easier to be performed, we determined SWB as the statistics of ISFC to detect the significantly movie-evoked connectivity. However, no significant ISFC was observed including visual networks, suggesting that though the naturalistic paradigm could enhance the inter-subject synchronization, the enhancement is not strong enough to pass the statistics. The reason may be that different subjects have different responses to the complex movie stimuli. Furthermore, non-significance of ISFC may also be because that the statistics approaches of ISC are not suitable for ISFC. ISFC is calculated between all of ROIs or networks across subjects, but ISC is evaluated between subjects in a same ROI or network.

The heat maps were performed to estimate the associations between static and dynamic properties during two conditions and the associations of connectivity indices between the naturalistic viewing and the resting-state. We found positive correlations between sFC of the resting-state and sFC of the naturalistic condition in GM, WM, and GM-WM. We also observed the relatively positive correlations between dFC of two conditions in whole-brain, suggesting a degree of similarity of FC between the resting-state and the movie-watching. Furthermore,

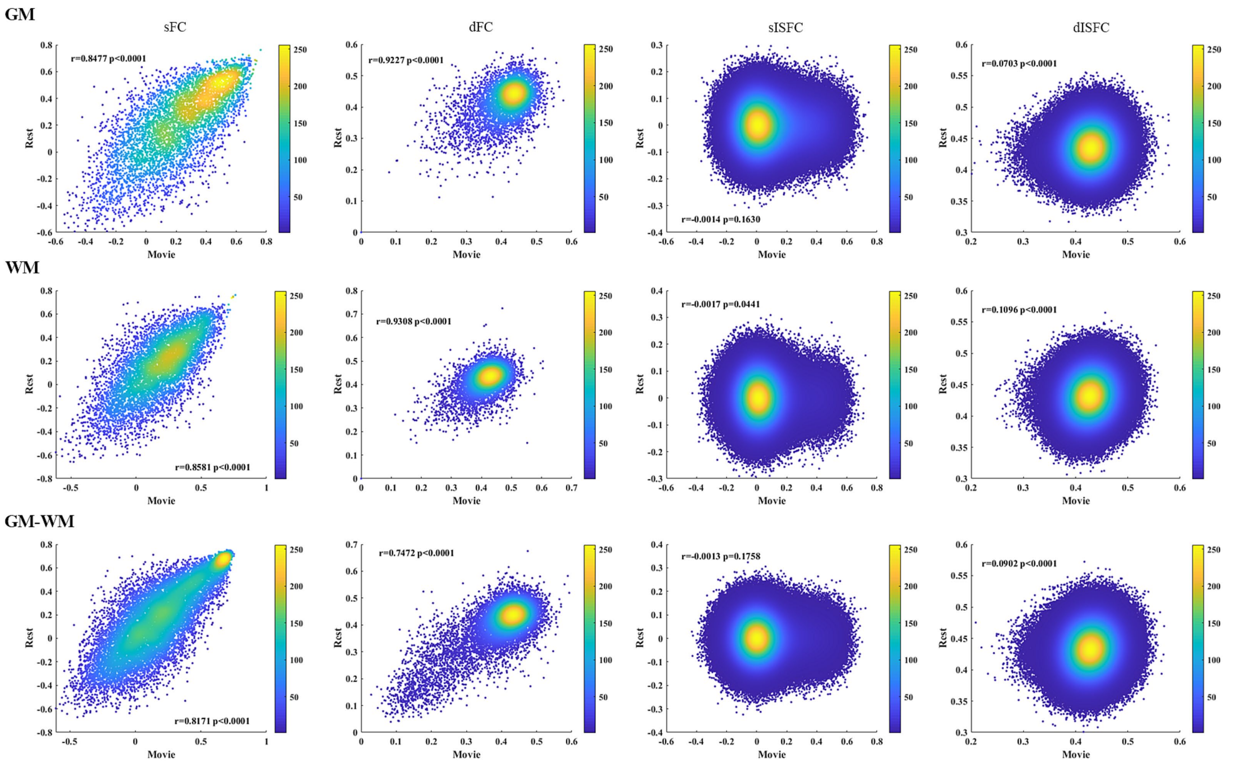

FIGURE 9
Heat maps of sFC, dFC, sISFC, and dISFC between the resting-state and the movie-watching in GM, WM, and GM-WM. We calculated the Pearson correlation coefficients for all connectivity indices between the resting-state and the naturalistic viewing. The densities were evaluated based on these correlation coefficients by using circles method.

both sISFC and dISFC showed no correlations between the two conditions, as there was scarcely any ISFC between subjects under the resting-state. The resting-state and the movie-watching showed similarly negative correlations between sFC and dFC in GM, WM, and GM-WM. We did not find any correlation between sISFC and dISFC under the resting-state, but sISFC values had weakly negative correlations with dISFC values under the naturalistic paradigm in whole-brain, suggesting that the movie-watching enhanced ISFC compared with the resting-state. However, considering the statistic results and the range of ISFC values, the enhancement is relatively weak.

Previous study has shown that even though movie contents were different in different scanning runs, there was considerable resemblance among movie-watching FC based on different movies (Tian et al., 2021). The similarity was also demonstrated in our study, and the most obvious networks were visual networks in gray matter and occipital network in white matter. However, the functional networks connectivity was reasonably considered to be influenced by the movie content. In HCP data, MOVIE1 and MOVIE3 contained clips from independent films (both fiction and documentary) made freely available under Creative Commons license on Vimeo. MOVIE2 and MOVIE4 contained clips from Hollywood films including action, adventure, science fiction, biography, drama, crime, thriller, and so on. In this study, we combined MOVIE1 and MOVIE2 as MOVIE Day1, and combined MOVIE3 and MOVIE4 as MOVIE Day2. The different movie types between MOVIE Day1 and MOVIE Day2 were science fiction (Day1), crime (Day1), thriller (Day1), comedy (Day2), family (Day2), and fantasy (Day2). The ICC values of LIMN, DAN, STN-WM, and OFN-WM were lower than other networks. LIMN could mediate emotional regulation and reward processing (Chen Y. L. et al., 2020). There was an evidence for a modulatory role of the DAN on the orienting of attention in space (Ptak and Schnider, 2010). The correlation between STN-WM and LIMN was higher than 0.8. Therefore, STN-WM probably has the similar function as LIMN. OFN-WM performed over 0.7 correlation coefficient with DMN that works in unison with language networks at certain points in the narrative, while exhibiting antagonistic responses at other times (Simony et al., 2016). Overall, as these networks demonstrated emotion, attention, and so on brain functions, different types of movie clips might induce different signals in a brain. Therefore, the low ICC values of these networks might be affected by different scanning runs and different movie types.

In this study, there are some limitations. (1) When subjects were watching movies, the brains were in a higher arousal condition with less head motion (Vanderwal et al., 2017). The effect of the noise should be evaluated about connectivity between the resting-state and the movie-watching in the following studies. (2) In this study, the subject studied were mostly between 22 and 35 years of age and did not cover the entire life span. It is quite possible, as has been shown in recent papers, that there are differences in sFC and dFC as the age range is increased and across gender (Jiang et al., 2020; Wen et al., 2020; Sen and Parhi, 2021; Snyder et al., 2021; Di and Biswal, 2022). Thus, it is quite possible that as a greater age range is used the systematic differences of the spatiotemporal characteristic of FC may be present. (3) Whether parametric method is better than

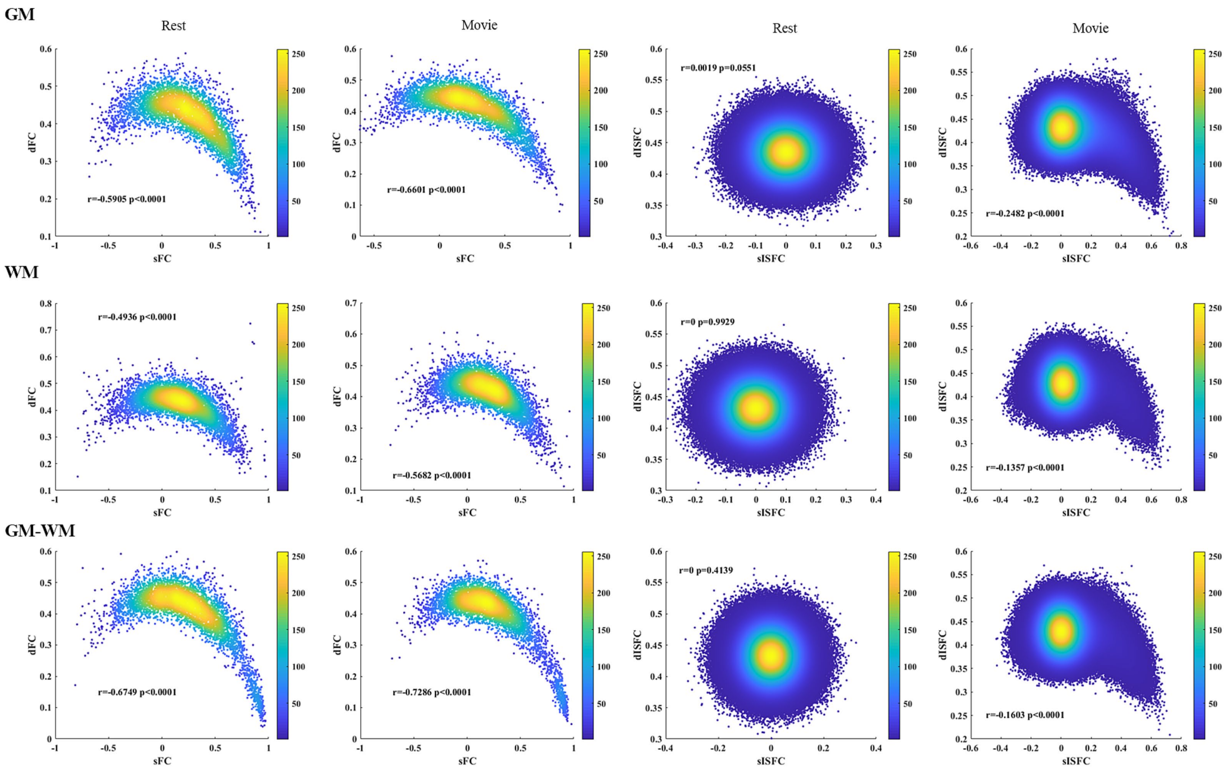

FIGURE 10
Heat maps of the resting-state and the movie-watching between sFC and dFC and between sISFC and dISFC in GM, WM, and GM-WM. Pearson correlation coefficients were performed between sFC and dFC as well as between sISFC and dISFC. The densities were evaluated based on these correlation coefficients by using circles method.

nonparametric method for ISFC, and whether the influence between ROIs or networks of different subject should be consider in the parametric statistics, they are needed to be clarified in the future studies. (4) As the FC metrics were calculated based on data obtained from Caucasian populations, therefore there is potential influence when performing same calculations to Chinese populations (or other ethnic populations). Ge and colleges have studied the influence of populations about brain function between Chinese and people living in Western countries that from HCP dataset, and found that the corresponding large-scale brain parcellations were highly reproducible across the two datasets, with the language processing task showing the largest differences (Ge et al., 2022). However, whether ISFC will be influenced by populations, it need to be clarified in the further. Also, we did not focus on gender differences, thus FC may show variations after regressing them. (5) As some windows spanned two different runs, there is a potential effect about dFC and dISFC values.

5. Conclusion

This study investigated the effect of naturalistic viewing for whole-brain FC and ISFC, including sFC, dFC, sISFC, and dISFC compared with the resting-state. And we also evaluated the reliability of FC and ISFC in two conditions. Moreover, we explored the associations between static and dynamic properties and the associations between the naturalistic and the resting-state conditions. Specifically, the movie-watching not only improved FC values of inter- and intra-networks, but the decrease also exited. Besides, ISFC was enhanced generally under the naturalistic viewing. In this study, we did not find any ROI or network passed statistics of SWB for ISFC. The naturalistic paradigm generally enhanced reliabilities of sFC, dFC, sISFC, and dISFC compared with the resting-state, especially for sISFC and dISFC. Finally, the resting-state was positive correlation with the naturalistic viewing for sFC and dFC. Furthermore, sFC had negative correlation with dFC under the resting-state and the movie-watching. sISFC also showed relatively weak negative correlation with dISFC in the naturalistic viewing. As there was no significant ISFC and the range of ISFC values was small, the movie-watching has limit improvement for ISFC in this study.

Data availability statement

The original contributions presented in the study are included in the article/Supplementary material, further inquiries can be directed to the corresponding authors.

Ethics statement

The studies involving humans were approved by Washington University—University of Minnesota Consortium of the

Human Connectome Project. The studies were conducted in accordance with the local legislation and institutional requirements. Written informed consent for participation in this study was provided by the participants' legal guardians/next of kin. Written informed consent was obtained from the individual(s), and minor(s)' legal guardian/next of kin, for the publication of any potentially identifiable images or data included in this article.

Author contributions

PH designed the study and wrote the original draft. PH, PW, RZ, and HY conducted the data analysis. PW and BB reviewed and edited the manuscript. All authors contributed to the article and approved the submitted version.

Funding

This work was supported by the China MOST2030 Brain Project No. 2022ZD0208500 and National Natural Science Foundation of China (grant numbers 61871420 and 62171101).

Conflict of interest

The authors declare that the research was conducted in the absence of any commercial or financial relationships that could be construed as a potential conflict of interest.

Publisher's note

Supplementary material

The Supplementary material for this article can be found online at: https://www.frontiersin.org/articles/10.3389/fnins.2023.1248610/full#supplementary-material

References

Aertsen, A. M. H. J., Gerstein, G. L., Habib, M. K., and Palm, G. (1989). Dynamics of neuronal firing correlation: modulation of "effective connectivity.". *J. Neurophysiol.* 61, 900–917. doi: 10.1152/jn.1989.61.5.900

Allen, E. A., Damaraju, E., Plis, S. M., Erhardt, E. B., Eichele, T., and Calhoun, V. D. (2014). Tracking whole-brain connectivity dynamics in the resting state. *Cereb. Cortex* 24, 663–676. doi: 10.1093/cercor/bhs352

Arai, K., and Lo, E. H. (2009). Oligovascular signaling in white matter stroke. *Biol. Pharm. Bull.* 32, 1639–1644. doi: 10.1248/bpb.32.1639

Biswal, B., Zerrin Yetkin, F., Haughton, V. M., and Hyde, J. S. (1995). Functional connectivity in the motor cortex of resting human brain using echo-planar MRI. *Magn. Reson. Med.* 34, 537–541. doi: 10.1002/mrm.1910340409

Bolton, T. A. W., Freitas, L. G. A., Jochaut, D., Giraud, A. L., and Van De Ville, D. (2020). Neural responses in autism during movie watching: inter-individual response variability co-varies with symptomatology. *Neuroimage* 216:116571. doi: 10.1016/j.neuroimage.2020.116571

Bolton, T. A. W., Jochaut, D., Giraud, A. L., and Van De Ville, D. (2019). Dynamic inter-subject functional connectivity reveals moment-to-moment brain network configurations driven by continuous or communication paradigms. *J. Vis. Exp.* 2019:e59083. doi: 10.3791/59083

Cantlon, J. F., and Li, R. (2013). Neural activity during natural viewing of sesame street statistically predicts test scores in early childhood. *PLoS Biol.* 11:e1001462. doi: 10.1371/journal.pbio.1001462

Cerliani, L., Bhandari, R., De Angelis, L., van der Zwaag, W., Bazin, P. L., Gazzola, V., et al. (2022). Predictive coding during action observation – a depth-resolved intersubject functional correlation study at 7T. *Cortex* 148, 121–138. doi: 10.1016/j.cortex.2021.12.008

Chang, C., Cunningham, J. P., and Glover, G. H. (2009). Influence of heart rate on the BOLD signal: the cardiac response function. *Neuroimage* 44, 857–869. doi: 10.1016/j.neuroimage.2008.09.029

Chao-Gan, Y., and Yu-Feng, Z. (2010). DPARSF: a MATLAB toolbox for "pipeline" data analysis of resting-state fMRI. *Front. Syst. Neurosci.* 4, 1–7. doi: 10.3389/fnsys.2010.00013

Chen, G., Shin, Y. W., Taylor, P. A., Glen, D. R., Reynolds, R. C., Israel, R. B., et al. (2016). Untangling the relatedness among correlations, part I: nonparametric approaches to inter-subject correlation analysis at the group level. *Neuroimage* 142, 248–259. doi: 10.1016/j.neuroimage.2016.05.023

Chen, G., Taylor, P. A., Qu, X., Molfese, P. J., Bandettini, P. A., Cox, R. W., et al. (2020). Untangling the relatedness among correlations, part III: inter-subject correlation analysis through Bayesian multilevel modeling for naturalistic scanning. *Neuroimage* 216:116474. doi: 10.1016/j.neuroimage.2019.116474

Chen, G., Taylor, P. A., Shin, Y. W., Reynolds, R. C., and Cox, R. W. (2017). Untangling the relatedness among correlations, part II: inter-subject correlation group analysis through linear mixed-effects modeling. *Neuroimage* 147, 825–840. doi: 10.1016/j.neuroimage.2016.08.029

Chen, Y. L., Tu, P. C., Huang, T. H., Bai, Y. M., Su, T. P., Chen, M. H., et al. (2020). Using minimal-redundant and maximal-relevant whole-brain functional connectivity to classify bipolar disorder. *Front. Neurosci.* 14, 1–13. doi: 10.3389/fnins.2020.563368

Cole, M. W., Bassett, D. S., Power, J. D., Braver, T. S., and Petersen, S. E. (2014). Intrinsic and task-evoked network architectures of the human brain. *Neuron* 83, 238–251. doi: 10.1016/j.neuron.2014.05.014

Cordes, D., Haughton, V. M., Arfanakis, K., Wendt, G. J., Turski, P. A., Moritz, C. H., et al. (2000). Mapping functionally related regions of brain with functional connectivity MR imaging. *Am. J. Neuroradiol.* 21, 1636–1644.

Córdova-Palomera, A., Kaufmann, T., Persson, K., Alnæs, D., Doan, N. T., Moberget, T., et al. (2017). Disrupted global metastability and static and dynamic brain connectivity across individuals in the Alzheimer's disease continuum. *Sci. Rep.* 7, 1–14. doi: 10.1038/srep40268

Craddock, R. C., James, G. A., Holtzheimer, P. E., Hu, X. P., and Mayberg, H. S. (2012). A whole brain fMRI atlas generated via spatially constrained spectral clustering. *Hum. Brain Mapp.* 33, 1914–1928. doi: 10.1002/hbm.21333

Demirci, O., Stevens, M. C., Andreasen, N. C., Michael, A., Liu, J., White, T., et al. (2009). Investigation of relationships between fMRI brain networks in the spectral domain using ICA and granger causality reveals distinct differences between schizophrenia patients and healthy controls. *Neuroimage* 46, 419–431. doi: 10.1016/j.neuroimage.2009.02.014

Dennis, E. L., and Thompson, P. M. (2014). Functional brain connectivity using fMRI in aging and Alzheimer's disease. *Neuropsychol. Rev.* 24, 49–62. doi: 10.1007/s11065-014-9249-6

Di, X., and Biswal, B. B. (2020). Intersubject consistent dynamic connectivity during natural vision revealed by functional MRI. *Neuroimage* 216:116698. doi: 10.1016/j.neuroimage.2020.116698

Di, X., and Biswal, B. B. (2022). Principal component analysis reveals multiple consistent responses to naturalistic stimuli in children and adults. *Hum. Brain Mapp.* 43, 3332–3345. doi: 10.1002/hbm.25568

Dosenbach, N. U. F., Nardos, B., Cohen, A. L., Fair, D. A., Power, J. D., Church, J. A., et al. (2010). Prediction of individual brain maturity using fMRI. *Science* 329, 1358–1361. doi: 10.1126/science.1194144

Fan, Y. S., Li, Z., Duan, X., Xiao, J., Guo, X., Han, S., et al. (2020). Impaired interactions among white-matter functional networks in antipsychotic-naive first-episode schizophrenia. *Hum. Brain Mapp.* 41, 230–240. doi: 10.1002/hbm.24801

Finn, E. S., and Bandettini, P. A. (2021). Movie-watching outperforms rest for functional connectivity-based prediction of behavior. *Neuroimage* 235:117963. doi: 10.1016/j.neuroimage.2021.117963

Finn, E. S., Shen, X., Scheinost, D., Rosenberg, M. D., Huang, J., Chun, M. M., et al. (2015). Functional connectome fingerprinting: identifying individuals using patterns of brain connectivity. *Nat. Neurosci.* 18, 1664–1671. doi: 10.1038/nn.4135

Fong, A. H. C., Yoo, K., Rosenberg, M. D., Zhang, S., Li, C. S. R., Scheinost, D., et al. (2019). Dynamic functional connectivity during task performance and rest predicts individual differences in attention across studies. *Neuroimage* 188, 14–25. doi: 10.1016/j.neuroimage.2018.11.057

Friston, K. J., Frith, C. D., Liddle, P. F., and Frackowiak, R. S. J. (1993). Functional connectivity: the principal-component analysis of large (PET) data sets. *J. Cereb. Blood Flow Metab.* 13, 5–14. doi: 10.1038/jcbfm.1993.4

Friston, K. J., Williams, S., Howard, R., Frackowiak, R. S. J., and Turner, R. (1996). Movement-related effects in fMRI time-series. *Magn. Reson. Med.* 35, 346–355. doi: 10.1002/mrm.1910350312

Ge, J., Yang, G., Han, M., Zhou, S., Men, W., Qin, L., et al. (2022). Increasing diversity in connectomics with the Chinese human connectome project. *Nat. Neurosci.* 26, 163–172. doi: 10.1038/s41593-022-01215-1

Gratton, C., Laumann, T. O., Gordon, E. M., Adeyemo, B., and Petersen, S. E. (2016). Evidence for two independent factors that modify brain networks to meet task goals. *Cell Rep.* 17, 1276–1288. doi: 10.1016/j.celrep.2016.10.002

Greene, D. J., Koller, J. M., Hampton, J. M., Wesevich, V., Van, A. N., Nguyen, A. L., et al. (2018). Behavioral interventions for reducing head motion during MRI scans in children. *Neuroimage* 171, 234–245. doi: 10.1016/j.neuroimage.2018.01.023

Greicius, M. D., Krasnow, B., Reiss, A. L., and Menon, V. (2003). Functional connectivity in the resting brain: a network analysis of the default mode hypothesis. *Proc. Natl. Acad. Sci. U. S. A.* 100, 253–258. doi: 10.1073/pnas.0135058100

Harris, J. J., and Attwell, D. (2012). The energetics of CNS white matter. *J. Neurosci.* 32, 356–371. doi: 10.1523/JNEUROSCI.3430-11.2012

Hasson, U., Nir, Y., Levy, I., Fuhrmann, G., and Malach, R. (2004). Intersubject synchronization of cortical activity during natural vision. *Science* 303, 1634–1640. doi: 10.1126/science.1089506

Huijbers, W., Van Dijk, K. R. A., Boenniger, M. M., Stirnberg, R., and Breteler, M. M. B. (2017). Less head motion during MRI under task than resting-state conditions. *Neuroimage* 147, 111–120. doi: 10.1016/j.neuroimage.2016.12.002

Hutchison, R. M., Womelsdorf, T., Allen, E. A., Bandettini, P. A., Calhoun, V. D., Corbetta, M., et al. (2013). Dynamic functional connectivity: promise, issues, and interpretations. *Neuroimage* 80, 360–378. doi: 10.1016/j.neuroimage.2013.05.079

Jefferys, J. G. R., Jiruska, P., de Curtis, M., and Avoli, M. (2012). "Limbic network synchronization and temporal lobe epilepsy," in *Jasper's basic mechanisms of the epilepsies [Internet]. 4th edn*. Eds. J. L. Noebels, M. Avoli and M. A. Rogawski (Bethesda (MD): National Center for Biotechnology Information (US)).

Ji, F., Pasternak, O., Ng, K. K., Chong, J. S. X., Liu, S., Zhang, L., et al. (2019). White matter microstructural abnormalities and default network degeneration are associated with early memory deficit in Alzheimer's disease continuum. *Sci. Rep.* 9, 4749–4711. doi: 10.1038/s41598-019-41363-2

Ji, G. J., Ren, C., Li, Y., Sun, J., Liu, T., Gao, Y., et al. (2019). Regional and network properties of white matter function in Parkinson's disease. *Hum. Brain Mapp.* 40, 1253–1263. doi: 10.1002/hbm.24444

Jiang, R., Calhoun, V. D., Fan, L., Zuo, N., Jung, R., Qi, S., et al. (2020). Gender differences in connectome-based predictions of individualized intelligence quotient and sub-domain scores. *Cereb. Cortex* 30, 888–900. doi: 10.1093/cercor/bhz134

Jiang, Y., Luo, C., Li, X., Li, Y., Yang, H., Li, J., et al. (2019). White-matter functional networks changes in patients with schizophrenia. *Neuroimage* 190, 172–181. doi: 10.1016/J.NEUROIMAGE.2018.04.018

Jie, B., Liu, M., and Shen, D. (2018). Integration of temporal and spatial properties of dynamic connectivity networks for automatic diagnosis of brain disease. *Med. Image Anal.* 47, 81–94. doi: 10.1016/j.media.2018.03.013

Jones, D. T., Vemuri, P., Murphy, M. C., Gunter, J. L., Senjem, M. L., Machulda, M. M., et al. (2012). Non-stationarity in the "resting brain's" modular architecture. *PloS One* 7:e39731. doi: 10.1371/journal.pone.0039731

Kim, J., Criaud, M., Cho, S. S., Díez-Cirarda, M., Mihaescu, A., Coakeley, S., et al. (2017). Abnormal intrinsic brain functional network dynamics in Parkinson's disease. *Brain* 140, 2955–2967. doi: 10.1093/brain/awx233

Krienen, F. M., Thomas Yeo, B. T., and Buckner, R. L. (2014). Reconfigurable task-dependent functional coupling modes cluster around a core functional architecture. *Philos. Trans. R. Soc. B Biol. Sci.* 369:20130526. doi: 10.1098/rstb.2013.0526

Lahnakoski, J. M., Glerean, E., Salmi, J., Jääskeläinen, I. P., Sams, M., Hari, R., et al. (2012). Naturalistic fMRI mapping reveals superior temporal sulcus as the hub for the distributed brain network for social perception. *Front. Hum. Neurosci.* 6, 1–14. doi: 10.3389/fnhum.2012.00233

Leonardi, N., and Van De Ville, D. (2015). On spurious and real fluctuations of dynamic functional connectivity during rest. *Neuroimage* 104, 430–436. doi: 10.1016/j.neuroimage.2014.09.007

Liu, A., Lin, S. J., Mi, T., Chen, X., Chan, P., Wang, Z. J., et al. (2018). Decreased subregional specificity of the putamen in Parkinson's disease revealed by dynamic connectivity-derived parcellation. *NeuroImage Clin.* 20, 1163–1175. doi: 10.1016/j.nicl.2018.10.022

Lowe, M. J., Mock, B. J., and Sorenson, J. A. (1998). Functional connectivity in single and multislice echoplanar imaging using resting-state fluctuations. *Neuroimage* 7, 119–132. doi: 10.1006/nimg.1997.0315

Lowther, E. R., O'Brien, J. T., Firbank, M. J., and Blamire, A. M. (2014). Lewy body compared with Alzheimer dementia is associated with decreased functional connectivity in resting state networks. *Psychiatry Res. Neuroimaging* 223, 192–201. doi: 10.1016/j.pscychresns.2014.06.004

Lynch, L. K., Lu, K. H., Wen, H., Zhang, Y., Saykin, A. J., and Liu, Z. (2018). Task-evoked functional connectivity does not explain functional connectivity differences between rest and task conditions. *Hum. Brain Mapp.* 39, 4939–4948. doi: 10.1002/hbm.24335

Madhyastha, T. M., Askren, M. K., Boord, P., and Grabowski, T. J. (2015). Dynamic connectivity at rest predicts attention task performance. *Brain Connect.* 5, 45–59. doi: 10.1089/brain.2014.0248

Müller, R., and Büttner, P. (1994). A critical discussion of intraclass correlation coefficients. *Stat. Med.* 13, 2465–2476. doi: 10.1002/sim.4780132310

Nastase, S. A., Gazzola, V., Hasson, U., and Keysers, C. (2019). Measuring shared responses across subjects using intersubject correlation. *Soc. Cogn. Affect. Neurosci.* 14, 667–685. doi: 10.1093/scan/nsz037

Patanaik, A., Tandi, J., Ong, J. L., Wang, C., Zhou, J., and Chee, M. W. L. (2018). Dynamic functional connectivity and its behavioral correlates beyond vigilance. *Neuroimage* 177, 1–10. doi: 10.1016/j.neuroimage.2018.04.049

Peer, M., Nitzan, M., Bick, A. S., Levin, N., and Arzy, S. (2017). Evidence for functional networks within the human brain's white matter. *J. Neurosci.* 37, 6394–6407. doi: 10.1523/JNEUROSCI.3872-16.2017

Peraza, L. R., Kaiser, M., Firbank, M., Graziadio, S., Bonanni, L., Onofrj, M., et al. (2014). FMRI resting state networks and their association with cognitive fluctuations in dementia with Lewy bodies. *NeuroImage Clin.* 4, 558–565. doi: 10.1016/j.nicl.2014.03.013

Plitta, M., Barnes, K. A., Wallace, G. L., Kenworthy, L., and Martin, A. (2015). Resting-state functional connectivity predicts longitudinal change in autistic traits and adaptive functioning in autism. *Proc. Natl. Acad. Sci. U. S. A.* 112, E6699–E6706. doi: 10.1073/pnas.1510098112

Power, J. D., Barnes, K. A., Snyder, A. Z., Schlaggar, B. L., and Petersen, S. E. (2012). Spurious but systematic correlations in functional connectivity MRI networks arise from subject motion. *Neuroimage* 59, 2142–2154. doi: 10.1016/j.neuroimage.2011.10.018

Ptak, R., and Schnider, A. (2010). The dorsal attention network mediates orienting toward behaviorally relevant stimuli in spatial neglect. *J. Neurosci.* 30, 12557–12565. doi: 10.1523/JNEUROSCI.2722-10.2010

Qin, J., Chen, S. G., Hu, D., Zeng, L. L., Fan, Y. M., Chen, X. P., et al. (2015). Predicting individual brain maturity using dynamic functional connectivity. *Front. Hum. Neurosci.* 9:418. doi: 10.3389/FNHUM.2015.00418/BIBTEX

Ren, Y., Nguyen, V. T., Guo, L., and Guo, C. C. (2017). Inter-subject functional correlation reveal a hierarchical Organization of Extrinsic and Intrinsic Systems in the brain. *Sci. Rep.* 7, 1–12. doi: 10.1038/s41598-017-11324-8

Sanchez-Alonso, S., Rosenberg, M. D., and Aslin, R. N. (2021). Functional connectivity patterns predict naturalistic viewing versus rest across development. *Neuroimage* 229:117630. doi: 10.1016/j.neuroimage.2020.117630

Sastry, N. C., Roy, D., and Banerjee, A. (2022). Stability of sensorimotor network sculpts the dynamic repertoire of resting state over lifespan. *Cereb. Cortex* 33, 1246–1262. doi: 10.1093/cercor/bhac133

Satterthwaite, T. D., Elliott, M. A., Gerraty, R. T., Ruparel, K., Loughead, J., Calkins, M. E., et al. (2013). An improved framework for confound regression and filtering for control of motion artifact in the preprocessing of resting-state functional connectivity data. *Neuroimage* 64, 240–256. doi: 10.1016/j.neuroimage.2012.08.052

Sen, B., and Parhi, K. K. (2021). Predicting biological gender and intelligence from fMRI via dynamic functional connectivity. *I.E.E.E. Trans. Biomed. Eng.* 68, 815–825. doi: 10.1109/TBME.2020.3011363

Simony, E., Honey, C. J., Chen, J., Lositsky, O., Yeshurun, Y., Wiesel, A., et al. (2016). Dynamic reconfiguration of the default mode network during narrative comprehension. *Nat. Commun.* 7, 1–13. doi: 10.1038/ncomms12141

Snyder, W., Uddin, L. Q., and Nomi, J. S. (2021). Dynamic functional connectivity profile of the salience network across the life span. *Hum. Brain Mapp.* 42, 4740–4749. doi: 10.1002/hbm.25581

Su, H., Young, C. B., Han, Z. R., Xu, J., and Xiong, B. (2022). Brain-to-brain concordance in child-parent dyads underlies children' s psychological wellbeing. bioRxiv [Preprint], 1–32.

Tang, C., Huang, Z., Zhou, S., Wang, Q., Yi, F., and Nie, J. (2019). Movie-watching fMRI reveals inter-subject synchrony alteration in functional brain activity in ADHD. *Lect. Notes Comput. Sci.* 11849, 104–111. doi: 10.1007/978-3-030-35817-4_13

Teo, P. C., Sapiro, G., and Wandell, B. A. (1997). Creating connected representations of cortical gray matter for functional MRI visualization. *IEEE Trans. Med. Imaging* 16, 852–863. doi: 10.1109/42.650881

Tian, L., Ye, M., Chen, C., Cao, X., and Shen, T. (2021). Consistency of functional connectivity across different movies. *Neuroimage* 233:117926. doi: 10.1016/j.neuroimage.2021.117926

Vanderwal, T., Eilbott, J., and Castellanos, F. X. (2019). Movies in the magnet: naturalistic paradigms in developmental functional neuroimaging. *Dev. Cogn. Neurosci.* 36:100600. doi: 10.1016/j.dcn.2018.10.004

Vanderwal, T., Eilbott, J., Finn, E. S., Craddock, R. C., Turnbull, A., and Castellanos, F. X. (2017). Individual differences in functional connectivity during naturalistic viewing conditions. *Neuroimage* 157, 521–530. doi: 10.1016/j.neuroimage.2017.06.027

Vanderwal, T., Kelly, C., Eilbott, J., Mayes, L. C., and Castellanos, F. X. (2015). Inscapes: A movie paradigm to improve compliance in functional magnetic resonance imaging. *Neuroimage* 122, 222–232. doi: 10.1016/j.neuroimage.2015.07.069

Villa, L. M., Goodyer, I. M., Tait, R., Kelvin, R., Reynolds, S., Wilkinson, P. O., et al. (2020). Cognitive behavioral therapy may have a rehabilitative, not normalizing, effect on functional connectivity in adolescent depression. *J. Affect. Disord.* 268, 1–11. doi: 10.1016/j.jad.2020.01.103

Wang, P., Meng, C., Yuan, R., Wang, J., Yang, H., Zhang, T., et al. (2020). The Organization of the Human Corpus Callosum Estimated by intrinsic functional connectivity with White-matter functional networks. *Cereb. Cortex* 30, 3313–3324. doi: 10.1093/cercor/bhz311

Wang, J., Ren, Y., Hu, X., Nguyen, V. T., Guo, L., Han, J., et al. (2017). Test–retest reliability of functional connectivity networks during naturalistic fMRI paradigms. *Hum. Brain Mapp.* 38, 2226–2241. doi: 10.1002/hbm.23517

Wang, P., Wang, J., Michael, A., Wang, Z., Klugah-Brown, B., Meng, C., et al. (2021). White matter functional connectivity in resting-state fMRI: robustness, reliability, and relationships to Gray matter. *Cereb. Cortex* 32, 1547–1559. doi: 10.1093/cercor/bhab181

Wen, X., He, H., Dong, L., Chen, J., Yang, J., Guo, H., et al. (2020). Alterations of local functional connectivity in lifespan: a resting-state fMRI study. *Brain Behav.* 10, 1–10. doi: 10.1002/brb3.1652

Wong, W. W., Cabral, J., Rane, R., Ly, R., Kringelbach, M. L., and Feusner, J. D. (2021). Effects of visual attention modulation on dynamic functional connectivity during own-face viewing in body dysmorphic disorder. *Neuropsychopharmacology* 46, 2030–2038. doi: 10.1038/s41386-021-01039-w

Xie, H., and Redcay, E. (2022). A tale of two connectivities: Intra- and inter-subject functional connectivity jointly enable better prediction of social abilities. bioRxiv [Preprint], 1–17.

Yang, M., He, H., Duan, M., Chen, X., Chang, X., Lai, Y., et al. (2018). The effects of music intervention on functional connectivity strength of the brain in schizophrenia. *Neural Plast.* 2018, 1–10. doi: 10.1155/2018/2821832

Zhang, C., Baum, S. A., Adduru, V. R., Biswal, B. B., and Michael, A. M. (2018a). Test-retest reliability of dynamic functional connectivity in resting state fMRI. *Neuroimage* 183, 907–918. doi: 10.1016/j.neuroimage.2018.08.021

Zhang, C., Cahill, N. D., Arbabshirani, M. R., White, T., Baum, S. A., and Michael, A. M. (2016). Sex and age effects of functional connectivity in early adulthood. *Brain Connect.* 6, 700–713. doi: 10.1089/brain.2016.0429

Zhang, C., Dougherty, C. C., Baum, S. A., White, T., and Michael, A. M. (2018b). Functional connectivity predicts gender: evidence for gender differences in resting brain connectivity. *Hum. Brain Mapp.* 39, 1765–1776. doi: 10.1002/hbm.23950

Zhang, X., Liu, J., Yang, Y., Zhao, S., Guo, L., Han, J., et al. (2021). Test–retest reliability of dynamic functional connectivity in naturalistic paradigm functional magnetic resonance imaging. *Hum. Brain Mapp.* 43, 1463–1476. doi: 10.1002/hbm.25736

Zhang, K., and Sejnowski, T. J. (2000). A universal scaling law between gray matter and white matter of cerebral cortex. *Proc. Natl. Acad. Sci. U. S. A.* 97, 5621–5626. doi: 10.1073/pnas.090504197

frontiers | Frontiers in Neuroscience

TYPE Review
PUBLISHED 20 February 2024
DOI 10.3389/fnins.2024.1340345

OPEN ACCESS

EDITED BY
Xi-Nian Zuo,
Beijing Normal University, China

REVIEWED BY
James Mac Shine,
The University of Sydney, Australia
Aniruddha Das,
Cleveland Clinic, United States

*CORRESPONDENCE
Simoni Helena Avansini
✉ simoni.avansini@lnbio.cnpem.br

†These authors have contributed equally to this work and share last authorship

RECEIVED 17 November 2023
ACCEPTED 29 January 2024
PUBLISHED 20 February 2024

CITATION
Caznok Silveira AC, Antunes ASLM, Athié MCP, da Silva BF, Ribeiro dos Santos JV, Canateli C, Fontoura MA, Pinto A, Pimentel-Silva LR, Avansini SH and de Carvalho M (2024) Between neurons and networks: investigating mesoscale brain connectivity in neurological and psychiatric disorders. *Front. Neurosci.* 18:1340345.
doi: 10.3389/fnins.2024.1340345

Between neurons and networks: investigating mesoscale brain connectivity in neurological and psychiatric disorders

Ana Clara Caznok Silveira[1,2],
Andre Saraiva Leão Marcelo Antunes[1],
Maria Carolina Pedro Athié[1], Bárbara Filomena da Silva[1],
João Victor Ribeiro dos Santos[1], Camila Canateli[1],
Marina Alves Fontoura[1], Allan Pinto[3],
Luciana Ramalho Pimentel-Silva[4], Simoni Helena Avansini[1*†]
and Murilo de Carvalho[1,3†]

[1]National Laboratory of Biosciences, Brazilian Center for Research in Energy and Materials, Campinas, Brazil, [2]School of Electrical and Computer Engineering, University of Campinas, Campinas, Brazil, [3]Brazilian Synchrotron Light Laboratory, Brazilian Center for Research in Energy and Materials, Campinas, Brazil, [4]Neuroimaging Laboratory, Neurology Department, University of Campinas, School of Medical Sciences, Campinas, Brazil

The study of brain connectivity has been a cornerstone in understanding the complexities of neurological and psychiatric disorders. It has provided invaluable insights into the functional architecture of the brain and how it is perturbed in disorders. However, a persistent challenge has been achieving the proper spatial resolution, and developing computational algorithms to address biological questions at the multi-cellular level, a scale often referred to as the mesoscale. Historically, neuroimaging studies of brain connectivity have predominantly focused on the macroscale, providing insights into inter-regional brain connections but often falling short of resolving the intricacies of neural circuitry at the cellular or mesoscale level. This limitation has hindered our ability to fully comprehend the underlying mechanisms of neurological and psychiatric disorders and to develop targeted interventions. In light of this issue, our review manuscript seeks to bridge this critical gap by delving into the domain of mesoscale neuroimaging. We aim to provide a comprehensive overview of conditions affected by aberrant neural connections, image acquisition techniques, feature extraction, and data analysis methods that are specifically tailored to the mesoscale. We further delineate the potential of brain connectivity research to elucidate complex biological questions, with a particular focus on schizophrenia and epilepsy. This review encompasses topics such as dendritic spine quantification, single neuron morphology, and brain region connectivity.

We aim to showcase the applicability and significance of mesoscale neuroimaging techniques in the field of neuroscience, highlighting their potential for gaining insights into the complexities of neurological and psychiatric disorders.

KEYWORDS

connectivity, mesoscale, NeuroImage, schizophrenia, epilepsy, computer vision, segmentation, deep learning

1 Introduction

The human brain is a remarkably intricate network composed of billions of neurons, encompassing diverse cell types interconnected through trillions of synapses (Luo et al., 2008). Different brain regions exhibit distinct microstructural architectures, functional specializations, interconnectivity, and often an orderly topographic arrangement. The major task in connectivity-related research is capturing the hierarchical multiscale organization of the brain by mapping network relationships across various spatial dimensions (Sporns, 2013). It extends beyond structural considerations and encompasses functionality, denoted by the degree of correlation and covariance among brain signals, influenced by both experimental parameters and temporal context (Cabral et al., 2017).

The organization of brain connections plays a pivotal role in shaping interactions between different brain areas, giving rise to a multitude of functional networks. Structural data provide the anatomical framework, while functional data reveal how different brain regions work together and respond to various stimuli or tasks. The multimodal correlation of imaging techniques, integrating both structural and functional neuroimaging methods, allows the harnessing of their best features, offering a broader approach and better understanding of brain connectivity (Howard et al., 2023). This multidimensional approach is essential for advancing our knowledge of complex neurological and cognitive processes (Hirsch et al., 2015).

Multiple, albeit subtle, non-physiological shifts in brain organization likely lead to network disorders which encompass a wide range of neurological and psychiatric conditions arising from aberrant neural connections. These include autism spectrum, schizophrenia, attention-deficit/hyperactivity, epilepsy, depression, and anxiety disorders (Kaiser, 2013; Contreras-Rodríguez et al., 2015; Holmes et al., 2023).

Most of the data used to reconstruct brain networks comes from bidimensional (2D) images. However, the correlation between a single cell interacting with the whole neuronal tissue in a tridimensional (3D) manner remains an open problem. This 3D spatial-scale context holds the key to bridging morphological mechanisms and functional outcomes to better understand the complexities of brain connectivity-related disorders. The complex 3D circuits that define brain connectivity comprise a variety of organizational structures and microarchitectures that can be arduous to discern (Sporns et al., 2005), presenting a significant challenge in the field of neuroscience and computational analysis. Additionally, to preserve the volumetric information of the network it can be necessary to work with samples as thick as possible coupling to 3D-imaging techniques, as extensively applied in image-based neuroresearch and diagnosis (Kim et al., 2021).

The brain connectome *sensu* (Sporns et al., 2005) takes on different definitions at various scales, presenting a defying task in translating morphological and functional measurements to the symptoms of brain disorders affected by connectivity. Understanding integrated brain function demands a multitude of measurements across various scales. Neurophysiological and neuroimaging methods, along with the use of whole-brain models to provide fresh insights into its underlying mechanisms (Hallett et al., 2020). Thus, brain connectivity conventionally encompasses three scales: nano/microscale, mesoscale, and macroscale (Bohland et al., 2009), each one with its optimized imaging method (**Figure 1**).

At the nano/microscale, lies the ultrastructural information, that can reveal synaptic morphology, their components and connections in individual cells, often employing Electron Microscopy (EM), demanding sample chemical preservation and physical sectioning. The opposite extreme encompasses the macroscale, which examines the anatomical and connective patterns between distinct brain regions, such as long-range connections, often inferred from fiber tracts, and frequently revealed by techniques also capable of retrieving functional aspects, such as Magnetic Resonance Imaging (MRI), Positron Emission Tomography (PET), Single Photon Emission Computed Tomography (SPECT). These approaches prove particularly valuable for non-invasive studies of living tissues (Bennett et al., 2018).

Between both spatial extremities lies the multi-cellular level (Mitra, 2014), also known as the mesoscale, which plays a pivotal role in the investigation of the intricate network of the brain. Mesoscale spans from the structural and functional properties of single neurons to local neural circuits and their intrinsic connectivity (Mitra, 2014; Haueis, 2021).

Most neuroimaging studies on humans and human samples have primarily used macroscale techniques like PET and functional magnetic resonance imaging (fMRI) for *in vivo* imaging, and microscale techniques such as thin-depth light microscopy for tissue samples. Although substantial insights into brain networks and abnormal connectivity have been acquired using these techniques, they lack the spatial resolution needed to resolve the 3D conformation of local neuronal connections (Tyson and Margrie, 2022). Consequently, further progress in the understanding of brain functions within complex neuronal circuits requires exploration at the mesoscale level (Rah et al., 2015). It depicts

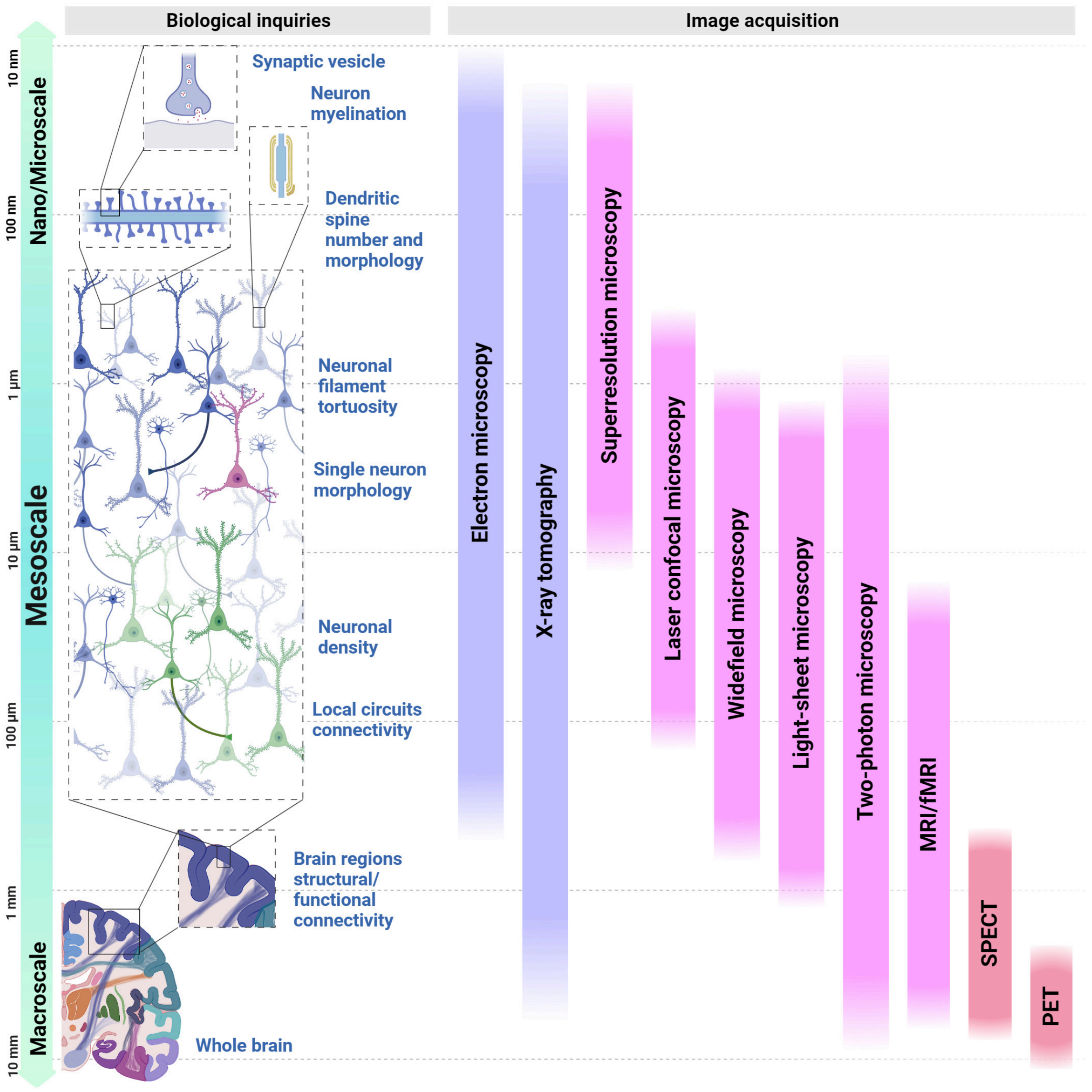

FIGURE 1
Overview of experimental bioimage tools currently available for studying neural connectivity across a range of spatial scales and biological questions. At the left, different human brain organization structures are presented under the perspective of spatial scales: from the study of the dendritic spine **(top)** to the whole brain **(bottom)**, with a focus on the structures that can be studied using mesoscale imaging. From the **top** to the **bottom**, spatial scales range from 10 nanometers to 10 millimeters. The second section, denoted Biological Inquiries, displays the cellular elements that contribute and shape neural connectivity across the different scales, followed by a repertoire of image acquisition techniques displayed as vertical bars in the last section. Purple bars represent techniques suited to structural imaging while the pink bars represent the ones suited for functional purposes; lastly, the red bars represent techniques that incorporate both. MRI, magnetic resonance imaging; fMRI, functional magnetic resonance Imaging; SPECT, single photon emission computed tomography; PET, positron emission tomography.

connections, networks, and spatial cellular gradients of distinct neuronal populations, improving resolution and the analysis of interactions that form the basis of cognitive and behavioral processes (Haueis, 2021). Intact/live samples can be used, albeit sample preparation is necessary according to the specific imaging technique. Optical microscopies (wide field, laser confocal, light sheet, and two-photons) allow both high spatial and temporal resolution, often used to study live cells.

In this landscape, data acquisition and image processing emerge as a critical domain of local neural circuits, i.e., spatially co-localized neurons of the same kind or with shared organizational traits (Bohland et al., 2009). It also generates a huge amount of data to be processed and may not be as easily quantifiable (Lang et al., 2012; Chen et al., 2019). Currently, artificial intelligence algorithms have proved their ability to help researchers in image processing and analysis: from contrast enhancement/normalization to segmentation and extraction of morphological features necessary for structural correlation of connectivity (Durkee et al., 2021).

As stated above, neuroimaging encompasses a diverse array of techniques for exploring different scales of magnitude and activities within cells and tissues. Consequently, data analyses are predominantly linked to the complexities of the images, posing a challenge for neuroscientists who may not be familiar with the intricacies of the field. In this review, we aim to explore mesoscale brain imaging and processing, arranging the main methodologies traditionally used to investigate brain functioning throughout its network. It begins by exploring the state-of-the-art in neurological and psychiatric disorders research and imaging techniques relevant to the field; it then addresses image processing strategies suited to solving these questions. Recent literature was compiled on various imaging modalities to study neural connections and the respective computational methods to identify misorganization in schizophrenia and epilepsy. It also organizes concepts in network neurological disorders to guide non-expert and advanced readers in the field of neuroimaging and processing. Finally, to accommodate the diverse readership in this multidisciplinary field, a **Glossary** tailored to the terminology of some key concepts in neurobiology, imaging, and computational processing is included.

2 Brain connectivity in disorders of the central nervous system

This section explores a selection of connectivity-related issues and the bioimaging techniques employed to address them. Disorders affected by brain connectivity encompass a wide range of neurological and psychiatric conditions arising from aberrant neural connections. These include autism spectrum disorder, schizophrenia, attention-deficit/hyperactivity disorder, epilepsy, depression, and anxiety disorders (Kaiser, 2013; Contreras-Rodríguez et al., 2015; Holmes et al., 2023). Although substantial insights into the network of the brain and abnormal connectivity in these disorders have been gained using macroscale imaging techniques such as MRI and PET, further progress in our understanding requires the exploration at the mesoscale level for increased resolution. In this section, we examine brain connectivity in two different disorders, representing examples from psychiatric and neurological conditions. Our analysis highlights the crucial role of advanced neuroimaging techniques in uncovering the complexities of these conditions. We particularly focus on the potential of mesoscale neuroimaging to further enhance our understanding of their underlying mechanisms.

2.1 Schizophrenia

Schizophrenia is a multifactorial mental condition that impacts over 23 million individuals worldwide. It involves positive symptoms such as delusions and hallucinations, negative symptoms such as reduced motivation and social withdrawal, and cognitive impairment. The pathophysiology of schizophrenia involves molecular and morphological abnormalities within the nervous system, encompassing faulty brain connectivity, altered myelination of brain regions and white matter tracts, as well as abnormal neuronal morphology and defects in neurotransmitter systems (Schultz and Andreasen, 1999; Kahn et al., 2015).

Recent years have witnessed significant advancements in imaging studies, shedding light on the neurobiological basis of schizophrenia. In this section, we delve into the contribution of imaging studies to our understanding of the connectivity basis of the disorder.

2.1.1 Structural and functional brain network abnormalities

Coordinated functioning of multiple brain regions is crucial for normal brain function, encompassing perception, cognition, emotions, and mood responses. A significant amount of evidence points to a dysfunctional local circuitry in schizophrenia in the prefrontal cortex (PFC) and its connections with other brain regions, particularly those associated with the limbic system (Lewis et al., 2005). In the past two decades, numerous studies involving neuroimaging techniques like fMRI have yielded compelling findings indicating abnormal activity within the local prefrontal network and disrupted integration of information processes in the PFC and other brain regions among individuals with schizophrenia (Anticevic et al., 2014, 2015; Hunt et al., 2017). Although the evidence supporting disconnectivity in schizophrenia is robust, understanding its causes is complex, and there is ongoing debate regarding its mechanisms and significance concerning clinical symptoms (Gao W. et al., 2022).

Investigations using fMRI have consistently revealed disrupted connectivity in individuals with schizophrenia, both during resting-state conditions and while engaged in specific cognitive tasks (Garrity et al., 2007; Whitfield-Gabrieli et al., 2009; Sheffield and Barch, 2016; Erdeniz et al., 2017; Godwin et al., 2017). More recently, a meta-analysis and an original article reported consistent changes in local functional connectivity in schizophrenia. It was found that patients showed significantly higher Regional Homogeneity (ReHo) in the bilateral medial superior frontal gyrus, while lower ReHo in the bilateral post-central gyrus, right pre-central gyrus, and right middle occipital gyrus (Cai et al., 2022); and differences in the functional connectivity between the salience network and certain brain regions, including the right inferior and middle temporal gyrus, left caudate, and right pre-central gyrus (Huang H. et al., 2022). These findings suggest that there are consistent aberrant local functional connectivity patterns in schizophrenia.

The assessment of functional connectivity in schizophrenia relies predominantly on fMRI scanning data acquired from adult individuals diagnosed with the disorder. However, due to the dependence of fMRI on hemodynamic fluctuations associated with neural activity, it is unsuitable for capturing rapid transitions in brain functional connectivity configurations with high temporal resolution (Jamadar et al., 2021). Moreover, the spatial resolution of this technique is limited to a millimeter scale. As a result, our comprehension of the cellular mechanisms underlying the aberrant brain functional connectivity observed in schizophrenia remains incomplete.

2.1.2 Neurotransmitter systems

Multiple etiological hypotheses have been proposed to elucidate the abnormal brain connectivity seen in schizophrenia. The dopaminergic hypothesis posits that abnormal dopaminergic neurotransmission contributes to the development and manifestation of schizophrenia (Creese et al., 1976; Toda and Abi-Dargham, 2007). Several lines of evidence support the dopaminergic hypothesis such as alterations in dopamine receptor density and availability in affected individuals revealed by PET and SPECT imaging (Patel et al., 2010). Specifically, an increased number of dopamine D2 receptors has been observed in the limbic striatum. Hyperactivity of D2 receptors in the mesolimbic pathway is thought to contribute to the positive symptoms of schizophrenia (Howes et al., 2009).

The glutamatergic hypothesis was also proposed as an additional perspective on the pathophysiology of schizophrenia (McCutcheon et al., 2020). For instance, decreased glutamate levels have been found in the anterior cingulate cortex and prefrontal cortex, regions implicated in cognitive and emotional processing (Chen et al., 2017). Moreover, PET studies have shown abnormalities in the expression, binding, and availability of glutamate receptors in various brain regions of individuals with schizophrenia (Beck et al., 2021).

It is becoming increasingly evident that the dopaminergic and glutamatergic hypotheses alone fall short of providing a comprehensive explanation for the disorder highlighting the need to consider additional neurochemical systems involved in schizophrenia, such as the GABAergic system (Jahangir et al., 2021). fMRI and PET studies have also provided insights into the altered neural connectivity and network dynamics associated with GABAergic abnormalities in the disorder (Shukla et al., 2019; Marques et al., 2021).

2.1.3 Myelin and white matter tracts

Employing MRI, researchers investigated gray/white-matter contrast in sensory and motor regions of the cortex in schizophrenia revealing reduced myelin in three bilateral sensory and motor regions (Jørgensen et al., 2016). Furthermore, a study employing Diffusion Tensor Imaging (DTI-fMRI) observed significantly lower fractional anisotropy (FA) values in white matter tracts of patients with psychosis compared to healthy controls (Xu et al., 2022). Additionally, the study demonstrated a positive correlation between decreased white matter tract integrity and cognitive performance in patients with psychosis. Electron microscopy of brain tissue from individuals with schizophrenia revealed ultrastructural signs of apoptosis and necrosis in oligodendroglial cells within the cortex and the caudate nucleus with damage to myelin sheath lamellae, and a significant decrease in the nucleus area and volume density of mitochondria (Uranova et al., 2001).

2.1.4 Dendritic pathology

Dendritic spines are the primary sites of excitatory synaptic connections (Papa et al., 1995). As such, alterations to their morphology directly impact the neuronal circuitry within and across multiple brain regions, potentially contributing to the pathogenesis of schizophrenia. Studies on schizophrenia subjects have revealed reductions in dendritic spine density, dendritic arborization and plasticity in several cortical and non-cortical areas (Glantz and Lewis, 2000; Konopaske et al., 2014; MacDonald et al., 2017). By employing confocal microscopy, researchers have investigated the formation, maturation, and pruning of synaptic connections, using *in vitro* models (Sellgren et al., 2019). Studies in human stem cell-derived neural models have revealed increased synapse elimination and significant developmental and connectivity issues, including the abnormal spread of proliferating neural progenitor cells from the ventricular zone to the intermediate and cortical zones (Stachowiak et al., 2017). Interestingly, maturing neurons were found to be abundantly developed in the deeper neural structure (analogous to subcortical regions) but were notably depleted in surface layers (analogous to the cortical region) of schizophrenia neural organoids.

2.2 Epilepsy

Epilepsy is recognized as a network disorder with multifactorial causes, representing a multiscale challenge that includes cellular, network, and systems levels. It encompasses widespread areas that stretch well beyond the pinpointed site of a seizure, displaying distinctive patterns that might be specific to each particular syndrome (Stafstrom and Carmant, 2015). To gain a comprehensive understanding of the mechanisms underlying hyperexcitability in epilepsy, it is essential to highlight two primary epilepsy classifications. The first is *focal epilepsy*, which is characterized by seizures originating from a specific focal onset within one hemisphere of the brain, as determined by clinical patterns or electroencephalogram (EEG) localization. Common examples of focal epilepsy encompass conditions like mesial temporal lobe epilepsy associated or not with hippocampal sclerosis and malformations of cortical development. The second classification, *generalized epilepsy*, is defined by seizures occurring simultaneously in both hemispheres (Fisher, 2017). In this topic, we review the literature on abnormal neural networks and harness the potential of imaging techniques to address critical knowledge gaps in epilepsy-related brain connectivity.

2.2.1 Structural and functional brain network abnormalities

In vivo mapping of the regional distribution of network abnormalities is a crucial way to define precisely the site of seizure onset. The identification of the site where seizures start and how they propagate is critical to understanding both the pathophysiology of epilepsies and developing therapeutic approaches. Macroscale neuroimaging techniques, such as high-resolution MRI and fMRI, are the entrance step in providing insights into the topological organization of brain networks and connectivity disruptions in epilepsy patients.

Extensive findings have emerged from quantitative structural MRI investigations employing volumetry, voxel-based morphometry, cortical thickness mapping, and structural covariance analysis. In DTI investigations, several parameters can be obtained to characterize white matter microstructure including tractography, tensor-derived metrics, and connectivity matrices (Bartolomei et al., 2005).

In structural MRI, volumetric analysis frequently reveals atrophy in limbic structures, such as the hippocampus, entorhinal cortex, and amygdala, which often correlates with histological evidence of neuronal loss in excised temporal lobe epilepsy (TLE) brain tissue (Bartolomei et al., 2005; Bernhardt et al., 2013). Likewise, post-processing methods in quantitative MRI, such as voxel-based morphometry and cortical thickness analysis, have also revealed that TLE is linked to widespread neocortical irregularities. Covariance analyses of these abnormalities extend beyond mesial temporal structures to comprise prefrontal, frontocentral, cingulate, occipitotemporal, and lateral temporal neocortex (Bernasconi et al., 2004; Bernhardt et al., 2012, 2013).

ENIGMA-Epilepsy MRI scans showed gray and white matter changes in different epilepsy types, with more widespread and bilateral extra-hippocampal gray matter differences in left TLE (Whelan et al., 2018; Hatton et al., 2020; Sisodiya et al., 2020). Also, in individuals with TLE, the investigation of preoperative structural connectivity using DTI-fMRI and its association with post-operative seizure control outcomes revealed specific preoperative connectivity patterns that are associated with improved surgical outcomes (Bonilha et al., 2013).

While there has been substantial progress in understanding structural connectivity abnormalities at the macroscale, we face limitations due to our access being restricted to network topology without achieving a finer neuronal resolution and specificity. In this regard, the mesoscale provides a more precise comprehension by pinpointing the particular neural components contributing to local connectivity. Thus, the gold standard for noticing abnormal structural connectivity in a mesoscale is anterograde and retrograde viral neuronal tracing (Lanciego and Wouterlood, 2020). These tracers exhibit high accuracy and sensitivity, especially when mapping long-range connections, thus contributing to a comprehensive and detailed understanding of connectivity across various brain areas (Saleeba et al., 2019). Their invasive nature restricts the use to animal models. Du et al. (2017) employed a rat model induced by pilocarpine and utilized rabies tracing techniques to discern intricate morphological details of projections within the dynamic hippocampal circuit. This study revealed that newly formed dentate granule cells (DGCs) in adults, triggered by seizures, receive excitatory signals from pyramidal cells in the cornu Ammonis (CA3) and repeated excitatory inputs from other DGCs.

In fMRI, Englot et al. (2016) explored local and distant synchronization of resting-state fMRI signals in TLE and focal epilepsy patients. They observed altered connectivity within and between various brain regions, highlighting the impact of epilepsy on network organization. Likewise, analysis of resting state in focal cortical dysplasia (FCD) identified distinct patterns of functional connectivity with the hypo-connected patterns in cases with FCD type IIB, whereas the hyperconnected lesions were predominantly associated with type IIA (Hong et al., 2019).

2.2.2 Abnormal neuron morphology

Alterations in the size and shape of neuronal cell bodies have been detected across diverse brain regions, encompassing the hippocampus, neocortex, and other regions linked to abnormal neural connectivity (Stouffer et al., 2016). The connection between these morphological alterations and epileptogenesis has already been confirmed (Abdijadid et al., 2015). These deviations in neuronal cell body structure can influence the interconnection and communication between neurons, potentially influencing the onset and advancement of epilepsy (Hsieh et al., 2016; Wu et al., 2022). More precisely, these alterations in local and global connectivity can impact the manifestation of seizures, determining whether abnormal connectivity and hyperexcitability result in focal or generalized seizures (Sheybani et al., 2018; Represa, 2019).

In focal epilepsies, malformations of cortical development are associated as the primary substrate in which the presence of morphologically abnormal neurons significantly affects neural connectivity (Mainen and Sejnowski, 1996; Richards and Van Hooser, 2018). The existence of atypical neurons could influence the subsequent stages of development that regulate cortical synaptic connectivity (Subramanian et al., 2020). Avansini et al. (2022) observed an enhanced level of network connectivity (termed effective connectivity) along with increased neuronal excitability in human neural organoids derived from pluripotent stem cells of patients with FCD. The aberrant connectivity seen in FCD appears to be influenced by neuronal morphological abnormalities, particularly the presence of dysmorphic neurons. Using 3D confocal microscopy, the researchers detected enlarged cell bodies and increased dendritic complexity, potentially contributing to a more interconnected neural circuitry and the formation of an epileptogenic network in FCD.

Using high-resolution synchrotron x-ray microtomography and Golgi-Cox staining, Fonseca et al. noticed an altered distribution of neurons and a reduction of cell number in the hippocampus in a *status epilepticus* mouse model. These approaches allowed the assessment of the 3D cytoarchitecture, neuron density, and morphology (Fonseca et al., 2018).

2.2.3 Abnormal neuronal localization

The integration of dendrites and synapses into functional networks is heavily affected by how neocortical neurons are positioned during development (Martineau et al., 2018). Malpositioned neurons in the cortex cytoarchitecture are called heterotopic neurons (Ishii et al., 2015). These neurons alone may play a role but do not seem to be sufficient to trigger seizures (Aghakhani et al., 2005). The aberrant organization of cortical cytoarchitecture potentially leads to aberrant connections within these developing neuronal networks. Additionally, the recruitment of distinct microcircuits from different cortical locations could alter synchronicity, leading to abnormal neural oscillations (Dubeau et al., 1995; Abdijadid et al., 2015).

Neuronal disorganization and clusters of heterotopic neurons are primarily observed in human specimens from cortical migration malformations such as periventricular heterotopia (Ekşioğlu et al., 1996) and FCD type I (Coras et al., 2021) using light microscopy with immunohistochemical and DiI tracing techniques. Additionally, in animal epilepsy models (Mello et al., 1993), there have been observations of heterotopic granule cells in the dentate gyrus, resembling those found in human epilepsy. Heterotopic granule cells establish new connections and potentially impact synaptic reorganization (Babb, 1991).

2.2.4 Dendritic pathology

The presence of dendritic spine pathologies and abnormal dendritic arborization have been suggested to be implicated in epilepsy worsening, increasing neuronal hyperexcitability in the circuits, and contributing to cognitive deficits, synaptic remodeling, and aberrant plasticity (Fiala et al., 2002).

Dendritic spines are mostly observed in excitatory synapses and neurons respond to epileptogenic changes in the circuitry by modifying the structure of their dendritic trees. Alterations in the distribution, quantity, and morphology of dendritic spines have been proposed to have a direct impact on seizures and epileptogenesis (Jiang et al., 1998; Jean et al., 2023). However, it remains unclear whether these changes are the cause or are a consequence of seizure recurrence (Wong and Guo, 2013).

Dendritic pathology in epilepsy can be broadly categorized into two main fields, as described below:

Neuronal dendritic arborization: Morphological changes of dendrites can affect neuronal excitability. Abnormalities in dendritic length, shape, and branching patterns have been described in epilepsies associated with either hippocampal sclerosis, or tumors, or microdysgenesis (von Campe et al., 1997), and also associated with the presence of varicose swelling of the dendrites of granular dentate neurons of the hippocampus (Blümcke et al., 1999).

Dendritic spine pathology: The initial observation of dendritic spine loss occurred in hippocampal pyramidal neurons and dentate granule cells among individuals with TLE (Scheibel et al., 1974), providing a plausible mechanism to elucidate the learning and memory challenges experienced by these patients (Chen et al., 2010). In Lennox-Gastaut syndrome, a childhood epileptic disorder linked to intellectual disability, pyramidal neurons from brain biopsy were observed to possess a reduced number of spines using EM (Renier et al., 1988). In human cerebral cortices derived from FCD patients, a reduction of dendritic spines, and sporadic filopodia-like protrusions emerging from the soma in dysmorphic neurons were noticed using Golgi impregnation and confocal microscopy (Rossini et al., 2023).

Employing Golgi-Cox staining, optionally combined with immunohistochemistry, as well as DiI tracing, and utilizing both confocal microscopy and EM techniques, provides a comprehensive method for assessing the morphology and structure of dendritic arborization, as well as the density and morphology of neuronal dendritic spines in epilepsy.

2.3 Exploring connectivity in central nervous system disorders via mesoscale imaging for deeper insights

Functional and structural imaging studies have consistently identified aberrant connectivity as a fundamental feature in the pathogenesis of various brain disorders. These investigations have primarily involved live human subjects and focused on a macroscale level, employing techniques such as MRI/fMRI and PET/SPECT, which deliver the overall spatial context of a large field of views, albeit at lower resolution. As seen in **Table 1**, which compiles brain connectivity studies in schizophrenia and epilepsy from the literature, there has historically been an over-representation of use of macroscale techniques to try to answer biological questions. While these studies have provided valuable insights into the presence of aberrant connectivity, they have fallen short in uncovering its precise etiological underpinnings in different brain disorders. Mesoscale imaging provides a means to address the potential untapped source of information for novel insights pertaining to brain connectivity, as observed in this context.

To gain more understanding of the etiology of these disorders, the integration of morphological and functional 3D data at mesoscale resolution is imperative. Multimodal imaging techniques, including confocal microscopy, light-sheet microscopy, EM, and x-ray tomography, present promising opportunities to obtain a more comprehensive perspective on alterations in neural connectivity. Nevertheless, it is essential to recognize the impracticality of performing live imaging at a mesoscale level in human subjects. In this scenario, robust *in vitro* models, such as 2D neuronal cultures and 3D neural organoid cultures, play a critical role in investigating the complexities of human aberrant connectivity within a controlled environment in a model that more closely resembles human brain development. These combined efforts have the potential to enhance our comprehension of the origins and establishment of aberrant connectivity, and may ultimately contribute to the development of innovative therapeutic approaches.

In recent years, significant advancements have been achieved in the field of mesoscale multimodal imaging, enabling the integration of diverse techniques for comprehensive analysis. Notably, it is now possible to merge a myriad of imaging modalities, resulting in the complete 3D morphological reconstruction of individual neurons while simultaneously acquiring invaluable functional data in view to study global connectivity (Keller and Ahrens, 2015; Kuan et al., 2020; Santuy et al., 2020; Muñoz-Castañeda et al., 2021; Walsh et al., 2021; Bosch et al., 2022; Pisano et al., 2022). Among these techniques are Genetically Encoded Calcium Indicators (GECIs) (Miyawaki et al., 1997; Nakai et al., 2001), with the recently developed CaMPARI (calcium-modulated photoactivatable ratiometric integrator) emerging as a notable standout in mesoscale imaging (Fosque et al., 2015). CaMPARI distinguishes itself by its unique feature of irreversibly labeling photoconverted neurons, extending the observation of active networks beyond the initial snapshot of activity. This capability has been leveraged to capture task-dependent activity patterns across brain regions and visualize hippocampal synaptic plasticity in freely moving animals (Berndt et al., 2023; Das et al., 2023). Notably, the practicality of CaMPARI is enhanced by its capability for multiple uses in longitudinal *in vivo* studies (Das et al., 2023). Furthermore, the single-cell precision of CaMPARI facilitates the exploration of interconnected microcircuits, allowing for the evaluation of disruptions in excitatory and inhibitory (E/I) signaling (Martin and Plavicki, 2020), a crucial factor in connectivity influencing conditions such as schizophrenia and epilepsy. This remarkable progress reflects the convergence of innovative technologies and methodologies, leading to a deeper understanding of neural structures and their structural and functional connections at the mesoscale level.

In this context, there are several gaps in understanding disorders affected by brain connectivity that could be addressed by leveraging mesoscale-related approaches. In schizophrenia, delayed PFC maturation, specifically GABAergic interneurons, contributes to cognitive and social deficits in adolescence (Lewis, 1997; Caballero and Tseng, 2016; Delevich et al., 2018). Investigating prefrontal circuitry formation and the impact of excitatory inputs from subcortical regions on interneurons vs. pyramidal neurons in the PFC is crucial. CaMPARI, for example, could offer valuable means to investigate these dynamics. Integrating 3D models with mesoscale imaging (e.g., confocal or live cell imaging and functional calcium imaging) can address these questions, revealing dynamic processes and synaptic development in the neuronal circuitry.

Likewise, in epilepsy research, we may inquire about the processes involved in the conversion of a focal seizure into a generalized event encompassing several cortical areas by addressing questions such as: What factors drive this electrical propagation? Is

TABLE 1 Compilation of brain connectivity studies in schizophrenia and epilepsy: synthesis across different scales, data acquisition modalities, and image processing strategies.

Biological question	Scale	Data acquisition	Output	Image processing	References
Structural and functional brain network abnormalities	Macroscale	MRI	Functional connectivity	Seg.: in house MATLAB tools	Anticevic et al. (2015)
Functional connectivity	Macroscale	MRI	Task-based functional connectivity	Seg.: registration to neuroanatomical atlas	Garrity et al. (2007)
Functional connectivity	Macroscale	MRI	Task-based functional connectivity	Prep.,[1] seg.: registration to neuroanatomical atlas coordinates	Whitfield-Gabrieli et al. (2009)
Functional connectivity	Macroscale	MRI	Functional connectivity	Prep.,[1] seg.: registration to neuroanatomical atlas coordinates	Erdeniz et al. (2017)
Functional connectivity	Macroscale	MRI	Intra- and inter-network task-based functional connectivity	Prep.,[1] seg.: cortical parcellation of functional connectivity boundaries maps	Godwin et al. (2017)
Functional connectivity	Macroscale	MRI	Functional connectivity	Prep.,[1] seg.: voxel-wise meta-analysis–SDM-PSI software	Cai et al. (2022)
Functional connectivity	Macroscale	MRI	Functional connectivity	Prep.,[1] seg.: independent component analysis–CONN toolbox	Huang H. et al. (2022)
Neurotransmitter systems	Macroscale	PET	18F-DOPA uptake	Prep.,[1] seg: semi-automatic, probabilistic registration to neuroanatomical atlas	Howes et al. (2009)
Neurotransmitter systems	Macroscale	MRI	Glu and GABA levels	Metabolite quantification. Voxel seg: not detailed	Chen et al. (2017)
Neurotransmitter systems	Macroscale	PET	NMDAR ligand tracer volume distribution	Prep.,[1] seg.: neuroanatomical atlas registration	Beck et al. (2021)
Neurotransmitter systems	Macroscale	MRI	Glu and GABA levels and functional connectivity	Prep.,[1] seg.: automatic metabolite quantification; functional connectivity in MRS voxel	Shukla et al. (2019)
Neurotransmitter systems	Macroscale	PET	GABAAR ligand tracer volume distribution	Prep.,[1] seg.: neuroanatomical atlas registration	Marques et al. (2021)
Myelin and white matter tracts	Macroscale	MRI	GM/WM contrast	Seg.: surface-based mapping–FreeSurfer 5.3.0	Jørgensen et al. (2016)
Myelin and white matter tracts	Micro/Nanoscale	EM	Myelin sheath lamellae damage	Seg.: manual analysis–Kontron Mop–Videoplan image analyzer	Uranova et al. (2001)
Dendritic spine quantification	Micro/Nanoscale	LM	Mean diameter, total length, location and number of dendritic spines	Manual tracing	Glantz and Lewis (2000)
Dendritic spine quantification	Micro/Nanoscale	BM	Spine density and dendrite length	Manual tracing	Konopaske et al. (2014)
Dendritic spine quantification	Micro/Nanoscale	CM	Spine density, number, and area	Manual tracing	MacDonald et al. (2017)
Functional connectivity	Macroscale	FM	Cell density and FIM	Seg.: stereology–Visiopharm software, semi-automatic FIM: Zen 2.0 Blue Imaging software	Stachowiak et al. (2017)
Structural and functional brain network abnormalities	Macroscale	MRI	Volumes	Prep.,[1] Seg: surface-based mapping	Bernhardt et al. (2013)
Structural and functional brain network abnormalities	Macroscale	MRI	Volumes	Seg: histology-based volumetry	Bartolomei et al. (2005)
Structural and functional brain network abnormalities	Macroscale	MRI	Volumes	Prep.,[1] seg: voxel-based volumetry	Bernasconi et al. (2004)
Structural and functional brain network abnormalities	Macroscale	MRI	Volumes and cortical thickness	Prep.,[1] seg: semi-automatic, surface-based	Bernhardt et al. (2012)

(Continued)

TABLE 1 (Continued)

Biological question	Scale	Data acquisition	Output	Image processing	References
Structural and functional brain network abnormalities	Macroscale	MRI	Volumes and cortical thickness	Seg: surface-based mapping–FreeSurfer v5.3.0	Whelan et al. (2018)
Structural and functional brain network abnormalities	Macroscale	MRI	FA, MD, AD and RD	Prep.,[1] seg: tensor estimation and tractography	Hatton et al. (2020)
Structural and functional brain network abnormalities	Macroscale	MRI	Structural connectivity	Prep.,[1] seg.: diffusion tensor calculation and structural connectivity–FDT toolbox	Bonilha et al. (2013)
Structural and functional brain network abnormalities	Mesoscale	CM	Colocalization of immunoreactivity	Manual counting: Adobe Photoshop CS6	Du et al. (2017)
Structural and functional brain network abnormalities	Macroscale	MRI	Functional connectivity	Prep.,[1] seg: manual and automatic segmentation–AAL	Hong et al. (2019)
Abnormal neuron morphology	Mesoscale	FM, CM, MRI	Cell density, *ex-vivo* FA	Prep.: Image reconstruction–Imaris. Cell seg.: auto-thresholding–ImageJ. DTI seg.: not detailed.	Hsieh et al. (2016)
Abnormal neuron morphology	Mesoscale	CM	Cell density, Sholl analysis, dendritic spine morphology	Prep.: gray-scale conversion, Seg.: Manual cell counting, optical density, Sholl analysis: ImageJ. Dendritic spine: Imaris FilamentTracer module	Wu et al. (2022)
Abnormal neuron morphology	Mesoscale	CM	Cell morphology and density	Seg.: semi-automatic quantification–Analyze Particles on ImageJ and Imaris	Avansini et al. (2022)
Abnormal neuron morphology	Mesoscale	Synchrotron x-ray CT	Cell morphology and density	Prep.: noise reduction. Seg.: threshold, morphological filters and manual correction–Avizo software	Fonseca et al. (2018)
Abnormal neuronal localization	Multiscale:Meso (CM) and Micro: EM	CM, EM	Cell and dendritic spine density and morphology	Prep.: image and neuron reconstruction–Neurolucida. Seg.: automatic morphometry–L-measure. Dendritic spines: manual tracing on SynPAnal. Puncta analysis: ImageJ	Martineau et al. (2018)
Abnormal neuron morphology	Multiscale: macro (RM) and meso (LM)	MRI, LM	Type and number of lesions	Qualitative visual analysis	Dubeau et al. (1995)
Abnormal neuronal localization	Mesoscale	LM	Cell morphology	Qualitative analysis	Ekşioğlu et al. (1996)
Abnormal neuronal localization	Microscale	LM	Cell density	Manual cell counting	Mello et al. (1993)
Abnormal neuronal localization	Microscale	LM, EM	Densitometry, cell morphology	Manual densitometry–Ziess IBAS image analysis system	Babb (1991)

18F-DOPA, 18F-Fluoro-L-Phenylalanine tracer; AAL, automatic anatomic labeling; AD, MD, RD, axial, mean, and radial diffusivity, respectively; BM, brightfield microscopy; CM, confocal microscopy; CONN, functional connectivity toolbox; CT, computed tomography; DAPI, 4′,6-diamidino-2-phenylindole; DMN, default mode network; DTI, diffusion tensor imaging; EM, electron microscopy; FA, fractional anisotropy; FDT, FMRIB's Library's Diffusion Toolbox; FM, fluorescence microscopy; FIM, Fluorescence Intensity Measurements; GABA/GABAAR: γ-aminobutyric acid/GABA α-subunit receptor; Glu, glutamate; GM, gray matter; LM, light microscopy; MRI, magnetic resonance imaging; NMDAR, *N*-Methyl-D-aspartate receptor; ROI, region-of-interest; PET, positron emission tomography; Seg., segmentation; Prep., preprocessing; PSI, seed-based d Mapping with Permutation of Subject Images toolkit; T1WI, T1-weighted image; WM, white matter. [1]Reported preprocessing steps for neuroimaging: slice-timing, attenuation, and motion corrections, registration to T1WI, normalization to neuroanatomical atlas, field-map correction, and smoothing (for functional MRI); intensity correction, registration to neuroanatomic atlas, smoothing; eddy current and susceptibility artifacts correction (diffusion MRI); realignment, motion correction, PET registration to T1WI, normalization to neuroanatomical atlas (for PET).

it the result of abnormal neurite branching patterns or an unusual number of dendritic spines? Moreover, it remains imperative to determine the specific neural cell type responsible for orchestrating the shift from a localized circuit, synchronizing neighboring cells, to the initiation of a generalized ictal event. Thus, studying brain network development and organization in the mesoscale will allow us to understand seizure formation and spread.

3 Image processing: quantifying connectivity

Image processing tools are essential for quantifying data and revealing the intricate relationships between brain networks and aberrant connectivity. Image processing techniques can extract qualitative and quantitative measurements from a variety of neuroimaging modalities, including MRI, two-photon, confocal, super-resolution, microscopy, and EM. Initial steps involve the identification of which information the research needs to extract from the data (e.g., tiny structures), followed by the selection of algorithms and their fine-tuning on a particular data (e.g., noise filtering, contrast enhancement). After establishing an adequate workflow, the outcome must be validated by expert neurobiologists. During this stage of image processing, human input on several levels inevitably leads to undesired bias or even difficulties in identifying subtle information such as fine morphological structures. Adding to this equation, the amount of raw data is sometimes not feasible to be fully accomplished manually, and this is especially true for mesoscale generated data. In this scenario, the development of automated or semi-automated computerized processing is paramount to achieving an efficient large-scale data processing. In general, a typical processing workflow consists of three fundamental steps: image preprocessing, image analysis, and quantification (**Figure 2**). However, it is important to note that specific modifications on the pipeline are required based on the type of image used and the particular neural structure under investigation. While a general image analysis pipeline can find utility in various scenarios, it is important to recognize that each biological question has a unique demand, and this requires the development of dedicated processing pipelines.

In the following section, we will explore the most suitable image acquisition and processing techniques for tackling key issues associated with conditions affected by abnormal brain connectivity. These issues encompass inter-regions brain connectivity, axonal and soma density, single neuron morphology, and dendritic spine quantification and morphology. Our approach will commence with the macroscopic analysis of brain regional images and end with the micro-scale assessment of dendritic spine quantification and morphology. We will not address image contrast enhancement and noise reduction preprocessing strategies as they have several computational implementations in each of the acquisition techniques and it could divert our focus from the main goal of this section: understanding the crucial role of segmentation and data analysis in comprehending connectivity. For an in-depth review of image denoising, the interested reader is referred to Kollem et al. (2019), Kaur et al. (2021), and Huang C. et al. (2022). There is a plethora of manual image analysis tools but in this review we will focus on automatic or semi-automatic quantification.

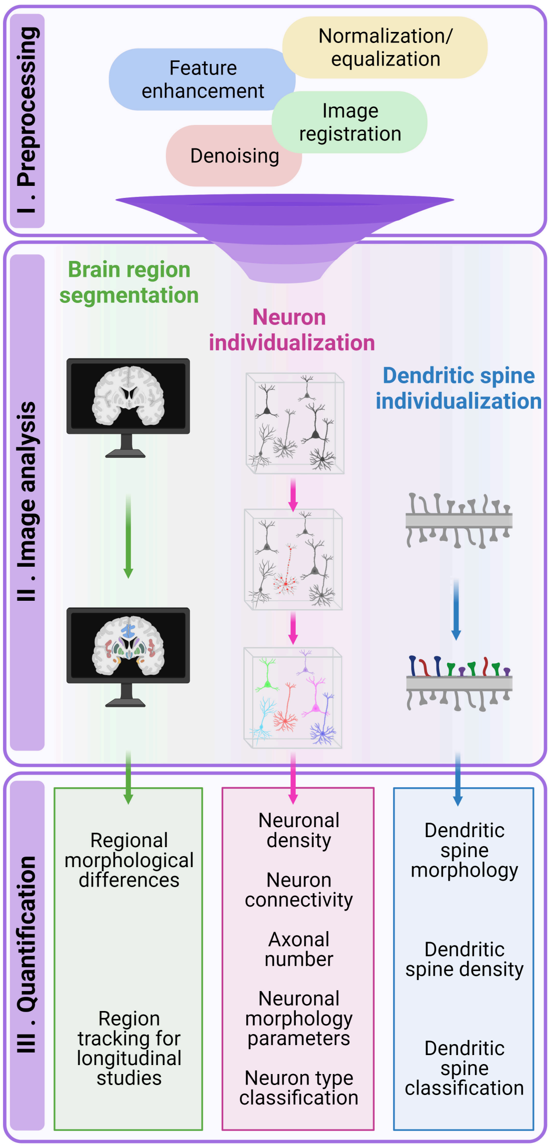

FIGURE 2
Overview of the bioimage analysis workflow. The pipeline generally comprises three fundamental steps: image preprocessing (I), image analysis (II), and quantification (III). In the preprocessing step, raw image quality is enhanced to facilitate subsequent analysis or visualization. Image analysis involves identifying and delineating specific regions or objects of interest, which is essential for extracting quantitative data from bioimages. The quantification step involves extracting meaningful quantitative measurements and deriving insights from the acquired images.

3.1 Quantifying inter-regional brain connectomics

Anatomically, the brain is compartmentalized into distinct regions, each with designated functions that collectively contribute to a range of high-order cognitive processes. Inter-regional brain connectomics consists of mapping and studying the complex networks between different regions (Behrens and Sporns, 2012). By analyzing these connections, using either macro, meso, or multiscale imaging strategies, it is possible to gain insights into how different regions cooperate or compete (Behrens and Sporns, 2012), and how disruptions in these networks may lead to neurological or psychiatric disorders. The macroscale approach focuses on imaging techniques that encompass the entire brain, ideally *in vivo*, with a selection of modalities such as MRI for structural covariance, fMRI, diffusion weighted image (DWI–including DTI and tractography), and PET. Structural connectivity, primarily addressed through DWI/DTI and tractography, when combined with fMRI, can also reveal structural connectivity (Axer and Amunts, 2022).

In the context of computational processing for macroscale images, artificial intelligence methods for image analysis are widely utilized in diagnosis contexts to understand neurological and psychological disorders (Zhang et al., 2020). For meso and micro scales, image analysis techniques currently available to extract neural connectivity lie within the segmentation and neuron individualization. Pixel/voxel classification, frequently called Region of Interest (ROI) delimitation, is the first step to a multitude of tasks. Once an ROI is defined, it becomes possible to trace morphological markers in longitudinal or comparative studies. Furthermore, it aids in the precise delineation of abnormal regions, guiding surgeons in tasks such as tumor extraction or identifying the epileptogenic zone by PET/fMRI images. In longitudinal developmental studies, segmenting regions like the prefrontal cortex over time provides valuable insights into the maturation of connectivity networks associated with cognitive development (Liu et al., 2023). ROI segmentation is also a crucial step for morphological quantification assessment as it enables researchers to access region volume or identify morphological differences in patients compared to control individuals in MRI.

Within psychiatric imaging, schizophrenia research has consistently revealed two prominent observations: increased cerebroventricular size and reductions in cerebral gray matter volume (Ananth et al., 2002; Shapleske et al., 2002). Automatic ROI segmentation and morphometric quantification of gray matter volume in MRI images decrease human biases and help to evaluate different groups in comparative or longitudinal studies (Fornito et al., 2017; Nemoto et al., 2020). While traditional image processing techniques such as thresholding-based segmentation, watershed labeling, neuroanatomical-atlas-based segmentation, or semi-manual masking [using tools like FreeSurfer (Fischl, 2012) or BET (Smith, 2002) are available, the medical context often requires greater accuracy even on images with unclear borders or blurred definition (Wang et al., 2023)]. In this context, several machine learning techniques have been successfully used in analysis of complex datasets, including k-means clustering, Support Vector Machines (SVM), Random Forest, Adaptive Boosting (AdaBoost), eXtreme Gradient Boosting (XGBoost) and Deep Learning strategies like Convolutional Neural Networks (CNN), Generative Adversarial Networks (GAN), Recurrent Neural Networks (RNN) (Wang et al., 2014; Zhang Z. et al., 2021; Verma et al., 2023).

In the field of epilepsy, image segmentation or ROI delimitation primarily aims to locate the epileptogenic zone and define pre-operative surgical areas. While this kind of analysis is commonly applied to MRI-T1 and fMRI images (Segato et al., 2020), its applicability extends to PET, DTI, and DWI scans (Sollee et al., 2022). For instance, in the study conducted by Lee et al. (2020), the authors used deep-learning CNN to pinpoint specific regions for surgical resection in DWI and tractography images of pediatric patients. Additionally, (Zhang Q. et al., 2021) constructed a pair-of-cube (PoC)-based Siamese CNN using two identical 18-layer ResNet to identify epileptic focus in F-fluorodeoxyglucose (F-FDG) PET images. After localization, the metabolic abnormality level of the predicted focus was automatically determined using the asymmetric index (AI). In another instance (Li K. et al., 2019; Vakharia et al., 2019) conducted detailed segmentation of critical areas, including the ventricular system, brainstem, amygdalohippocampal complex, parahippocampal gyrus, and sulci, from MRI-T1 9 images. Subsequently, they employed Random Forest algorithms to preplan laser trajectories of respective surgeries of epileptic zones with less adverse events associated with epilepsy surgery. For a comprehensive exploration of how deep learning techniques can be used in epilepsy, we recommend Sollee et al. (2022) review.

3.2 Multiscale imaging: bridging micro to macroscale

Macroscale inter-regional insights are directly associated with microscale synaptic organization and arborization (Wei et al., 2019). The overall cortico-cortical connectivity observed at the macroscale in BigBrain profiles is strongly correlated to microscale laminar cytoarchitectonic patterns (Wei et al., 2019). Essentially, cortical regions exhibiting higher similarity in microscale patterns are more likely to be interconnected (Wei et al., 2019).

Additionally, multiscale approaches, which integrate data from various imaging modalities, hold the potential to interlink micro and macro scales. For example, the BigMac dataset, developed by Howard et al. (2023), combines *in vivo* MRI images with post-mortem microscopy data and ultra-high angular resolution diffusion imaging and enables the mapping of microscale cellular structures to macroscale features. This comprehensive approach allows researchers to study brain connections at both macro and micro levels, bridging the gap between them.

However, Haueis (2021) cautioned against oversimplifying the micro-to-macro correlation by merely averaging microscale details. Failing to account for the intermediate mesoscale structure and organization in this practice may lead to analytical errors. Haueis further emphasized the critical role of mesoscale circuit organization in accurately depicting the structure-function relationship, particularly in the context of cortical gradient modeling. This is a compelling piece of evidence that bridging micro-to-macro scale connectivity should pass through mesoscale circuit understanding.

3.3 Mesoscale imaging

The trade-off between image resolution and sample size in 3D is a well-known limitation. The higher spatial resolution comes at the cost of a smaller field of view (FOV). Nonetheless, mesoscale brain imaging strategies combine cellular-level resolution and an extended spatial range. The primary approach employed in mesoscale imaging involves the use of wide-field or laser-scanning confocal microscopies, heavily impacted by the thickness of the sample. Recent methodologies such as light-sheet and two-photon partially overcome this limitation by going deeper inside intact tissues, while preserving high spatial resolution (Cazemier et al., 2016; Tyson and Margrie, 2022). For example, Li et al. (2010) used an automatic micro-optical sectioning tomography (MOST) to obtain a mesoscale atlas of the mouse brain. This strategy integrates a microtome, light microscope, and image recorder, and allows for simultaneous imaging and sectioning (Li et al., 2010). Another possible approach was the use of post-mortem axonal projections enhanced by green fluorescent protein (EGFP)-labeling (Oh et al., 2014). They imaged many small patches of brain tissue with two-photon microscopy to form a big image with cellular-level resolution (Oh et al., 2014). Imaging at this scale in larger FOV took 18.5 h of scanning and resulted in a 750 GB raw dataset. Likewise, (Wang et al., 2019) developed the VISoR system, a sophisticated adaptation of light sheet microscopy, to obtain 3D mouse brain images with neurite resolution within 1.5 h.

Another time-optimizing approach for mesoscale involves the use of synchrotron X-ray imaging. Especially in 3D computed tomography is becoming popular since the higher energies of x-rays allow deeper penetration and very high resolution. Although it can take a few hours to measure a sample in benchtop equipment, synchrotron sources emerge as a solution for fast measurements and even higher spatial and temporal resolutions, which also allow a combination of several tomograms to reconstitute large FOV (Fonseca et al., 2018; Rodrigues et al., 2021; Claro et al., 2023). Image processing pipelines are usually developed for a specific imaging acquisition technique. A comprehensive summary of primary mesoscale image processing methods for the main image acquisition modalities can be found in **Figure 3**.

3.3.1 Processing at the mesoscale level: insights into neurite and soma regional density

Extensively imaging and tracing axons throughout the brain provides a mesoscale view of regional connectivity, offering insights into soma and neurite density as well as assessing total cell reductions and identifying cell death in specific brain regions (Bazinet et al., 2023). Although mesoscale imaging strategies can unveil a series of histological structures, they present their computational challenges.

The first challenge encountered in the mesoscale is usually the stitching of large quantities of high-resolution microscopy images. Image stitching refers to the process of aligning and overlaying two or more images of the same object taken from different, consecutive, and overlapping FOV. Through image registration processing (Sarvaiya et al., 2009), corresponding features or structures in these images are spatially aligned, making it possible to combine them into a single and panoramic image. In the case of brain microscopy, this involves merging multiple images, sometimes acquired at varying scales, into a comprehensive, high-resolution representation of the brain. Registering can mean either tile stitching multiple consecutive FOVs, without overlapping or positioning microscopic images into a larger dataset using fiducial markers, or a common reference frame to localize them into the brain. In both cases, it is expected that mesoscale imaging strategies generate the largest amount of raw data. BigStitcher is a method of stitching consecutive FOVs into a single high-resolution image (Hörl et al., 2019). To manage such large amounts of data, the BigSticher software computes shifts between overlapping image tiles by using a phase correlation method in downsampled images, which optimizes the computational time necessary for image stitching (Hörl et al., 2019). Moreover, DeepSlice is a CNN specifically trained on a substantial histological dataset to automatically align coronal mouse brain two-photon microscopy images with the Allen Common Coordinate Framework (CCF) (Carey et al., 2023).

The following step is to detect neuronal cell bodies in the entire image and quantify soma density across brain regions. The size of mesoscale data makes manual handling impractical and prone to biases; hence, automatic or semi-automatic tools are more suitable for its processing (Bjerke et al., 2023). Soma detection can be made either by traditional image enhancement filters followed by intensity thresholds, such as in ClearMap (Renier et al., 2016) and MIRACL (Goubran et al., 2019), or by advanced machine learning techniques for pixel classification as deep learning approaches (Tyson and Margrie, 2022). Intensity thresholding approaches also work well with DAPI-stained nuclei images (Kim et al., 2015), and modifications of thresholding can be done to address large-scale GFP images even with a large variability in contrast (Frasconi et al., 2014). These modifications consist of first using mean shift clustering to detect soma centers followed by image deconvolution and finally manifold learning for filtering false positives (Frasconi et al., 2014). However, intensity thresholding and morphological approaches fail especially with densely packed images and that is precisely where deep learning can be used. For example, (Hu et al., 2021) combined 3D U-shaped full CNN with multi-task learning to perform soma segmentation in Nissl stained images. This strategy is done in small patches and would take a long time to train in teravoxel mesoscale images. As a faster approach, (Wei et al., 2023) used a lightweight MCC-Net to reduce computational complexity in soma detection. Then, in the second stage, they employed SFS-Net for precise soma localization in mouse brain images, utilizing advanced segmentation techniques. Experimental results confirmed the excellent performance of the method and its capacity to provide valuable information for neuron reconstruction (Wei et al., 2023). The user-friendly software CellPose (Stringer et al., 2021) also has a DeepLearning module that has been used to count pyramidal neurons in histopathological images (Oltmer et al., 2023). An alternative option is to employ Suite2p software (Pachitariu et al., 2017), which offers AutoROI cell segmentation designed for simultaneous analysis of functional and morphological two-photon calcium images. The compilation of the main soma quantification methods for mesoscale connectivity is presented in **Table 2**.

The next step to a mesoscale connectivity view is to detect, trace, and quantify neurites across the brain. In the study conducted by Allen Mouse Brain Connectivity Atlas (Oh et al., 2014), axonal detection at the mesoscale level starts with a very similar process to single neuron morphology mesh tracing. Signal detection algorithms, such as filament tracing, can be used as an initial segmentation. The authors then rescale image intensity and remove noise using filters and morphological techniques. Candidate signal objects were identified based on adaptive edge/line detection and morphological attributes such as length and area. Additionally, high-intensity pixels near these objects were considered. In a post-segmentation step, objects considered artifacts were removed. It is important to note that passing fibers and terminals were not differentiated. The outcome is a high-resolution mask classifying each 0.35 μm × 0.35 μm pixel as a signal or background (Oh et al., 2014).

Also in the mesoscale, TRAILMAP uses a modification of a 3D UNet to extract axonal projections from uncleared brain tissue in light-sheet microscopy (Friedmann et al., 2020). This method focuses on segmenting axons from the background in a generalized way that can be applied to all brain regions. Unlike filament tracing methods, it does not address neurite branching numbers or spatial positions. The purpose is mainly to address axonal fiber density and compare it across brain regions (Tyson and Margrie, 2022).

Another possibility is to use the MIRACL pipeline and toolbox. MIRACL is based on a multimodal approach that integrates CLARITY data at the microscopic level with macroscopic *in vivo* and *ex vivo* imaging data, including structural, diffusion, and quantitative MRI, all aligned to the Allen atlas reference frame "ARA." This integration facilitates various analyses, including the

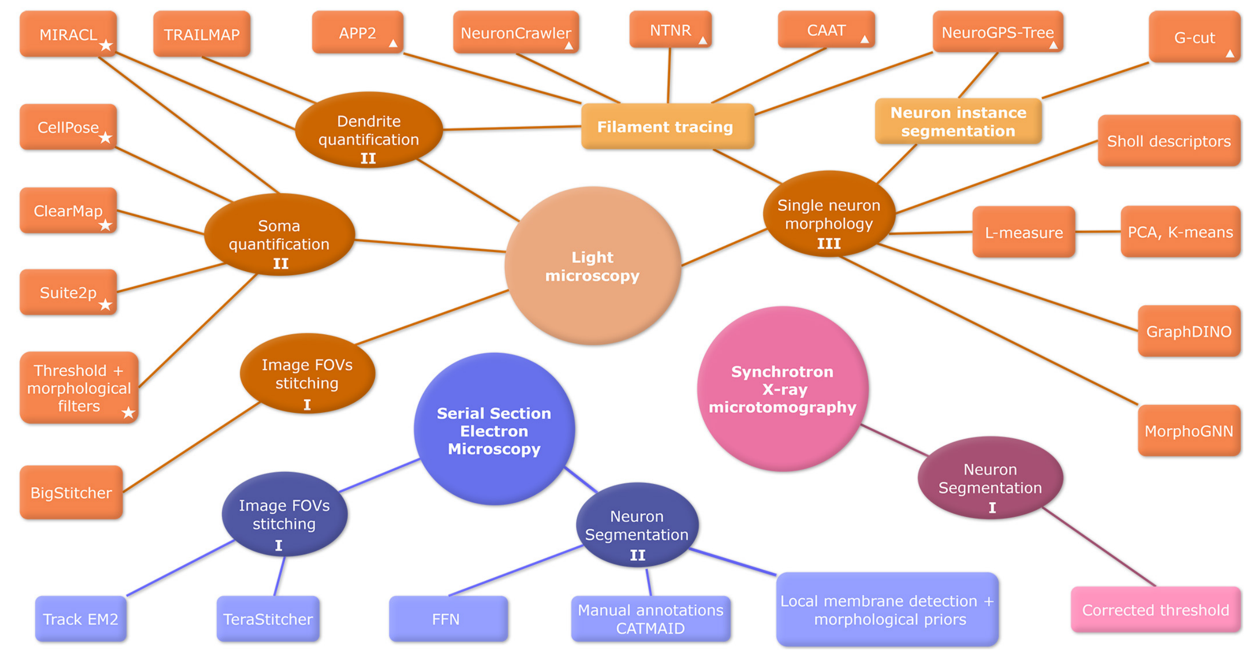

FIGURE 3
Overview of mesoscale bioimage processing methods. Image acquisition techniques are represented by big circles: Light Microscopy (orange), Serial Section Electron Microscopy (blue), and Synchrotron X-ray (pink). Image processing steps are depicted by ellipses, and algorithms of analysis are represented by boxes. Labels I, II, and III denote the fundamental steps of mesoscale image analysis: preprocessing, segmentation, and data analysis, respectively. Algorithms tools are referenced in Table 2 (☆) and Table 3 (Δ). FOV, field of view; FFN, flood-filling network; CNN, convolutional neural network; EM, electron microscopy; PCA, principal component analysis.

TABLE 2 Main soma quantification methods for mesoscale connectivity.

Soma quantification method	Sample preparation/microscopy	Principle
Kim et al. (2015)	DAPI stained nuclei	Intensity threshold
Frasconi et al. (2014)	GFP transgenic mice	Adaptation of intensity threshold: mean shift clustering to detect soma centers, supervised semantic deconvolution by means of neural networks for image enhancement and manifold learning for filtering false positives
ClearMap	YFP	Nuclei detection with background subtraction, filters, morphological operations, and 3D peak detection, followed by watershed segmentation and volume-based filtering to identify cells.
MIRACL Pipeline	YFP + DTI registering	Segmentation workflow in ImageJ, utilizing optimized pre-processing, morphological analysis algorithms, and a parallelized feature extraction algorithm for 3D cellular features.
CellPose (Stringer et al., 2021; Oltmer et al., 2023)	Light microscopy, HE stained histopathological images	A simulated diffusion process generates spatial gradients pointing toward the center of a cell, and a neural network trained on these gradients, along with pixel categorization, forms a gradient vector field used to predict masks by constructing a dynamical system with fixed points.
Suite2p (Pachitariu et al., 2017)	Two-photon calcium images	Greedy segmentation of nearby pixels
Hu et al. (2021)	Nissl stained	Modified 3D fully connected Unet
Wei et al. (2023)	fMOST	Lightweight neural network for quick soma detection in low resolution, followed by a network with multi-scale context and a module for precise soma localization.

DAPI, 4′,6-diamidino-2-phenylindole; GFP, green fluorescent protein; YFP, yellow fluorescent protein; DTI, diffusion tensor imaging; fMOST, fluorescence micro-optical sectioning tomography; 3D, three-dimensional; HE, Hematoxylin and eosin stain.

examination of histological features across network graphs and fiber tracts, as well as connectivity analyses based on projection terminals. Additionally, MIRACL supports group-level statistics, multimodal correlations, and comparisons of connectivity maps across different scales (Goubran et al., 2019).

3.3.2 Single neuron morphology

The morphology of a neuron can have a big impact on its connectivity with other local neuronal circuits. Neurons with a complex dendritic branching pattern tend to have a larger surface area and a denser synaptic field, allowing them to have more

TABLE 3 Main filament tracing and neuron individualization methods for mesoscale connectivity.

Method	Microscopy	Overview	Sparse/dense	References
APP2	Confocal	Image enhancement step followed by seed point detection on local maxima and FFM	Originally created for single neuron use. But can be used on sparse images	Xiao and Peng (2013)
NeuronCrawler	Confocal	Similar to APP2 but improved to large images	Originally created for single neuron use	Zhou et al. (2015)
CAAT	fMOST	3D CNN predicts object probability, followed by an adaptive voxel scooping approach on the probability map,	Dense and large scale neuron tracing	Huang et al. (2021)
NTNR	Ultra-scale optical microscopy	A hybrid model. CNN backbone merged with a Transformer encoder-decoder architecture	Dense	Wang et al. (2022)
G-Cut	Confocal	Requires prior tracing and soma identification. Somas are used as seeds and adaptation of Djikstra's algorithm based on morphological priors is used to segment neuron instances	Dense	Li R. et al. (2019)
Neuro-GPS-Tree	Many modalities	Uses local and global cues to automatically classify neurites and reconstruct large-scale neuronal populations with dense neurites	Dense	Quan et al. (2016)

FFM, fast marching method; fMOST, fluorescence micro optical sectioning tomography. Adapted from Magliaro et al. (2019).

candidate synapses (van Pelt and van Ooyen, 2013). According to Peter's rule, the colocalization of dendritic and axonal arbors are reasonable predictors of connectivity among neuron types (Rees et al., 2017). Nevertheless, a greater number of potential synapses does not always mean a greater number of functional synapses (Rees et al., 2017). Axo-dendritic overlapping is a necessary but not sufficient condition to ensure a synaptic connection. Light microscopy is the ideal imaging technique to study both neuronal morphology (using cytoplasmic markers) and synaptic connectivity (using puncta colocalization) (Wang et al., 2020). In contrast, neuron morphology has recently been described to predict non-random connectivity in local networks and circuits (Udvary et al., 2022). The authors state that the specificity in neural wiring is influenced by morphological factors such as similarities in neurite projections, packing density, and the diversity of cell types in the neuropil (Udvary et al., 2022). High values in these factors lead to recurring patterns in the network, while lower values result in a more feedforward network structure (Udvary et al., 2022).

To address single neuron morphology using imaging techniques we must first extract from the image which pixels belong to each neuron. This process is called instance segmentation or neuron instance individualization (You et al., 2019). The main techniques used to measure multiple neurons are light microscopy (including confocal, two-photon, STED, and light-sheet) and serial-section EM.

3.3.2.1 Single neuron morphology using light microscopy

Traditionally in light microscopy (confocal, light sheet, and STED), neuron instance individualization starts with filament tracing methods (Xiao and Peng, 2013; Feng et al., 2015; Liu et al., 2016; Quan et al., 2016; Shih et al., 2021). These methods work as an initial segmentation and are responsible for differentiating the neural mass foreground from the noisy scattered background (Magliaro et al., 2019). They transform an image into a graph of connected points. Filament tracing pipelines consist mainly of four steps: (i) an image pre-processing step to improve signal-to-noise ratio enhancing filaments and smoothing background; (ii) a seed point detection step followed by (iii) "energy minimization algorithms" such as Fast Marching Method (FMM) (Sethian, 1996) and Dijkstra algorithm (Dijkstra, 1959); and (iv) a pruning step to reduce redundant traces and improve overall segmentation (Liu Y. et al., 2022).

In the pre-processing step, the main goal is to significantly enhance the signal-to-noise ratio. In confocal imaging techniques, the pre-processing involves PSF (point spread function) deconvolution, feature-enhancing filters (Frangi et al., 1998), or deep learning techniques that enhance neurons based on a predicted morphology (Yang et al., 2021a). Then, seed point detection usually includes the detection of somata searching for the brightest point on the image (Xiao and Peng, 2013). After that, energy minimization algorithms find the shortest path between a starting point and all other points in a graph, using a cost function usually based on image intensity or transformed distance of a filament. The final step is filament pruning and morphological corrections (Liu Y. et al., 2022). These traditional tracing methods are very robust and widely used in neuron imaging. Nonetheless, most algorithms are not optimized for large volumetric images (giga or tera voxels) and images with densely packed cells. If the traced image contains multiple neurons this will result in a mesh containing all cells and will require further neuron individualization.

Nonetheless, filament tracing has improved a lot since the 2008's DIADEM golden age. The Big Neuron Project and Mouse Light Project have reconstructed over 1000 neurons and are constructing a database. Neuron Crawler (Zhou et al., 2015) has begun solving the big data problem and, Deep Learning methods have been helping to improve the tracing framework (Dai et al., 2019; Tan et al., 2020; Huang et al., 2021; Yang et al., 2021b; Liu C. et al., 2022; Wang et al., 2022). **Table 3** summarizes the main filament tracing methods used in the mesoscale connectivity.

Once the neuronal mesh is accurately traced by filament tracing strategies, the next step is to individualize each neuron. Algorithms such as G-Cut (Li R. et al., 2019) and NeuroGPS-Tree (Quan et al., 2016) use the soma identity and position, and from previously learned morphological parameters trace the most probable neuron given the soma and the traced neuronal mesh.

3.3.2.2 Single neuron morphology using electron microscopy

Electron Microscopy can also uncover single neuron morphology and local connectomics with nanometric synapse level resolution. Using EM to reconstruct neuron wiring and connectivity involves multiple steps: high-throughput data acquisition, image registration, image segmentation, proofreading, and tracking (Beyer et al., 2022). Unlike confocal or light sheet microscopy, 3D EM neuron reconstruction requires physical sectioning of the sample. The samples are cut into about 30 nm thick samples and individually imaged. A 1 mm^3 brain sample requires about 5000 slices, 2.1 petabytes of raw microscopy data, and 326 days to finish data acquisition (Shapson-Coe et al., 2021). Similarly, (Winding et al., 2023) imaged 3016 neurons and 548,000 synapses in a Drosophila larval brain. The resulting image contained 4841 z-slices and processing it took manual annotation of multiple users and a specialized annotation tool for big images (CATMAID) (Winding et al., 2023).

After each image has been acquired the next step is to stitch adjacent 2D images and correctly stack (register) them to form a 3D volume. During 3D thin-sliced EM image acquisition, the most fundamental step for proper 3D reconstruction is image registration. Aligning microscopy slices can be challenging since they are not perfectly aligned and often have different quality and acquisition parameters (Beyer et al., 2022). The main 2D stitching includes plugins such as TeraSticher (Bria and Iannello, 2012) and 3D registration can be done with the ImageJ plugin TrackEM2 (Cardona et al., 2012). Once the image volume is completed, the next step is to individualize and segment each neuron. Due to the highly textured nature of EM images, segmentation is typically accomplished using deep learning techniques (Shapson-Coe et al., 2021), using a flood-filling network (FFN). Most of the EM segmentation algorithms rely on detecting cell membranes to separate neurons, and even small errors in this detection could split or merge neurons, significantly impacting the reconstructed neural circuit (Krasowski et al., 2018). In this context, combining neuro-morphological priors with local membrane information can be a viable resource to reduce errors in the neuronal individualization process (Krasowski et al., 2018; Hong et al., 2023).

3.3.3 Morphology quantification of individual neurons

The first and most important parameter to quantify single neuron morphology is the radial profile of neuron dendrite spanning tree, also known as the Sholl Intersection Profile (SIP) (Bird and Cuntz, 2019). The complete Sholl analysis includes measuring the total length of the dendrite, the axon domain maximum and minimum from the soma, and the angular distribution of dendritic segments that deviate from a direct path to the soma. According to the authors (Bird and Cuntz, 2019), a larger dendrite extension length implies a larger region where synapses can occur, peaks in the SIPs are related to regions where synapses have a higher probability to occur and valleys in the SIPs are regions to where synapses have a lower probability to occur. The angular distribution is related to a neuron's centripetal bias and implies a neuron that minimizes wiring to ensure an efficient propagation of electrical impulses.

Alternative ways to measure neuronal shape include parameters such as the total length of neurites, the minimal occupied volume, the distribution of branch lengths as represented in histograms, and the frequency of distances between successive bifurcations along the neural trajectory. These measurements are obtained through the open-source software L-measure, as outlined in the work of Scorcioni et al. (2008).

A further challenge is to classify neuron types using only their morphological assets without any molecular markers (Polavaram et al., 2014) used L-measure to extract morphological features of neurons in the NeuroMorpho database. They subsequently applied principal component analysis (PCA) as a statistical tool to identify key morphological parameters capable of effectively classifying dendritic structures across diverse metadata categories. Their findings highlight the importance of specific measures like branching density, size, tortuosity, bifurcation angles, arbor flatness, and topological asymmetry in capturing meaningful features of dendritic trees. Similarly, Khalil et al. (2021) extracted L-measure metrics and modified Sholl descriptors from the NeuroMorpho database and used PCA and KNN clustering to classify neuronal types.

Deep learning revolutionized feature extraction and image classification and has been used to classify neurons. For example, GraphDINO used a Transformer-based Graph Neural Network to create 3D spatial embedding representations of neuronal graphs and later classified them into neuronal types (Weis et al., 2021). The authors adapted positional encoding and introduced a novel attention mechanism called AC-Attention to fit neuronal graphs and achieved results comparable to expert-manual classification without prior knowledge about neuronal structural features and outperforms previous methods in predicting expert labels on quantitative benchmarks (Weis et al., 2021). Similarly, MorphoGNN is a novel approach for embedding single neuron morphologies using graph neural networks (GNN) and learns spatial relationships between nodes in reconstructed neuron fibers by considering their nearest neighbors on each layer. This process generates a reduced-dimensional representation of individual neurons using an end-to-end model that incorporates densely connected Densely Connected Convolutional layers and a dual pooling operator (Zhu et al., 2023).

3.4 Dendritic spine quantification and morphology

Dendritic spines are small protrusions from dendrites that constitute the center of excitatory synaptic interaction among central neurons (Papa et al., 1995). They are crucial structures for interneuronal communication and play a crucial role in learning and memory. Neuronal spines can range in size from tiny, barely visible protrusions to larger and more complex structures. This variety suggests that neuronal spines have a wide range of functions and are essential for neural plasticity and cognitive and sensory functions (Rochefort and Konnerth, 2012; Ekaterina et al., 2023).

The analytical approach is often used to study dendritic spines, including their density and respective morphological features

(Chang et al., 2017). Light microscopy and EM can image dendritic spines and monitor their dynamic alterations in response to neural network activity (Arellano et al., 2007). In this section, we have chosen to emphasize image processing tools obtained by light microscopy.

Traditionally, dendritic spine images are obtained through Golgi staining and wide-field microscopy. 3D studies of such structures can benefit from confocal reflection imaging, although manual dendrite tracing is still in place. Popular software like Imaris (Govindan et al., 2021), or NeuroLucida (Dickstein et al., 2016), followed by the utilization of semi-automatic measurement tools such as software like SPINEJ (Levet et al., 2020) and NeuronStudio (Rodriguez et al., 2008) have a broad use. To employ deep learning for automated methods, it requires extensive datasets comprising meticulously segmented, high-quality images, known as *"ground truth images"*(Vidaurre-Gallart et al., 2022). However, it's important to note that even with such datasets, there may still be limitations to achieving precise reconstructions (Vidaurre-Gallart et al., 2022).

The image processing routine for analyzing dendritic spines involves a five-step pipeline: (i) data pre-processing as described before, (ii) spine location detection, (iii) segmentation to isolate them, (iv) quantification of morphological characteristics, and (v) classification or clustering based on their morphology (Li et al., 2023).

The primary objective in the spine detection phase is the precise identification of individual entities' locations within the 3D image (Rodriguez et al., 2008). This process begins delineating dendrite boundaries, utilizing information extracted from the dendrite 3D mesh (Mukai et al., 2011; Okabe, 2020). There are four main spine detection automatic approaches. The most prevalent method is skeletonization, which involves the removal of consecutive layers of pixels from the dendritic boundary (Okabe, 2020). To detect spines using skeletons, it is necessary to binarize the original images correctly and extract all spines that are still connected to dendritic shafts. If any spines become disconnected during the binarization process, they need to be reattached through further processing (Rusakov and Stewart, 1995). The Rayburst sampling (Rodriguez et al., 2006, 2008), gradient-based methods (Zhang et al., 2010), and analysis of 3D surfaces (Li and Deng, 2012) represent alternative automated approaches for spine detection.

For spike detection, it is necessary to establish the boundary that separates the spines from the dendritic shafts, using iterative methods (Okabe, 2020). One way to perform automatic spine segmentation using light microscopy involves a calculation of the distance to the surface of the neuritic shaft for each voxel outside the shaft (Rodriguez et al., 2008; Singh et al., 2017).

After segmentation, a variety of spine morphological measurements and posterior spine classification can be automatized. Parameters of the 3D structure of spines encompassing spine length, head diameter, neck length, volume, curvature, basal radius, maximum and minimum radius, and head-to-neck ratio (Rodriguez et al., 2006; Janoos et al., 2009). After 3D neuronal morphometry, various principles for spine classification have been proposed and the commonly employed method involves categorizing spines into four main groups stubby, thin, filopodia, and mushroom-shaped (Hering and Sheng, 2001). While traditional phenotypic classification often relies on manual inspection, machine learning approaches, aided by labeled training datasets, have demonstrated comparable accuracy to human operators (Basu et al., 2018), most of them using semi-supervised learning (Shi et al., 2009, 2014). Computational analysis of 3D spine morphology has the potential to unveil novel spine characteristics by fusing clustering methods to automatically group spines with similar structures. Luengo-Sanchez et al. (2018) proposed a probabilistic approach that categorized the spine in clusters based on a selected set of morphology features, with a Gaussian finite mixture model.

The rise of the high-resolution light microscopy image era has led to an expansion of techniques for automated spine detection, segmentation, and measurement. For a comprehensive overview, we recommend a thorough review presented by Okabe (2020).

4 Challenges and perspectives

In the examination of mesoscale connectivity within the context of connectivity-related brain disorders, we highlighted the following challenges: (i) refinement of human models; (ii) enhancement of imaging acquisition; and (iii) optimization of computational processing.

Human neural organoids are revolutionizing the study of neural development and diseases in a controlled *in vitro* setting, overcoming the limitations of traditional animal models. These organoids recapitulate the complexities of neural development, offering insights into health and diseases (Avansini et al., 2022). The *in vitro* system allows for drug testing, intervention studies, and close observation of potential side effects. Organoid models support experiments and correlative microscopy in multimodal platforms, enabling comprehensive characterizations of entire samples *in vivo*. This approach represents a significant stride in neurobiology and drug development. Neural tracing using viral vectors and X-ray markers offers precise tools to investigate neural connections and circuitry, enhancing imaging capabilities for detailed visualization and mapping of neural structures. This combination facilitates a deeper understanding of neural development.

From the perspective of image acquisition, EM provides unparalleled spatial resolution at the sub-micron to nanoscale, but it comes with challenges, including difficulties in measuring samples several micrometers thick due to the destructive nature of sample preparation for transmission images and limitations on molecular markers. Photon-based microscopies offer an alternative, capable of imaging multiple cell layers with single-cell identification resolution. Visible light microscopies simultaneously label numerous molecular markers, but a new physical phenomenon limits resolution due to the larger wavelength of light. Super-resolution microscopies (e.g., STED, SIM, PALM/STORM) overcome this limitation and are now widely available in bioimaging facilities, paving the way for enhanced imaging beyond traditional light microscopy constraints.

Expansion microscopy techniques have recently proven effective in reconstructing neuronal connections by employing a water-swellable polymer to expand tissue samples, overcoming optical microscopy limitations (Chen et al., 2015; Gallagher and Zhao, 2021; Lillvis et al., 2022; Kraft et al., 2023). This approach preserves sample integrity while providing detailed insights into cellular and sub-cellular details, including cell projections and connections.

A complementary approach involves increasing photon energy (i.e., shortening the wavelength), with X-rays being a prominent choice due to their deep penetration and high resolution. Although not practical for most benchtop equipment, synchrotron radiation techniques have demonstrated feasibility in neuronal connectomics, offering effective contrast for both unstained (phase propagation) and contrast-enhanced (absorption) samples (Kuan et al., 2020; Rodrigues et al., 2021; Claro et al., 2023). Scanning X-ray fluorescence can map cellular and subcellular chemical elements, potentially providing a biochemical signature for specific disorders (Finnegan et al., 2019; Álvarez-Marimon et al., 2021). Correlative Light and Electron Microscopy (CLEM) is a promising technique that seamlessly combines the advantages of light microscopy, such as molecular markers, with the high spatial resolution of EM. Particularly valuable for studying neural circuits, CLEM generates synaptic-level resolution images across a large field of view, revealing extensive neural circuitry. Its ability to incorporate fluorescent markers streamlines post-processing segmentation, resulting in a more precise reconstruction of neural networks (Iwasaki et al., 2022). It is important to highlight additional aspects of multimodal imaging. APEX2 and MiniSOG serve as genetic tags that are applicable not only in EM as molecular markers but are also suitable for X-ray tomography absorption contrast, as noted by Kuan et al. (2020). These tags, when fused with specific proteins, enable researchers to selectively label and study the dynamics of organelles, membrane structures, and the localization of proteins within cells in 3D space.

Computational processing in a High-Performance Computing (HPC) environment imposes several challenges, including storage of large datasets and models, memory capacity, and parallelization of algorithms (Zhang et al., 2023). Although deep learning techniques have been demonstrated as a cornerstone approach for image analysis, the use of such algorithms on large-scale datasets in HPC environments still requires advanced expertise in the design of parallel algorithms and programming in specialized language programming (e.g., C/C++, CUDA). To overcome this limitation, a new research area, called High-Performance Machine Learning, has recently emerged to provide methodologies and tools that explore data and model parallelism in a heterogeneous computing environment, i.e., composed of hundreds of CPU cores and GPUs, transparently to the users (Website, no date). Thus, the researchers can focus efforts on solving the problem by designing proper algorithms, without caring about model size and how to feed the neural networks with large datasets.

Another crucial limitation of deep learning techniques is their dependency on labeling data. Machine learning has streamlined the manual processing of imaging data, yet the scarcity of validated annotated datasets are bottlenecks. Collaboration within neuroscience is vital for creating integrated, standardized and multiscale validated datasets, akin to efforts by the Allen Institute. The demand for multidisciplinary experts in neurosciences and computational vision is rising to evaluate machine learning model predictions. Synthetic data generated by artificial intelligence serves as a data augmentation resource, mitigating the scarcity of labeled data in deep learning training. Vision transformers and morphological features for neuron classification are reshaping image analysis, enhancing algorithm performance, particularly with large datasets, and providing efficient methods to quantify mesoscale connectivity.

5 Conclusion

To attain a comprehensive understanding of brain function it is essential to seamlessly integrate cellular functions into the broader framework of brain organization. This integration involves incorporating fine details, ranging from the intricacies of dendritic spines to the branching patterns and interactions of individual neurons, into tridimensional models of neuronal network formation and adaptation to stimuli. A critical aspect of this integration is the preservation of the hierarchical organization of brain tissue, ensuring that cellular and sub-cellular data become an intrinsic part of the entire network. The mesoscale (cell-cell interactions) information links the micro/nanoscale (cellular and subcellular data) to the macro scale (whole brain functioning network). As such, integrative data can retrieve meaningful connections between cells, providing deeper insights into the complex neural network and reveal mechanisms underlying neurological and psychiatric disorders. Our review article aimed to highlight the state-of-the-art of the innovative field of neuroimaging in the context of the mesoscale, giving particular attention to its importance for a better comprehension of schizophrenia and epilepsy. This work presented the main techniques for image acquisition, data processing, and analysis optimized for mesoscale, emphasizing their distinctive aspects in analyzing specific structures, as well as acknowledging their limitations, especially concerning sample integrity. In this regard, we pinpoint multimodal imaging techniques like CLEM are emerging as the next frontier to capture large volumes in fine detail. Additionally, the latest (4th) generation of synchrotron accelerators offers approximately 1000x faster measurement capacities, enabling objective data generation through scanning, volume registration studies, and increased sample sizes (Winding et al., 2023).

Like every frontier of knowledge, neuroimaging is continuously expanding and experiencing rapid innovations. Its interdisciplinarity should not, therefore, be the primary limitation to its advancement. It is crucial that neuroscientists and computer scientists can comprehend the uses and potentials within the field of neuroimaging through a shared language.

Author contributions

AC: Conceptualization, Writing – original draft, Writing – review and editing. AA: Conceptualization, Writing – original draft, Writing – review and editing. MA: Conceptualization, Writing – original draft, Writing – review and editing. BS: Conceptualization, Writing – original draft, Writing – review and editing. JR: Writing – original draft, Writing – review and editing.

CC: Writing – review and editing. MF: Writing – review and editing. AP: Supervision, Writing – review and editing. LP-S: Writing – review and editing. SA: Conceptualization, Supervision, Writing – original draft, Writing – review and editing. MC: Conceptualization, Supervision, Writing – review and editing.

Funding

The author(s) declare financial support was received for the research, authorship, and/or publication of this article. This work was supported by a grant to SA by International Brain Research Organization (IBRO) and to MC and MF by São Paulo Research Foundation - FAPESP (grant No. 2018/16453-8). Thanks to scholarship to MF by Brazilian National Council for Scientific and Technological Development-CNPq (grant No. 141253/2019-3) and Coordenação de Aperfeiçoamento de Pessoal de Nível Superior – Brasil-CAPES (PROEX, 33003017040P8). CNPEM (FNDCT-MCTI) is acknowledged for supporting and open-access of the core facilities.

Acknowledgments

Artificial intelligence: Chatgpt (GPT-3.5 version) and Bard (2023.10.30 release) were employed in this article to refine the academic language of this review article.

Conflict of interest

The authors declare that the research was conducted in the absence of any commercial or financial relationships that could be construed as a potential conflict of interest.

Publisher's note

References

Abdijadid, S., Mathern, G., Levine, M., and Cepeda, C. (2015). Basic mechanisms of epileptogenesis in pediatric cortical dysplasia. *CNS Neurosci. Ther.* 21, 92–103.

Aghakhani, Y., Kinay, D., Gotman, J., Soualmi, L., Andermann, F., Olivier, A., et al. (2005). The role of periventricular nodular heterotopia in epileptogenesis. *Brain* 128(Pt 3), 641–651.

Alexander, A., Lee, J., Lazar, M., and Field, A. (2007). Diffusion tensor imaging of the brain. *Neurotherapeutics* 4, 316–329.

Álvarez-Marimon, E., Castillo-Michel, H., Reyes-Herrera, J., Seira, J., Aso, E., Carmona, M., et al. (2021). Synchrotron X-ray fluorescence and FTIR signatures for amyloid fibrillary and nonfibrillary plaques. *ACS Chem. Neurosci.* 12, 1961–1971. doi: 10.1021/acschemneuro.1c00048

Ananth, H., Popescu, I., Critchley, H., Good, C., Frackowiak, R., and Dolan, R. (2002). Cortical and subcortical gray matter abnormalities in schizophrenia determined through structural magnetic resonance imaging with optimized volumetric voxel-based morphometry. *Am. J. Psychiatry* 159, 1497–1505. doi: 10.1176/appi.ajp.159.9.1497

Anticevic, A., Cole, M., Repovs, G., Murray, J., Brumbaugh, M., Winkler, A., et al. (2014). Characterizing thalamo-cortical disturbances in schizophrenia and bipolar illness. *Cereb. Cortex* 24, 3116–3130. doi: 10.1093/cercor/bht165

Anticevic, A., Haut, K., Murray, J., Repovs, G., Yang, G., Diehl, C., et al. (2015). Association of thalamic dysconnectivity and conversion to psychosis in youth and young adults at elevated clinical risk. *JAMA Psychiatry* 72, 882–891. doi: 10.1001/jamapsychiatry.2015.0566

Arellano, J., Benavides-Piccione, R., Defelipe, J., and Yuste, R. (2007). Ultrastructure of dendritic spines: correlation between synaptic and spine morphologies. *Front. Neurosci.* 1:131–143. doi: 10.3389/neuro.01.1.1.010.2007

Avansini, S., Puppo, F., Adams, J., Vieira, A., Coan, A., Rogerio, F., et al. (2022). Junctional instability in neuroepithelium and network hyperexcitability in a focal cortical dysplasia human model. *Brain* 145, 1962–1977. doi: 10.1093/brain/awab479

Axer, M., and Amunts, K. (2022). Scale matters: the nested human connectome. *Science* 378, 500–504. doi: 10.1126/science.abq2599

Babb, T. (1991). Bilateral pathological damage in temporal lobe epilepsy. *Can. J. Neurol. Sci.* 18 4(Suppl.), 645–648.

Baliyan, V., Das, C. J., Sharma, R., and Gupta, A. K. (2016). Diffusion weighted imaging: technique and applications. *World J. Radiol.* 8, 785–798.

Bartolomei, F., Khalil, M., Wendling, F., Sontheimer, A., Régis, J., Ranjeva, J., et al. (2005). Entorhinal cortex involvement in human mesial temporal lobe epilepsy: an electrophysiologic and volumetric study. *Epilepsia* 46, 677–687.

Basu, S., Saha, P., Roszkowska, M., Magnowska, M., Baczynska, E., Das, N., et al. (2018). Quantitative 3-D morphometric analysis of individual dendritic spines. *Sci Rep.* 8:3545.

Bazinet, V., Hansen, J., Vos, de Wael, R., Bernhardt, B., van den Heuvel, M., et al. (2023). Assortative mixing in micro-architecturally annotated brain connectomes. *Nat. Commun.* 14:2850. doi: 10.1038/s41467-023-38585-4

Beck, K., Arumuham, A., Veronese, M., Santangelo, B., McGinnity, C., Dunn, J., et al. (2021). N-methyl-D-aspartate receptor availability in first-episode psychosis: a PET-MR brain imaging study. *Transl. Psychiatry* 11:425.

Behrens, T., and Sporns, O. (2012). Human connectomics. *Curr. Opin. Neurobiol.* 22, 144–153.

Belgiu, M., and Drăguţ, L. (2016). Random forest in remote sensing: a review of applications and future directions. *ISPRS J. Photogrammetry Remote Sens.* 114, 24–31.

Bennett, S. H., Kirby, A. J., and Finnerty, G. T. (2018). Rewiring the connectome: evidence and effects. *Neurosci. Biobehav. Rev.* 88, 51–62. doi: 10.1016/j.neubiorev.2018.03.001

Bernasconi, N., Duchesne, S., Janke, A., Lerch, J., Collins, D., and Bernasconi, A. (2004). Whole-brain voxel-based statistical analysis of gray matter and white matter in temporal lobe epilepsy. *Neuroimage* 23, 717–723. doi: 10.1016/j.neuroimage.2004.06.015

Berndt, M., Trusel, M., Roberts, T., Pfeiffer, B., and Volk, L. (2023). Bidirectional synaptic changes in deep and superficial hippocampal neurons following in vivo activity. *Neuron* 111, 2984–2994.e4. doi: 10.1016/j.neuron.2023.08.014

Bernhardt, B., Bernasconi, N., Kim, H., and Bernasconi, A. (2012). Mapping thalamocortical network pathology in temporal lobe epilepsy. *Neurology* 78, 129–136.

Bernhardt, B., Hong, S., Bernasconi, A., and Bernasconi, N. (2013). Imaging structural and functional brain networks in temporal lobe epilepsy. *Front. Hum. Neurosci.* 7:624. doi: 10.3389/fnhum.2013.00624

Betz, O., Wegst, U., Weide, D., Heethoff, M., Helfen, L., Lee, W., et al. (2007). Imaging applications of synchrotron X-ray phase-contrast microtomography in biological morphology and biomaterials science. I. general aspects of the technique and its advantages in the analysis of millimetre-sized arthropod structure. *J. Microsc.* 227, 51–71. doi: 10.1111/j.1365-2818.2007.01785.x

Beyer, J., Trodil, J., Boorboor, S., Hadwiger, M., Kaufman, A., and Pfister, H. (2022). A survey of visualization and analysis in high-resolution connectomics. *Comput. Graphics Forum* 41, 573–607. doi: 10.3389/fncir.2018.00090

Bird, A., and Cuntz, H. (2019). Dissecting sholl analysis into its functional components. *Cell* Rep. 27, 3081–3096.e5. doi: 10.1016/j.celrep.2019.04.097

Biswal, B., Yetkin, F., Haughton, V., and Hyde, J. (1995). Functional connectivity in the motor cortex of resting human brain using echo-planar MRI. *Magn. Reson. Med.* 34, 537–541.

Bjerke, I., Yates, S., Carey, H., Bjaalie, J., and Leergaard, T. (2023). Scaling up cell-counting efforts in neuroscience through semi-automated methods. *iScience* 26:107562. doi: 10.1016/j.isci.2023.107562

Blümcke, I., Zuschratter, W., Schewe, J., Suter, B., Lie, A., Riederer, B., et al. (1999). Cellular pathology of hilar neurons in Ammon's horn sclerosis. *J. Comp. Neurol.* 414, 437–453.

Bohland, J., Wu, C., Barbas, H., Bokil, H., Bota, M., Breiter, H., et al. (2009). A proposal for a coordinated effort for the determination of brainwide neuroanatomical connectivity in model organisms at a mesoscopic scale. *PLoS Comput. Biol.* 5:e1000334. doi: 10.1371/journal.pcbi.1000334

Bonilha, L., Helpern, J., Sainju, R., Nesland, T., Edwards, J., Glazier, S., et al. (2013). Presurgical connectome and postsurgical seizure control in temporal lobe epilepsy. *Neurology* 81, 1704–1710.

Bosch, C., Ackels, T., Pacureanu, A., Zhang, Y., Peddie, C., Berning, M., et al. (2022). Functional and multiscale 3D structural investigation of brain tissue through correlative in vivo physiology, synchrotron microtomography and volume electron microscopy. *Nat. Commun.* 13:2923. doi: 10.1038/s41467-022-30199-6

Bria, A., and Iannello, G. (2012). TeraStitcher - a tool for fast automatic 3D-stitching of teravoxel-sized microscopy images. *BMC Bioinformatics* 13:316. doi: 10.1186/1471-2105-13-316

Caballero, A., and Tseng, K. (2016). GABAergic function as a limiting factor for prefrontal maturation during adolescence. *Trends Neurosci.* 39, 441–448. doi: 10.1016/j.tins.2016.04.010

Cabral, J., Kringelbach, M., and Deco, G. (2017). Functional connectivity dynamically evolves on multiple time-scales over a static structural connectome: models and mechanisms. *Neuroimage* 160, 84–96. doi: 10.1016/j.neuroimage.2017.03.045

Cai, M., Wang, R., Liu, M., Du, X., Xue, K., Ji, Y., et al. (2022). Disrupted local functional connectivity in schizophrenia: an updated and extended meta-analysis. *Schizophrenia* 8:93. doi: 10.1038/s41537-022-00311-2

Cardona, A., Saalfeld, S., Schindelin, J., Arganda-Carreras, I., Preibisch, S., Longair, M., et al. (2012). TrakEM2 software for neural circuit reconstruction. *PLoS One* 7:e38011. doi: 10.1371/journal.pone.0038011

Carey, H., Pegios, M., Martin, L., Saleeba, C., Turner, A., Everett, N., et al. (2023). DeepSlice: rapid fully automatic registration of mouse brain imaging to a volumetric atlas. *Nat. Commun.* 14:5884. doi: 10.1038/s41467-023-41645-4

Cazemier, J., Clascá, F., and Tiesinga, P. (2016). Connectomic analysis of brain networks: novel techniques and future directions. *Front. Neuroanat.* 10:110. doi: 10.3389/fnana.2016.00110

Chang, J.-B., Chen, F., Yoon, Y., Jung, E., Babcock, H., and Kang, J. (2017). Iterative expansion microscopy. *Nat. Methods* 14, 593–599. doi: 10.1016/bs.mcb.2020.06.003

Chen, F., Tillberg, P., and Boyden, E. (2015). Optical imaging expansion microscopy. *Science* 347, 543–548.

Chen, S., He, Z., Han, X., He, X., Li, R., Zhu, H., et al. (2019). How big data and high-performance computing drive brain science. *Genomics Proteomics Bioinformatics* 17, 381–392.

Chen, T., Wang, Y., Zhang, J., Wang, Z., Xu, J., Li, Y., et al. (2017). Abnormal concentration of GABA and glutamate in the prefrontal cortex in schizophrenia.-an in vivo 1H-MRS study. *Shanghai Arch. Psychiatry* 29, 277–286. doi: 10.11919/j.issn.1002-0829.217004

Chen, Y., Almarzouqi, S. J., Morgan, M. L., and Lee, A. G. (2018). "T1-weighted image", *in Encyclopedia of Ophthalmology*, eds U. Schmidt-Erfurth and T. Kohnen. Berlin: Springer.

Chen, Y., Rex, C., Rice, C., Dubé, C., Gall, C., Lynch, G., et al. (2010). Correlated memory defects and hippocampal dendritic spine loss after acute stress involve corticotropin-releasing hormone signaling. *Proc. Natl. Acad. Sci. U S A.* 107, 13123–13128. doi: 10.1073/pnas.1003825107

Claro, P. I. C., Borges, E. P. S., Schleder, G. R., Archilha, N. L., Pinto, A., and Carvalho, M. (2023). From micro- to nano- and time-resolved x-ray computed tomography: bio-based applications, synchrotron capabilities, and data-driven processing. *Appl. Phys. Rev.* 10:021301.

Contreras-Rodríguez, O., Pujol, J., Batalla, I., Harrison, B., Soriano-Mas, C., Deus, J., et al. (2015). Functional connectivity bias in the prefrontal cortex of psychopaths. *Biol. Psychiatry* 78, 647–655. doi: 10.1016/j.biopsych.2014.03.007

Coras, R., Holthausen, H., and Sarnat, H. (2021). Focal cortical dysplasia type 1. *Brain Pathol.* 31:e12964.

Corle, T. R., and Kino, G. S. (1996). "Chapter 1 – Introduction," in *Confocal Scanning Optical Microscopy and Related Imaging Systems*, eds T. R. Corle and G. S. Kino (Cambridge, MA: Academic Press), doi: 10.1016/B978-012408750-7/50009-4

Creese, I., Burt, D., and Snyder, S. (1976). Dopamine receptor binding predicts clinical and pharmacological potencies of antischizophrenic drugs. *Science* 192, 481–483.

Cristianini, N., and Ricci, E. (2008). "Support vector machines," in *Encyclopedia of Algorithms*, ed. M. Y. Kao (Boston, MA: Springer).

Dai, T., Dubois, M., Arulkumaran, K., Campbell, J., Bass, C., Billot, B., et al. (2019). *Deep Reinforcement Learning for Subpixel Neural Tracking*. Available Online at: https://openreview.net/pdf?id=HJxrNvv0JN (accessed 21 June 2023).

Das, A., Holden, S., Borovicka, J., Icardi, J., O'Niel, A., Chaklai, A., et al. (2023). Large-scale recording of neuronal activity in freely-moving mice at cellular resolution. *Nat. Commun.* 14:6399. doi: 10.1038/s41467-023-42083-y

Delevich, K., Thomas, A., and Wilbrecht, L. (2018). Adolescence and late blooming synapses of the prefrontal cortex. *Cold Spring Harb. Symp. Quant. Biol.* 83, 37–43.

Denk, W., Strickler, J., and Webb, W. (1990). Two-photon laser scanning fluorescence microscopy. *Science* 248, 73–76.

Desai, A., and Mitchison, T. (1997). Microtubule polymerization dynamics. *Annu. Rev. Cell Dev. Biol.* 13, 83–17.

Devous, M. (1995). SPECT functional brain imaging. technical considerations. *J. Neuroimaging.* 5, S2–S13.

Dickstein, D., Dickstein, D., Janssen, W., Hof, P., Glaser, J., Rodriguez, A., et al. (2016). Automatic dendritic spine quantification from confocal data with neurolucida 360. *Curr. Protoc. Neurosci.* 77, 1.27.1–1.27.21. doi: 10.1002/cpns.16

Dijkstra, E. W. (1959). A note on two problems in connexion with graphs. *Numerische Mathematik* 1, 269–271.

Du, X., Zhang, H., and Parent, J. (2017). Rabies tracing of birthdated dentate granule cells in rat temporal lobe epilepsy. *Ann. Neurol.* 81, 790–803. doi: 10.1002/ana.24946

Dubeau, F., Tampieri, D., Lee, N., Andermann, E., Carpenter, S., Leblanc, R., et al. (1995). Periventricular and subcortical nodular heterotopia. a study of 33 patients. *Brain* 118, 1273–1287.

Durkee, M., Abraham, R., Clark, M., and Giger, M. (2021). Artificial intelligence and cellular segmentation in tissue microscopy images. *Am. J. Pathol.* 191, 1693–1701.

Ekaterina, P., Peter, V., Smirnova, D., Vyacheslav, C., and Ilya, B. (2023). SpineTool is an open-source software for analysis of morphology of dendritic spines. *Sci. Rep.* 13:10561. doi: 10.1038/s41598-023-37406-4

Ekşioğlu, Y., Scheffer, I., Cardenas, P., Knoll, J., DiMario, F., Ramsby, G., et al. (1996). Periventricular heterotopia: an X-linked dominant epilepsy locus causing aberrant cerebral cortical development. *Neuron* 16, 77–87. doi: 10.1016/s0896-6273(00)80025-2

Englot, D., Konrad, P., and Morgan, V. (2016). Regional and global connectivity disturbances in focal epilepsy, related neurocognitive sequelae, and potential mechanistic underpinnings. *Epilepsia* 57, 1546–1557. doi: 10.1111/epi.13510

Erdeniz, B., Serin, E., İbadi, Y., and Taş, C. (2017). Decreased functional connectivity in schizophrenia: the relationship between social functioning, social cognition and graph theoretical network measures. *Psychiatry Res. Neuroimaging* 270, 22–31. doi: 10.1016/j.pscychresns.2017.09.011

Feng, L., Zhao, T., and Kim, J. (2015). neuTube 1.0: a new design for efficient neuron reconstruction software based on the SWC format. *eNeuro* 2:ENEURO.0049-14.2014. doi: 10.1523/ENEURO.0049-14.2014

Fiala, J., Spacek, J., and Harris, K. (2002). Dendritic spine pathology: cause or consequence of neurological disorders? *Brain Res. Rev.* 39, 29–54.

Finnegan, M., Visanji, N., Romero-Canelon, I., House, E., Rajan, S., Mosselmans, J., et al. (2019). Synchrotron XRF imaging of Alzheimer's disease basal ganglia reveals linear dependence of high-field magnetic resonance microscopy on tissue iron concentration. *J. Neurosci. Methods* 319, 28–39. doi: 10.1016/j.jneumeth.2019.03.002

Fischl, B. (2012). FreeSurfer. *NeuroImage* 62, 774–781.

Fisher, R. (2017). An overview of the 2017 ILAE operational classification of seizure types. *Epilepsy Behav.* 70, 271–273.

Fisher, R., Scharfman, H., and deCurtis, M. (2014). How can we identify ictal and interictal abnormal activity? *Adv. Exp. Med. Biol.* 813, 3–23.

Foley, J. D. (1990). *Computer Graphics: Principles and Practice.* Boston, MA: Addison-Wesley.

Fonseca, M., Araujo, B., Dias, C., Archilha, N., Neto, D., Cavalheiro, E., et al. (2018). High-resolution synchrotron-based X-ray microtomography as a tool to unveil the three-dimensional neuronal architecture of the brain. *Sci Rep.* 8:12074. doi: 10.1038/s41598-018-30501-x

Fornito, A., Bullmore, E., and Zalesky, A. (2017). Opportunities and challenges for psychiatry in the connectomic era. *Biol. Psychiatry Cogn. Neurosci. Neuroimaging* 2, 9–19.

Fosque, B., Sun, Y., Dana, H., Yang, C., Ohyama, T., Tadross, M., et al. (2015). Neural circuits. labeling of active neural circuits in vivo with designed calcium integrators. *Science* 347, 755–760. doi: 10.1126/science.1260922

Frangi, A. F., Niessen, W. J., Vincken, K. L., and Viergever, M. A. (1998). "Multiscale vessel enhancement filtering," in *Medical Image Computing and Computer-Assisted*

Intervention — MICCAI'98. MICCAI 1998. Lecture Notes in Computer Science, eds W. M. Wells, A. Colchester, and S. Delp (Berlin: Springer), doi: 10.1007/BFb0056195

Frasconi, P., Silvestri, L., Soda, P., Cortini, R., Pavone, F. S., and Iannello, G. (2014). Large-scale automated identification of mouse brain cells in confocal light sheet microscopy images. *Bioinformatics* 30, i587–i593. doi: 10.1093/bioinformatics/btu469

Friedmann, D., Pun, A., Adams, E., Lui, J., Kebschull, J., Grutzner, S., et al. (2020). Mapping mesoscale axonal projections in the mouse brain using a 3D convolutional network. *Proc. Natl. Acad. Sci. U S A.* 117, 11068–11075. doi: 10.1073/pnas.1918465117

Gallagher, B., and Zhao, Y. (2021). Expansion microscopy: a powerful nanoscale imaging tool for neuroscientists. *Neurobiol. Dis.* 154:105362. doi: 10.1016/j.nbd.2021.105362

Gao, S., Yang, K., Shi, H., Wang, K., and Bai, J. (2022). *Review on Panoramic Imaging and its Applications in Scene Understanding.* Piscataway, NJ: IEEE.

Gao, W., Yang, S., Mack, N., and Chamberlin, L. (2022). Aberrant maturation and connectivity of prefrontal cortex in schizophrenia-contribution of NMDA receptor development and hypofunction. *Mol. Psychiatry* 27, 731–743. doi: 10.1038/s41380-021-01196-w

Garrity, A., Pearlson, G., McKiernan, K., Lloyd, D., Kiehl, K., and Calhoun, V. (2007). Aberrant default mode functional connectivity in schizophrenia. *Am. J. Psychiatry* 164, 450–457.

Gay, H., and Anderson, T. (1954). Serial sections for electron microscopy. *Science* 120, 1071–1073.

Glantz, L., and Lewis, D. (2000). Decreased dendritic spine density on prefrontal cortical pyramidal neurons in schizophrenia. *Arch. Gen. Psychiatry* 57, 65–73.

Godwin, D., Ji, A., Kandala, S., and Mamah, D. (2017). Functional connectivity of cognitive brain networks in schizophrenia during a working memory task. *Front. Psychiatry* 8:294. doi: 10.3389/fpsyt.2017.00294

Goodfellow, I. J., Pouget-Abadie, J., Mirza, M., Xu, B., Warder-Farley, D., and Ozair, S. (2014). *Generative Adversarial Networks*. Available online at: http://arxiv.org/abs/1406.2661 (accessed 7 November 2023).

Goubran, M., Leuze, C., Hsueh, B., Aswendt, M., Ye, L., Tian, Q., et al. (2019). Multimodal image registration and connectivity analysis for integration of connectomic data from microscopy to MRI. *Nat. Commun.* 10:5504. doi: 10.1038/s41467-019-13374-0

Govindan, S., Batti, L., Osterop, S., Stoppini, L., and Roux, A. (2021). Mass generation, neuron labeling, and 3D imaging of minibrains. *Front. Bioeng. Biotechnol.* 8:582650. doi: 10.3389/fbioe.2020.582650

Hagmann, P., Cammoun, L., Gigandet, X., Meuli, R., Honey, C., Wedeen, V., et al. (2008). Mapping the structural core of human cerebral cortex. *PLoS Biol.* 6:e159. doi: 10.1371/journal.pbio.0060159

Hallett, M., de Haan, W., Deco, G., Dengler, R., Di Iorio, R., Gallea, C., et al. (2020). Human brain connectivity: clinical applications for clinical neurophysiology. *Clin. Neurophysiol.* 131, 1621–1651.

Hatton, S., Huynh, K., Bonilha, L., Abela, E., Alhusaini, S., Altmann, A., et al. (2020). White matter abnormalities across different epilepsy syndromes in adults: an ENIGMA-epilepsy study. *Brain* 143, 2454–2473. doi: 10.1093/brain/awaa200

Haueis, P. (2021). Multiscale modeling of cortical gradients: the role of mesoscale circuits for linking macro- and microscale gradients of cortical organization and hierarchical information processing. *Neuroimage* 232:117846. doi: 10.1016/j.neuroimage.2021.117846

Hayes, T., and Pease, R. (1968). The scanning electron microscope: principles and applications in biology and medicine. *Adv. Biol. Med. Phys.* 12, 85–37. doi: 10.1016/b978-1-4831-9928-3.50006-0

He, K., Zhang, X., Ren, S., and Sun, J. (2015). Deep residual learning for image recognition. *arXiv [Preprint]*. Available Online at: http://arxiv.org/abs/1512.03385 (accessed October 10, 2024).

Henze, D., Urban, N., and Barrionuevo, G. (2000). The multifarious hippocampal mossy fiber pathway: a review. *Neuroscience* 98, 407–427. doi: 10.1016/s0306-4522(00)00146-9

Hering, H., and Sheng, M. (2001). Dendritic spines: structure, dynamics and regulation. *Nat. Rev. Neurosci.* 2, 880–888.

Hillman, E., Voleti, V., Li, W., and Yu, H. (2019). Light-sheet microscopy in neuroscience. *Annu Rev Neurosci.* 42, 295–313.

Hirsch, G., Bauer, C., and Merabet, L. (2015). Using structural and functional brain imaging to uncover how the brain adapts to blindness. *Ann. Neurosci. Psychol.* 2:5.

Holmes, A., Levi, P., Chen, Y., Chopra, S., Aquino, K., Pang, J., et al. (2023). Disruptions of hierarchical cortical organization in early psychosis and schizophrenia. *Biol. Psychiatry Cogn. Neurosci. Neuroimaging* 8, 1240–1250.

Hong, B., Liu, J., Shen, L., Xie, Q., Yuan, J., Emrouznejad, A., et al. (2023). Graph partitioning algorithms with biological connectivity decisions for neuron reconstruction in electron microscope volumes. *Exp. Sys. Appl.* 222:119776.

Hong, S., Lee, H., Gill, R., Crane, J., Sziklas, V., Bernhardt, B., et al. (2019). A connectome-based mechanistic model of focal cortical dysplasia. *Brain* 142, 688–699. doi: 10.1093/brain/awz009

Hörl, D., Rojas Rusak, F., Preusser, F., Tillberg, P., Randel, N., Chhetri, R., et al. (2019). BigStitcher: reconstructing high-resolution image datasets of cleared and expanded samples. *Nat. Methods* 16, 870–874. doi: 10.1038/s41592-019-0501-0

Howard, A., Huszar, I., Smart, A., Cottaar, M., Daubney, G., Hanayik, T., et al. (2023). An open resource combining multi-contrast MRI and microscopy in the macaque brain. *Nat. Commun.* 14:4320. doi: 10.1038/s41467-023-39916-1

Howes, O., Montgomery, A., Asselin, M., Murray, R., Valli, I., Tabraham, P., et al. (2009). Elevated striatal dopamine function linked to prodromal signs of schizophrenia. *Arch. Gen. Psychiatry* 66, 13–20. doi: 10.1001/archgenpsychiatry.2008.514

Hsieh, L., Wen, J., Claycomb, K., Huang, Y., Harrsch, F., Naegele, J., et al. (2016). Convulsive seizures from experimental focal cortical dysplasia occur independently of cell misplacement. *Nat. Commun.* 7:11753. doi: 10.1038/ncomms11753

Hu, T., Xu, X., Chen, S., and Liu, Q. (2021). Accurate neuronal soma segmentation using 3D multi-task learning u-shaped fully convolutional neural networks. *Front. Neuroanat.* 14:592806. doi: 10.3389/fnana.2020.592806

Huang, C., Wang, J., Wang, S., and Zhang, Y. (2022). Applicable artificial intelligence for brain disease: a survey. *Neurocomputing* 504, 223–239.

Huang, H., Chen, C., Rong, B., Wan, Q., Chen, J., Liu, Z., et al. (2022). Resting-state functional connectivity of salience network in schizophrenia and depression. *Sci. Rep.* 12:11204.

Huang, Q., Cao, T., Chen, Y., Li, A., Zeng, S., and Quan, T. (2021). Automated neuron tracing using content-aware adaptive voxel scooping on CNN predicted probability map. *Front. Neuroanat.* 15:712842. doi: 10.3389/fnana.2021.712842

Hunt, M. J., Kopell, N., Traub, R., and Whittington, M. (2017). Aberrant network activity in Schizophrenia. *Trends Neurosci.* 40, 371–382.

Ishii, K., Kubo, K., Endo, T., Yoshida, K., Benner, S., Ito, Y., et al. (2015). Neuronal heterotopias affect the activities of distant brain areas and lead to behavioral deficits. *J. Neurosci.* 35, 12432–12445. doi: 10.1523/JNEUROSCI.3648-14.2015

Iwasaki, H., Ichinose, S., Tajika, Y., and Murakami, T. (2022). Recent technological advances in correlative light and electron microscopy for the comprehensive analysis of neural circuits. *Front. Neuroanat.* 16:1061078. doi: 10.3389/fnana.2022.1061078

Jahangir, M., Zhou, J., Lang, B., and Wang, X. (2021). GABAergic system dysfunction and challenges in Schizophrenia research. *Front. Cell Dev. Biol.* 9:663854. doi: 10.3389/fcell.2021.663854

Jamadar, S., Ward, P., Liang, E., Orchard, E., Chen, Z., and Egan, G. (2021). Metabolic and hemodynamic resting-state connectivity of the human brain: a high-temporal resolution simultaneous BOLD-fMRI and FDG-fPET multimodality study. *Cereb. Cortex* 31, 2855–2867.

Janoos, F., Mosaliganti, K., Xu, X., Machiraju, R., Huang, K., and Wong, S. (2009). Robust 3D reconstruction and identification of dendritic spines from optical microscopy imaging. *Med. Image Anal.* 13, 167–179. doi: 10.1016/j.media.2008.06.019

Jean, G., Carton, J., Haq, K., and Musto, A. (2023). The role of dendritic spines in epileptogenesis. *Front Cell Neurosci.* 17:1173694. doi: 10.3389/fncel.2023.1173694

Jehi, L. (2018). The epileptogenic zone: concept and definition. *Epilepsy Curr.* 18, 12–16.

Jeurissen, B., Descoteaux, M., Mori, S., and Leemans, A. (2019). Diffusion MRI fiber tractography of the brain. *NMR Biomed.* 32:e3785.

Jiang, M., Lee, C., Smith, K., and Swann, J. (1998). Spine loss and other persistent alterations of hippocampal pyramidal cell dendrites in a model of early-onset epilepsy. *J. Neurosci.* 18, 8356–8368. doi: 10.1523/JNEUROSCI.18-20-08356.1998

Jin, X., and Han, J. (2011). "K-Means Clustering," in *Encyclopedia of Machine Learning*, eds C. Sammut and G. I. Webb (Boston, MA: Springer).

Jolliffe, I. T. (2002). *Principal Component Analysis*, 2nd Edn. New York, NY: Springer.

Jonkman, J., and Brown, C. (2015). Any way you slice it-a comparison of confocal microscopy techniques. *J. Biomol. Tech.* 26, 54–65. doi: 10.7171/jbt.15-2602-003

Jørgensen, K., Nerland, S., Norbom, L., Doan, N., Nesvåg, R., Mørch-Johnsen, L., et al. (2016). Increased MRI-based cortical grey/white-matter contrast in sensory and motor regions in schizophrenia and bipolar disorder. *Psychol. Med.* 46, 1971–1985. doi: 10.1017/S0033291716000593

Kahn, R., Sommer, I., Murray, R., Meyer-Lindenberg, A., Weinberger, D., Cannon, T., et al. (2015). Schizophrenia. *Nat. Rev. Dis. Primers* 1:15067.

Kaiser, M. (2013). The potential of the human connectome as a biomarker of brain disease. *Front. Hum. Neurosci.* 7:484. doi: 10.3389/fnhum.2013.00484

Kapuscinski, J. (1995). DAPI: a DNA-specific fluorescent probe. *Biotech. Histochem.* 70, 220–233.

Kaur, S., Singla, J., Nikita, and Singh, A. (2021). "Review on medical image denoising techniques," in *2021 International Conference on Innovative Practices in Technology and Management (ICIPTM)*, (Piscatawy, NJ: IEEE).

Keller, P., and Ahrens, M. (2015). Visualizing whole-brain activity and development at the single-cell level using light-sheet microscopy. *Neuron* 85, 462–483. doi: 10.1016/j.neuron.2014.12.039

Khalil, R., Kallel, S., Farhat, A., and Dlotko, P. (2021). Topological sholl descriptors for neuronal clustering and classification. *bioRxiv [Preprint]*. Available online at: https://doi.org/10.1101/2021.01.15.426800 (accessed October 10, 2023).

Khan, S., Naseer, M., Hayat, M., Zamir, S. W., Khan, F. S., and Shah, M. (2022). Transformers in vision: a survey. *ACM Comput. Surv.* 54, 1–41.

Kim, B., Kim, H., Kim, S., and Hwang, Y. (2021). A brief review of non-invasive brain imaging technologies and the near-infrared optical bioimaging. *Appl. Microsc.* 51:9. doi: 10.1186/s42649-021-00058-7

Kim, K., Son, K., and Palmore, G. (2015). Neuron image analyzer: automated and accurate extraction of neuronal data from low quality images. *Sci. Rep.* 5:17062.

Koch, G., Amara, I., Davis, G., and Gillings, D. (1982). A review of some statistical methods for covariance analysis of categorical data. *Biometrics* 38, 563–595.

Kollem, S., Reddy, K. R. L., and Rao, D. S. (2019). A review of image denoising and segmentation methods based on medical images. *Int. J. Mach. Learn. Comput.* 9, 288–295.

Konopaske, G., Lange, N., Coyle, J., and Benes, F. (2014). Prefrontal cortical dendritic spine pathology in schizophrenia and bipolar disorder. *JAMA Psychiatry* 71, 1323–1331.

Kraft, N., Muenz, T., Reinhard, S., Werner, C., Sauer, M., Groh, C., et al. (2023). Expansion microscopy in honeybee brains for high-resolution neuroanatomical analyses in social insects. *Cell Tissue Res.* 393, 489–506. doi: 10.1007/s00441-023-03803-4

Krasowski, N., Beier, T., Knott, G., Kothe, U., Hamprecht, F., and Kreshuk, A. (2018). Neuron segmentation with high-level biological priors. *IEEE Trans. Med. Imaging* 37, 829–839. doi: 10.1109/TMI.2017.2712360

Kuan, A., Phelps, J., Thomas, L., Nguyen, T., Han, J., Chen, C., et al. (2020). Dense neuronal reconstruction through X-ray holographic nano-tomography. *Nat. Neurosci.* 23, 1637–1643. doi: 10.1038/s41593-020-0704-9

Lanciego, J., and Wouterlood, F. (2020). Neuroanatomical tract-tracing techniques that did go viral. *Brain Struct. Funct.* 225, 1193–1224. doi: 10.1007/s00429-020-02041-6

Lang, E., Tomé, A., Keck, I., Górriz-Sáez, J., and Puntonet, C. (2012). Brain connectivity analysis: a short survey. *Comput. Intell. Neurosci.* 2012:412512. doi: 10.1155/2012/412512

Lee, M., O'Hara, N., Sonoda, M., Kuroda, N., Juhasz, C., Asano, E., et al. (2020). Novel deep learning network analysis of electrical stimulation mapping-driven diffusion MRI tractography to improve preoperative evaluation of pediatric epilepsy. *IEEE Trans. Biomed. Eng.* 67, 3151–3162. doi: 10.1109/TBME.2020.2977531

Levet, F., Tønnesen, J., Nägerl, U., and Sibarita, J. (2020). SpineJ: a software tool for quantitative analysis of nanoscale spine morphology. *Methods* 174, 49–55. doi: 10.1016/j.ymeth.2020.01.020

Lewis, D. (1997). Development of the prefrontal cortex during adolescence: insights into vulnerable neural circuits in schizophrenia. *Neuropsychopharmacology* 16, 385–398.

Lewis, D., Hashimoto, T., and Volk, D. (2005). Cortical inhibitory neurons and schizophrenia. *Nat. Rev. Neurosci.* 6, 312–324.

Li, A., Gong, H., Zhang, B., Wang, Q., Yan, C., Wu, J., et al. (2010). Micro-optical sectioning tomography to obtain a high-resolution atlas of the mouse brain. *Science* 330, 1404–1408.

Li, B., Sumera, A., Booker, S., and McCullagh, E. (2023). Current best practices for analysis of dendritic spine morphology and number in neurodevelopmental disorder research. *ACS Chem. Neurosci.* 14, 1561–1572. doi: 10.1021/acschemneuro.3c00062

Li, K., Vakharia, V. N., Sparks, R., França, L. G. S., Granados, A., McEvoy, A. W., et al. (2019). Optimizing trajectories for cranial laser interstitial thermal therapy using computer-assisted planning: A machine learning approach. *Neurotherapeutics* 16, 182–191. doi: 10.1007/s13311-018-00693-1

Li, Q., and Deng, Z. (2012). A surface-based 3-D dendritic spine detection approach from confocal microscopy images. *IEEE Trans. Image Process.* 21, 1223–1230. doi: 10.1109/TIP.2011.2166973

Li, R., Zhu, M., Li, J., Bienkowski, M., Foster, N., Xu, H., et al. (2019). Precise segmentation of densely interweaving neuron clusters using G-Cut. *Nat. Commun.* 10:1549. doi: 10.1038/s41467-019-09515-0

Lillvis, J., Otsuna, H., Ding, X., Pisarev, I., Kawase, T., Colonell, J., et al. (2022). Rapid reconstruction of neural circuits using tissue expansion and light sheet microscopy. *Elife* 11:e81248. doi: 10.7554/eLife.81248

Liu, C., Fan, J., Bailey, B., Müller, R., and Linke, A. (2023). Assessing predictive ability of dynamic time warping functional connectivity for ASD classification. *Int. J. Biomed. Imaging* 2023:8512461. doi: 10.1155/2023/8512461

Liu, C., Wang, D., Zhang, H., Wu, W., Sun, W., Zhao, T., et al. (2022). Using simulated training data of voxel-level generative models to improve 3D neuron reconstruction. *IEEE Trans. Med. Imaging* 41, 3624–3635. doi: 10.1109/TMI.2022.3191011

Liu, S., Zhang, D., Liu, S., Feng, D., Peng, H., and Cai, W. (2016). Rivulet: 3D neuron morphology tracing with iterative back-tracking. *Neuroinformatics* 14, 387–401. doi: 10.1007/s12021-016-9302-0

Liu, Y., Leong, A., Zhao, Y., Xiao, L., Mak, H., Tsang, A., et al. (2021). A low-cost and shielding-free ultra-low-field brain MRI scanner. *Nat. Commun.* 12:7238. doi: 10.1038/s41467-021-27317-1

Liu, Y., Wang, G., Ascoli, G., Zhou, J., and Liu, L. (2022). Neuron tracing from light microscopy images: automation, deep learning and bench testing. *Bioinformatics* 38, 5329–5339. doi: 10.1093/bioinformatics/btac712

Luengo-Sanchez, S., Fernaud-Espinosa, I., Bielza, C., Benavides-Piccione, R., Larrañaga, P., and DeFelipe, J. (2018). 3D morphology-based clustering and simulation of human pyramidal cell dendritic spines. *PLoS Comput. Biol.* 14:e1006221. doi: 10.1371/journal.pcbi.1006221

Luo, L., Callaway, E., and Svoboda, K. (2008). Genetic dissection of neural circuits. *Neuron* 57, 634–660.

MacDonald, M., Alhassan, J., Newman, J., Richard, M., Gu, H., Kelly, R., et al. (2017). Selective loss of smaller spines in Schizophrenia. *Am. J. Psychiatry* 174, 586–594. doi: 10.1176/appi.ajp.2017.16070814

Magliaro, C., Callara, A., Vanello, N., and Ahluwalia, A. (2019). Gotta Trace 'em all: a mini-review on tools and procedures for segmenting single neurons toward deciphering the structural connectome. *Front. Bioeng. Biotechnol.* 7:202. doi: 10.3389/fbioe.2019.00202

Mainen, Z., and Sejnowski, T. (1996). Influence of dendritic structure on firing pattern in model neocortical neurons. *Nature* 382, 363–366.

Marques, T., Ashok, A., Angelescu, I., Borgan, F., Myers, J., Lingford-Hughes, A., et al. (2021). GABA-A receptor differences in schizophrenia: a positron emission tomography study using [11C]Ro154513. *Mol. Psychiatry* 26, 2616–2625.

Martin, N., and Plavicki, J. (2020). Advancing zebrafish as a model for studying developmental neurotoxicology. *J. Neurosci. Res.* 98, 981–983. doi: 10.1002/jnr.24621

Martineau, F., Sahu, S., Plantier, V., Buhler, E., Schaller, F., Fournier, L., et al. (2018). Correct laminar positioning in the neocortex influences proper dendritic and synaptic development. *Cereb. Cortex* 28, 2976–2990. doi: 10.1093/cercor/bhy113

Mason, L. no date. "Boosting algorithms as gradient descent," in *Proceedings of the 12th International Conference on Neural Information Processing Systems*, (New York, NY: ACM).

McCutcheon, R., Krystal, J., and Howes, O. (2020). Dopamine and glutamate in schizophrenia: biology, symptoms and treatment. *World Psychiatry* 19, 15–33.

Mello, L., Cavalheiro, E., Tan, A., Kupfer, W., Pretorius, J., Babb, T., et al. (1993). Circuit mechanisms of seizures in the pilocarpine model of chronic epilepsy: cell loss and mossy fiber sprouting. *Epilepsia* 34, 985–995. doi: 10.1111/j.1528-1157.1993.tb02123.x

Mitra, P. (2014). The circuit architecture of whole brains at the mesoscopic scale. *Neuron* 83, 1273–1283.

Miyawaki, A., Llopis, J., Heim, R., McCaffery, J., Adams, J., Ikura, M., et al. (1997). Fluorescent indicators for Ca2+ based on green fluorescent proteins and calmodulin. *Nature* 388, 882–887.

Möhler, H. (2012). The GABA system in anxiety and depression and its therapeutic potential. *Neuropharmacology* 62, 42–53.

Motta, A., Berning, M., Boergens, K., Staffler, B., Beining, M., Loomba, S., et al. (2019). Dense connectomic reconstruction in layer 4 of the somatosensory cortex. *Science* 366:eaay3134.

Mukai, H., Hatanaka, Y., Mitsuhashi, K., Hojo, Y., Komatsuzaki, Y., Sato, R., et al. (2011). Automated analysis of spines from confocal laser microscopy images: application to the discrimination of androgen and estrogen effects on spinogenesis. *Cereb. Cortex* 21, 2704–2711. doi: 10.1093/cercor/bhr059

Muñoz-Castañeda, R., Zingg, B., Matho, K., Chen, X., Wang, Q., Foster, N., et al. (2021). Cellular anatomy of the mouse primary motor cortex. *Nature* 598, 159–166.

Najman, L., and Schmitt, M. (1994). Watershed of a continuous function. *Signal Process.* 38, 99–112.

Nakai, J., Ohkura, M., and Imoto, K. (2001). A high signal-to-noise Ca(2+) probe composed of a single green fluorescent protein. *Nat. Biotechnol.* 19, 137–141. doi: 10.1038/84397

Nemoto, K., Shimokawa, T., Fukunaga, M., Yamashita, F., Tamura, M., Yamamori, H., et al. (2020). Differentiation of schizophrenia using structural MRI with consideration of scanner differences: a real-world multisite study. *Psychiatry Clin. Neurosci.* 74, 56–63. doi: 10.1111/pcn.12934

Oh, J., Lee, C., and Kaang, B. (2019). Imaging and analysis of genetically encoded calcium indicators linking neural circuits and behaviors. *Korean J. Physiol. Pharmacol.* 23, 237–249.

Oh, S., Harris, J., Ng, L., Winslow, B., Cain, N., Mihalas, S., et al. (2014). A mesoscale connectome of the mouse brain. *Nature* 508, 207–214.

Okabe, S. (2020). Recent advances in computational methods for measurement of dendritic spines imaged by light microscopy. *Microscopy* 69, 196–213.

Oltmer, J., Rosenblum, E., Williams, E., Roy, J., Llamas-Rodriguez, J., Perosa, V., et al. (2023). Stereology neuron counts correlate with deep learning estimates in the human hippocampal subregions. *Sci. Rep.* 13:5884. doi: 10.1038/s41598-023-32903-y

Østerlund, I., Persson, S., and Nikoloski, Z. (2022). Tracing and tracking filamentous structures across scales: a systematic review. *Comput. Struct. Biotechnol. J.* 21, 452–462. doi: 10.1016/j.csbj.2022.12.023

Pachitariu, M., Stringer, C., Dipoppa, M., Schroder, S., Rossi, F., Dalgelshi, H., et al. (2017). Suite2p: beyond 10,000 neurons with standard two-photon microscopy. *bioRxiv [Preprint]*. Available online at: https://doi.org/10.1101/061507 (accessed January 1, 2024).

Papa, M., Bundman, M., Greenberger, V., and Segal, M. (1995). Morphological analysis of dendritic spine development in primary cultures of hippocampal neurons. *J. Neurosci.* 15(1 Pt 1), 1–11.

Patel, N., Vyas, N., Puri, B., Nijran, K., and Al-Nahhas, A. (2010). Positron emission tomography in schizophrenia: a new perspective. *J. Nucl. Med.* 51, 511–520.

Paşca, S. P., Arlotta, P., Bateup, H. S., Camp, J. G., Cappello, S., Gage, F. H., et al. (2022). A nomenclature consensus for nervous system organoids and assembloids. *Nature* 609, 907–910. doi: 10.1038/s41586-022-05219-6

Phelps, M. (2000). Positron emission tomography provides molecular imaging of biological processes. *Proc. Natl. Acad. Sci. U S A.* 97, 9226–9233.

Pisano, T., Hoag, A., Dhanerawala, Z., Guariglia, S., Jung, C., Boele, H., et al. (2022). Automated high-throughput mouse transsynaptic viral tracing using iDISCO+ tissue clearing, light-sheet microscopy, and BrainPipe. *STAR Protoc.* 3:101289. doi: 10.1016/j.xpro.2022.101289

Polavaram, S., Gillette, T., Parekh, R., and Ascoli, G. (2014). Statistical analysis and data mining of digital reconstructions of dendritic morphologies. *Front. Neuroanat.* 8:138. doi: 10.3389/fnana.2014.00138

Poldrack, R. (2007). Region of interest analysis for fMRI. *Soc. Cogn. Affect. Neurosci.* 2, 67–70.

Quan, T., Zhou, H., Li, J., Li, S., Li, A., Li, Y., et al. (2016). NeuroGPS-Tree: automatic reconstruction of large-scale neuronal populations with dense neurites. *Nat. Methods* 13, 51–54. doi: 10.1038/nmeth.3662

Rah, J., Feng, L., Druckmann, S., Lee, H., and Kim, J. (2015). From a meso- to micro-scale connectome: array tomography and mGRASP. *Front. Neuroanat.* 9:78. doi: 10.3389/fnana.2015.00078

Rajotte, J., Bergen, R., Buckeridge, D., El Emam, K., Ng, R., and Strome, E. (2022). Synthetic data as an enabler for machine learning applications in medicine. *iScience* 25:105331. doi: 10.1016/j.isci.2022.105331

Rees, C., Moradi, K., and Ascoli, G. (2017). Weighing the evidence in peters' rule: does neuronal morphology predict connectivity? *Trends Neurosci.* 40, 63–71. doi: 10.1016/j.tins.2016.11.007

Renier, N., Adams, E., Kirst, C., Wu, Z., Azevedo, R., Kohl, J., et al. (2016). Mapping of brain activity by automated volume analysis of immediate early genes. *Cell* 165, 1789–1802. doi: 10.1016/j.cell.2016.05.007

Renier, W., Gabreëls, F., and Jaspar, H. (1988). Morphological and biochemical analysis of a brain biopsy in a case of idiopathic lennox-gastaut syndrome. *Epilepsia* 29, 644–649. doi: 10.1111/j.1528-1157.1988.tb03776.x

Represa, A. (2019). Why malformations of cortical development cause epilepsy. *Front. Neurosci.* 13:250. doi: 10.3389/fnins.2019.00250

Richards, S., and Van Hooser, S. (2018). Neural architecture: from cells to circuits. *J. Neurophysiol.* 120, 854–866.

Rochefort, N., and Konnerth, A. (2012). Dendritic spines: from structure to in vivo function. *EMBO Rep.* 13, 699–708.

Rodrigues, P., Tostes, K., Bosque, B., de Godoy, J., Amorim Neto, D., Dias, C., et al. (2021). Illuminating the brain With X-rays: contributions and future perspectives of high-resolution microtomography to neuroscience. *Front. Neurosci.* 15:627994. doi: 10.3389/fnins.2021.627994

Rodriguez, A., Ehlenberger, D. B., Dickstein, D. L., Hof, P. R., and Wearne, S. L. (2008). Automated three-dimensional detection and shape classification of dendritic spines from fluorescence microscopy images. *PLoS One* 3:e1997. doi: 10.1371/journal.pone.0001997

Rodriguez, A., Ehlenberger, D., Hof, P., and Wearne, S. (2006). Rayburst sampling, an algorithm for automated three-dimensional shape analysis from laser scanning microscopy images. *Nat. Protoc.* 1, 2152–2161.

Ronneberger, O., Fischer, P., and Brox, T. (2015). "U-Net: convolutional networks for biomedical image segmentation," in *Proceedings of the International Medical Image Computing and Computer-Assisted Intervention – MICCAI 2015*, eds N. Navab, J. Hornegger, W. Wells, and A. Frangi (Cham: Springer).

Rossini, L., De Santis, D., Cecchini, E., Cagnoli, C., Maderna, E., Cartelli, D., et al. (2023). Dendritic spine loss in epileptogenic type II focal cortical dysplasia: role of enhanced classical complement pathway activation. *Brain Pathol.* 33:e13141. doi: 10.1111/bpa.13141

Rusakov, D., and Stewart, M. (1995). Quantification of dendritic spine populations using image analysis and a tilting disector. *J. Neurosci. Methods* 60, 11–21. doi: 10.1016/0165-0270(94)00215-3

Saleeba, C., Dempsey, B., Le, S., Goodchild, A., and McMullan, S. (2019). A student's guide to neural circuit tracing. *Front Neurosci.* 13:897. doi: 10.3389/fnins.2019.00897

Santuy, A., Tomás-Roca, L., Rodríguez, J., González-Soriano, J., Zhu, F., Qiu, Z., et al. (2020). Estimation of the number of synapses in the hippocampus and brain-wide by volume electron microscopy and genetic labeling. *Sci. Rep.* 10:14014. doi: 10.1038/s41598-020-70859-5

Sarvaiya, J. N., Patnaik, S., and Bombaywala, S. (2009). "Image registration by template matching using normalized cross-correlation," in *Proceedings of the 2009 International Conference on Advances in Computing, Control, and Telecommunication Technologies. Telecommunication Technologies (ACT)*, (Piscataway, NJ: IEEE).

Schapire, R. E., and Singer, Y. (1999). Improved boosting algorithms using confidence-rated predictions. *Machine Learn.* 37, 297–336. doi: 10.1007/s10994-005-1123-6

Scheibel, M., Davies, T., Lindsay, R., and Scheibel, A. (1974). Basilar dendrite bundles of giant pyramidal cells. *Exp. Neurol.* 42, 307–319. doi: 10.1016/0014-4886(74)90028-4

Schultz, S. K., and Andreasen, N. C. (1999). Schizophrenia. *Lancet* 353, 1425–1430.

Scorcioni, R., Polavaram, S., and Ascoli, G. (2008). L-Measure: a web-accessible tool for the analysis, comparison and search of digital reconstructions of neuronal morphologies. *Nat. Protoc.* 3, 866–876. doi: 10.1038/nprot.2008.51

Segato, A., Marzullo, A., Calimeri, F., and De Momi, E. (2020). Artificial intelligence for brain diseases: a systematic review. *APL Bioeng.* 4:041503.

Sellgren, C., Gracias, J., Watmuff, B., Biag, J., Thanos, J., Whittredge, P., et al. (2019). Increased synapse elimination by microglia in schizophrenia patient-derived models of synaptic pruning. *Nat. Neurosci.* 22, 374–385. doi: 10.1038/s41593-018-0334-7

Sethian, J. (1996). A fast marching level set method for monotonically advancing fronts. *Proc. Natl. Acad. Sci. U S A.* 93, 1591–1595. doi: 10.1073/pnas.93.4.1591

Shapleske, J., Rossell, S., Chitnis, X., Suckling, J., Simmons, A., Bullmore, E., et al. (2002). A computational morphometric MRI study of schizophrenia: effects of hallucinations. *Cereb. Cortex* 12, 1331–1341.

Shapson-Coe, A., Januszewski, M., Berger, D. R., Pope, A., Wu, Y., and Blakley, T. (2021). A connectomic study of a petascale fragment of human cerebral cortex. *bioRxiv [Preprint]*. Available Online at: https://doi.org/10.1101/2021.05.29.446289 (accessed January 1, 2024).

Sheffield, J., and Barch, D. (2016). Cognition and resting-state functional connectivity in schizophrenia. *Neurosci. Biobehav. Rev.* 61, 108–120.

Shenton, M., Hamoda, H., Schneiderman, J., Bouix, S., Pasternak, O., Rathi, Y., et al. (2012). A review of magnetic resonance imaging and diffusion tensor imaging findings in mild traumatic brain injury. *Brain Imaging Behav.* 6, 137–192.

Sheybani, L., Birot, G., Contestabile, A., Seeck, M., Kiss, J., Schaller, K., et al. (2018). Electrophysiological evidence for the development of a self-sustained large-scale epileptic network in the kainate mouse model of temporal lobe epilepsy. *J. Neurosci.* 38, 3776–3791. doi: 10.1523/JNEUROSCI.2193-17.2018

Shi, P., Huang, Y., and Hong, J. (2014). Automated three-dimensional reconstruction and morphological analysis of dendritic spines based on semi-supervised learning. *Biomed. Opt. Express* 5, 1541–1553. doi: 10.1364/BOE.5.001541

Shi, P., Zhou, X., Li, Q., Baron, M., Teylan, M., Kim, Y., et al. (2009). Online three-dimensional dendritic spines mophological classification based on semi-supervised learning. *Proc. IEEE Int. Symp. Biomed Imaging* 1019–1022. doi: 10.1109/ISBI.2009.5193228

Shih, C., Chen, N., Wang, T., He, G., Wang, G., Lin, Y., et al. (2021). NeuroRetriever: automatic neuron segmentation for connectome assembly. *Front. Syst. Neurosci.* 15:687182. doi: 10.3389/fnsys.2021.687182

Shukla, D., Wijtenburg, S., Chen, H., Chiappelli, J., Kochunov, P., Hong, L., et al. (2019). Anterior cingulate glutamate and GABA associations on functional connectivity in Schizophrenia. *Schizophr. Bull.* 45, 647–658.

Singh, P., Hernandez-Herrera, P., Labate, D., and Papadakis, M. (2017). Automated 3-D detection of dendritic spines from in vivo two-photon image stacks. *Neuroinformatics* 15, 303–319. doi: 10.1007/s12021-017-9332-2

Sisodiya, S., Whelan, C., Hatton, S., Huynh, K., Altmann, A., Ryten, M., et al. (2020). The ENIGMA-epilepsy working group: mapping disease from large data sets. *Hum Brain Mapp.* 43, 113–128. doi: 10.1002/hbm.25037

Smith, S. (2002). Fast robust automated brain extraction. *Hum. Brain Mapp.* 17, 143–155.

Sollee, J., Tang, L., Igiraneza, A., Xiao, B., Bai, H., and Yang, L. (2022). Artificial intelligence for medical image analysis in epilepsy. *Epilepsy Res.* 182:106861.

Spocter, M., Hopkins, W., Barks, S., Bianchi, S., Hehmeyer, A., Anderson, S., et al. (2012). Neuropil distribution in the cerebral cortex differs between humans and chimpanzees. *J. Comp. Neurol.* 520, 2917–2929.

Sporns, O. (2013). The human connectome: origins and challenges. *Neuroimage* 80, 53–61.

Sporns, O., Tononi, G., and Kötter, R. (2005). The human connectome: a structural description of the human brain. *PLoS Comput. Biol.* 1:e42. doi: 10.1371/journal.pcbi.0010042

Spruston, N. (2008). Pyramidal neurons: dendritic structure and synaptic integration. *Nat. Rev. Neurosci.* 9, 206–221.

Squire, L., Stark, C., and Clark, R. (2004). The medial temporal lobe. *Annu. Rev. Neurosci.* 27, 279–306.

Stachowiak, E., Benson, C., Narla, S., Dimitri, A., Chuye, L., Dhiman, S., et al. (2017). Cerebral organoids reveal early cortical maldevelopment in schizophrenia-computational anatomy and genomics, role of FGFR1. *Transl. Psychiatry* 7:6. doi: 10.1038/s41398-017-0054-x

Stafstrom, C., and Carmant, L. (2015). Seizures and epilepsy: an overview for neuroscientists. *Cold Spring Harb. Perspect. Med.* 5:a022426.

Stephan, K., and Friston, K. (2010). Analyzing effective connectivity with functional magnetic resonance imaging. *Wiley Interdiscip. Rev. Cogn. Sci.* 1, 446–459.

Stouffer, M., Golden, J., and Francis, F. (2016). Neuronal migration disorders: focus on the cytoskeleton and epilepsy. *Neurobiol. Dis.* 92, 18–45.

Stringer, C., Wang, T., Michaelos, M., and Pachitariu, M. (2021). Cellpose: a generalist algorithm for cellular segmentation. *Nat. Methods* 18, 100–106. doi: 10.1038/s41592-020-01018-x

Subramanian, L., Calcagnotto, M., and Paredes, M. (2020). Cortical malformations: lessons in human brain development. *Front. Cell Neurosci.* 13:576. doi: 10.3389/fncel.2019.00576

Tan, Y., Liu, M., Chen, W., Wang, X., Peng, H., and Wang, Y. (2020). DeepBranch: deep neural networks for branch point detection in biomedical images. *IEEE Trans. Med. Imaging* 39, 1195–1205. doi: 10.1109/TMI.2019.2945980

Toda, M., and Abi-Dargham, A. (2007). Dopamine hypothesis of schizophrenia: making sense of it all. *Curr. Psychiatry Rep.* 9, 329–336. doi: 10.1007/s11920-007-0041-7

Tyson, A., and Margrie, T. (2022). Mesoscale microscopy and image analysis tools for understanding the brain. *Prog. Biophys. Mol. Biol.* 168, 81–93.

Udvary, D., Harth, P., Macke, J., Hege, H., de Kock, C., Sakmann, B., et al. (2022). The impact of neuron morphology on cortical network architecture. *Cell Rep.* 39:110677.

Uranova, N., Orlovskaya, D., Vikhreva, O., Zimina, I., Kolomeets, N., Vostrikov, V., et al. (2001). Electron microscopy of oligodendroglia in severe mental illness. *Brain Res. Bull.* 55, 597–610.

Vakharia, V., Sparks, R., Li, K., O'Keeffe, A., Pérez-García, F., França, L., et al. (2019). Multicenter validation of automated trajectories for selective laser amygdalohippocampectomy. *Epilepsia* 60, 1949–1959. doi: 10.1111/epi.16307

van Pelt, J., and van Ooyen, A. (2013). Estimating neuronal connectivity from axonal and dendritic density fields. *Front. Comput. Neurosci.* 7:160. doi: 10.3389/fncom.2013.00160

Verma, S., Goel, T., Tanveer, M., Ding, W., Sharma, R., and Murugan, R. (2023). Machine learning techniques for the Schizophrenia diagnosis: a comprehensive review and future research directions. *J. Ambient Intelligence Humanized Comput.* 14, 4795–4807.

Vicidomini, G., Bianchini, P., and Diaspro, A. (2018). STED super-resolved microscopy. *Nat. Methods* 15, 173–182.

Vidaurre-Gallart, I., Fernaud-Espinosa, I., Cosmin-Toader, N., Talavera-Martínez, L., Martin-Abadal, M., Benavides-Piccione, R., et al. (2022). A deep learning-based workflow for dendritic spine segmentation. *Front. Neuroanat.* 16:817903. doi: 10.3389/fnana.2022.817903

von Campe, G., Spencer, D., and de Lanerolle, N. (1997). Morphology of dentate granule cells in the human epileptogenic hippocampus. *Hippocampus* 7, 472–488.

Walsh, C., Tafforeau, P., Wagner, W., Jafree, D., Bellier, A., Werlein, C., et al. (2021). Imaging intact human organs with local resolution of cellular structures using hierarchical phase-contrast tomography. *Nat. Methods* 18, 1532–1541. doi: 10.1038/s41592-021-01317-x

Wang, H., Zhu, Q., Ding, L., Shen, Y., Yang, C., Xu, F., et al. (2019). Scalable volumetric imaging for ultrahigh-speed brain mapping at synaptic resolution. *Natl. Sci. Rev.* 6, 982–992. doi: 10.1093/nsr/nwz053

Wang, L., Ye, X., Ju, L., He, W., Zhang, D., Wang, X., et al. (2023). Medical matting: medical image segmentation with uncertainty from the matting perspective. *Comput. Biol. Med.* 158:106714. doi: 10.1016/j.compbiomed.2023.106714

Wang, R., Wang, J., Ding, J., and Zhang, S. (2014). "Automatic segmentation and quantitative analysis of gray matter on MR images of patients with epilepsy based on unsupervised learning methods," in *Trends and Applications in Knowledge Discovery and Data Mining. PAKDD 2014. Lecture Notes in Computer Science*, eds W. Peng, et al. (Cham: Springer), doi: 10.1007/978-3-319-13186-3_54

Wang, Y., Lang, R., Li, R., and Zhang, J. (2022) *NRTR: Neuron Reconstruction with Transformer from 3D Optical Microscopy Images.* Available online at: http://arxiv.org/abs/2212.04163 (accessed 21, June 2023).

Wang, Y., Wang, C., Ranefall, P., Broussard, G. J., Wang, Y., Shi, G., et al. (2020). SynQuant: An automatic tool to quantify synapses from microscopy images. *Bioinformatics* 36, 1599–1606. doi: 10.1093/bioinformatics/btz760

Website no date. Available online at: https://dl.acm.org/doi/pdf/10.5555/3454287.3454297 (accessed November 15, 2023).

Wei, X., Liu, Q., Liu, M., Wang, Y., and Meijering, E. (2023). 3D soma detection in large-scale whole brain images via a two-stage neural network. *IEEE Trans. Med. Imaging* 42, 148–157. doi: 10.1109/TMI.2022.3206605

Wei, Y., Scholtens, L., Turk, E., and van den Heuvel, M. (2019). Multiscale examination of cytoarchitectonic similarity and human brain connectivity. *Netw. Neurosci.* 3, 124–137. doi: 10.1162/netn_a_00057

Weis, M. A., Hansel, L., Luddecke, T., and Ecker, A. S. (2021). Self-supervised graph representation learning for neuronal morphologies. *arXiv [Preprint]*. Available online at: http://arxiv.org/abs/2112.12482 (accessed 10 October 2023).

Welvaert, M., and Rosseel, Y. (2013). On the definition of signal-to-noise ratio and contrast-to-noise ratio for FMRI data. *PLoS One* 8:e77089. doi: 10.1371/journal.pone.0077089

Whelan, C., Altmann, A., Botía, J., Jahanshad, N., Hibar, D., Absil, J., et al. (2018). Structural brain abnormalities in the common epilepsies assessed in a worldwide ENIGMA study. *Brain* 141, 391–408. doi: 10.1093/brain/awx341

Whitfield-Gabrieli, S., Thermenos, H., Milanovic, S., Tsuang, M., Faraone, S., McCarley, R., et al. (2009). Hyperactivity and hyperconnectivity of the default network in schizophrenia and in first-degree relatives of persons with schizophrenia. *Proc. Natl. Acad. Sci. U S A.* 106, 1279–1284. doi: 10.1073/pnas.0809141106

Winding, M., Pedigo, B., Barnes, C., Patsolic, H., Park, Y., Kazimiers, T., et al. (2023). The connectome of an insect brain. *Science* 379:eadd9330.

Wong, M., and Guo, D. (2013). Dendritic spine pathology in epilepsy: cause or consequence? *Neuroscience* 251, 141–150.

Wu, C., Lin, T., Chiou, G., Lee, C., Luan, H., Tsai, M., et al. (2021). A systematic review of MRI neuroimaging for education research. *Front. Psychol.* 12:617599. doi: 10.3389/fpsyg.2021.617599

Wu, X., Sosunov, A., Lado, W., Teoh, J., Ham, A., Li, H., et al. (2022). Synaptic hyperexcitability of cytomegalic pyramidal neurons contributes to epileptogenesis in tuberous sclerosis complex. *Cell Rep.* 40:111085. doi: 10.1016/j.celrep.2022.111085

Xiao, H., and Peng, H. (2013). APP2: automatic tracing of 3D neuron morphology based on hierarchical pruning of a gray-weighted image distance-tree. *Bioinformatics* 29, 1448–1454. doi: 10.1093/bioinformatics/btt170

Xu, F., Jin, C., Zuo, T., Wang, R., Yang, Y., and Wang, K. (2022). Segmental abnormalities of superior longitudinal fasciculus microstructure in patients with schizophrenia, bipolar disorder, and attention-deficit/hyperactivity disorder: an automated fiber quantification tractography study. *Front. Psychiatry* 13:999384. doi: 10.3389/fpsyt.2022.999384

Xu, Z., Lai, J., Zhang, H., Ng, C., Zhang, P., Xu, D., et al. (2019). Regional homogeneity and functional connectivity analysis of resting-state magnetic resonance in patients with bipolar II disorder. *Medicine* 98:e17962.

Yamashita, R., Nishio, M., Do, R., and Togashi, K. (2018). Convolutional neural networks: an overview and application in radiology. *Insights Imaging* 9, 611–629.

Yang, B., Chen, W., Luo, H., Tan, Y., Liu, M., and Wang, Y. (2021a). Neuron image segmentation via learning deep features and enhancing weak neuronal structures. *IEEE J. Biomed. Health Informatics* 25, 1634–1645. doi: 10.1109/JBHI.2020.3017540

Yang, B., Huang, J., Wu, G., and Yang, J. (2021b). Classifying the tracing difficulty of 3D neuron image blocks based on deep learning. *Brain Inform.* 8:25. doi: 10.1186/s40708-021-00146-0

You, Z., Balbastre, Y., Bouvier, C., Hérard, A., Gipchtein, P., Hantraye, P., et al. (2019). Automated individualization of size-varying and touching neurons in macaque cerebral microscopic images. *Front. Neuroanat.* 13:98. doi: 10.3389/fnana.2019.00098

Zhang, L., Wang, M., Liu, M., and Zhang, D. (2020). A survey on deep learning for neuroimaging-based brain disorder analysis. *Front. Neurosci.* 14:779. doi: 10.3389/fnins.2020.00779

Zhang, P., Lee, B., and Qiao, Y. (2023). 'Experimental evaluation of the performance of Gpipe parallelism'. *Future Generations Comput. Syst.* 147, 107–118.

Zhang, Q., Liao, Y., Wang, X., Zhang, T., Feng, J., Deng, J., et al. (2021). A deep learning framework for 18F-FDG PET imaging diagnosis in pediatric patients with temporal lobe epilepsy. *Eur. J. Nucl. Med. Mol. Imaging* 48, 2476–2485. doi: 10.1007/s00259-020-05108-y

Zhang, Y., Chen, K., Baron, M., Teylan, M., Kim, Y., Song, Z., et al. (2010). A neurocomputational method for fully automated 3D dendritic spine detection and segmentation of medium-sized spiny neurons. *Neuroimage* 50, 1472–1484. doi: 10.1016/j.neuroimage.2010.01.048

Zhang, Z., Li, G., Xu, Y., and Tang, X. (2021). Application of artificial intelligence in the MRI classification task of human brain neurological and psychiatric diseases: a scoping review. *Diagnostics* 11:1402. doi: 10.3390/diagnostics11081402

Zhou, J., Cui, G., Hu, S., Zhang, Z., Yang, C., and Liu, Z. (2020). Graph neural networks: a review of methods and applications. *AI Open* 1, 57–81.

Zhou, Z., Sorensen, S. A., and Peng, H. (2015). "Neuron crawler: an automatic tracing algorithm for very large neuron images," in *Proceedings of the 2015 IEEE 12th International Symposium on Biomedical Imaging (ISBI)*, (Piscataway, NJ: IEEE).

Zhu, T., Yao, G., Hu, D., Xie, C., Li, P., Yang, X., et al. (2023). Data-driven morphological feature perception of single neuron with graph neural network. *IEEE Trans. Med. Imaging* 42, 3069–3079. doi: 10.1109/TMI.2023.3275209

Zolkefley, M., Firwana, Y., Hatta, H., Rowbin, C., Nassir, C., Hanafi, M., et al. (2021). An overview of fractional anisotropy as a reliable quantitative measurement for the corticospinal tract (CST) integrity in correlation with a Fugl-meyer assessment in stroke rehabilitation. *J. Phys. Ther. Sci.* 33, 75–83. doi: 10.1589/jpts.33.75

Glossary

Adaptive Boosting (AdaBoost):	is a meta-learning algorithm that combines weak learners, slightly outperforming random guessing, into a weighted sum during the training process (Schapire and Singer, 1999).
3D neural organoids:	three-dimensional structures generated from stem cells that can mimic certain aspects of the developing human brain (Paşca et al., 2022).
Calcium-modulated photoactivatable ratiometric integrator (CaMPARI):	a photoconvertible calcium indicator to investigate network dynamics. CaMPARI shifts from green to red fluorescence when exposed to calcium influx and violet light, allowing for precise identification of activated neuronal populations (Fosque et al., 2015).
Confocal microscopy:	light microscopy technique that uses a laser to illuminate a single plane eliminating out-of-focus light to produce sharp, high-contrast images (Jonkman and Brown, 2015).
Convolutional Neural Network (CNN):	neural network architecture for images that uses a hierarchical stack of convolutional layers to extract features (Yamashita et al., 2018).
Covariance:	statistical tool used to understand the relationship between two variables. A positive covariance means both variables increase together, while a negative covariance suggests that they move in opposite directions (Koch et al., 1982).
DAPI (4′,6-diamidino-2-phenylindole):	fluorescent probe that binds to the minor groove (A-T rich) of double-stranded DNA (Kapuscinski, 1995).
Diffusion weighted image (DWI):	MRI technique that measures water diffusion in tissues. DWI images are used to diagnose and monitor a variety of neurological disorders (Baliyan et al., 2016).
Diffusion MRI tractography:	allow assessing the topological organization of brain networks (Jeurissen et al., 2019).
Diffusion Tensor Imaging (DTI):	MRI-based technique that measures the diffusion of water molecules within the brain. DTI and tractography are employed to visualize and map the pathways of nerve fiber bundles and the white matter tracts (Alexander et al., 2007).
Dijkstra algorithm:	greedy graph algorithm for finding the shortest path from a single source node to all other nodes in a weighted graph (Dijkstra, 1959).
Effective connectivity:	the causal interactions among neural elements within a neural system aiming to identify their intricate interrelation (Stephan and Friston, 2010).
Electron microscopy (EM):	technique that uses electron beams instead of visible light to achieve much higher resolution in imaging (Hayes and Pease, 1968).
Epileptogenic zone:	macroscopic/microscopic brain lesion responsible for the generation of seizures (Jehi, 2018).
Fast Marching Method (FMM):	numerical method for finding the global minimum of an energy function (Sethian, 1996).
Fields Of View (FOV):	in optical instruments is the angle at the camera's vertex, created by the two edges that represent the maximum range within which the measured target's object can traverse (Gao S. et al., 2022).
Filament tracing:	bioimaging technique used to reconstruct the three-dimensional (3D) morphology of neuronal filaments, such as axons and dendrites (Østerlund et al., 2022).
Fractional Anisotropy (FA):	metric in diffusion imaging that measures the directionality and integrity of water diffusion in tissues. Higher FA values indicate healthy white matter, while lower values suggest disruption or damage (Zolkefley et al., 2021).
Functional connectivity:	measurement of the synchronization of neural activity between different brain regions (Biswal et al., 1995).
GABA:	main inhibitory neurotransmitter in the brain, reduces neuronal excitability by binding to GABA receptors on neurons (Möhler, 2012).
Genetically Encoded Calcium Indicator (GECI):	a molecular probe designed to monitor intracellular calcium ion (Caˆ2+) levels within living cells (Oh et al., 2019).
Generative Adversarial Networks (GAN):	type of deep learning model consisting of two neural networks, a generator and a discriminator, trained in a competitive manner to generate realistic data (Goodfellow et al., 2014).
Graph:	data structure composed of nodes or vertices connected by edges or links, representing their relationships (Zhou et al., 2020).
Hippocampus:	region of the brain located in the medial temporal lobe and involved in processes related to memories (Squire et al., 2004).
Ictal event:	seizure caused by abnormal electrical activity in the brain (Fisher et al., 2014).

K-Means clustering:	unsupervised learning technique that subdivides data into groups based on their characteristics. This algorithm operates by placing so-called centroids within the data's vector space, and data points are classified by the centroid closest to them (Jin and Han, 2011).
L-measure:	software tool for quantifying the morphology of neurons (Scorcioni et al., 2008).
Light sheet microscopy or Selective Plane Illumination Microscopy (SPIM):	imaging technique that uses a thin sheet of laser light to illuminate a specimen from the side, minimizing photodamage and allowing for fast 3D imaging (Hillman et al., 2019).
Magnetic resonance imaging (MRI):	non-invasive, non-ionizing, quantitative, and multi-parametric imaging technique (Liu et al., 2021). It includes functional MRI (fMRI) and structural MRI (sMRI) (Shenton et al., 2012; Wu et al., 2021).
MCC-Net:	deep learning model for medical image segmentation that learns robust features at different scales of the image using contrastive learning (Wei et al., 2023).
Microtubules:	tube-like structures that provide structural support and facilitate intracellular transport (Desai and Mitchison, 1997).
Mossy fiber:	excitatory axons that project to and modulate hippocampal activity for spatial memory formation and consolidation (Henze et al., 2000).
MRI-T1:	type of MRI scan that produces images with high contrast between water and fat (Chen et al., 2018).
Neuropil:	defined as the space between neuronal and glial cell bodies that is composed of dendrites, axons, synapses, glial cell processes, and microvasculature (Spocter et al., 2012).
Point spread function (PSF) deconvolution:	method that attempts to correct the optical distortion. It serves as a mathematical representation of the blurring effect that occurs when a point source of light is recorded by an optical system (Corle and Kino, 1996).
Positron emission tomography (PET):	medical imaging technique that uses small amounts of radioactive tracers to visualize and measure physiological processes in the body (Phelps, 2000).
Principal Component Analysis (PCA):	statistical method for reducing the dimensionality of data while preserving as much of the variation in the data as possible (Jolliffe, 2002).
Pyramidal neurons:	Neurons exhibit a distinctive cellular structure, featuring apical and basal dendritic trees, as well as a pyramidal-shaped soma (Spruston, 2008).
RandomForest:	machine learning algorithm used for classification and regression, where the result is generated from the combination of multiple decision trees. Each decision tree is an independent model that divides the data into subsets based on a sequence of rules for data features (Belgiu and Drăguţ, 2016).
Regional homogeneity (ReHo):	concept and analysis technique to measure the similarity or coherence of the blood oxygen level-dependent (BOLD) signal within a specific brain region or voxel (Xu et al., 2019).
Region of interest (ROI):	significant portion of an image to be focused on or analyzed (Poldrack, 2007).
Residual Network (ResNet):	neural network architecture designed to address the vanishing gradient problem in very deep convolutional neural networks. It introduces skip connections, which allow gradients to flow more easily during training, improving the training of deeper networks in tasks like image recognition (He et al., 2015).
Resting state:	state in which a person is awake and alert but not actively engaged in a specific task or mental activity, also known as a baseline functional connectivity, when the brain continues to exhibit spontaneous neural activity (Biswal et al., 1995).
Serial section electron microscopy:	EM technique that sections and images a specimen to create 3D models of its internal structures, aiding in mapping neuronal connections within the brain (Gay and Anderson, 1954; Motta et al., 2019).
Sholl descriptors:	rule that links each neuron to a specific feature, associating neuron morphology with a function that produces numeric values in a metric space (Khalil et al., 2021).
Signal-to-Noise Ratio (SNR):	measure used to quantify the quality or strength of a signal in relation to the level of background noise or interference. A higher SNR indicates a more reliable and discernible signal compared to unwanted or random variations (noise) (Welvaert and Rosseel, 2013).
Single-photon emission computed tomography (SPECT):	nuclear medicine imaging technique that uses gamma-ray-emitting radiotracers to create 3D images of the distribution of radioactive compounds within the body (Devous, 1995).
Stimulated Emission Depletion (STED):	super-resolution microscopy technique that uses a combination of laser beams to overcome the diffraction limit, achieving extremely high spatial resolution in imaging (Vicidomini et al., 2018).

Structural connectivity:	Anatomical connections between different brain regions. It represents the physical pathways formed by bundles of nerve fibers (axons) that connect neurons in one part of the brain to neurons in another part (Hagmann et al., 2008).
Support Vector Machines (SVM):	supervised machine learning algorithm used for classification operates by identifying a hyperplane that separates different classes with a larger margin (Cristianini and Ricci, 2008).
Synchrotron x-ray microtomography:	non-destructive image technique that uses intense x-ray beams generated by a synchrotron particle accelerator to create high-resolution, 3D images of the internal structures of biological specimens (Betz et al., 2007).
Synthetic data:	artificially generated data used for various purposes, including training machine learning models (Rajotte et al., 2022).
Two-photon microscopy:	microscopy technique able to image a cm-thick biological specimen to create 3D images of its internal structures, aiding in mapping neuronal connections within the brain (Denk et al., 1990).
UNet:	Architecture employed for image segmentation. Uses convolutional layers for feature extraction and employs upsampling and transposed convolutional layers to create a segmentation mask (Ronneberger et al., 2015).
Voxel:	three-dimensional pixel, which is the smallest unit of a 3D space in a digital image or a 3D dataset (Foley, 1990).
Vision Transformers (ViT):	neural network architectures that utilize attention mechanisms to transform image patches into embedded representations, replacing traditional convolutional layers in computer vision tasks (Khan et al., 2022).
XGBoost (eXtreme Gradient Boosting):	an optimized version of the Gradient Boosting algorithm for classification and regression problems (Mason, no date).
Watershed:	image segmentation and instance labeling algorithm. It starts by dropping seeds to mark different regions, then these labeled seeds expand and delimitate the image into different areas, helping to identify individual instances in the image (Najman and Schmitt, 1994).

frontiers | Frontiers in Neuroscience

TYPE Original Research
PUBLISHED 21 March 2024
DOI 10.3389/fnins.2024.1306283

A brain functional network feature extraction method based on directed transfer function and graph theory for MI-BCI decoding tasks

Pengfei Ma[1,2,3], Chaoyi Dong[1,2,4]*, Ruijing Lin[1,2], Huanzi Liu[1,2], Dongyang Lei[1,2], Xiaoyan Chen[1,2,4] and Huan Liu[3]

[1]College of Electric Power, Inner Mongolia University of Technology, Hohhot, China, [2]Intelligent Energy Technology and Equipment Engineering Research Centre of Colleges and Universities in Inner Mongolia Autonomous Region, Hohhot, Inner Mongolia, China, [3]College of Computer and Software Engineering, Dalian Neusoft University of Information, Dalian, China, [4]Engineering Research Center of Large Energy Storage Technology, Ministry of Education, Hohhot, Inner Mongolia, China

OPEN ACCESS

EDITED BY
Federico Giove,
Centro Fermi - Museo Storico della Fisica e Centro Studi e Ricerche Enrico Fermi, Italy

REVIEWED BY
Emma Colamarino,
Sapienza University of Rome, Italy
Davide Borra,
University of Bologna, Italy

*CORRESPONDENCE
Chaoyi Dong
✉ dongchaoyi@imut.edu.cn

RECEIVED 03 October 2023
ACCEPTED 08 March 2024
PUBLISHED 21 March 2024

CITATION
Ma P, Dong C, Lin R, Liu H, Lei D, Chen X and Liu H (2024) A brain functional network feature extraction method based on directed transfer function and graph theory for MI-BCI decoding tasks.
Front. Neurosci. 18:1306283.
doi: 10.3389/fnins.2024.1306283

Background: The development of Brain-Computer Interface (BCI) technology has brought tremendous potential to various fields. In recent years, prominent research has focused on enhancing the accuracy of BCI decoding algorithms by effectively utilizing meaningful features extracted from electroencephalographic (EEG) signals.

Objective: This paper proposes a method for extracting brain functional network features based on directed transfer function (DTF) and graph theory. The method incorporates the extracted brain network features with common spatial pattern (CSP) to enhance the performance of motor imagery (MI) classification task.

Methods: The signals from each electrode of the EEG, utilizing a total of 32 channels, are used as input signals for the network nodes. In this study, 26 healthy participants were recruited to provide EEG data. The brain functional network is constructed in Alpha and Beta bands using the DTF method. The node degree (ND), clustering coefficient (CC), and global efficiency (GE) of the brain functional network are obtained using graph theory. The DTF network features and graph theory are combined with the traditional signal processing method, the CSP algorithm. The redundant network features are filtered out using the Lasso method, and finally, the fused features are classified using a support vector machine (SVM), culminating in a novel approach we have termed CDGL.

Results: For Beta frequency band, with 8 electrodes, the proposed CDGL method achieved an accuracy of 89.13%, a sensitivity of 90.15%, and a specificity of 88.10%, which are 14.10, 16.69, and 11.50% percentage higher than the traditional CSP method (75.03, 73.46, and 76.60%), respectively. Furthermore, the results obtained with 8 channels were superior to those with 4 channels (82.31, 83.35, and 81.74%), and the result for the Beta frequency band were better than those for the Alpha frequency band (87.42, 87.48, and 87.36%). Similar results were also obtained on two public datasets, where the CDGL algorithm's performance was found to be optimal.

Conclusion: The feature fusion of DTF network and graph theory features enhanced CSP algorithm's performance in MI task classification. Increasing the number of channels allows for more EEG signal feature information, enhancing the model's sensitivity and discriminative ability toward specific activities in brain regions. It should be noted that the functional brain network features in the Beta band exhibit superior performance improvement for the algorithm compared to those in the Alpha band.

KEYWORDS

brain–computer interface, motor imagery, directed transfer function, graph, brain network

1 Introduction

Brain–computer interface (BCI) is a technology that directly connects the human brain to external devices, and it has gained significant attention in the fields of neuroscience and engineering (Värbu et al., 2022). BCI technology provides a novel means of communication and operation for individuals facing challenges in motor function, neurological impairments, or other physical limitations, thus enabling them to overcome difficulties in normal communication and interaction (Cheng et al., 2020; Chen et al., 2022; Davis and Meschede-Krasa, 2022; Hu et al., 2023; Wang et al., 2023). The motor imagery (MI) paradigm holds significant potential in the field of BCI, particularly in rehabilitation medicine and assisted living technology, owing to its high feasibility and adaptability (Pichiorri et al., 2015). In recent years, research on MI paradigms has been focused in two directions. One direction aims to improve the decoding algorithm, enhancing the accuracy of MI categorization tasks (Vallabhaneni et al., 2021). The other direction involves constructing a brain network model to investigate the associations and patterns of information transfer between different brain regions (Yu et al., 2022).

Despite the advancements in BCI technology for recognizing and decoding brain signals, there are still limitations in terms of accuracy and reliability. The decoding process of brain signals is prone to errors and uncertainties, resulting in less stable and reliable performance of BCI systems. While traditional algorithms like discrete wavelet transform (DWT) (Ji et al., 2019) and common spatial patterns (CSP) (Blankertz et al., 2008) are simple and convenient, they do not yield satisfactory classification results (Amin et al., 2015; Jin et al., 2021). The Filter Bank Common Spatial Pattern (FBCSP) algorithm, which combines band filtering and CSP analysis, aims to enhance the accuracy of MI recognition. However, individual differences and noise significantly impair its effectiveness. To address this problem, Mammone et al. (2023) proposed AutoEncoder-Filter Bank Common Spatial Patterns (AE-FBCSP), incorporating an autoencoder into the FBCSP algorithm, and Park et al. (2018) introduced regularization in the Filter Bank Regularized Common Spatial Pattern (FBRCSP), both of which greatly improved the classification accuracy of FBCSP. However, these approaches primarily focus on the spatial domain features of EEG signals with a single attribute and do not consider the transmission mode of brain information during MI. Deep learning, as a powerful machine learning method, has garnered significant interest and research in the field of BCI (Amin et al., 2019; Dai et al., 2020). Convolutional neural networks (CNNs) have shown great potential in capturing information in BCI (Simões et al., 2020; Borra et al., 2022; An et al., 2023). However, the performance of CNNs relies not only on the choice of convolutional kernels (Song et al., 2021) but also on the number of convolutional layers. On the other hand, recurrent neural networks (RNNs) process EEG time-series information more effectively and can be successful in classifying MI tasks (Bore et al., 2021). Lawhern et al. (2018) proposed a lightweight deep learning approach which is called EEGNet for the task classifications of EEG-based BCIs. EEGNet exhibited an exceptional generalization ability for classifying both within-subject and cross-subject tasks, even when faced with limited training data. Across various tested paradigms, such as P300 Visual Evoked Potentials, Error-Related Negativity (ERN), Movement-Related Cortical Potentials (MRCP), and Sensory Motor Rhythms (SMR), the classification accuracies of the EEGNet algorithm have consistently been superior to those of many benchmark algorithms (Lawhern et al., 2018). While deep learning has achieved remarkable results in BCI, it also faces common disadvantages, such as high data volume requirements and challenges in obtaining physiological interpretations. Brain network research methods offer a high degree of physiological interpretability. These methods view the brain as a complex network structure, where brain regions or electrodes are considered nodes, and the connections between them indicate functional or structural relationships. By applying concepts and methods from graph theory (de Vico et al., 2014) and network science, researchers can uncover the topology of brain networks, information transfer properties, and interactions between brain regions (Rodrigues et al., 2019). Most studies on functional brain networks have focused on functional connectivity metrics. Zhang et al. (2016) constructed brain networks using Pearson correlation coefficients and observed significant differences in small-world network metrics during different MI periods. Gong et al. (2017) proposed a brain functional network modeling method based on time-frequency Cross Mutual Information (CMI) and found significant differences in small-world network metrics across different tasks. Additionally, they discovered significant differences in brain response levels, reaction times, and activation targets under different tasks. Wang et al. (2022) used a phase-locked-value approach to construct functional brain networks, providing a better functional connectivity perspective for neurofeedback training. In the MI paradigm, directed causal connectivity provides insights into the causal interactions between nodes, making it more adept at uncovering hidden and overlooked connectivity compared to functional connectivity. Varsehi and Firoozabadi (2021) utilized Granger causality analysis (GC) to choose 8 channels from EEG signals, leading to enhanced model classification accuracy, specificity, and sensitivity. However, GC analysis is less suitable for non-linear signals despite its effectiveness in capturing the dynamics and temporal order of causality in EEG signals. Li and Zhang (2022) constructed a brain functional network for MI data classification using continuous wavelet transform (CWT) and symbolic transfer entropy (TE). However, it should be noted that TE is dependent on data distribution and has a high computational time complexity (Li and Zhang, 2022). In the field of BCI, directed transfer function (DTF) outperforms other effective connectivity metrics due to its ability to capture frequency-specific causality, high temporal resolution, and model simplicity. Therefore, utilizing DTF to construct brain functional networks is advantageous. Ma et al. (2022) enhanced the classification accuracy of a MI task by incorporating DTF features into an Auto-Regressive (AR) mode. However, their study did not investigate the impact of different frequency bands on classification performance. Awais et al. (2021) combined DTF with a probabilistic neural network (PNN), achieving a classification accuracy of 82.81%, thereby validating the activation of multiple brain regions during MI tasks. However, their study lacked an exploration of graph theoretic features and the number of channels.

Traditional electroencephalogram (EEG) signal processing methods, such as DWT and CSP, are limited in obtaining a satisfying classification accuracy. FBCSP, as an improved version of CSP, yields an increased accuracy but still focuses primarily on EEG's spatial characteristics, overlooking the brain's intricate multidimensional dynamical information. Deep learning techniques, despite significantly enhancing classification performance, however, depend heavily on large datasets and struggle with physiological interpretation. Furthermore, some studies have utilized TE to measure brain network connectivity, forming TE-based functional brain networks. However, TE's computational demand is high, especially with large datasets, presenting a significant challenge for the computational capability of devices. Addressing these aforementioned issues, the proposed fusion method combines graph theory features with DTF features to further improve classification accuracy. The fusion method, call CSP+DTF+Graph theory feature+Lasso (CDGL) method, combined DTF's capability to detect frequency-specific causal links and graph theory's potential for in-depth physiological analysis of EEG signals, aiming to enhance classification precision in BCI applications and also offering a novel insight for graphic characteristics of the MI-BCI tasks. Therefore, the objective of this study is to propose and validate a brain functional network feature extraction method based on DTF and graph theory. The proposed CDGL incorporating DTF network features and graph theory features together achieves the highest classification accuracy among the other feature fusion methods. Furthermore, the study aims to assess the effectiveness of this method in classifying MI tasks with different frequency bands and channels. The research presented in this paper aims to investigate the influence of brain network features on decoding algorithms. The specific objectives are as follows: (1) test the ability of CSP, DTF and graph theory features to classify MI-EEG data (left vs. right hand MI), (2) test the ability of combination of features to classify MI-EEG data (left vs. right hand MI), including the novel method proposed in the study, on EEG data collected from 26 healthy participants and on public EEG dataset. In each comparison the impact of the channel numbers and the frequency band (alpha and beta) was investigated.

The remainder of this paper is organized as follows: Section 2 presents the classification algorithms of CSP, DTF and graph theory, the feature classification of Lasso algorithm, and the acquisition and processing method of EEG data. Section 3 shows the comparison experimental results with different feature incorporation and experimental setup. In Section 4, a thorough analysis and discussion of the results is provided. Finally, Section 5 presents the conclusions according to the aforementioned three objectives of this research.

2 Methods

2.1 Feature extraction methods

2.1.1 CSP

Common spatial pattern is a commonly employed feature extraction method in the classification of MI EEG signals (Sun et al., 2022). Its fundamental concept involves projecting the data sequence onto a specific surface through the computation of a set of spatial filters. These filters aim to maximize the variance of the projections for the two categories on that surface, thereby accentuating the most distinctive features of each category. The CSP method is highly effective in extracting EEG signal features that exhibit exceptional discriminative capabilities among different categories, thereby offering robust performance for classification tasks.

The two types of EEG signal time series data, namely X_1 and X_2, were normalized. Subsequently, the covariance matrices of the normalized data were computed using Eq. 2.1.

$$R_1 = \frac{X_1 X_1^T}{trace\left(X_1 X_1^T\right)}, R_2 = \frac{X_2 X_2^T}{trace\left(X_2 X_2^T\right)}, \tag{2.1}$$

where X^T denotes the transpose of X and $trace(X)$ is the trace of the matrix.

For each series of data, its corresponding covariance matrix was calculated. Subsequently, the covariance matrices of the two series of data were separately averaged and then added together to obtain the mixed covariance matrix. This calculation is demonstrated in Eq. 2.2.

$$R = \bar{R}_1 + \bar{R}_2, \tag{2.2}$$

The resulting mixed covariance matrix was subjected to an eigen-decomposition, as demonstrated in Eq. 2.3.

$$R = U \lambda U^T, \tag{2.3}$$

where U represents the eigenvector matrix of the mixed covariance matrix R, and λ represents the diagonal array of eigenvalues.

Next, the whitening matrix is computed from the eigenvector matrix and the diagonal array of eigenvalues, as demonstrated in Eq. 2.4.

$$P = \sqrt{\lambda^{-1}} U^T, \tag{2.4}$$

A whitening transformation is performed on the two types of mean covariance matrices, denoted as R_1 and R_2. The whitening matrices, denoted as S_1 and S_2, are computed using Eq. 2.5.

$$S_1 = P \bar{R}_1 P^T, \ S_2 = P \bar{R}_2 P^T, \tag{2.5}$$

S_1 and S_2 are decomposed in Eq. 2.6.

$$S_1 = B_1 \lambda_1 B_1^T,\ S_2 = B_2 \lambda_2 B_2^T, \tag{2.6}$$

where the eigenvectors of the S_1 and S_2 matrices are the same and the diagonal array λ_1 and λ_2 consisting of the two types of eigenvalues sums to a unit array, there is the expression of Eq. 2.7.

$$B_1 = B_2 = B,\ \lambda_1 + \lambda_2 = I, \tag{2.7}$$

When the eigenvalue of matrix S_1 is the largest and the eigenvalue of matrix S_2 is the smallest, the two types of signals can be classified using the matrix B. This classification enables the derivation of the projection matrix W, which serves as the spatial filter. The formula is shown in Eq. 2.8.

$$W = B^T P, \tag{2.8}$$

The feature matrix Z, obtained by applying the spatial filter W to the two types of data, is calculated using Eq. 2.9.

$$Z_{\ 1} = WX_1, Z_2 = WX_2, \tag{2.9}$$

The feature matrix Z is logarithmically computed for variance, and the resulting values are used as a new feature denoted as f. The calculation process is shown in Eq. 2.10.

$$f = \log\left(\frac{\operatorname{var}(Z)}{\sum \operatorname{var}(Z)}\right), \tag{2.10}$$

The classification of the two types of signals can be achieved by inputting the feature vector f into the classifier. For a detailed mathematical discussion, see reference Koles et al. (1990).

2.1.2 Dtf

The DTF method, proposed by Kamiński et al. (2001) is a universal multivariate approach for computing the directed connections between any pair of signals within a multidimensional dataset. DTF is developed based on GC theory, which has stronger robustness and directionality compared with GC analysis. The DTF algorithm is able to analyze signals in different frequency ranges, thus revealing the interaction of brain regions in different frequency bands, which is important for the study of brain activity and functional connectivity patterns in specific frequency bands.

The acquired multichannel EEG signal is denoted as X. Subsequently, the multivariate autoregressive model (MVAR) (Shibata et al., 2004) is used to fit the multichannel EEG data. This fitting process results in Eq. 2.11.

$$\sum_{k=0}^{p} \Lambda(k) X(t-k) = E(t), \tag{2.11}$$

Here, the elements in the $N*N$ matrix $\Lambda(k)$ represent the parameters of the MVAR model, where N is the number of channels. The vector $E(t)$ represents the multivariate zero-mean white noise. The parameter p denotes the order of the MVAR model, which influences the fitting performance. To accommodate subsequent computational needs, Eq. 2.12. is transformed into the frequency domain.

$$X(f) = \Lambda^{-1}(f) E(f) = H(f) E(f), \tag{2.12}$$

Among them, detailed information is shown in Eq. 2.13.

$$\Lambda(f) = \sum_{k=0}^{p} \Lambda(k) e^{-j2\pi f \Delta t k}, \tag{2.13}$$

$H(f)$ is the system transfer matrix. The value of element H_{ij} in $H(f)$ describes the strength of the connection between two leads with j as input and i as output (Kamiński et al., 2001). The DTF matrix can be constructed as follows (Kaminski and Blinowska, 1991). The DTF matrix can be constructed in Eq. 2.14.

$$\theta_{ij}^2(f) = \left|H_{ij}(f)\right|^2, \tag{2.14}$$

To alleviate the impact of singular sample data, the DTF matrix is normalized (He et al., 2011). The feature matrix is then obtained using Eq. 2.15.

$$\gamma_{ij}^2(f) = \left|H_{ij}(f)\right|^2 / \sum_{m=1}^{N} \left|H_{im}(f)\right|^2, \tag{2.15}$$

where γ_{ij} represents the information inflow ratio from node j to node i, with a value ranging between 0 and 1. γ_{ij} value closer to 1 indicates that a larger proportion of information in node i originates from node j. Conversely, a value closer to 0 suggests that there is less information flow from node j to node i.

The normalized DTF matrix is vectorized and utilized as feature vectors in the classifier for the purpose of classifying the MI tasks. The coefficient matrix of the 15-channel DTF network features is depicted in Figure 1.

2.1.3 Graph theory method

The human brain, consisting of hundreds of millions of interconnected nerve cells, is widely regarded as one of the most complex systems in nature. This intricate neural network exhibits highly structured and functional characteristics. Through the application of graph theory, which is widely employed for the structural analysis of complex brain connectomes, we can uncover specific organizational patterns between brain structure and function. This approach provides a powerful tool to enhance our understanding of the structural connectivity networks within the brain.

Functional brain networks based on graph theory encompass crucial network features that quantify network performance. Binarizing the effective connectivity matrix, however, can lead to the loss of significant network information. In this study, the method described in Filho et al. (2018) is employed to compute characteristic parameters of the weighted network. The DTF coefficient matrix is utilized as a weighted directed graph to facilitate graph theory analysis. The graph

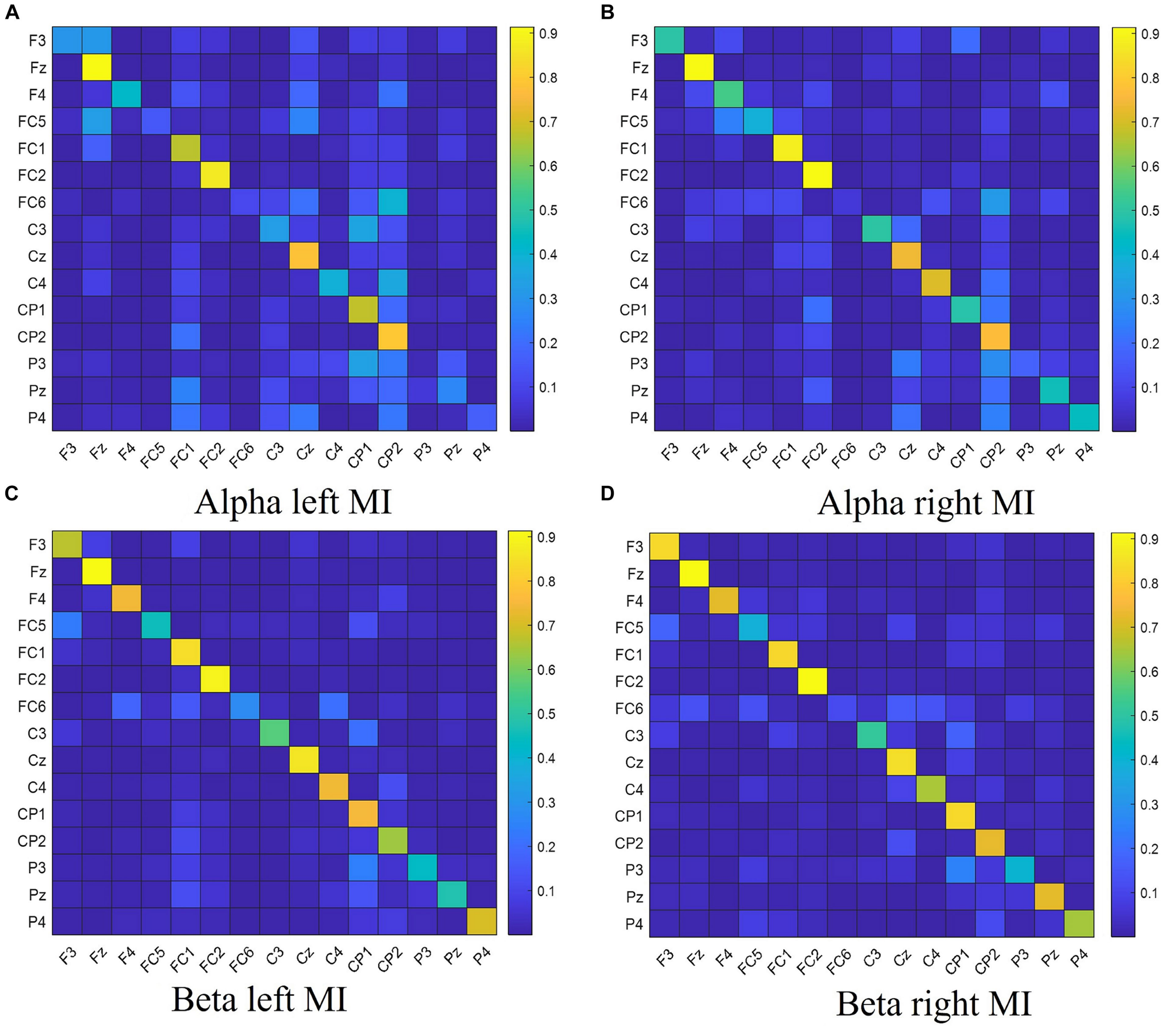

FIGURE 1
The DTF coefficient matrix of left hand and right hand MI tasks for different frequency bands. Panel **(A)** shows the DTF coefficient matrix for left hand MI in the Alpha frequency band. Panel **(B)** shows the DTF coefficient matrix for right hand MI in the Alpha frequency band. Panel **(C)** shows the DTF coefficient matrix for left hand MI in the Beta frequency band. Panel **(D)** shows the DTF coefficient matrix for right hand MI in the Beta frequency band.

theory metrics used in this article are as follows (Bullmore and Bassett, 2011):

(1) The calculation of ND is shown in Eq. 2.16.

$$S_i = \sum_j w_{ij}, \tag{2.16}$$

where w_{ij} is the connectivity between node i and node j, and S_i is the node strength, which is calculated by summing up the individual weights connected to that node. The greater the node strength, the stronger the connectivity between that node and other nodes.

(2) The calculation of CC is shown in Eq. 2.17.

$$C_i = \frac{\sum_j \sum_k w_{ij} w_{jk} w_{ki}}{\left(\sum_j w_{ij}\right)^2 - \sum_j w_{ij}^2}, \tag{2.17}$$

The clustering coefficient is a metric used in graph theory to measure the degree of node aggregation within a network. It quantifies the extent to which neighboring nodes of a given node are connected to each other, thus indicating the presence of community structures in the network. A higher clustering coefficient indicates a more interconnected network.

(3) The calculation of GE is shown in Eq. 2.18.

$$G = \frac{1}{n(n-1)} \sum_{i \neq j} \frac{1}{d_{ij}}, \tag{2.18}$$

where n is the number of nodes, d_{ij} is the shortest path length between node i and node j. Global efficiency is a metric used to quantify the effectiveness of information dissemination in a network. It provides a measure of how efficiently information is transferred and spread across the network. A higher global efficiency indicates a more efficient and rapid dissemination of information within the network.

2.2 Feature selection and classification methods

2.2.1 Lasso

Feature selection is a crucial aspect in the field of BCI. Its objective is to identify the most relevant and discriminative features from EEG signals, facilitating accurate classification and control of EEG signals (Lin et al., 2022). The Lasso algorithm is employed to reduce the dimensionality of the original feature space by selecting and compressing the variables (Zhang et al., 2021). The basic concept of the Lasso algorithm involves imposing a constraint on the sum of absolute values of regression coefficients, ensuring it remains below a specified threshold during the construction of a linear regression model. By applying this constraint, the Lasso algorithm effectively compresses regression coefficients with smaller absolute values to zero, thereby achieving feature sparsity and interpretability. The cost function associated with the Lasso algorithm is Zhang et al. (2021). The formula is shown in Eq. 2.19:

$$J(\beta)=\frac{1}{2}\sum_{i=1}^{m}\left(\hat{y}_i-y_i\right)^2+\lambda\sum_{j=1}^{n}\left|\beta_j\right|, \qquad (2.19)$$

In the context of the Lasso algorithm, the variables are defined as follows: m represents the number of training samples, n represents the dimensionality of the original spatial features. Additionally, the cost function includes two important components: λ, which represents the weight of the penalty term and controls the dimensionality of feature selection and compression, and β, which denotes the parameter in the regression model.

2.2.2 SVM

Support vector machine (SVM) is a robust machine learning algorithm that has gained significant popularity in the field of BCI in recent years (Wang et al., 2021). SVM effectively performs classification task by identifying the optimal hyperplane that separates samples belonging to different classes. It exhibits strong generalization ability and can handle high-dimensional data effectively. The underlying model of SVM is Jia et al. (2019). The formula is shown in Eq. 2.20:

$$f(x)=\operatorname{sgn}\left[\sum_{i=1}^{L}a_i y_i k\left(x_i\cdot x\right)+b\right], \qquad (2.20)$$

where *sgn* is the sign function, $k\left(x_i\cdot x\right)$ is the kernel function, and a_i and b are the parameters that determine the optimal classification plane. The kernel function takes the RBF kernel function.

This paper evaluates the generalization ability of the classification models using a 10-fold cross-validation, a typical statistical method for assessing machine learning models' generalization capability. This method is particularly useful in situations where limited data is available for model evaluation. In 10-fold cross-validation, the division ratio of training and test sets is consistent, with each fold involving a 90% training data and 10% test data. Upon completing 10 iterations, an array of performance metrics is obtained, and their average is calculated to gauge the overall model performance. Figure 2 illustrates the process of the 10-fold cross-validation.

2.2.3 CDGL classification method

A method incorporating CSP, DTF, graph theory feature, and Lasso regularization (CDGL) is proposed in this paper, which innovatively integrates five features with the aim of enhancing classification accuracy in MI-BCI applications. The choices of CSP, DTF, ND, CC, and GE features were made in order to provide a comprehensive representation of brain activity. In this study, these five features were initially combined, and subsequently selected by a Lasso method to eliminate redundant features. The resulting integrated features were then fed into the SVM classifier. Each of these features adds a unique dimension to the analysis, facilitating the exploration of different temporal, spatial, frequency, and connective information of EEG signals. The amalgamation of these diverse features

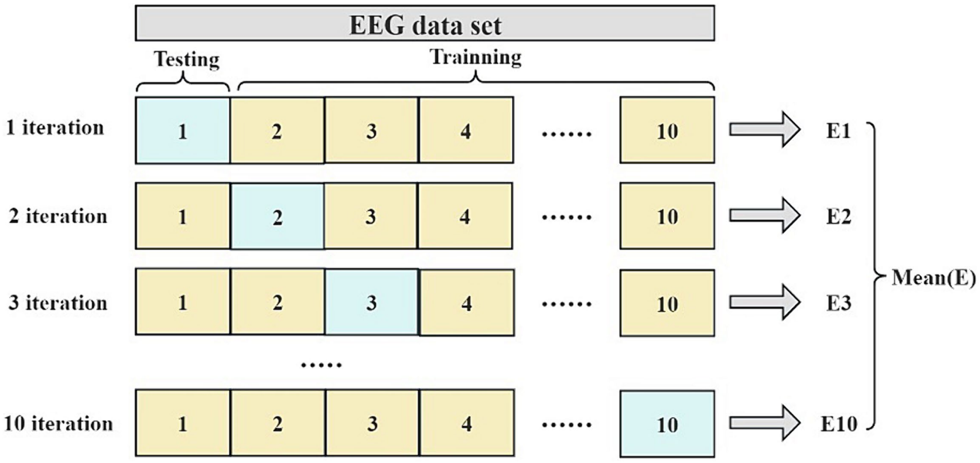

FIGURE 2
The flowchart of the 10-fold cross-validation.

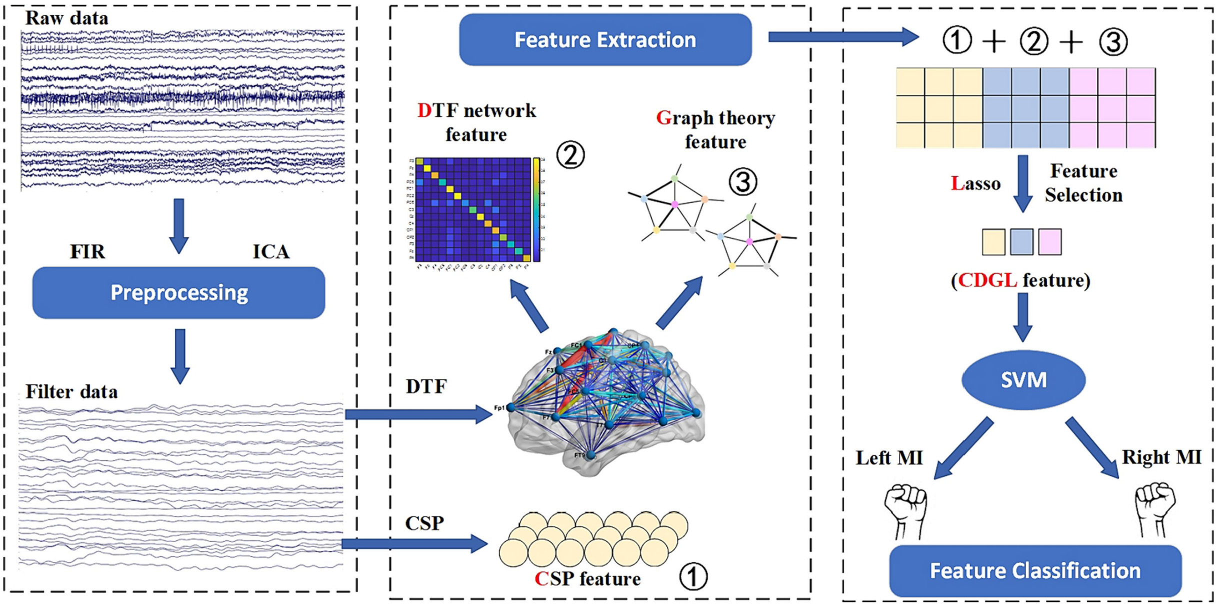

FIGURE 3
The flowchart of the CDGL method.

significantly enhances the robustness and accuracy of the SVM classifier. The flowchart of the CDGL method is shown in Figure 3.

To assess the efficacy of the CDGL algorithm, this study conducts a comparative analysis with EEGNet, a widely recognized deep learning algorithm for EEG signal processing. EEGNet is a specialized lightweight convolutional neural network, which is tailored for EEG signal processing. Its architecture encompasses standard convolutional layers, depthwise convolutional layers, and separable convolutional layers, which can integrate spatial and temporal features effectively. This integration renders EEGNet adept at various EEG analysis tasks. This paper adopted a standard architecture of EEGNet, consistent with the framework presented in the reference literature (Lawhern et al., 2018), without any modifications. The training and testing sets were divided into 80 and 20%, respectively. The loss function was chosen to be *Cross Entropy Loss*, and the optimizer selected was *Adam*. The number of epochs was set as 100, and the batch size was set as 16. The 'kernLength' was set to 32, and the dropout rate was established at 0.5. The dimension of input for EEGNet was # of trials × # of channels × sampling time, where # of channels was set to 4 or 8.

2.3 Evaluating metric

Three evaluation metrics: accuracy, sensitivity, and specificity, are primarily utilized in this paper for testing classification results. These metrics provide a comprehensive framework for assessing model performance.

(1) The calculation of accuracy is shown in Eq. 2.21.

$$accuracy = \frac{TP + TN}{TP + TN + FP + FN}, \tag{2.21}$$

where *TP* is the number of samples that are actually positive and have been classified as positive by the classifier. *TN* is the number of samples that are actually negative and have been classified as negative by the classifier. *FP* is the number of samples that are actually negative but have been classified as positive by the classifier. *FN* is the number of samples that are actually positive but have been classified as negative by the classifier. Accuracy is the most intuitive performance metric, representing the overall proportion of correct predictions for both positive and negative classes by the model.

(2) The calculation of sensitivity is shown in Eq. 2.22.

$$sensitivity = \frac{TP}{TP + FN}, \tag{2.22}$$

where sensitivity is a measure of a classifier's ability to correctly identify positive samples, with the advantage of being able to accurately capture positive samples.

(3) The calculation of specificity is shown in Eq. 2.23.

$$specificity = \frac{TN}{TN + FP}, \tag{2.23}$$

where is a measure of a classifier's ability to correctly identify negative samples, enabling accurate exclusion of these instances and reducing false positives.

2.4 Statistical analysis methods

In this study, ANOVA and dependent sample *t*-test are used as the statistical analysis methods. To avoid errors associated with repeated measurements, the Bonferroni correction method is also employed here. Specifically, if five comparisons were made, the significance level was adjusted from the nominal $\alpha = 0.05$ to $\alpha = 0.01$ (0.05/5), thus maintaining a very stringent criteria for statistical significance. In ANOVA, this study employed both one-way ANOVA and two-way ANOVA. The two-way ANOVA was used to compare the effects of two factors on the experimental outcomes, as well as to determine whether there is an interaction effect between these factors. The ANOVA can analyze the significant changes of means across multiple groups effectively, whereas the dependent sample *t*-test is more suitable for comparing means within the same group under varying conditions, offering sensitivity for detecting changes within the group. Actually, this paper performed the within-subjects test. To demonstrate the authenticity of the study, this research utilizes a paired *t*-test and Bonferroni correction method on a public dataset to discern the notable differences between CDGL and EEGNet.

To be aligned with the research objectives, this study organized the statistical analysis methods. For objective 1, one-way ANOVA, two-way ANOVA, and paired *t*-test were employed to analyze and compare the capabilities of different features in classifying MI-EEG data. For objective 2, one-way ANOVA was used to assess the effect of feature combinations and to investigate the impact of the number of channels and frequency bands. Additionally, paired *t*-tests and Bonferroni correction methods were utilized to validate the differences between CDGL and EEGNet on public datasets.

2.5 Data acquisition and preprocessing

2.5.1 Data acquisition instructions

In this paper, an EEG signal acquisition experiment was conducted on a MI tasks involving 26 subjects aged between 23 and 27. The MI task is described as the mental simulation of hand grasping action being performed by an individual without the actual execution of the action. In the experiment, a 32-lead EEG equipment from Brain Products (BP) Inc. was used to collect EEG data from the MI BCI, and the sampling frequency was set at 500 Hz. Prior to the experiment, various steps were taken to ensure the suitability of the subjects. Firstly, all subjects underwent vision correction to ensure normal visual acuity. Additionally, a thorough examination was conducted to verify their mental health and overall well-being. The subjects were informed about the purpose and significance of the experiment beforehand. Following this, the subjects wore an EEG cap and were seated in front of a computer as instructed by the experimenter. The experimenter applied the conductive paste to the EEG cap, reducing the resistance to less than 5 kΩ. Throughout the experimental period, the subjects were instructed to maintain a stable mental state and avoid intense emotional fluctuations, ensuring data integrity. The electrode positions were set based on the international 10–20 lead standard, as shown in Figure 4. The AFz electrode (marked in black in Figure 4) serves as the ground electrode, and the FCz electrode (marked in blue in Figure 4) is used as the reference electrode, and the IO electrode (marked in red Figure 4) is used as the Electrooculography electrode.

During the acquisition process, the subjects performed corresponding tasks based on the interface displayed on the computer screen. Each experiment had a duration of 10 s, consisting of different stages. Firstly, there was a 2-s period where the screen would display a blank interface, and subjects were expected to be in a relaxed state. Following this, a 2-s period followed where a cross interface appeared, indicating the preparation state for the MI tasks. Lastly, the screen displayed either a left hand fist or a right hand fist for 6 s, during which subjects were required to carry out the MI tasks corresponding to the displayed hand. The flow of the experiment is summarized in Figure 5.

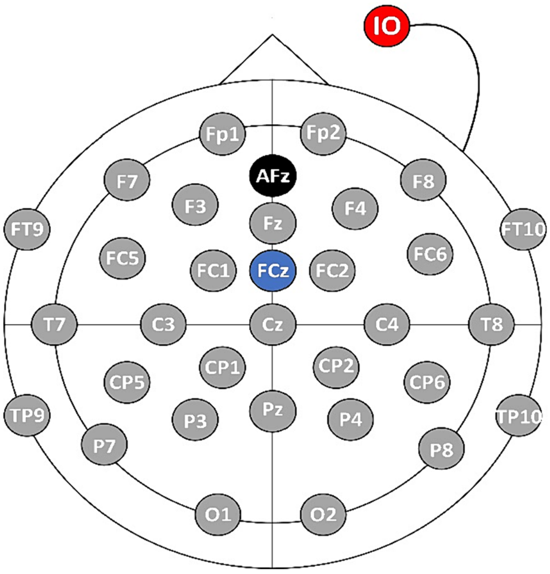

FIGURE 4
The distribution diagram of electrode positions.

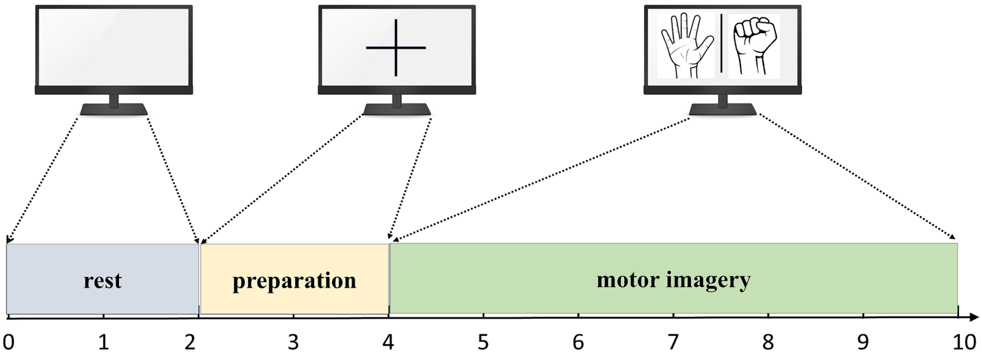

FIGURE 5
The flow of the MI experiment.

Each subject performed two sets of experiments, one set of experiments performed a left hand MI tasks 40 times, and one set of experiments performed a right hand MI tasks for a total of 80 experiments, obtaining EEG data in the shape of 32*3000*80 (32 represents the number of EEG channels, 3,000 represents the data length sampled over 6 s at a sampling frequency of 500 Hz, and 80 represents the number of trials).

2.5.2 Data preprocessing

EEG signal preprocessing is a crucial process that involves applying a series of steps to raw EEG data. The goal is to purify the signal, eliminate noise, and prepare the data for subsequent analysis. Pure EEG signals are of crucial importance for accurate analysis. In the pre-processing phase, an 8 Hz to 40 Hz bandpass filter was applied to extract the study's key frequency components and eliminate potential low-frequency artifacts and high-frequency noises. With a Finite Impulse Response (FIR) design, the filter was configurated for achieving its linear phase response, effectively preventing a phase distortion. The filter's order was algorithmically determined, based on a predefined multiple of the sampling rate and the lower cutoff frequency. Post-filtering, the Independent Component Analysis (ICA) algorithm from EEGLAB (Delorme and Makeig, 2004) was employed to eliminate artifacts, including eye movements and muscle activity, resulting in purified EEG signals. To ensure the validity of MI, a time window of 3 s was selected for analysis.

2.5.3 Public datasets

To validate the effectiveness of the proposed algorithm, this study employs the datasets from BCI Competition IV 2a (Tangermann et al., 2012) and PhysioNet's BCI2000 (Schalk et al., 2004). The BCI IV 2a dataset records EEG data through 22 scalp electrodes at a 250 Hz sampling frequency. In the experiment, each subject performed 6 experimental runs, totaling 48 trials (12 each for left-hand, right-hand, both feet, and tongue MI). The average duration of each trial was approximately 8 s, with an actual MI period of 3 s. On the other hand, the BCI2000 dataset employs 64 scalp electrodes and captures data at a 160 Hz sampling frequency, featuring eight tasks that include MI of the left hand, right hand, both hands, both feet, and actual movement tasks. Each subject performed 14 experimental runs, totaling 84 trials. Each trial lasted for 4 s. The MI task studied in this article is a binary classification task with a left-hand MI class and a right-hand MI class. To ensure consistency with our experimental tasks, the same electrodes and MI tasks (left and right hand) were also selected from these public datasets.

3 Results

3.1 Data collected by IMUT

3.1.1 The effect of CSP, DTF, graph theory features on MI task classification performance

To investigate the effect of network features on the classification performance of MI tasks, a DTF brain network model was constructed using various channel configurations, including 4-channel (FC1, FC2, C3, and C4), 8-channel (Fz, FC1, FC2, C3, Cz, C4, CP1, and CP2), 12-channel (Fz, FC1, FC2, C3, Cz, C4, CP1, CP2, F3, F4, P3, and P4), 15-channel (Fz, FC1, FC2, C3, Cz, C4, CP1, CP2, F3, F4, P3, P4, FC5, and FC6), and 32-channel configurations. The actual values of DTF matrices are used here to construct the feature set.

The DTF coefficient connection matrix was selected as the feature set for the classification task, and a SVM was employed as the classifier. To ensure the stability of the classification results, a 10-fold cross-validation method was utilized. The study involved 26 participants who performed MI classification task in both the Alpha and Beta frequency bands. The average classification performance of the DTF + SVM method is presented in Table 1.

Table 1 demonstrates that DTF network features possess the capability to distinguish between left and right hand MI tasks, enabling accurate recognition of these tasks. It was observed that as the number of channels increased, the classification accuracy also improved. Notably, when utilizing 32 channels, the classification system not only reached a high level of accuracy at 91.74%, but also demonstrated a sensitivity of 92.32% and a specificity of 90.51%. Furthermore, analysis of the Alpha and Beta bands revealed that the DTF coefficient matrix yielded slightly higher classification accuracy for the Beta band compared to the Alpha band. In this study, a Two-Factor Analysis of Variance (ANOVA) was performed to provide a detailed analysis of the results. This analysis is crucial for evaluating the effects of various channel combinations (X1) and frequency band (X2) analyses on the essential metrics of the research.

Table 2 displays the results of ANOVA analyses, which provide a comparative overview of accuracy, specificity, and sensitivity under different conditions. The results indicated significant effects of channel combinations on the three metrics: accuracy [$F(4, 250) = 33.16$, $p < 0.0001$], specificity [$F(4, 250) = 28.35$, $p < 0.0001$], and sensitivity [$F(4, 250) = 19.89$, $p < 0.0001$], each showing considerable differences. Similarly, frequency band types significantly influenced these metrics, as shown by accuracy [$F(1, 250) = 14.73$, $p = 0.000157$], specificity [$F(1, 250) = 17.47$, $p < 0.0001$], and sensitivity [$F(1, 250) = 16.05$, $p < 0.0001$]. However, no significant interaction effect was observed between

TABLE 1 The average classification performance of the DTF + SVM method using different channel configurations for 26 subjects.

	Accuracy				Sensitivity				Specificity			
	Alpha		Beta		Alpha		Beta		Alpha		Beta	
	Mean	*SD*	Mean	*SD*	Mean	*SD*	Mean	*SD*	Mean	*SD*	Mean	*SD*
Channels = 4	72.03	7.9	75.70	8.9	74.33	9.6	76.15	9.1	69.72	9.9	76.44	10.8
Channels = 8	76.03	9.1	81.14	8.7	77.12	9.2	81.48	9.2	75.69	9.8	79.81	10.2
Channels = 12	79.65	8.3	84.30	7.8	80.71	8.6	84.39	7.7	78.01	10.9	83.91	9.7
Channels = 15	82.43	7.8	85.54	9.3	83.30	8.1	86.73	7.5	80.33	11.2	85.45	9.5
Channels = 32	89.17	6.7	91.74	5.9	90.30	7.6	92.32	6.5	87.12	8.8	90.51	8.3

TABLE 2 The comparison of accuracy, specificity, and sensitivity for DTF+SVM using a two-way ANOVA analysis.

	Accuracy		Sensitivity		Specificity	
	F	*P*	*F*	*P*	*F*	*P*
X1	33.16	3.46e-22	28.35	1.51e-19	19.89	3.07e-14
X2	17.47	4.03e-5	11.57	7.79e-4	16.05	8.12e-5
X1*X2	0.1678	0.9546	0.2714	0.8941	0.2842	0.8881

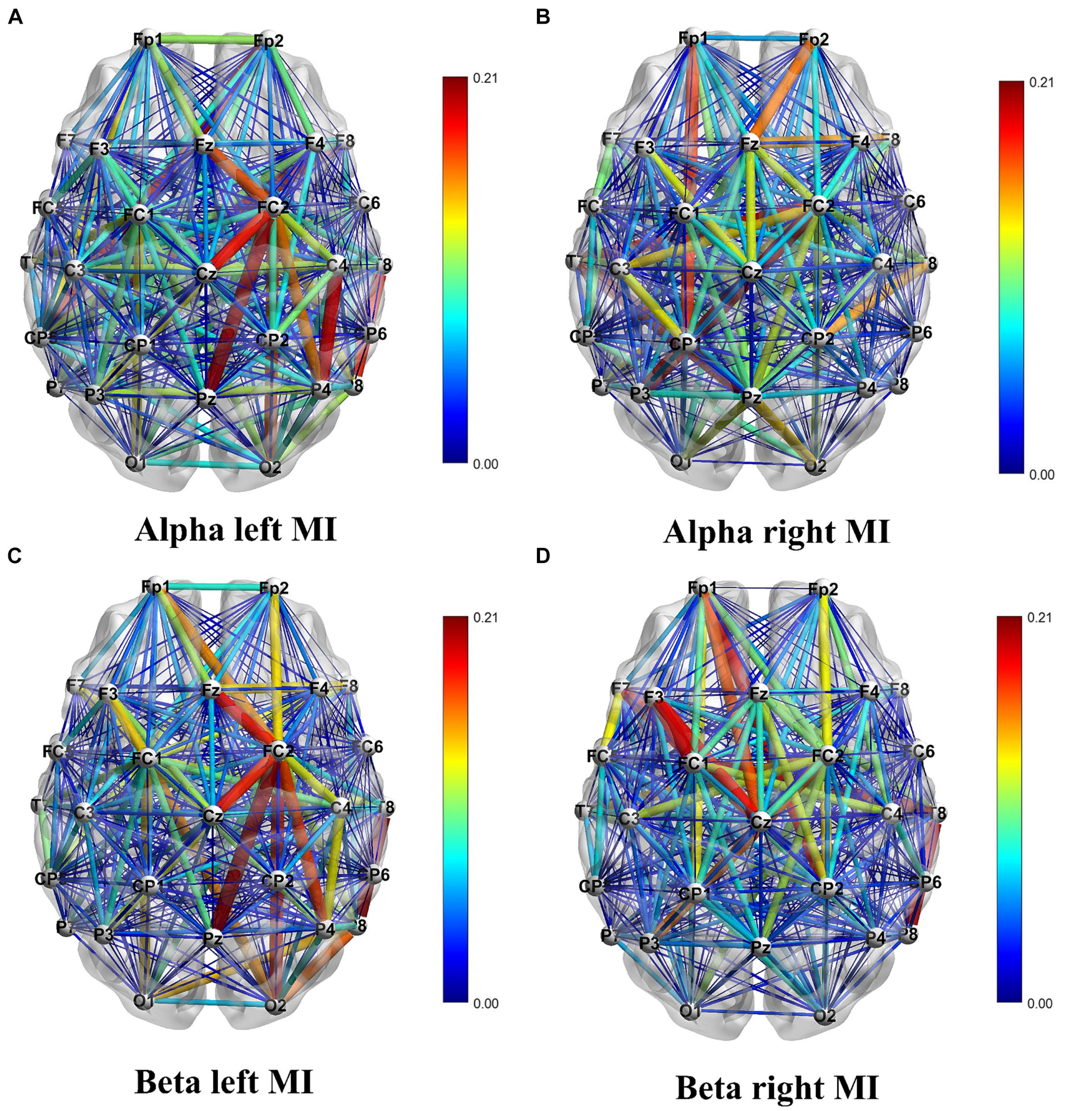

FIGURE 6
Visualization of the DTF connectivity matrix. Panel **(A)** shows the DTF connectivity matrix for left hand MI in the Alpha frequency band. Panel **(B)** shows the DTF connectivity matrix for right hand MI in the Alpha frequency band. Panel **(C)** shows the DTF connectivity matrix for left hand MI in the Beta frequency band. Panel **(D)** shows the DTF connectivity matrix for right hand MI in the Beta frequency band.

channel combination and frequency band [Accuracy: $F(4, 250) = 0.17$, $p = 0.9546$; Specificity: $F(4, 250) = 0.27$, $p = 0.8941$; Sensitivity: $F(4, 250) = 0.28$, $p = 0.8881$], suggesting that the interaction of channel combination and frequency band type does not significantly alter these outcomes. BrainNet Viewer (Xia et al., 2013) software was employed to visualize the connectivity matrix. It is worth noting that IO, TP9, and TP10 electrodes were excluded from the visualization due to channel position considerations.

The analysis of Figure 6 reveals a distinction in the direction of EEG signal transmission during MI tasks involving different hands. The color gradient from blue to red signifies weaker to stronger connections, respectively. This difference is a reliable foundation for

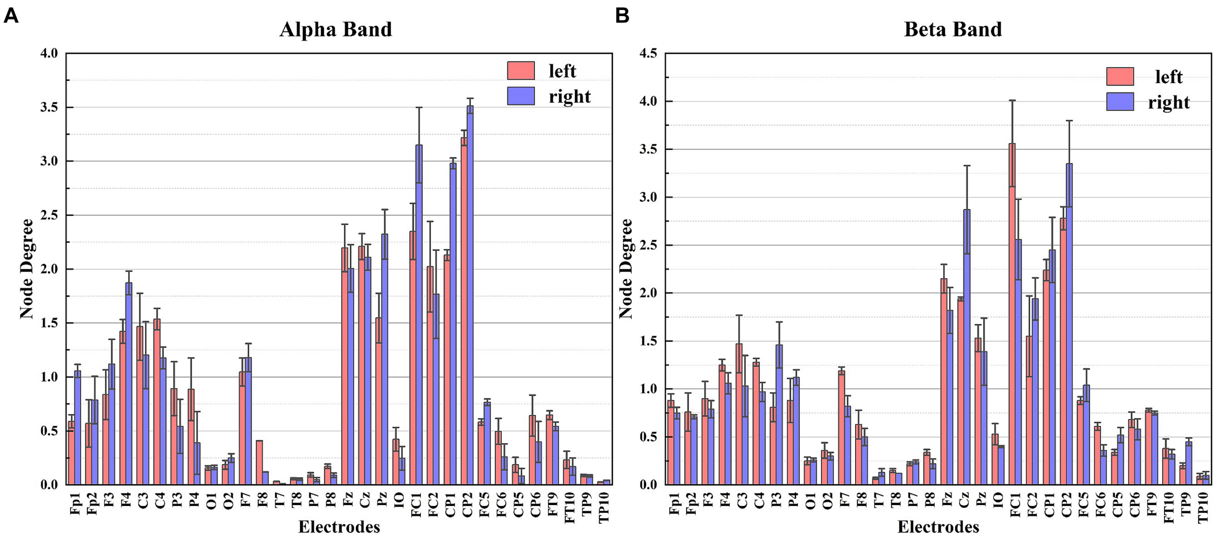

FIGURE 7
The node degree of each electrode for different frequency bands. Panel **(A)** shows the node degree of each electrode in the Alpha frequency band. Panel **(B)** shows the node degree of each electrode in the Beta frequency band.

accurately classifying left and right hands movements. When performing MI tasks with the left and right hands, the information connectivity patterns within the brain regions exhibit significant variations. To be more specific, there is an increase in connectivity strength within the right hemisphere of the brain when engaging in MI of the left hand, and conversely, an increase within the left hemisphere when MI of the right hand.

The DTF graph-theoretic features serve to depict the information transfer relationships between different brain regions by transforming the DTF coefficient connectivity matrix into graph structures and extracting relevant features. The topology of the brain network is represented by feature vectors derived from three graph theory features: node degree (ND), clustering coefficient (CC), and global efficiency (GE). This paper directly utilizes the DTF coefficient matrix as a directed weighted graph for calculating the graph-theoretic features. Notably, ND assumes a pivotal role in graph theory analysis as it quantifies the significance or activity level of individual nodes within the network.

Based on the ND in Figure 7, notable distinctions in ND are observed among the electrodes during the two different MI tasks, particularly for the C3, C4, Cz, P3, P4, FC1, and FC2 electrodes. These discrepancies highlight the regions of the brain where these electrodes are positioned, which exhibit significant information flow and strong connectivity with other electrodes during MI tasks. Taking this characteristic as a feature in the classification of MI tasks proves effective in accurately distinguishing between left and right hand MI tasks.

Figure 8 illustrates the average performance achieved using an SVM classifier for five distinct features of EEG signals extracted from 26 subjects. These features include CSP features, DTF network features, ND features, CC features, and GE features.

Analysis of Figure 8 reveals how the number of electrodes influences complexity of the brain functional network and the discriminative ability of feature selections. As the number of electrodes increases, the classification accuracy using the graph theory features for the MI-BCI tasks demonstrates an increasing trend [confirmed by a one-way ANOVA under Alpha for ND feature, $F(4, 250) = 2.95$, $p < 0.001$]. In the Alpha band, utilizing 32 channels, ND features exhibited average classification accuracy, sensitivity, and specificity of 86.88, 87.54, and 86.06%. CC features showed values of 85.22, 87.61, and 84.75%, while GE features had 86.04, 87.17, and 84.62%. In the Beta band, ND features demonstrated corresponding values of 87.51, 89.33, and 89.64%; CC features presented 89.15, 88.38, and 86.59%; and GE features had 87.57, 88.35, and 87.08%, respectively. ND's performance between Alpha and Beta frequency bands revealed significant differences by one-way ANOVA in the results of $F(1, 50) = 4.19$, $p = 0.04$ for accuracy, $F(1, 50) = 4.08$, $p = 0.04$ for sensitivity, and $F(1, 50) = 4.67$, $p = 0.03$ for specificity. CC's performance: $F(1, 50) = 4.61$, $p = 0.03$; $F(1, 50) = 4.94$, $p = 0.03$; $F(1, 50) = 4.6$, $p = 0.03$ for the three metrics, respectively. GE's performance: $F(1, 50) = 4.16$, $p = 0.04$; $F(1, 50) = 4.19$, $p = 0.04$; $F(1, 50) = 4.23$, $p = 0.04$ for the three metrics, respectively. However, due to feature redundancy, the effectiveness of these graph theory features on classification tasks remains slightly lower than the performance of the traditional CSP algorithm, which achieves an accuracy of 94.91% [In Beta: ANOVA in the results of $F(1, 50) = 12$, $p < 0.001$ for ND feature, $F(1, 50) = 19.82$, $p < 0.001$ for CC feature, and $F(1, 50) = 19.22$, $p < 0.001$ for GE feature].

3.1.2 The effect of feature fusion on MI task classification performance (including the new method proposed)

The CSP algorithm is effective in extracting spatial features from EEG signals. However, since the brain exhibits time-varying characteristics during MI tasks, a single spatial feature cannot fully capture all the information relating to the left and the right hand MI. To address this limitation, the DTF network features and graph theory features are integrated into the CSP algorithm to explore the impact of the DTF brain functional network on the classification effectiveness of MI tasks. As the fused features possess high dimensionality, they are susceptible to feature redundancy, which can

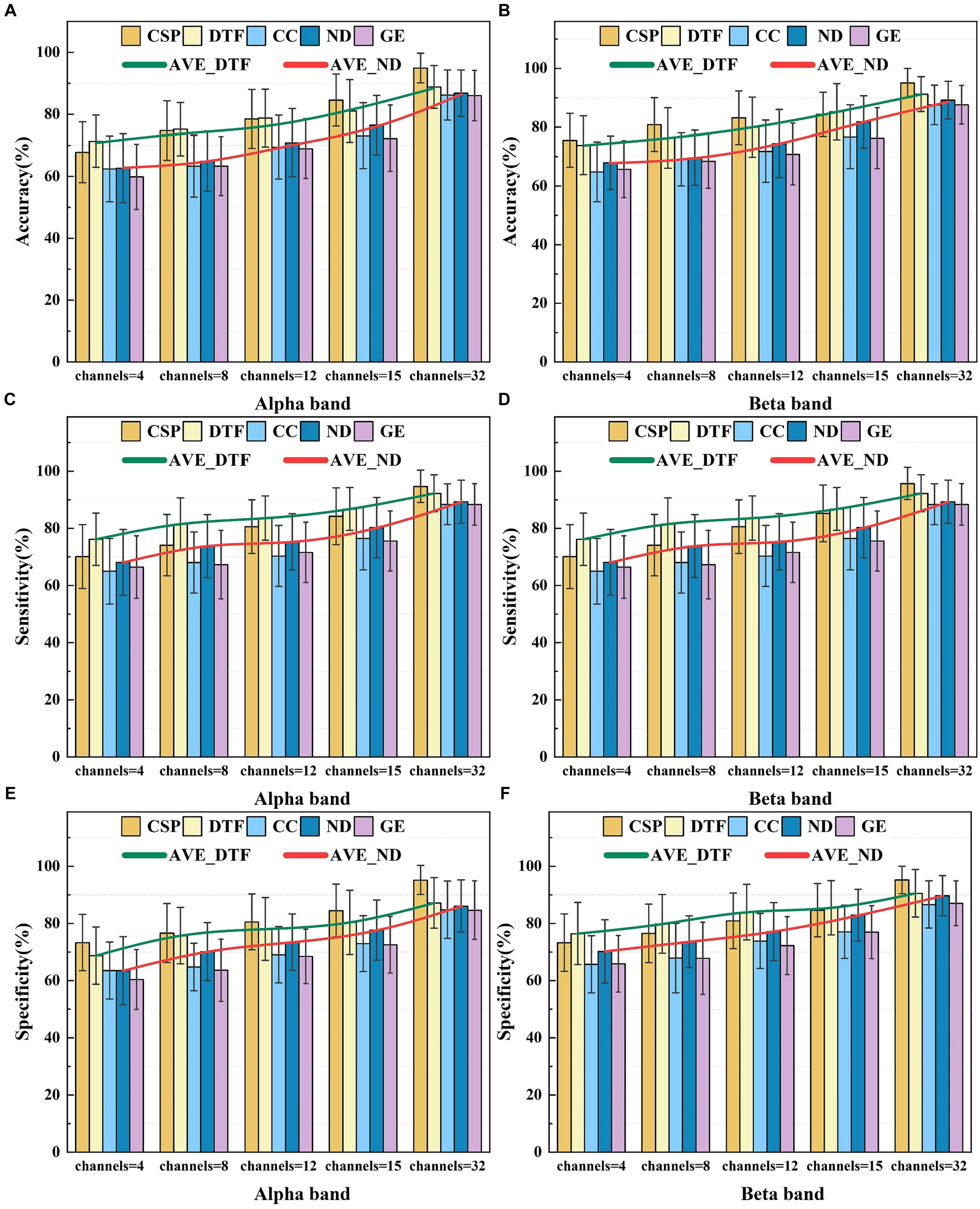

FIGURE 8
The average classification performance of five feature selections for different frequency bands. Panel **(A)** shows the average classification accuracy in the Alpha frequency band. Panel **(B)** shows the average classification accuracy in the Beta frequency band. Panel **(C)** shows the average classification sensitivity in the Alpha frequency band. Panel **(D)** shows the average classification sensitivity in the Beta frequency band. Panel **(E)** shows the average classification specificity in the Alpha frequency band. Panel **(F)** shows the average classification specificity in the Beta frequency band.

lead to a decrease in the classification accuracy. To avoid this issue, the Lasso method is employed to screen the fused features, selecting the optimal ones for classification. Figure 9 presents box-and-line plots for four MI EEG decoding algorithms under two frequency bands: the CSP algorithm, the CSP added DTF with Lasso regularization (CDL), the CSP added graph theory with Lasso regularization (CGL), and

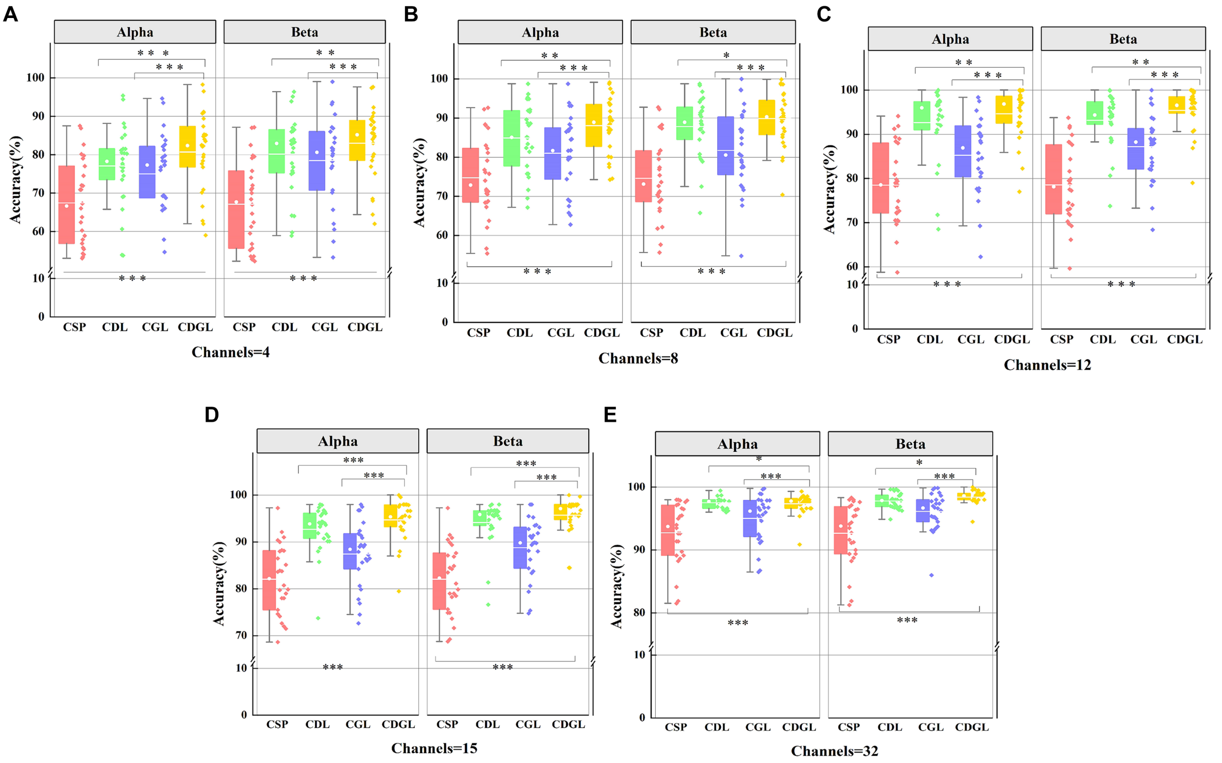

FIGURE 9
The classification accuracies of four methods for two frequency bands with five different channel combinations. Panel **(A)** shows the classification accuracy for two frequency band and 4 channels. Panel **(B)** shows the classification accuracy for two frequency band and 8 channels. Panel **(C)** shows the classification sensitivity for two frequency band and 12 channels. Panel **(D)** shows the classification sensitivity for two frequency band and 15 channels. Panel **(E)** shows the classification specificity for two frequency band and 32 channels.

CSP added DTF and graph theory with Lasso regularization (CDGL). Due to the relatively balance between different classes for the datasets, only one metric "accuracy" is chosen to evaluate the algorithm performance.

Figure 9 reveals that the accuracy of CSP algorithms can be enhanced by integrating DTF network features and graph theory features into traditional CSP algorithms. As the number of channels increases, all four algorithms' average classification accuracy improves. Notably, both the CDL, CGL, and CDGL algorithms outperform the traditional CSP algorithms. A One-way ANOVA was used here to test for significance, yielding a result of $F(3, 100) = 15.12$, $p < 0.001$. Following this result, a *post hoc* analysis was further conducted using the "*multcompare*" function in MATLAB, with a "*CType*" parameter set to "*tukey–kramer*," which means the Tukey HSD method was used. The analysis indicated that there are significant differences between the CSP algorithm and the other three algorithms, with all p-values being less than 0.005. When the number of channels reaches 32, the CDGL algorithm achieves higher accuracy in the Beta frequency band than in the Alpha frequency band [confirmed by a one-way ANOVA, $F(1, 50) = 4.55$, $p = 0.03$]. This observation suggests that the Beta band exhibits more intricate and diverse signal features, which may be attributed to highlight brain activity and enhanced information processing capacity during cognitive tasks. Here, in Figure 9, one single asterisk (*) indicates a significance level of 0.05, double asterisks (**) indicates 0.01 level, and triple asterisks (***) indicates 0.001 level.

3.2 Data from BCI competition and PhysioNet BCI2000

3.2.1 The effect of CSP, DTF, graph theory features on MI task classification performance

To validate the aim drawn in this paper, the algorithms discussed in this article were also tested using the BCI Competition IV 2a dataset and PhysioNet's BCI2000 dataset. To maintain data consistency, the validation was conducted using the same electrodes, specifically the 4-channel and 8-channel configurations. The broken lines depict the accuracy, sensitivity, and specificity metrics of the six classification methods according to different channels and different frequency band. Panels (a), (b), and (c) present the results obtained from the BCI IV 2a dataset, whereas panels (d), (e), and (f) show the results from PhysioNet's BCI2000 dataset.

It can be easily seen from Figure 10 that the algorithms involved in 4-channel are less correctly classified than 8-channel, both in the Alpha band and in the Beta band. The accuracy, sensitivity, and specificity of CDGL (CSP+DTF+Graph theory feature+Lasso) are significantly higher than that of CSP, DTF, CSPL (CSP+Lasso), CDL (CSP+DTF+Lasso), and CGL (CSP+Graph theory feature+Lasso). As the analysis focuses on discerning significant differences among various algorithms applied to the same datasets, a paired sample t-test is employed to ascertain the statistical disparities between the CDGL

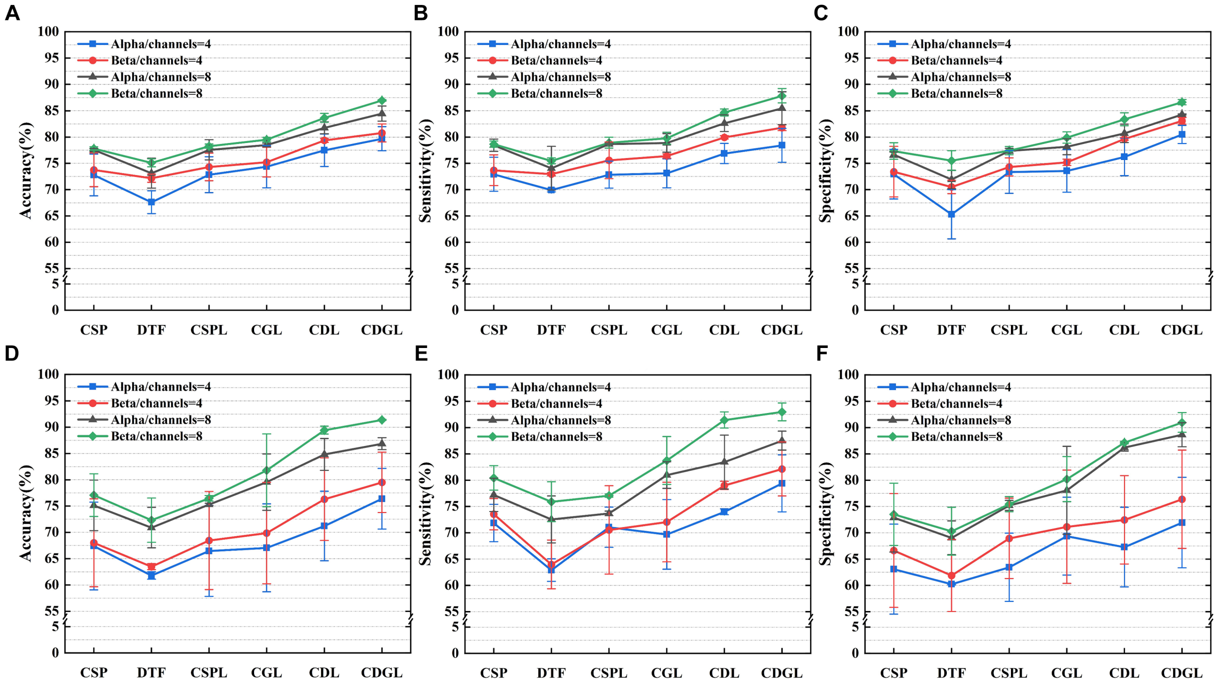

FIGURE 10
Three metrics of the six algorithms for the MI-BCI task classifications for two frequency bands and the two different datasets. Panels **(A–C)** display the classification accuracy, sensitivity, and specificity, respectively, for the BCI competition dataset. Panels **(D–F)** display the classification accuracy, sensitivity, and specificity, respectively, for the PhysioNet BCI2000 dataset.

algorithm and others. Due to requiring multiple comparisons, therefore, the Bonferroni correction was employed, leading to the adjustment of the *p*-value from 0.05 to 0.01 (0.05/5). The findings reveal that the *p*-values of the three assessment model indicators are consistently below the significance threshold of 0.01, whether within the BCI IV 2a dataset or the PhysioNet's BCI2000 dataset.

3.2.2 The effect of feature fusion on MI task classification performance (including the new method proposed) and comparison with EEGNet method

In the validation using public datasets, this paper also explored the impact of the feature fusion algorithm CDGL on classification performance. As shown in Figure 10, the CDGL algorithm's performance was rigorously evaluated under varying conditions of channel and frequency band configurations using the three specific evaluation metrics. Comparisons were conducted in two primary scenarios: First, the algorithm's performance were compared between alpha band and beta band while maintaining constant channel settings. This involved an assessment of the performance in alpha and beta bands separately configured at channels = 4 or channels = 8. Secondly, the study focused on comparing the algorithm's performance metrics across different channel configurations, channels = 4 and channels = 8, within unchanged frequency band. The results of each comparison show significant differences (all *p*-value <0.0125). This comparative analysis was aimed at exploring the impact of channel and frequency band variations on the effectiveness of the CDGL algorithm.

In addition, this paper also made a comparison with one of gold-standard methods (EEGNet) commonly used for MI-BCI classification tasks. The comparison results of the three performance indicators of the two algorithms are shown in Figure 11.

The parameter selection for CDGL is as channel numbers = 8, Beta band, the model's order = 8. A comparative analysis of two models—EEGNet and CDGL—was conducted using the standardized BCI IV 2a and PhysioNet's BCI2000 dataset. It was indicated that for the three key metrics (accuracy, sensitivity, and specificity), CDGL performs better than EEGNet, affirming the superior capability and dependability of CDGL for the classification of MI-BCI tasks. On the BCI IV 2a dataset, the CDGL achieved 84.98% accuracy, 86.08% sensitivity, and 84.82% specificity respectively, surpassing the values of 80.77, 78.13, and 82.65% reported by EEGNet (Paired *t*-test, $p = 0.008$ for accuracy, $p = 0.01$ for sensitivity and $p = 0.012$ for specificity). Similarly, for the PhysioNet's BCI2000 dataset, CDGL attained an accuracy of 91.37%, a sensitivity rate of 86.08%, and a specificity rate of 90.96%, in contrast to the 81.84, 78.82, and 75.57% obtained by EEGNet (Paired *t*-test, $p = 0.012$ for accuracy, $p = 0.014$ for sensitivity and $p = 0.003$ for specificity).

4 Discussion

This article presents an exploration of a brain functional network construction method based on the DTF. We demonstrate its discriminative ability in left and right hand MI tasks by extracting DTF network features and graph theory features. Specifically, for the left-hand MI tasks, there is a noticeable enhancement in the strength

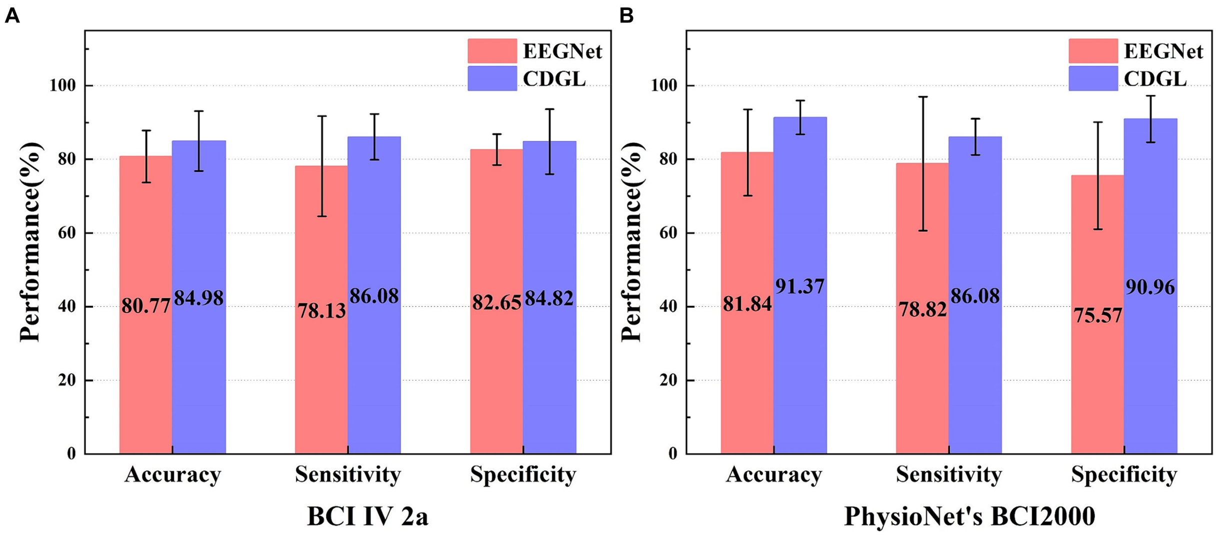

FIGURE 11
The performance comparison of two algorithms (EEGNet and CDGL) on two different datasets (BCI IV 2a and PhysioNet's BCI2000). Panel **(A)** shows the classification performance of two algorithms for the BCI IV 2A dataset. Panel **(B)** shows the classification performance of two algorithms for the PhysioNet BCI2000 dataset.

of neural connections within the left hemisphere, indicating an increased neural activity and a significant flow of information (as demonstrated in Figure 6). This increment in activity not only results in reduced energy within the left hemisphere but is also correlated with a decline in power within specific frequency bands (namely, the alpha and beta bands), consistent with the Event-Related Desynchronization (ERD) phenomenon observed in the contralateral sensorimotor cortex. Similarly, this phenomenon occurs within the right hemisphere during right hand MI tasks.

The findings of this study offer a novel approach to enhancing the performance of traditional CSP algorithms. We showed the improved classification results by integrating DTF network features and graph theory features into CSP. These findings are consistent with previous findings (Ghosh et al., 2015; Filho et al., 2018; Li and Zhang, 2022) that indicators of functional brain connectivity have the potential for categorization in the domain of MI tasks. Compared to the methods used in previous research, we innovatively integrate DTF network features with graph theory features, obtaining significantly improved experimental results. Our study further demonstrates the effectiveness of the DTF-based brain functional network construction method for MI tasks. Graph feature application effectively captures the spatial correlations and network structures in EEG data, which are the aspects often overlooked in traditional time-frequency feature analysis. Insight into this spatial correlation is crucial for deeply understanding the brain's activity patterns while MI tasks. Our use of graph features aims not merely to achieve superior performance on datasets but is based on a profound understanding of brain network analysis and signal processing. Our research delves deeply into the brain activity analysis during the MI process, seeking a comprehensive understanding of these complex activities rather than a mere accumulation of features. It is worth noting that our study was limited to the dichotomous categorization problem for left and right hand MI tasks. Future studies could extend it to more complex multi-categorization MI tasks. This will further validate our proposed approach for various tasks and contexts. In addition, we plan to explore the impact of multiple network feature fusion techniques on motion imagery decoding algorithms. By combining different types of features, such as time-domain features, frequency-domain features, and spatial features, we can expect to further improve the decoding accuracy and robustness of the MI tasks.

The algorithm's information transmission rate in offline experiments, which utilized 3 s of data, was not enough for a real-time application, for examples brain-controlled wheel chair and robots. The sliding time window sampling might be a reasonable choice to enhance this rate in forthcoming real-time studies. The further research will focus on evaluating the real-time performance of the proposed algorithm, applying it to develop a brain-controlled robotic arm for enhancing the rehabilitation of patients suffering from nerve injuries.

5 Conclusion

In this paper, a brain functional network feature extraction method based on DTF network features and graph theory features is proposed for classifying two MI tasks. The following conclusions were reached:

(1) Both DTF network features and graph theory features have demonstrated their effectiveness in classifying MI tasks and have positively contributed to the performance improvement of the CSP algorithm. Especially, the proposed CDGL incorporating DTF network features and graph theory features together achieves the highest classification accuracy among the other feature fusion methods. This indicates that analyzing the features of brain functional networks can provide essential information for distinguishing between different MI tasks.

(2) Increasing the number of channels provides more information about the EEG signals, which improves the model's sensitivity and

ability to discriminate between specific activities in brain regions. Specifically, as the number of channels increases, the ability to characterize the expression of EEG signals is enhanced.

(3) The Beta band functional brain network features exhibited superior performance enhancement for the CDGL algorithm compared to the Alpha band. This suggests that EEG signals in the Beta band may contain more valuable information and have a greater impact on the accuracy and robustness of the classification algorithm in MI tasks.

These findings contribute significantly to our understanding of the mechanisms underlying BCIs and MI tasks, offering fresh insights and novel possibility for further research in the field of neuroscience. Future studies can focus on exploring and refining feature extraction methods based on DTF and graph theory, extending their applicability to a wider range of tasks and practical applications.

Data availability statement

The raw data supporting the conclusions of this article will be made available by the authors, without undue reservation.

Ethics statement

The studies involving humans were approved by Ethics Review Committee of Inner Mongolia University of Technology. The studies were conducted in accordance with the local legislation and institutional requirements. The participants provided their written informed consent to participate in this study. Written informed consent was obtained from the individual(s) for the publication of any potentially identifiable images or data included in this article.

Author contributions

PM: Formal analysis, Investigation, Methodology, Software, Writing – original draft. CD: Conceptualization, Funding acquisition, Resources, Supervision, Writing – review & editing. RL: Visualization, Writing – original draft. HZL: Data curation, Investigation, Writing – original draft. DL: Validation, Writing – original draft. XC: Software, Validation, Writing – review & editing. HL: Investigation, Software, Writing – review & editing.

Funding

The author(s) declare that financial support was received for the research, authorship, and/or publication of this article. This work was supported by the National Natural Science Foundation of China (61364018 and 61863029), Inner Mongolia Natural Science Foundation (2016JQ07, 2020MS06020, and 2021MS06017), Inner Mongolia Scientific and Technological Achievements Transformation Project (CGZH2018129), Industrial Technology Innovation Program of IMAST (2023JSYD01006), and Science and Technology Plan Project of Inner Mongolia Autonomous Region (2021GG0264 and 2020GG0268).

Conflict of interest

The authors declare that the research was conducted in the absence of any commercial or financial relationships that could be construed as a potential conflict of interest.

Publisher's note

References

Amin, S. U., Alsulaiman, M., Muhammad, G., Mekhtiche, M. A., and Shamim Hossain, M. (2019). Deep learning for EEG motor imagery classification based on multi-layer CNNs feature fusion. *Futur. Gener. Comput. Syst.* 101, 542–554. doi: 10.1016/j.future.2019.06.027

Amin, H. U., Malik, A. S., Ahmad, R. F., Badruddin, N., Kamel, N., Hussain, M., et al. (2015). Feature extraction and classification for EEG signals using wavelet transform and machine learning techniques. *Australas. Phys. Eng. Sci. Med.* 38, 139–149. doi: 10.1007/s13246-015-0333-x

An, J., Chen, X., and Wu, D. (2023). Algorithm contest of motor imagery BCI in the world robot contest 2022: a survey. *Brain Sci. Adv.* 9, 166–181. doi: 10.26599/BSA.2023.9050011

Awais, M. A., Yusoff, M. Z., Khan, D. M., Yahya, N., Kamel, N., and Ebrahim, M. (2021). Effective connectivity for decoding electroencephalographic motor imagery using a probabilistic neural network. *Sensors* 21:6570. doi: 10.3390/s21196570

Blankertz, B., Tomioka, R., Lemm, S., Kawanabe, M., and Muller, K. R. (2008). Optimizing spatial filters for robust EEG single-trial analysis. *IEEE Signal Process. Mag.* 25, 41–56. doi: 10.1109/MSP.2008.4408441

Bore, J. C., Li, P., Jiang, L., Ayedh, W. M. A., Chen, C., Harmah, D. J., et al. (2021). A long short-term memory network for sparse spatiotemporal EEG source imaging. *IEEE Trans. Med. Imaging* 40, 3787–3800. doi: 10.1109/TMI.2021.3097758

Borra, D., Magosso, E., Castelo-Branco, M., and Simões, M. (2022). A Bayesian-optimized design for an interpretable convolutional neural network to decode and analyze the P 300 response in autism. *J. Neural Eng.* 19:046010. doi: 10.1088/1741-2552/ac7908

Bullmore, E. T., and Bassett, D. S. (2011). Brain graphs: graphical models of the human brain connectome. *Annu. Rev. Clin. Psychol.* 7, 113–140. doi: 10.1146/annurev-clinpsy-040510-143934

Chen, X., Yu, Y., Tang, J., Zhou, L., Liu, K., Liu, Z., et al. (2022). Clinical validation of BCI-controlled wheelchairs in subjects with severe spinal cord injury. *IEEE Trans. Neural Syst. Rehabil. Eng.* 30, 579–589. doi: 10.1109/TNSRE.2022.3156661

Cheng, N., Phua, K. S., Lai, H. S., Tam, P. K., Tang, K. Y., Cheng, K. K., et al. (2020). Brain-computer Interface-based soft robotic glove rehabilitation for stroke. *IEEE Trans. Biomed. Eng.* 67, 3339–3351. doi: 10.1109/TBME.2020.2984003

Dai, G., Zhou, J., Huang, J., and Wang, N. (2020). HS-CNN: a CNN with hybrid convolution scale for EEG motor imagery classification. *J. Neural Eng.* 17:016025.1-016025. 11. doi: 10.1088/1741-2552/ab405f

Davis, K. C., and Meschede-Krasa, B. (2022). Design-development of an at-home modular brain–computer interface (BCI) platform in a case study of cervical spinal cord injury. *J. Neuroeng. Rehabilit.* 19:53. doi: 10.1186/s12984-022-01026-2

de Vico, F. F., Richiardi, J., Chavez, M., and Achard, S. (2014). Graph analysis of functional brain networks: practical issues in translational neuroscience. *Philos. Trans. R. Soc. B Biol. Sci.* 369:20130521. doi: 10.1098/rstb.2013.0521

Delorme, A., and Makeig, S. (2004). EEGLAB: an open source toolbox for analysis of single-trial EEG dynamics including independent component analysis. *J. Neurosci. Methods* 134, 9–21. doi: 10.1016/j.jneumeth.2003.10.009

Filho, C. A. S., Attux, R., and Castellano, G. (2018). Can graph metrics be used for EEG-BCIs based on hand motor imagery? *Biomed. Signal Process. Control.* 40, 359–365. doi: 10.1016/j.bspc.2017.09.026

Ghosh, P., Mazumder, A., Bhattacharyya, S., Tibarewala, D. N., and Hayashibe, M. *Functional connectivity analysis of motor imagery EEG signal for brain-computer interfacing application*. In International IEEE/EMBS Conference on Neural Engineering; (2015).

Gong, A., Liu, J., Chen, S., and Fu, Y. (2017). Time–frequency cross mutual information analysis of the brain functional networks underlying multiclass motor imagery. *J. Mot. Behav.* 50, 1–14. doi: 10.1080/00222895.2017.1327417

He, B., Dai, Y., Astolfi, L., Babiloni, F., Yuan, H., and Yang, L. (2011). eConnectome: a MATLAB toolbox for mapping and imaging of brain functional connectivity. *J. Neurosci. Methods* 195, 261–269. doi: 10.1016/j.jneumeth.2010.11.015

Hu, L., Zhu, J., Chen, S., Zhou, Y., Song, Z., and Li, Y. (2023). A wearable asynchronous brain-computer Interface based on EEG-EOG signals with fewer channels. *IEEE Trans. Biomed. Eng.* 71, 504–513. doi: 10.1109/TBME.2023.3308371

Ji, N., Ma, L., Dong, H., and Zhang, X. (2019). EEG signals feature extraction based on DWT and EMD combined with approximate entropy. *Brain Sci.* 9:201. doi: 10.3390/brainsci9080201

Jia, H., Wang, S., Zheng, D., Qu, X., and Fan, S. (2019). Comparative study of motor imagery classification based on BP-NN and SVM. *J. Eng.* 2019, 8646–8649. doi: 10.1049/joe.2018.9075

Jin, J., Xiao, R. C., Daly, I., Miao, Y., Wang, X., and Cichocki, A. (2021). Internal feature selection method of CSP based on L1-norm and Dempster-Shafer theory. *IEEE Trans. Neural Netw. Learn. Syst.* 32, 4814–4825. doi: 10.1109/TNNLS.2020.3015505

Kaminski, M. J., and Blinowska, K. J. (1991). A new method of the description of the information flow in the brain structures. *Biol. Cybern.* 65, 203–210. doi: 10.1007/BF00198091

Kamiński, M., Ding, M., Truccolo, W. A., and Bressler, S. L. (2001). Evaluating causal relations in neural systems: granger causality, directed transfer function and statistical assessment of significance. *Biol. Cybern.* 85, 145–157. doi: 10.1007/s004220000235

Koles, Z. J., Lazar, M. S., and Zhou, S. Z. (1990). Spatial patterns underlying population differences in the background EEG. *Brain Topogr.* 2, 275–284. doi: 10.1007/BF01129656

Lawhern, V. J., Solon, A. J., Waytowich, N. R., Gordon, S. M., Hung, C. P., and Lance, B. J. (2018). EEGNet: a compact convolutional neural network for EEG-based brain–computer interfaces. *J. Neural Eng.* 15:056013. doi: 10.1088/1741-2552/aace8c

Li, M., and Zhang, Y. (2022). A brain functional network based on continuous wavelet transform and symbolic transfer entropy. *Acta Electron. Sin.* 50, 1600–1608. doi: 10.12263/DZXB.20210298

Lin, R., Dong, C., Ma, P., Ma, S., Chen, X., and Liu, H. (2022). A fused multidimensional EEG classification method based on an extreme tree feature selection. *Comput. Intell. Neurosci.* 2022, 7609196–7609110. doi: 10.1155/2022/7609196

Ma, S., Dong, C., Jia, T., Ma, P., Xiao, Z., Chen, X., et al. (2022). A feature extraction algorithm of brain network of motor imagination based on a directed transfer function. *Comput. Intell. Neurosci.* 2022, 1–7. doi: 10.1155/2022/4496992

Mammone, N., Ieracitano, C., Adeli, H., and Morabito, F. C. (2023). Auto encoder filter Bank common spatial patterns to decode motor imagery from EEG. *IEEE J. Biomed. Health Inform.* 27, 2365–2376. doi: 10.1109/JBHI.2023.3243698

Park, S. H., Lee, D., and Lee, S. G. (2018). Filter Bank regularized common spatial pattern ensemble for small sample motor imagery classification. *IEEE Trans. Neural Syst. Rehabil. Eng.* 26, 498–505. doi: 10.1109/TNSRE.2017.2757519

Pichiorri, F., Morone, G., Petti, M., Toppi, J., Pisotta, I., Molinari, M., et al. (2015). Brain–computer interface boosts motor imagery practice during stroke recovery. *Ann. Neurol.* 77, 851–865. doi: 10.1002/ana.24390

Rodrigues, P. G., Filho, C. A. S., Attux, R., Castellano, G., and Soriano, D. C. (2019). Space-time recurrences for functional connectivity evaluation and feature extraction in motor imagery brain-computer interfaces. *Med. Biol. Eng. Comput.* 57, 1709–1725. doi: 10.1007/s11517-019-01989-w

Schalk, G., McFarland, D. J., Hinterberger, T., Birbaumer, N. R., and Wolpaw, J. (2004). BCI2000: a general-purpose brain-computer interface (BCI) system. *IEEE Trans. Biomed. Eng.* 51, 1034–1043. doi: 10.1109/TBME.2004.827072

Shibata, T., Suhara, Y., Oga, T., Ueki, Y., Mima, T., and Ishii, S. (2004). Application of multivariate autoregressive modeling for analyzing the interaction between EEG and EMG in humans. *Int. Cong.* 1270, 249–253. doi: 10.1016/j.ics.2004.05.048

Simões, M., Borra, D., Santamaría-Vázquez, E., GBT-UPMBittencourt-Villal pando, M., Krzemiński, D., et al. (2020). BCIAUT-P 300: a multi-session and multi-subject benchmark dataset on autism for P 300-based brain-computer-interfaces [original research]. *Front. Neurosci.* 14:14. doi: 10.3389/fnins.2020.568104

Song, Y., Jia, X., Yang, L., and Xie, L. (2021). Transformer-based spatial-temporal feature learning for EEG decoding. arXiv:2106.11170, 1–10. doi: 10.48550/arXiv.2106.11170

Sun, J., Wei, M., Luo, N., Li, Z., and Wang, H. (2022). Euler common spatial patterns for EEG classification. *Med. Biol. Eng. Comput.* 60, 753–767. doi: 10.1007/s11517-021-02488-7

Tangermann, M., Müller, K-R., Aertsen, A., Birbaumer, N., Braun, C., Brunner, C., et al. (2012). Review of the BCI Competition IV [Review]. *Front. Neurol.* 6:21084. doi: 10.3389/fnins.2012.00055

Vallabhaneni, R. B., Sharma, P., Kumar, V., Kulshreshtha, V., Reddy, K. J., Kumar, S. S., et al. (2021). Deep learning algorithms in EEG signal decoding application: a review. *IEEE Access* 99:1. doi: 10.1109/ACCESS.2021.3105917

Värbu, K., Muhammad, N., and Muhammad, Y. (2022). Past, present, and future of EEG-based BCI applications. *Sensors* 22:3331. doi: 10.3390/s22093331

Varsehi, H., and Firoozabadi, S. M. P. (2021). An EEG channel selection method for motor imagery based brain–computer interface and neurofeedback using granger causality. *Neural Netw.* 133, 193–206. doi: 10.1016/j.neunet.2020.11.002

Wang, Q. S., Cao, T. N., Liu, D., Zhang, M., Lu, J. Y., Bai, O., et al. (2021). A motor-imagery channel-selection method based on SVM-CCA-CS. *Meas. Sci. Technol.* 32:035701. doi: 10.1088/1361-6501/abc205

Wang, F., Wen, Y., Bi, J., Li, H., and Sun, J. (2023). A portable SSVEP-BCI system for rehabilitation exoskeleton in augmented reality environment. *Biomed. Signal Process. Control.* 83:104664. doi: 10.1016/j.bspc.2023.104664

Wang, Z., Wong, C. M., Nan, W. Y., Tang, Q., Rosa, A. C., Xu, P., et al. (2022). Learning curve of a short-time neurofeedback training: reflection of brain network dynamics based on phase-locking value. *IEEE Trans. Cogn. Dev. Syst.* 14, 1282–1295. doi: 10.1109/TCDS.2021.3125948

Xia, M., Wang, J., and He, Y. (2013). BrainNet viewer: a network visualization tool for human brain connectomics. *PLoS One* 8:e68910. doi: 10.1371/journal.pone.0068910

Yu, H., Ba, S., Guo, Y., Guo, L., and Xu, G. (2022). Effects of motor imagery tasks on brain functional networks based on EEG mu/Beta rhythm. *Brain Sci.* 12:194. doi: 10.3390/brainsci12020194

Zhang, J., Li, Y., Chen, H., Ding, J., and Yuan, Z. (2016). An investigation of the differences and similarities between generated small-world networks for right-and left-hand motor imageries. *Sci. Rep.* 6:36562. doi: 10.1038/srep36562

Zhang, S., Zhu, Z., Zhang, B., Feng, B., Yu, T., Li, Z., et al. (2021). Fused group lasso: a new EEG classification model with spatial smooth constraint for motor imagery-based brain–computer Interface. *IEEE Sensors J.* 21, 1764–1778. doi: 10.1109/JSEN.2020.3016402

frontiers | Frontiers in Neuroimaging

TYPE Original Research
PUBLISHED 09 May 2024
DOI 10.3389/fnimg.2024.1356713

OPEN ACCESS

EDITED BY
Xi-Nian Zuo,
Beijing Normal University, China

REVIEWED BY
Nian Wang,
Indiana University Bloomington, United States
Tsen-Hsuan Lin,
GlaxoSmithKline, United States

*CORRESPONDENCE
Jiang Du
✉ jiangdu@ucsd.edu

†PRESENT ADDRESS
Robert Bussell,
CorTechs AI, San Diego, CA, United States

‡These authors have contributed equally to this work

RECEIVED 16 December 2023
ACCEPTED 15 April 2024
PUBLISHED 09 May 2024

CITATION
Searleman AC, Ma Y, Sampath S, Sampath S, Bussell R, Chang EY, Deaton L, Schumacher AM and Du J (2024) 3D inversion recovery ultrashort echo time MRI can detect demyelination in cuprizone-treated mice. *Front. Neuroimaging* 3:1356713. doi: 10.3389/fnimg.2024.1356713

3D inversion recovery ultrashort echo time MRI can detect demyelination in cuprizone-treated mice

Adam C. Searleman[1‡], Yajun Ma[1‡], Srihari Sampath[1], Srinath Sampath[1], Robert Bussell[1†], Eric Y. Chang[1,2], Lisa Deaton[3], Andrew M. Schumacher[3] and Jiang Du[1,2,4]*

[1]Department of Radiology, University of California, San Diego, San Diego, CA, United States, [2]Radiology Service, Veterans Affairs San Diego Healthcare System, San Diego, CA, United States, [3]Novartis Institutes for BioMedical Research, San Diego, CA, United States, [4]Department of Bioengineering, University of California, San Diego, San Diego, CA, United States

Purpose: To test the ability of inversion-recovery ultrashort echo time (IR-UTE) MRI to directly detect demyelination in mice using a standard cuprizone mouse model.

Methods: Non-aqueous myelin protons have ultrashort T_2s and are “invisible” with conventional MRI sequences but can be detected with UTE sequences. The IR-UTE sequence uses an adiabatic inversion-recovery preparation to suppress the long T_2 water signal so that the remaining signal is from the ultrashort T_2 myelin component. In this study, eight 8-week-old C57BL/6 mice were fed cuprizone ($n = 4$) or control chow ($n = 4$) for 5 weeks and then imaged by 3D IR-UTE MRI. The differences in IR-UTE signal were compared in the major white matter tracts in the brain and correlated with the Luxol Fast Blue histochemical marker of myelin.

Results: IR-UTE signal decreased in cuprizone-treated mice in white matter known to be sensitive to demyelination in this model, such as the corpus callosum, but not in white matter known to be resistant to demyelination, such as the internal capsule. These findings correlated with histochemical staining of myelin content.

Conclusions: 3D IR-UTE MRI was sensitive to cuprizone-induced demyelination in the mouse brain, and is a promising noninvasive method for measuring brain myelin content.

KEYWORDS

MRI, IR-UTE, myelin imaging, mouse model, cuprizone

1 Introduction

In the central nervous system, myelin is a component of oligodendrocytes defined by its ultrastructure of multiple lamellae of protein-rich lipid bilayers; myelin insulates the axons of certain nerves to facilitate saltatory conduction and provides trophic support (Morell and Quarles, 1999a). The extent of myelination modulates the function and health of axons and is dynamically regulated throughout the lifespan and in response to a variety of neurologic conditions (Young et al., 2013; Duncan and Radcliff, 2016).

The development of robust and specific biomarkers of myelination would facilitate further advancements in the diagnosis, monitoring, and treatment of demyelinating diseases. For instance, there has been recent interest in the development of promoters of remyelination as complementary to the current immunosuppressive treatment of multiple sclerosis (Magalon et al., 2012; Deshmukh et al., 2013; Plemel et al., 2017; Lubetzki et al., 2020), an autoimmune demyelinating disease that most commonly affects young adults and ultimately results in progressive functional impairment, cognitive deficits, and early mortality (Lucchinetti et al., 2005; Popescu et al., 2013). An imaging-based biomarker of myelin would be crucial for the development of these potential remyelinating agents at both the pre-clinical and clinical stages.

Myelin imaging is challenging because the T_2 of myelin protons (T_2 from several μs to a few 100's of μs) is much shorter than the minimal echo times (TEs; no less than several ms) of conventional sequences (Horch et al., 2011; Wilhelm et al., 2012; Du et al., 2014a; Sheth et al., 2016). In addition, the longer T_2 water protons comprise over 90% of the MRI signal in the brain (Fan et al., 2018). We have previously shown that adiabatic inversion recovery prepared ultrashort echo time (IR-UTE) sequences with nominal TEs as short as 8 μs are able to robustly suppress long-T_2 water signals and generate a high contrast myelin image on a clinical 3T scanner (Du et al., 2014a,b). This short T_2 signal persists after removing most of the myelin-associated water fraction by D_2O exchange (Fan et al., 2017, 2018; Seifert et al., 2017), suggesting that the IR-UTE sequence is detecting signal from semisolid myelin protons. Myelin is comprised of ∼40–45% lipids/cholesterol, 10–15% protein, and 40% water (Morell and Quarles, 1999b). The majority of the myelin protons detected by UTE sequences are thought to originate from the long-chain methylenes of the bilayers, with additional contributions from cholesterol, choline, and proteins (Horch et al., 2011; Wilhelm et al., 2012). The IR-UTE sequence has also been shown to detect demyelinated MS lesions as confirmed by autopsy (Sheth et al., 2016, 2017).

This study was designed to test the capability of the IR-UTE sequence in detection of demyelination using an animal model. In adult C57BL/6 mice, the copper chelator cuprizone induces demyelination with well-characterized temporal and regional dynamics, notably resulting in pronounced demyelination of the caudal corpus callosum (CC) after 5–6 weeks of exposure (Hiremath et al., 1998; Mason et al., 2001; Matsushima and Morell, 2001; Taylor et al., 2010). Additional acute changes are likely reactive to demyelination including mild edema, microgliosis, astrocytosis, and axonal injury; however there is minimal inflammation compared to models such as experimental autoimmune encephalitis (Matsushima and Morell, 2001; Gudi et al., 2009). Thus, the C57BL/6 cuprizone model is well-suited for determining the sensitivity of IR-UTE for acute demyelination.

In this study, eight 8-week-old C57BL/6 mice were fed cuprizone ($n = 4$) or control chow ($n = 4$) for 5 weeks and then imaged by 3D IR-UTE MRI and compared with conventional diffusion tensor imaging (DTI). The differences in IR-UTE signal were compared in the major white matter tracts in the brain and correlated with the Luxol Fast Blue (LFB) histochemical marker of myelin.

2 Materials and methods

2.1 Sample preparation

All animal studies conformed to institutional IACUC-approved protocols. Ten 8-week-old female C57BL/6 mice were included in this study. Five mice were given 0.2% cuprizone chow (Sigma Aldrich, St Louis, MO; Harlan Laboratories, Inc., Madison, Wisconsin) *ad lib* for 5 weeks, and five controls were given chow lacking cuprizone for 5 weeks prior to being sacrificed for imaging and analysis. This cuprizone dose and duration were chosen to induce maximal regional demyelination in the caudal corpus callosum in this mouse strain (Horch et al., 2011; Wilhelm et al., 2012; Du et al., 2014a; Sheth et al., 2016). One mouse from each group was used for image optimization and excluded from further analysis due to extended imaging times, which may have altered the biological characteristics of the myelin and surrounding tissues. The mice were decapitated and their heads skinned and then flash frozen in liquid nitrogen until analysis to prevent temporal effects related to scan order. Each head was warmed in a room temperature water bath for 2 h immediately prior to MRI to allow for a consistent brain temperature between specimens given the effect of temperature on T_1 and thus nulling time.

2.2 MRI

Brain imaging was performed on a Bruker 7T BioSpec (Billerica, MA) scanner using a mouse brain surface coil for signal reception. The specimens were placed in 15 mL conical tubes on a cardboard insert to facilitate consistent positioning in the center of the coil. No solution was added to the tubes. A conventional T_2-weighted fast spin echo (T_2-FSE) sequence, with repetition time (TR) = 2,760 ms, TE = 40 ms, and echo train length (ETL) = 8, was used for anatomic imaging. A conventional two-dimensional adiabatic inversion recovery prepared FSE (2D IR-FSE) sequence, with TR = 8,000 ms, TE = 18.6 ms, and inversion times (TIs) = 60, 150, 300, 450, 600, 750, 900, 1,200, 1,500, and 2,000 ms, was used to measure T_1 of the long T_2 white matter components using a single coronal image of the ventral hippocampal commissure. A 3D IR-UTE sequence was used to image myelin, using the following parameters: TR = 1,000 ms, TI = 382.5 ms, TE = 20 μs, FOV = $2.0 \times 2.0 \times 2.0$ cm^3, matrix = $110 \times 110 \times 110$, flip angle = 15°, number of excitations (NEX) = 4. To speed up data acquisition, 25 spokes centered on TI were acquired per IR preparation, with 5 ms from the start of one spoke to the next, leading to a total scan time of 100 min. The same 3D IR-UTE sequence was repeated with TE = 2.0 ms and NEX = 1. Similar imaging parameters were used for the T_2-FSE and IR-FSE sequences. Echo planar imaging based DTI

Abbreviations: CC, Corpus callosum; DTI, Diffusion tensor imaging; ETL, Echo train length; FA, Fractional anisotropy; FSE, Fast spin echo; IR-UTE, Inversion-recovery ultrashort echo time (IR-UTE); LFB, Luxol Fast Blue; MT, Magnetic transference; NEX, Number of excitations; RD, Radial diffusivity; ROI, region of interest; TE, echo time; TI, Inversion time; TR, Repetition time; VHC, ventral hippocampal commissure.

MRI was performed using 30 non-colinear gradient directions with gradient b-values = 0, 750, 1,500, and 2,000 s/mm^2, TR = 4,000 ms, TE = 23 ms, and ETL = 13, for a total scan time of 25 min.

2.3 Histology

Immediately after imaging, mouse brains were removed intact, fixed in zinc formalin, and then embedded in paraffin using standard protocols as previously described (Beckmann et al., 2018). One of the control mouse brains was damaged during sample processing and excluded from further histological analysis. Five micron sections were stained with LFB using standard protocols as previously described (Beckmann et al., 2018). Myelin content was semi-quantitatively measured in the genu of the corpus callosum based on staining density as follows: the corpus callosum in each section was visually identified and outlined as the region of interest (ROI) for analysis using the NDP View software for NanoZoomer scanners (Hamamatsu, Photonics, Shizuoka, Japan). The myelin density was then calculated as the LFB optical density within this ROI. LFB densities from nine corpus callosum sections per animal were averaged, and this was compared across 3–4 animals per group.

2.4 Region of interest selection

The 3D IR-UTE images of a control mouse were mapped to anatomical structures using the Allen Mouse Brain Atlas as a reference (Allen Institute for Brain Science, 2004). Regions of interest (ROIs) were generated in two ways. First, ROIs were drawn manually for the genu and splenium of the CC, ventral hippocampal commissure (VHC), and internal capsule by an investigator blinded to group assignment using standardized criteria for ROI selection to ensure consistency. Secondly, ROIs were generated in a semi-automated fashion from a common IR-UTE template. To remove the influence of signal from the calvarium and other extracranial structures on the registration method, brain extraction was performed using custom Matlab scripts (The Mathworks Inc., Natick, MA). The IR-UTE template was generated using Advanced Normalization Tools (Avants et al., 2008) using symmetric diffeomorphic image registration with a cross-correlation metric from IR-UTE images of an untreated mouse. Each specimen was individually registered to this common template. The ROI analysis was done by manually drawing the ROI on the template and using the inverse transformation to map to the corresponding ROI in the original image space. Both ROI analyses were comparable; however, the backpropagation of the ROIs was not as reliable and therefore the first analysis is presented as it was considered to be more accurate. The template-registered IR-UTE images were also analyzed by averaging the registered IR-UTE images in the control mice and the cuprizone-treated mice to obtain averaged IR-UTE signal for each voxel. Subtraction of the averaged control IR-UTE map from the averaged cuprizone-treated IR-UTE map will demonstrate differences in signal for each voxel between these two groups, which was then analyzed for regional patterns of change.

2.5 Data analysis

The IR-UTE absolute signal was obtained from magnitude images. A coil sensitivity map was generated using the magnitude images from the same IR-UTE sequence on a degassed phantom of 20% H_2O and 80% D_2O with 35.5 mM $MnCl_2$ (for T_2^* of 355 ms) in a 15 mL conical tube. The map was then smoothened with a Gaussian filter with size = 4 and σ = 2 and scaled to a maximum value of 1. The IR-UTE signal from each specimen was normalized to this coil sensitivity map by simple division. The fractional anisotropy (FA), axial diffusivity (AD), and radial diffusivity (RD) were generated using the *dtifit* function in FDT (Jbabdi et al., 2012), and compared to the IR-UTE signal using the Pearson correlation coefficient. T_1 values of white matter were calculated using custom code in Matlab in the ventral hippocampal commissure using the normalized maximum likelihood estimate (assuming a Rician distribution) and non-linear least squares fitting. Statistical analysis was performed using the R statistical programming language (v3.4.1) using the Wilcoxon rank-sum test for each ROI. A p-value of < 0.05 was considered statistically significant.

3 Results

Representative images of the optimized IR-UTE sequence of a control mouse brain are shown in Figure 1. The IR-UTE image in Figures 1B, C demonstrates high signal intensity in the major white matter tracts, including the corpus callosum, internal capsule, dorsal and ventral hippocampal commissures, and deep cerebellar white matter; intermediate signal in mixed white and gray matter structures such as the basal ganglia and both superior and inferior colliculi; and minimal signal from cortical gray matter and cerebral spinal fluid (CSF). The high signal in the calvarium seen only on IR-UTE and not FSE images reflects ultrashort T_2 signal from cortical bone, and there is additional signal from retrobulbar fat. The later echo time of TE = 2 ms in Figure 1D has dramatically reduced signal intensities, notably with the majority of the white matter tracts now demonstrating less signal than residual CSF, indicating that the majority of the white matter IR-UTE signal has ultrashort T_2. The retrobulbar fat, bone marrow fat, and minimal CSF signal are more apparent in the TE = 2 ms image due to longer T_2s.

The IR-UTE signal visually decreased in the cuprizone-treated mice in several white matter tracts that are known to be sensitive to cuprizone-induced demyelination (Figure 2). Axial images through the ventral hippocampal commissure and splenium of the corpus callosum demonstrate the greatest decrease in signal intensity in the corpus callosum and to a lesser extent in the ventral hippocampal commissure and white matter of the basal ganglia. In contrast, there was no significant signal change in the internal capsule, which is known to be resistant to cuprizone (Yang et al., 2009). These findings are confirmed to be statistically significant with quantitative analysis using ROIs (Figure 3).

DTI imaging also was able to detect a difference between the control and cuprizone-treated mice. Demyelination is thought to be associated with a decrease in total fractional anisotropy, specifically with an increase in radial diffusivity as the loss of

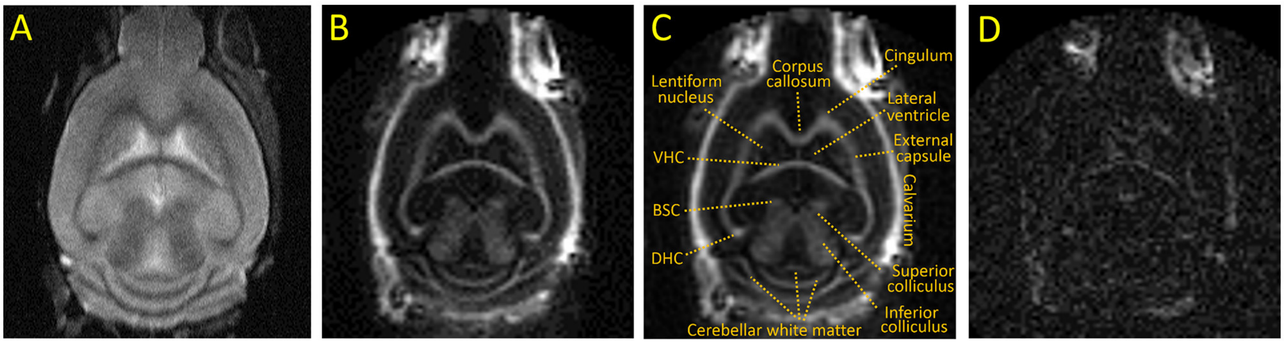

FIGURE 1
Representative coronal images of an untreated adult C57BL/6 mouse. **(A)** T2 weighted FSE, **(B, C)** IR-UTE at TE = 0.020 ms with and without annotations, **(D)** IR-UTE at TE = 2 ms [displayed with a 10X narrower window than **(B)** to show detail]. BSC, Brachium of the superior colliculus; DHC and VHC, dorsal and ventral hippocampal commissure, respectively.

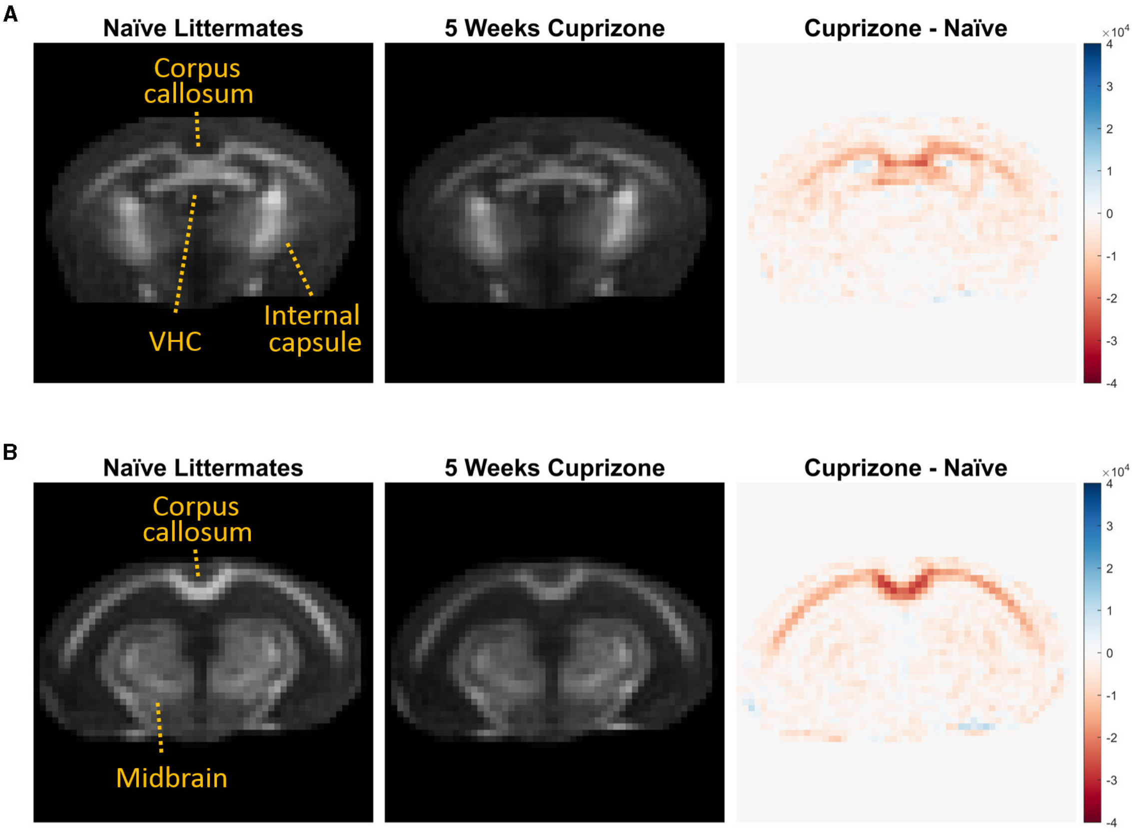

FIGURE 2
Averaged IR-UTE signal from untreated and cuprizone treated mice. IR-UTE images were registered to a common template after brain extraction and then averaged. These averaged axial images are displayed at the level of the **(A)** ventral hippocampal commissure and **(B)** splenium corpus callosum. On the right, subtraction images are shown such that areas of decreased signal in the cuprizone-treated mice are red, and areas of no change are white. Note that the largest decrease in signal was in the splenium of the corpus callosum **(B)**, and the lack of signal differences in the internal capsule **(A)** and midbrain structures **(B)** that are resistant to cuprizone.

myelin bilayers allows water molecules to diffuse in a radial direction from the axon tracts (Xie et al., 2010). In contrast, axial diffusivity is more sensitive to axonal damage, which transiently changes during early treatment with cuprizone (Sun et al., 2006). As expected and in line with prior studies of DTI imaging of cuprizone-treated mice, a decrease in fractional anisotropy and an increase in radial diffusivity were seen in the splenium of the corpus callosum, whereas there was no statistically significant change in axial diffusivity. The IR-UTE signal correlated with both fractional anisotropy and radial diffusivity, but only had a weak correlation with axial diffusivity that was not statistically significant (Figure 4).

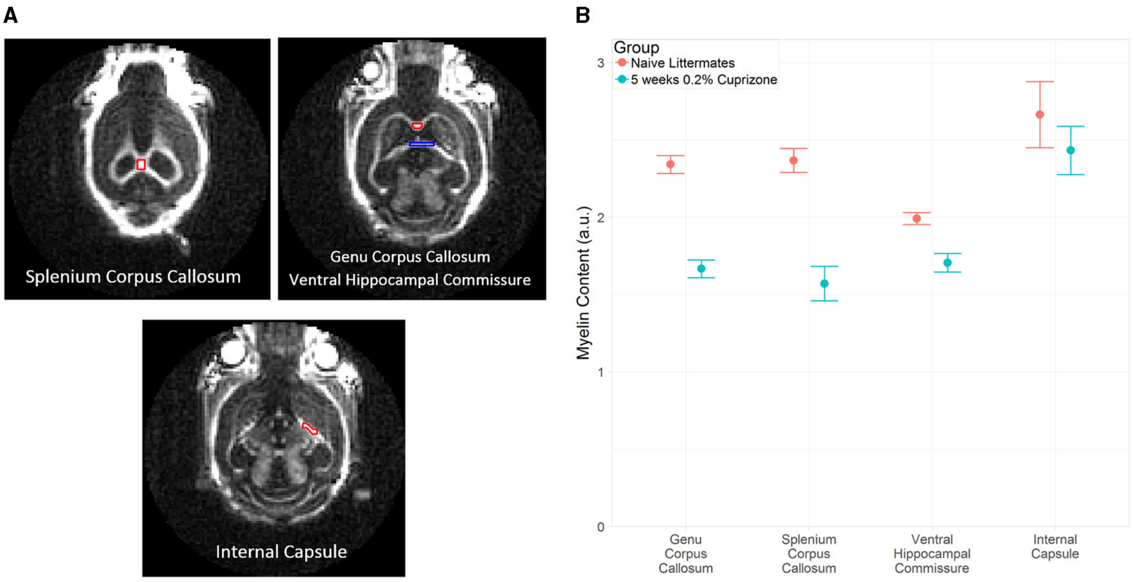

FIGURE 3
(A) Example of ROI placement in a representative control mouse on coronal IR-UTE images at TE = 0.02 ms. In the top right figure, the red ROI corresponds to the genu corpus callosum and the blue ROI corresponds to the ventral hippocampal commissure. **(B)** Average magnitude of IR-UTE images at TE = 0.02 ms for selected ROIs. Bars represent 95% confidence intervals. (a.u.), arbitrary units.

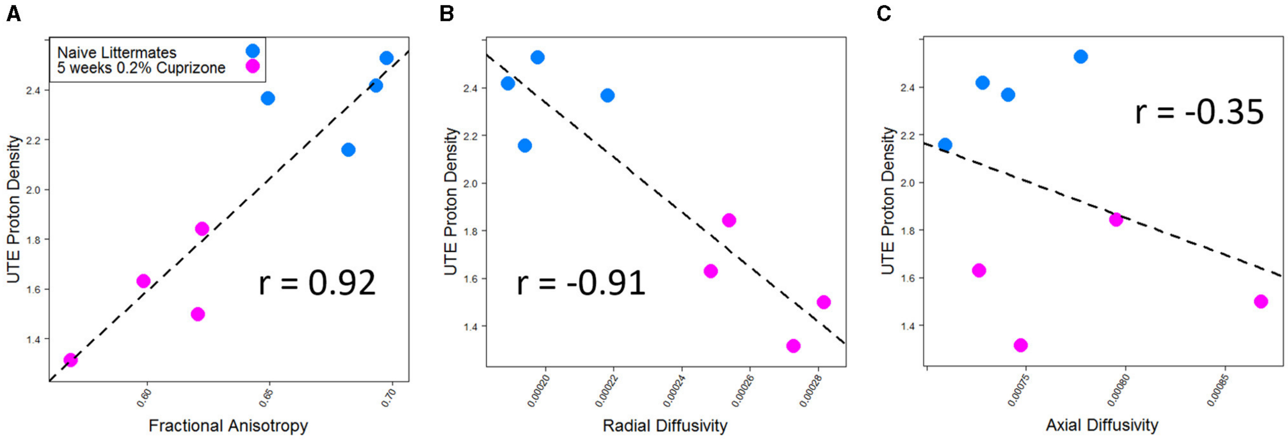

FIGURE 4
IR-UTE signal correlates with **(A)** fractional anisotropy and **(B)** radial diffusivity, but not **(C)** axial diffusivity in cuprizone-treated mice. Both fractional anisotropy and radial diffusivity but not axial diffusivity were different between cuprizone-treated and untreated mice with $p < 0.05$.

Both the IR-UTE and DTI imaging results are corroborated by semi-quantitative histochemical analysis of myelin using LFB staining (Figure 5). All of the cuprizone-treated mice had decreased myelin staining in the genu of the corpus callosum compared to the control mice; however complete demyelination was not achieved in this study. Additionally, T_1 mapping demonstrates that cuprizone treatment did not significantly change the T_1 of the ventral hippocampal commissure (Figure 6). Therefore, the TI_{null} of the long T_2^* components does not significantly change in this model. Otherwise, it could have resulted in artifactual signal intensity changes.

4 Discussion

This study demonstrated that the 3D IR-UTE sequence is able to detect demyelination with decreased myelin signal in an animal model of acute demyelination. The ability of the IR-UTE sequence to detect the ultrashort T_2 signal and suppress the long T_2 signal was demonstrated in mouse brains, similar to prior work using *in vitro* phantoms and human volunteers (Du et al., 2014a; Sheth et al., 2017; Fan et al., 2018). The mice treated with cuprizone demonstrated loss of IR-UTE signal in white matter tracts known to be sensitive to cuprizone but no changes in white matter tracts that are known to be resistant, whereas

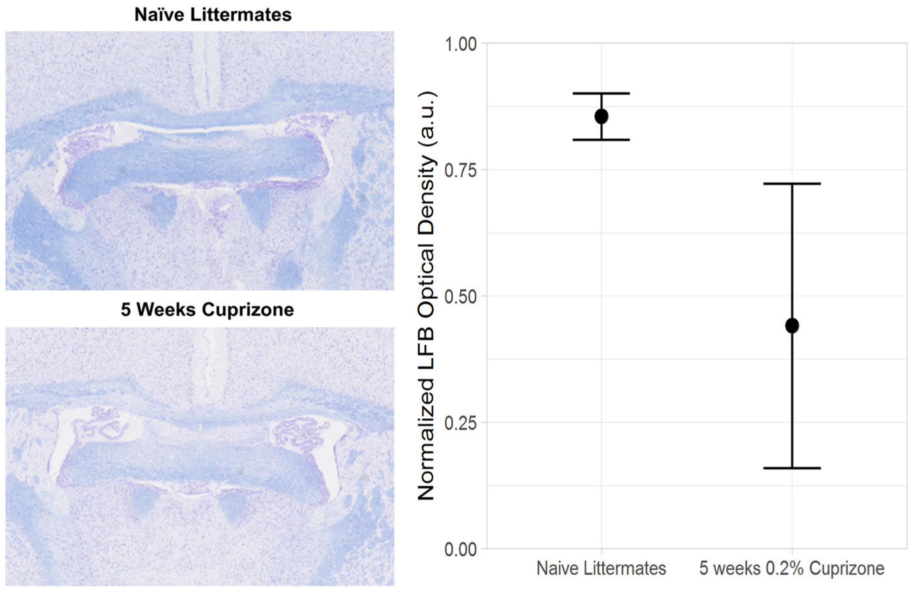

FIGURE 5
Decreased Luxol Fast Blue (LFB) staining in cuprizone treated mice compared with control mice. The plane of sectioning is analogous to Figure 2A, showing decreased myelin in both the genu of the corpus callosum and the ventral hippocampal commissure.

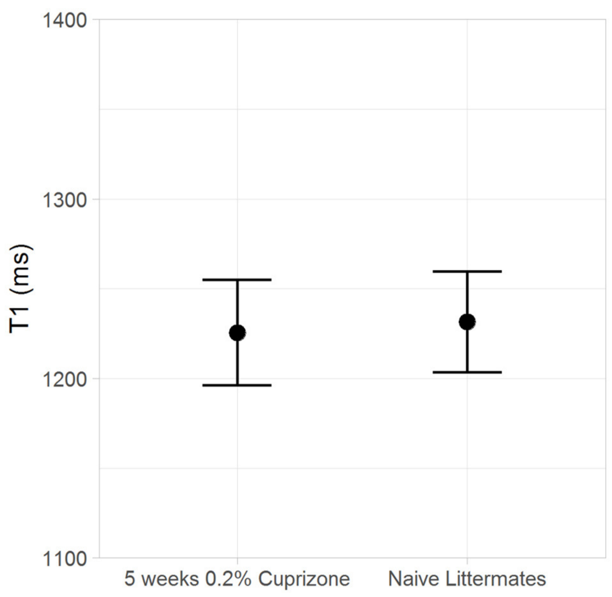

FIGURE 6
The T1 of myelin in the ventral hippocampal commissure is unchanged by cuprizone treatment.

the IR-UTE signal in white matter tracts of control mice was unchanged. The IR-UTE signal was also correlated with findings using DTI MRI. The 3D IR-UTE measurement of demyelination was further confirmed by LFB staining. These findings demonstrate that the IR-UTE signal was sensitive to myelin loss in the cuprizone mouse model.

Many of the existing methods for myelin imaging and quantification detect myelin indirectly through its interactions with myelin-associated water, and have been shown to detect demyelination in the cuprizone model and other animal models. These include magnetic transference (MT)-based imaging methods (Zaaraoui et al., 2008; Varma et al., 2015; Khodanovich et al., 2017), T_2 relaxometry/myelin water fraction imaging (Thiessen et al., 2013; Wood et al., 2016), diffusion based imaging methods (Song et al., 2005; Sun et al., 2006; Wang et al., 2011), quantitative susceptibility mapping (Wang et al., 2019), and others. However, these methods may also be sensitive to other pathologic changes including microgliosis, edema, and mild axonal injury that accompany demyelination in this model (Wood et al., 2016). Directly imaging myelin protons using IR-UTE would be expected to improve specificity for myelin loss in the setting of heterogeneous pathological changes, or may complement these other methods. The indirect measures of myelin are sensitive to B_1 and B_0 inhomogeneities and may be complicated by edema and iron deposition. Unlike IR-UTE, conventional MRI techniques also cannot measure myelin relaxation times (e.g., T1 and T2* relaxation times), which may allow for a direct assessment of myelin quality.

Recently, another UTE-based method was found to correlate with histological markers of myelin in the cuprizone model better than the myelin water fraction and RD and similar to the MT-based macromolecular fraction (Soustelle et al., 2019). This Diff-UTE sequence uses diffusion gradients for suppression of long T_2 water signals, which allows relative preservation of the ultrashort T_2 signal at a short TR. In contrast, the IR-UTE sequence uses IR preparation for long T_2 signal suppression, allowing for recovery of the ultrashort T_2 signal using a longer TR and multispoke acquisition per IR preparation (Carl et al., 2016; Ma et al., 2020b). The IR-UTE sequence is more robust to B_1 inhomogeneity and does not require assumptions about the T_1 and T_2 of myelin for gradient tuning, which is required in Diff-UTE imaging of myelin for appropriate signal nulling of diffusive long-T2 components of the white matter (Soustelle et al., 2019); however, inversion time needs to be carefully determined for IR-UTE imaging. We have recently designed a Double-Echo Sliding Inversion Recovery Ultrashort Echo Time (DESIRE-UTE) method which allows image reconstruction at a wide range of inversion times so that the optimal inversion time does not need to be chosen prospectively (Ma et al., 2020c). Another approach is a short-TR adiabatic inversion-recovery UTE (STAIR-UTE) method which allows robust long T_2 signal suppression with optimized short TR/TI pairs (Ma et al., 2020a). In addition, the Diff-UTE study was performed on mouse brains that had been fixed, which may alter the MR properties of myelin. The specificity of the IR-UTE and Diff-UTE sequences have not yet been tested during remyelination or in other models of demyelination.

There are several limitations of this study. First, the sample size of both the treated and control mice was small, owing to the fact that this study was designed as a proof-of-concept for future studies. Additionally, complete demyelination was not achieved, which limited the ability to examine other contributors to the ultrashort T_2 IR-UTE signal such as inflammation and gliosis. A possible reason for myelin not being as low as expected could be animals not eating enough, or variable amounts, of the cuprizone-containing diet. Future studies will be needed to test the specificity of the IR-UTE signal for myelin in the setting of both demyelination and remyelination using other models of demyelination, and to investigate the advantages and disadvantages over conventional MRI techniques for myelin quantification.

5 Conclusion

In conclusion, the 3D IR-UTE method was able to robustly detect the ultrashort T_2 components in major white matter tracts of the mouse brain with decreased IR-UTE signal of myelin during cuprizone-induced demyelination as confirmed by LFB staining. Therefore, 3D IR-UTE is a promising non-invasive method for measuring brain myelin content in mouse models of demyelination.

Data availability statement

The raw data supporting the conclusions of this article will be made available by the authors, without undue reservation.

Ethics statement

The animal study was approved by IACUC at UCSD and at Novartis Institutes for BioMedical Research. The study was conducted in accordance with the local legislation and institutional requirements.

Author contributions

ACS: Conceptualization, Data curation, Formal analysis, Investigation, Methodology, Software, Writing—original draft, Writing—review & editing. YM: Conceptualization, Data curation, Formal analysis, Investigation, Methodology, Software, Writing—original draft, Writing—review & editing. SrihS: Resources, Supervision, Writing—review & editing. SrinS: Resources, Supervision, Writing—review & editing. RB: Data curation, Methodology, Resources, Software, Writing—review & editing. EC: Conceptualization, Funding acquisition, Methodology, Resources, Supervision, Writing—review & editing. LD: Investigation, Methodology, Resources, Writing—review & editing. AMS: Investigation, Methodology, Resources, Writing—review & editing. JD: Conceptualization, Funding acquisition, Methodology, Project administration, Resources, Supervision, Writing—original draft, Writing—review & editing.

Funding

The author(s) declare financial support was received for the research, authorship, and/or publication of this article. The authors acknowledge grant support from the National Institutes of Health (1R01 NS092650, RF1AG075717, R01AR075825, R01AR079484, R21AR075851, and T32EB005970), VA Research and Development Services (Merit Awards I01CX001388, 1I01BX005952, and I01CX002211), and GE Healthcare. The animal model and histology was provided by Novartis Institutes for BioMedical Research, which did not contribute to the analysis and interpretation of the results of this study. Novartis was not involved in the decision to publish this manuscript or its preparation, but did review the manuscript prior to submission with no requested alterations.

Conflict of interest

LD and AMS were employed by Novartis.

The remaining authors declare that the research was conducted in the absence of any commercial or financial relationships that could be construed as a potential conflict of interest.

The author(s) declared that they were an editorial board member of Frontiers, at the time of submission. This had no impact on the peer review process and the final decision.

Publisher's note

References

Allen Institute for Brain Science (2004). *Allen Mouse Brain Atlas [Dataset]*. Washington, DC: Allen Institute for Brain Science.

Avants, B. B., Epstein, C. L., Grossman, M., and Gee, J. C. (2008). Symmetric diffeomorphic image registration with cross-correlation: evaluating automated labeling of elderly and neurodegenerative brain. *Med. Image Anal.* 12, 26–41. doi: 10.1016/j.media.2007.06.004

Beckmann, N., Giorgetti, E., Neuhaus, A., Zurbruegg, S., Accart, N., Smith, P., et al. (2018). Brain region-specific enhancement of remyelination and prevention of demyelination by the CSF1R kinase inhibitor BLZ945. *Acta Neuropathol. Commun.* 6:9. doi: 10.1186/s40478-018-0510-8

Carl, M., Bydder, G. M., and Du, J. (2016). UTE imaging with simultaneous water and fat signal suppression using a time-efficient multispoke inversion recovery pulse sequence. *Magn. Reson. Med.* 76, 577–582. doi: 10.1002/mrm.25823

Deshmukh, V. A., Tardif, V., Lyssiotis, C. A., Green, C. C., Kerman, B., Kim, H. J., et al. (2013). A regenerative approach to the treatment of multiple sclerosis. *Nature* 502, 327–332. doi: 10.1038/nature12647

Du, J., Ma, G., Li, S., Carl, M., Szeverenyi, N. M., VandenBerg, S., et al. (2014a). Ultrashort echo time (UTE) magnetic resonance imaging of the short T2 components in white matter of the brain using a clinical 3T scanner. *NeuroImage* 87(Suppl.C), 32–41. doi: 10.1016/j.neuroimage.2013.10.053

Du, J., Sheth, V., He, Q., Carl, M., Chen, J., Corey-Bloom, J., et al. (2014b). Measurement of T1 of the ultrashort T2* components in white matter of the brain at 3T. *PLoS ONE* 9:e103296. doi: 10.1371/journal.pone.0103296

Duncan, I. D., and Radcliff, A. B. (2016). Inherited and acquired disorders of myelin: the underlying myelin pathology. *Exp. Neurol.* 283, 452–475. doi: 10.1016/j.expneurol.2016.04.002

Fan, S. J., Ma, Y., Chang, E. Y., Bydder, G. M., and Du, J. (2017). Inversion recovery ultrashort echo time imaging of ultrashort T2 tissue components in ovine brain at 3 T: a sequential D_2O exchange study. *NMR Biomed.* 30:3767. doi: 10.1002/nbm.3767

Fan, S-J., Ma, Y., Zhu, Y., Searleman, A., Szeverenyi, N. M., Bydder, G. M., et al. (2018). Yet more evidence that myelin protons can be directly imaged with UTE sequences on a clinical 3T scanner: bicomponent T2* analysis of native and deuterated ovine brain specimens. *Magn. Reson. Med.* 80, 538–547. doi: 10.1002/mrm.27052

Gudi, V., Moharregh-Khiabani, D., Skripuletz, T., Koutsoudaki, P. N., Kotsiari, A., Skuljec, J., et al. (2009). Regional differences between grey and white matter in cuprizone induced demyelination. *Brain Res.* 1283(Suppl.C), 127–138. doi: 10.1016/j.brainres.2009.06.005

Hiremath, M. M., Saito, Y., Knapp, G. W., Ting, J. P. Y., Suzuki, K., Matsushima, G. K., et al. (1998). Microglial/macrophage accumulation during cuprizone-induced demyelination in C57BL/6 mice. *J. Neuroimmunol.* 92, 38–49. doi: 10.1016/S0165-5728(98)00168-4

Horch, R. A., Gore, J. C., and Does, M. D. (2011). Origins of the ultrashort-T21H NMR signals in myelinated nerve: a direct measure of myelin content? *Magn. Reson. Med.* 66, 24–31. doi: 10.1002/mrm.22980

Jbabdi, S., Sotiropoulos, S. N., Savio, A. M., Graña, M., and Behrens, T. E. J. (2012). Model-based analysis of multishell diffusion MR data for tractography: how to get over fitting problems. *Magn. Reson. Med.* 68, 1846–1855. doi: 10.1002/mrm.24204

Khodanovich, M. Y., Sorokina, I. V., Glazacheva, V. Y., Akulov, A. E., Nemirovich-Danchenko, N. M., Romashchenko, A. V., et al. (2017). Histological validation of fast macromolecular proton fraction mapping as a quantitative myelin imaging method in the cuprizone demyelination model. *Sci. Rep.* 7:46686. doi: 10.1038/srep46686

Lubetzki, C., Zalc, B., Williams, A., Stadelmann, C., and Stankoff, B. (2020). Remyelination in multiple sclerosis: from basic science to clinical translation. *Lancet Neurol.* 19, 678–688. doi: 10.1016/S1474-4422(20)30140-X

Lucchinetti, C. F., Parisi, J., and Bruck, W. (2005). The pathology of multiple sclerosis. *Neurol. Clin.* 23, 77–105. doi: 10.1016/j.ncl.2004.09.002

Ma, Y. J., Jang, H., Wei, Z., Cai, Z., Xue, Y., Lee, R. R., et al. (2020a). Myelin imaging in human brain using a short repetition time adiabatic inversion recovery prepared ultrashort echo time (STAIR-UTE) MRI sequence in multiple sclerosis. *Radiology* 297, 392–404. doi: 10.1148/radiol.2020200425

Ma, Y. J., Searleman, A. C., Jang, H., Fan, S. J., Wong, J., Xue, Y., et al. (2020b). Volumetric imaging of myelin *in vivo* using 3D inversion recovery-prepared ultrashort echo time cones magnetic resonance imaging. *NMR Biomed.* 33:e4326. doi: 10.1002/nbm.4326

Ma, Y. J., Searleman, A. C., Jang, H., Wong, J., Chang, E. Y., Corey-Bloom, J., et al. (2020c). Whole-brain myelin imaging using 3D double-echo sliding inversion recovery ultrashort echo time (DESIRE UTE) MRI. *Radiology* 294, 362–374. doi: 10.1148/radiol.2019190911

Magalon, K., Zimmer, C., Cayre, M., Khaldi, J., Bourbon, C., Robles, I., et al. (2012). Olesoxime accelerates myelination and promotes repair in models of demyelination. *Ann. Neurol.* 71, 213–226. doi: 10.1002/ana.22593

Mason, J. L., Langaman, C., Morell, P., Suzuki, K., and Matsushima, G. K. (2001). Episodic demyelination and subsequent remyelination within the murine central nervous system: changes in axonal calibre. *Neuropathol. Appl. Neurobiol.* 27, 50–58. doi: 10.1046/j.0305-1846.2001.00301.x

Matsushima, G. K., and Morell, P. (2001). The neurotoxicant, cuprizone, as a model to study demyelination and remyelination in the central nervous system. *Brain Pathol.* 11, 107–116. doi: 10.1111/j.1750-3639.2001.tb00385.x

Morell, P., and Quarles, R. H. (1999a). "Characteristic composition of myelin," in *Basic Neurochemistry: Molecular, Cellular and Medical Aspects, 6th Edn*, eds. G. J. Siegel, B. W. Agranoff, R. W. Albers, S. K. Fisher, and M. D. Uhler. Available online at: https://www.ncbi.nlm.nih.gov/books/NBK28221/ (accessed June 1, 2018).

Morell, P., and Quarles, R. H. (1999b). "The myelin sheath," in *Basic Neurochemistry: Molecular, Cellular and Medical Aspects, 6th Edn*, eds. G. J. Siegel, B. W. Agranoff, R. W. Albers, S. K. Fisher, and M. D. Uhler. Available online at: https://www.ncbi.nlm.nih.gov/books/NBK28221/ (accessed June 1, 2018).

Plemel, J. R., Liu, W. Q., and Yong, V. W. (2017). Remyelination therapies: a new direction and challenge in multiple sclerosis. *Nat. Rev. Drug Discov.* 16, 617–634. doi: 10.1038/nrd.2017.115

Popescu, B., Pirko, I., and Lucchinetti, C. F. (2013). Pathology of multiple sclerosis: where do we stand? *Contin. Lifelong Learn Neurol.* 19, 901–921. doi: 10.1212/01.CON.0000433291.23091.65

Seifert, A. C., Li, C., Wilhelm, M. J., Wehrli, S. L., and Wehrli, F. W. (2017). Towards quantification of myelin by solid-state MRI of the lipid matrix protons. *NeuroImage* 163, 358–367. doi: 10.1016/j.neuroimage.2017.09.054

Sheth, V., Shao, H., Chen, J., Vandenberg, S., Corey-Bloom, J., Bydder, G. M., et al. (2016). Magnetic resonance imaging of myelin using ultrashort echo time (UTE) pulse sequences: phantom, specimen, volunteer and multiple sclerosis patient studies. *NeuroImage* 136, 37–44. doi: 10.1016/j.neuroimage.2016.05.012

Sheth, V. R., Fan, S., He, Q., Ma, Y., Annese, J., Switzer, R., et al. (2017). Inversion recovery ultrashort echo time magnetic resonance imaging: a method for simultaneous direct detection of myelin and high signal demonstration of iron deposition in the brain - a feasibility study. *Magn. Reson. Imaging* 38, 87–94. doi: 10.1016/j.mri.2016.12.025

Song, S. K., Yoshino, J., Le, T. Q., Lin, S. J., Sun, S. W., Cross, A. H., et al. (2005). Demyelination increases radial diffusivity in corpus callosum of mouse brain. *NeuroImage* 26, 132–140. doi: 10.1016/j.neuroimage.2005.01.028

Soustelle, L., Antal, M. C., Lamy, J., Rousseau, F., Armspach, J. P., de Loureiro, P., et al. (2019). Correlations of quantitative MRI metrics with myelin basic protein (MBP) staining in a murine model of demyelination. *NMR Biomed.* 2019:e4116. doi: 10.1002/nbm.4116

Sun, S. W., Liang, H. F., Trinkaus, K., Cross, A. H., Armstrong, R. C., Song, S. K., et al. (2006). Noninvasive detection of cuprizone induced axonal damage and demyelination in the mouse corpus callosum. *Magn. Reson. Med.* 55, 302–308. doi: 10.1002/mrm.20774

Taylor, L. C., Gilmore, W., Ting, J. P. Y., and Matsushima, G. K. (2010). Cuprizone induces similar demyelination in male and female C57BL/6 mice and results in disruption of the estrous cycle. *J. Neurosci. Res.* 88, 391–402. doi: 10.1002/jnr.22215

Thiessen, J. D., Zhang, Y., Zhang, H., Wang, L., Buist, R., Bigio, M. R. D., et al. (2013). Quantitative MRI and ultrastructural examination of the cuprizone mouse model of demyelination. *NMR Biomed.* 26, 1562–1581. doi: 10.1002/nbm.2992

Varma, G., Duhamel, G., de Bazelaire, C., and Alsop, D. C. (2015). Magnetization transfer from inhomogeneously broadened lines: a potential marker for myelin: magnetization transfer from inhomogeneously broadened lines. *Magn. Reson. Med.* 73, 614–622. doi: 10.1002/mrm.25174

Wang, N., Zhuang, J., Wei, H., Dibb, R., Qi, Y., Liu, C., et al. (2019). Probing demyelination and remyelination of the cuprizone mouse model using multimodality MRI. *J. Magn. Reson. Imaging.* 2019, 1852–1865. doi: 10.1002/jmri.26758

Wang, Y., Wang, Q., Haldar, J. P., Yeh, F. C., Xie, M., Sun, P., et al. (2011). Quantification of increased cellularity during inflammatory demyelination. *Brain* 134, 3590–3601. doi: 10.1093/brain/awr307

Wilhelm, M. J., Ong, H. H., Wehrli, S. L., Li, C., Tsai, P. H., Hackney, D. B., et al. (2012). Direct magnetic resonance detection of myelin and prospects for quantitative imaging of myelin density. *Proc. Natl. Acad. Sci. U. S. A.* 109, 9605–9610. doi: 10.1073/pnas.1115107109

Wood, T. C., Simmons, C., Hurley, S. A., Vernon, A. C., Torres, J., Dell'Acqua, F., et al. (2016). Whole-brain *ex-vivo* quantitative MRI of the cuprizone mouse model. *PeerJ* 4:2632. doi: 10.7717/peerj.2632

Xie, M., Tobin, J. E., Budde, M. D., Chen, C. I., Trinkaus, K., Cross, A. H., et al. (2010). Rostrocaudal analysis of corpus callosum demyelination and axon damage across disease stages refines diffusion tensor imaging correlations with pathological features. *J. Neuropathol. Exp. Neurol.* 69, 704–716. doi: 10.1097/NEN.0b013e3181e3de90

Yang, H. J., Wang, H., Zhang, Y., Xiao, L., Clough, R. W., Browning, R., et al. (2009). Region-specific susceptibilities to cuprizone-induced lesions in the mouse forebrain: Implications for the pathophysiology of schizophrenia. *Brain Res.* 1270(Suppl.C), 121–130. doi: 10.1016/j.brainres.2009.03.011

Young, K. M., Psachoulia, K., Tripathi, R. B., Dunn, S-J., Cossell, L., Attwell, D., et al. (2013). Oligodendrocyte dynamics in the healthy adult CNS: evidence for myelin remodeling. *Neuron* 77, 873–885. doi: 10.1016/j.neuron.2013.01.006

Zaaraoui, W., Deloire, M., Merle, M., Girard, C., Raffard, G., Biran, M., et al. (2008). Monitoring demyelination and remyelination by magnetization transfer imaging in the mouse brain at 9.4 T. *Magn. Reson. Mater. Phys. Biol. Med.* 21, 357–362. doi: 10.1007/s10334-008-0141-3

frontiers | Frontiers in Neuroscience

TYPE Brief Research Report
PUBLISHED 19 July 2024
DOI 10.3389/fnins.2024.1366029

OPEN ACCESS

EDITED BY
Vince D. Calhoun,
Georgia State University, United States

REVIEWED BY
Mark Wagshul,
Albert Einstein College of Medicine,
United States
Diego Iacono,
Neuropathology & Neurology Research,
Neurodevelopmental and
Rare CNS Disorders,
Biomedical Research Institute of New Jersey
(BRInj) and MidAtlantic Neonatology
Associates, Atlantic Health System,
United States

*CORRESPONDENCE
Martina Del Giovane
✉ m.del-giovane@imperial.ac.uk

RECEIVED 05 January 2024
ACCEPTED 28 June 2024
PUBLISHED 19 July 2024

CITATION
Del Giovane M, David MCB, Kolanko MA, Gontsarova A, Parker T, Hampshire A, Sharp DJ, Malhotra PA and Carswell C (2024) Methodological challenges of measuring brain volumes and cortical thickness in idiopathic normal pressure hydrocephalus with a surface-based approach.
Front. Neurosci. 18:1366029.
doi: 10.3389/fnins.2024.1366029

Methodological challenges of measuring brain volumes and cortical thickness in idiopathic normal pressure hydrocephalus with a surface-based approach

Martina Del Giovane[1,2]*, Michael C. B. David[1,2], Magdalena A. Kolanko[1,2], Anastasia Gontsarova[2], Thomas Parker[1,2], Adam Hampshire[2,3], David J. Sharp[1,2], Paresh A. Malhotra[1,2,4] and Christopher Carswell[2,4]

[1]UK Dementia Research Institute, Care Research & Technology Centre, Imperial College and the University of Surrey, London, United Kingdom, [2]Department of Brain Sciences, Imperial College London, London, United Kingdom, [3]Centre for Neuroimaging Sciences, Institute of Psychiatry, Psychology and Neuroscience, King's College London, London, United Kingdom, [4]Department of Neurology, Imperial College Healthcare NHS Trust, London, United Kingdom

Identifying disease-specific imaging features of idiopathic Normal Pressure Hydrocephalus (iNPH) is crucial to develop accurate diagnoses, although the abnormal brain anatomy of patients with iNPH creates challenges in neuroimaging analysis. We quantified cortical thickness and volume using FreeSurfer 7.3.2 in 19 patients with iNPH, 28 patients with Alzheimer's disease (AD), and 30 healthy controls (HC). We noted the frequent need for manual correction of the automated segmentation in iNPH and examined the effect of correction on the results. We identified statistically significant higher proportion of volume changes associated with manual edits in individuals with iNPH compared to both HC and patients with AD. Changes in cortical thickness and volume related to manual correction were also partly correlated with the severity of radiological features of iNPH. We highlight the challenges posed by the abnormal anatomy in iNPH when conducting neuroimaging analysis and emphasise the importance of quality checking and correction in this clinical population.

KEYWORDS

normal pressure hydrocephalus, enlarged ventricles, (NPH), FreeSurfer, brain segmentation, dementia, Alzheimer's disease (AD)

Introduction

Idiopathic Normal Pressure Hydrocephalus (iNPH) is a neurological condition that affects approximately 0.3–3%, of individuals aged 60 and above (Jaraj et al., 2014). It is characterized by alterations in cerebrospinal fluid dynamics, leading to the enlargement of the ventricles to maintain a stable intracranial pressure (Carswell, 2022). A triad of symptoms; gait apraxia, urinary incontinence, and cognitive deficits, result from this compensatory ventricular expansion, which stretches and distorts the surrounding parenchyma (Carswell, 2022). Therapeutic redirection of cerebrospinal fluid to an area of lower pressure (i.e., shunting) can dramatically improve symptoms (Carswell, 2022).

iNPH occurs in the elderly population in which traditional neurodegenerative diseases are common (Jaraj et al., 2014), and identifying iNPH-specific clinical and imaging features is paramount to being able to distinguish these disorders. The anatomical features of iNPH introduce methodological challenges in neuroimaging analysis. Reduced callosal angle, ventriculomegaly, and disproportionately enlarged subarachnoid space hydrocephalus (DESH) are some of such distinctive features of iNPH seen on brain imaging (Hashimoto et al., 2010). Here, we would like to address potential limitations associated with the use of FreeSurfer,[1] a software used for the analysis and visualization of brain imaging data, in this specific patient group.

One notable advantage of FreeSurfer is its ability to employ a fully automated pipeline, enabling the segmentation of the brain into regions of interest. It is freely available, widely used and there is extensive experience within the field in implementing it within analysis pipelines aiding reproducibility. FreeSurfer registers the volume with the MNI305 atlas. It performs a surface-based reconstruction of the cortex, which classifies voxels as either white or non-white matter based on voxel intensity and neighbour constraints, and a volume-based stream for volume labelling of each point (voxel) of the brain mask (Dale et al., 1999; Fischl et al., 2002). It derives the white matter surface as the interface between the white and gray matter, and the pial surface as the boundary between the pial and cerebrospinal fluid (CSF). Cortical thickness and volumes can then be quantified in 34 different regions derived from the Desikan-Killiany atlas. This automated process is considerably less laborious and less prone to bias than manual regions of interest segmentation.

Quality control and manual editing can be performed to rectify errors related to skull stripping, grey-white matter segmentation, and intensity normalization.[2] Several studies have compared the outputs of the FreeSurfer's pipeline with and without manual edits in groups of healthy adults, individuals with genetic disorders, and severe head injuries and found mixed results (McCarthy et al., 2015; Guenette et al., 2018; Waters et al., 2019). There is also limited research investigating the significance of the manual editing step in clinical populations with extremely abnormal brain morphology, which can impact the registration and segmentation analysis stages.

Methods

We evaluated the importance of manually correcting the segmentation output produced by FreeSurfer 7.3.2[3] on the MRI scans of 19 patients with iNPH, 28 patients with Alzheimer's disease, and 30 healthy controls (HC). To improve the readability of the results and reduce multiple comparisons, the 34 regions segmented by FreeSurfer where clustered to derive cortical thickness and volumes for the frontal, temporal, parietal, occipital and cingulate lobes (see Footnote 1). Between-group differences in age and gender were analysed using Kruskal-Wallis test and Chi-Square test, respectively. All scans were visually checked to ensure their quality met appropriate research standards. We then ran the FreeSurfer recon-all command using the -bigventricles flag. Of the 19 iNPH patients, 12 were classified as probable, 4 as possible and 3 as asymptomatic iNPH, as defined by international criteria (Relkin et al., 2005). Among the 16 symptomatic iNPH patients, 15 received a lumbar puncture and had their CSF samples analysed to determine the presence of comorbid AD pathology. Amyloid deposition was detected in two patients. Radiological features of iNPH were assessed and calculated by a neuroradiologist. Participants were scanned on a 3 T Siemens scanner as part of a wider ongoing study run by the UK Dementia Research Institute, Care Research & Technology Centre focused on using sensor technology to monitor behaviours of people living with dementia. We visually inspected each output and performed manual editing when necessary (Figure 1). Wilcoxon signed-ranked tests were used to compare the FreeSurfer's measurements (volumes and cortical thickness) before and after manual edits while accounting for non-normally distributed data. Between-group differences in these changes were assessed via repeated measures ANOVA, followed by two-tailed t-tests with FDR correction for post-hoc comparisons. Finally, exploratory Spearman correlations were conducted between changes in cortical thickness/volumes pre and post manual correction and radiological features of iNPH (i.e., Radscale score, Evan's index, callosal angle and DESH score). To assess the potential for rectifying FreeSurfer's inaccuracies through alternative pre-processing software, we conducted two additional evaluations. First, we integrated the HD-BET tool for skull stripping before executing the FreeSurfer recon-all command. Notably, HD-BET has exhibited superior performance compared to various widely used brain extraction algorithms, even in the presence of brain pathology (Isensee et al., 2019). Additionally, we experimented with running the FreeSurfer recon-all command using a combination of T1 and FLAIR scans.[4]

This study was approved by the Health Research Authority's London-Surrey Borders Research Ethics Committee (19/LO/0102) and the Health Research Authority's London-Central Research Ethics Committee (18/LO/0249). All participants gave written and/or electronic consent.

Results

HC (14 females, mean age = 75.58 years, SD = 6.07), AD patients (12 females, mean age 75.25 years, SD = 7.64 years) and NPH patients (7 females, mean age = 71.58 years, SD = 5.92 years) did not differ significantly in terms of gender. No significant age difference was found between HC and AD patients. Conversely, iNPH participants were significantly younger than AD and HC ($p = 0.01$). The iNPH patients had a mean Evan's Index of 0.38 (SD = 0.04), mean callosal angle of 75.7 (SD = 15.83), mean Radscale score of 9.3 (SD = 1.51) and mean DESH score of 7.06 (SD = 1.77). Out of the 19 scans of patients with iNPH, 3 failed the segmentation step (Figure 2) and 15 required extensive manual corrections (Figure 1). Of the 3 patients whose Freesurfer segmentation failed, 2 were asymptomatic. Of the 28 patients with Alzheimer's disease, one failed the segmentation and 4 required manual corrections. In the HC group, only 2 participants needed manual editing of the segmentation output. No corrections of the white matter surface were required in any study group. In the iNPH group, manual edits aimed to improve the removal of skull and rectify inaccuracies in defining the pial surface, which had extended into the dura and skull. Following manual correction, the parietal, frontal and temporal regions exhibited the most substantial differences; with volume and cortical thickness measures decreasing bilaterally across the group (Table 1). Wilcoxon signed-ranked tests

---

[1] http://surfer.nmr.mgh.harvard.edu/

[2] https://surfer.nmr.mgh.harvard.edu/fswiki/FsTutorial/TroubleshootingData

[3] https://surfer.nmr.mgh.harvard.edu/fswiki/CorticalParcellation

[4] https://surfer.nmr.mgh.harvard.edu/fswiki/recon-all#UsingT2orFLAIRdatatoimprovepialsurfaces

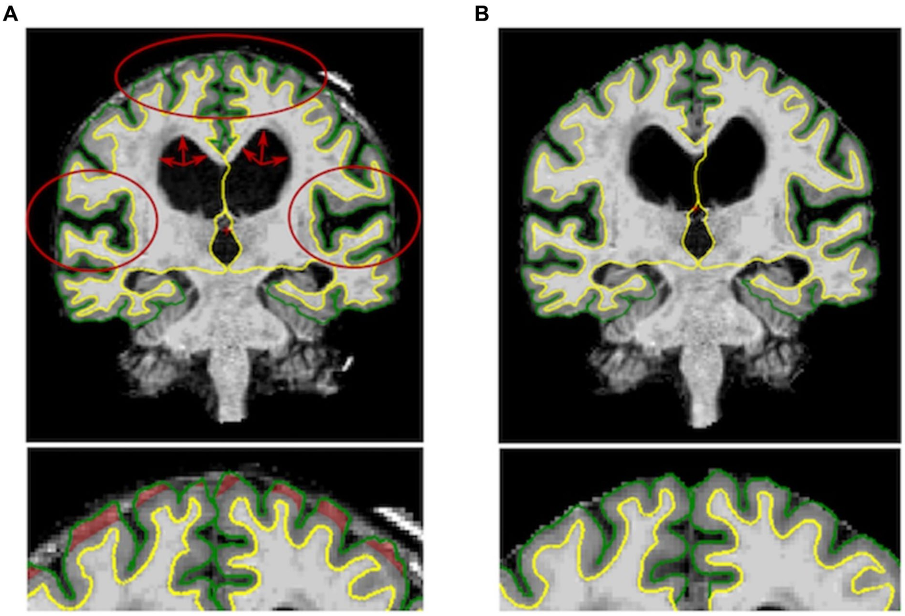

FIGURE 1
Left: Output of the Freesurfer's recon-all command before the manual editing step for one subject. DESH features (i.e., enlarged ventricles, widened sylvian fissure and tight high convexity) are marked in red. **Right**: Output of the manual editing step for the same subject showing reduced cortical thickness..

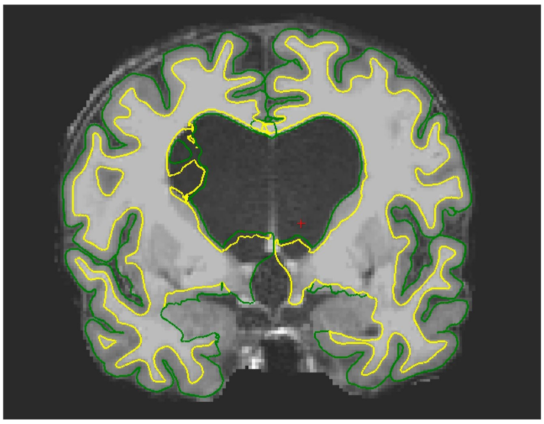

FIGURE 2
Example of failed segmentation for one iNPH patient. Due to the presence of oedema, the pial and white matter surface are wrongly estimated around the ventricles and extend into the CSF space.

comparing these measurements before and after manual edits did not reach significance, although we may have been underpowered by small participants' number. Repeated measures ANOVA indicated an effect of group on the delta values of the volumes ($F_{(19,630)} = 2.84$, $p < 0.001$), but not cortical thickness ($p > 0.05$), which suggest potential higher reliability of this measure relative to volumes. Between group differences were observed for the delta values of the frontal, parietal, temporal and cingulate volumes (Table 1). In Supplementary Table S1, we also report the differences in cortical thickness and volumes before and after manual correction for all the 34 individual regions segmented by FreeSurfer and the between-group comparisons of the delta values.

Spearman correlations showed that, in the left and right temporal lobe, cortical thickness changes significantly correlated with the Radscale score (rho = 0.61/60, $p = 0.01$), and the left temporal lobe volume also correlated with the callosal angle in isolation (rho = −0.53, $p = 0.03$). We also found a significant correlation between DESH scores and the change in volume of the right occipital lobe (rho = −0.51, $p = 0.04$).

The additional evaluations of FreeSurfer's accuracy using HD BET in the pre-processing step revealed 7 segmentation failures and the necessity of multiple manual edits in 11 scans. Similarly, employing a combination of FLAIR and T1 images also led to seven segmentation failures and required manual corrections in five outputs.

Discussion

The higher proportion of scans requiring correction within our sample of iNPH patients relative to the AD and HC groups underlines the importance of conducting and reporting this quality check in this group – which is not consistently done (Cogswell et al., 2021).

Whilst we acknowledge that the overall effect of the correction in these data is minor, it is important to note that this is a relatively small sample size and that we employed a conservative manual correction approach to mitigate the risk of bias associated with human judgement; the effect of this correction process might become substantial enough to influence results significantly when conducting larger studies. Our findings also reveal a statistically higher proportion of volume alterations attributed to manual edits in individuals with iNPH compared to both healthy controls and patients with AD. Changes in cortical thickness were in part correlated with the severity of radiological features of iNPH and underline the importance of exercising caution when using FreeSurfer with severe hydrocephalus. It is important to underline that one significant limitation of this study is the subjectivity of the visual inspections and manual corrections, which are prone to human error. However, we have followed the methodology and guidelines provided by

TABLE 1 Values of cortical thickness and volumes before and after manual correction for the 5 main lobes (left and right), and between-group comparisons of the delta values (FDR corrected).

Region	Group	Volume (mm^3)							Cortical Thickness (mm)						
		Pre correction		Post correction		Delta			Pre correction		Post correction		Delta		
		Mean	std	Mean	std	Mean	std	Group differences of delta	Mean	std	Mean	std	Mean	std	Group differences of delta
Frontal Right	iNPH	27982.59	32251.94	27484.46	31659.98	498.13	889.84	iNPH>AD** iNPH>HC ***	26.52	0.96	26.40	0.89	0.13	0.17	all $p > 0.05$
	AD	72282.74	9094.58	72247.37	9055.27	35.37	202.31		26.01	1.15	26.00	1.16	0.00	0.04	
	HC	77633.17	8287.50	77620.77	8295.22	12.40	47.48		26.32	1.13	26.42	1.18	−0.10	0.72	
Parietal Right	iNPH	23787.64	20635.75	23445.83	20257.78	341.81	706.61	iNPH>AD** iNPH>HC **	11.63	0.57	11.55	0.58	0.08	0.16	all $p > 0.05$
	AD	48385.96	6646.78	48353.67	6666.74	32.30	194.25		10.66	0.56	10.65	0.57	0.01	0.03	
	HC	52999.70	6776.29	52969.13	6758.55	30.57	138.82		11.13	0.53	11.09	0.60	0.04	0.24	
Temporal Right	iNPH	18742.05	20548.49	18548.28	20318.95	193.76	461.20	iNPH>HC*	24.29	1.29	24.15	1.30	0.13	0.35	all $p > 0.05$
	AD	44192.44	6443.66	44122.67	6435.27	69.78	211.15		22.82	1.50	22.83	1.47	0.00	0.06	
	HC	50096.23	5268.73	50099.43	5271.93	−3.20	35.51		24.75	1.01	24.39	1.74	0.36	1.39	
Occipital Right	iNPH	7150.50	4793.46	7164.83	4872.66	−14.33	191.05	all $p > 0.05$	7.86	0.46	7.80	0.49	0.06	0.18	all $p > 0.05$
	AD	24471.63	4030.69	24437.26	4048.02	34.37	165.71		7.69	0.33	7.68	0.34	0.00	0.05	
	HC	25645.37	3492.30	25643.50	3491.76	1.87	18.49		7.78	0.29	7.76	0.31	0.02	0.08	
Cingulate Right	iNPH	3379.86	2485.74	3295.53	2465.91	84.33	234.82	iNPH>AD* iNPH>HC *	8.98	0.45	9.01	0.45	−0.02	0.25	all $p > 0.05$
	AD	8382.74	1091.51	8379.07	1074.23	3.67	46.02		9.24	0.62	9.21	0.62	0.03	0.11	
	HC	8789.83	1348.99	8788.03	1351.10	1.80	12.32		9.35	0.57	9.43	0.54	−0.08	0.30	
Frontal Left	iNPH	28596.39	33052.43	28126.09	32465.30	470.30	989.51	iNPH>HC*	26.63	0.74	26.52	0.73	0.12	0.08	all $p > 0.05$
	AD	72453.30	9273.70	72371.37	9155.49	81.93	545.67		25.88	1.34	25.87	1.33	0.01	0.10	
	HC	77708.63	8387.38	77694.00	8392.59	14.63	72.29		26.66	1.14	26.79	1.18	−0.12	0.68	
Parietal Left	iNPH	24024.05	21592.56	23551.29	21031.64	472.76	1414.00	iNPH>HC*	11.82	0.49	11.77	0.48	0.05	0.06	all $p > 0.05$
	AD	46883.11	7368.76	46790.07	7290.69	93.04	316.13		10.55	0.61	10.54	0.60	0.01	0.02	
	HC	52576.80	6192.32	52563.13	6199.92	13.67	54.74		11.12	0.46	11.08	0.52	0.04	0.20	
Temporal Left	iNPH	18552.15	20247.22	18508.36	20237.00	43.78	163.17	all $p > 0.05$	23.78	1.37	23.70	1.35	0.08	0.07	all $p > 0.05$
	AD	43225.59	7460.71	43214.41	7450.57	11.19	78.14		22.45	1.71	22.45	1.70	0.00	0.06	
	HC	50498.93	5080.39	50501.70	5069.62	−2.77	55.24		24.47	1.08	24.11	1.81	0.37	1.44	
Occipital Left	iNPH	6968.31	4692.93	6921.50	4736.47	46.81	190.65	all $p > 0.05$	7.70	0.42	7.70	0.41	0.00	0.03	all $p > 0.05$
	AD	21937.30	3412.64	21891.44	3420.34	45.85	197.02		7.40	0.33	7.40	0.33	0.01	0.04	
	HC	23544.13	2652.42	23538.57	2654.60	5.57	23.25		7.58	0.30	7.58	0.35	−0.01	0.15	
Cingulate Left	iNPH	3539.31	2722.25	3469.56	2687.10	69.75	136.51	iNPH>AD* iNPH>HC*	9.09	0.52	9.08	0.55	0.00	0.14	all $p > 0.05$
	AD	8864.07	1590.36	8845.22	1581.45	18.85	64.79		9.24	0.65	9.24	0.65	0.00	0.05	
	HC	9556.57	1501.67	9552.33	1504.06	4.23	17.66		9.41	0.45	9.49	0.50	−0.07	0.29	

Delta values for each group have been calculated averaging the difference between pre and post cortical thickness and volume values for each subject. $^*p \leq 0.05$, $^{**}p \leq 0.01$, $^{***}p \leq 0.0001$.

the developers to mitigate bias and maximise consistency in our approach.[5]

The challenge for the field lies in establishing brain biomarkers that can differentiate between iNPH and other dementia types with overlapping clinical presentations and radiological features, such as ventriculomegaly, in order to identify patients to target with therapeutic shunting. Previous studies have demonstrated abnormal cortical thickening in the parietal lobe, and in the high convexity of the frontal, parietal, and occipital lobes in iNPH patients compared to healthy individuals and patients with Alzheimer's disease (Moore et al., 2012; Kang et al., 2020; Bianco et al., 2022). Studies have suggested that cortical thickening may be characteristic of iNPH and related to the ventricular expansion, which leads to compression and stretching of the brain tissue, which may then reduce the cerebrospinal fluid space in the high convexity regions (Kang et al., 2020; Han et al., 2022). We cautiously suggest that increased cortical thickness and tightness of the high-convexity space increase the likelihood of FreeSurfer failing to delineate the pia from the dura and hence erroneously classifying extra voxels to grey matter. If not corrected, these inaccuracies may provide even further and exaggerate evidence of increased cortical thickness and volumes in these areas. Interestingly, segmentation errors did not affect the white matter surface. FreeSurfer's failures seems to specifically impact the delineation of the pial surface. Since this is measured as the interface between the pial and the CSF, these inaccuracies could arise from the reduced CSF space and the tight high-convexity regions resulting from ventricular expansion.

In light of the challenges discussed above, we propose that researchers consider the likely lengthy process of manual correction that is required when using FreeSurfer in this clinical group and encourage the reporting of the completion of this step so that readers can have confidence in any associated results. However, there is a need for further, large-scale iNPH studies to reliably identify disease-specific biomarkers. In this case, conducting laborious manual corrections which can take several hours per subject (Lotan et al., 2022) may be unfeasible and introduce the likelihood of bias, especially given the challenges in blinding raters to the clinical group each scan comes from, given such apparent structural abnormalities.

With this in mind, alternative automatised software and analysis techniques with superior accuracy have been developed and may be preferential (Carass et al., 2017; Shao et al., 2019; Billot et al., 2023). Nevertheless, as shown above, FreeSurfer is still being widely used in current studies. This may be due to some limitations of these alternative tools. These in fact do not always provide segmentation of the individual compartments of the ventricles or are validated in small subsamples of iNPH patients (Shiee et al., 2011; Roy et al., 2015; Shao et al., 2019), do not improve the required processing time relative to FreeSurfer (Ellingsen et al., 2016), are not always freely available (Shao et al., 2019) or easily accessible as FreeSurfer (Ellingsen et al., 2016), or need manual delineation of new atlases when employed with new scanners (Roy et al., 2015).

Data availability statement

The raw data supporting the conclusions of this article will be made available by the authors upon reasonable request.

Ethics statement

The studies involving humans were approved by the Health Research Authority's London-Surrey Borders Research Ethics Committee (19/LO/0102) and the Health Research Authority's London-Central Research Ethics Committee (18/LO/0249). All participants gave written and/or electronic consent. The studies were conducted in accordance with the local legislation and institutional requirements. The participants provided their written informed consent to participate in this study.

Author contributions

MG: Conceptualization, Data curation, Formal analysis, Investigation, Methodology, Project administration, Writing – original draft, Writing – review & editing, Visualization. MD: Data curation, Visualization, Writing – review & editing, Resources. MK: Data curation, Writing – review & editing, Resources. AG: Data curation, Writing – review & editing, Investigation, Resources. TP: Supervision, Writing – review & editing, Methodology. AH: Supervision, Writing – review & editing. DS: Supervision, Writing – review & editing, Funding acquisition, Resources. PM: Conceptualization, Investigation, Supervision, Writing – review & editing. CC: Conceptualization, Investigation, Methodology, Project administration, Resources, Supervision, Writing – original draft.

Funding

The author(s) declare that financial support was received for the research, authorship, and/or publication of this article. This work was supported by UK Dementia Research Institute and the Alzheimer's society DRI-CORE2020-CRT. DS reports grants from NIHR Invention for innovation (i4i) (II-LB-0715-20006). CC reports grants from Medical Research Council (PA1804).

Conflict of interest

The authors declare that the research was conducted in the absence of any commercial or financial relationships that could be construed as a potential conflict of interest.

The handling editor VC declared a past co-authorship with the author DS.

Publisher's note

Supplementary material

The Supplementary material for this article can be found online at: https://www.frontiersin.org/articles/10.3389/fnins.2024.1366029/full#supplementary-material

---

[5] https://surfer.nmr.mgh.harvard.edu/fswiki/FsTutorial/PialEditsV6.0

References

Bianco, M. G., Quattrone, A., Sarica, A., Vescio, B., Buonocore, J., Vaccaro, M. G., et al. (2022). Cortical atrophy distinguishes idiopathic normal-pressure hydrocephalus from progressive supranuclear palsy: a machine learning approach. *Parkinsonism Relat. Disord.* 103, 7–14. doi: 10.1016/j.parkreldis.2022.08.007

Billot, B., Greve, D. N., Puonti, O., Thielscher, A., Van Leemput, K., Fischl, B., et al. (2023). SynthSeg: segmentation of brain MRI scans of any contrast and resolution without retraining. *Med. Image Anal.* 86:102789. doi: 10.1016/j.media.2023.102789

Carass, A., Shao, M., Li, X., Dewey, B. E., Blitz, A. M., Roy, S., et al. (2017). Whole brain Parcellation with pathology: validation on Ventriculomegaly patients. *Patch Based Tech. Med. Imaging*, 10530:20–28. doi: 10.1007/978-3-319-67434-6_3

Carswell, C. (2022). Idiopathic normal pressure hydrocephalus: historical context and a contemporary guide. *Pract. Neurol.* 23, 15–22. doi: 10.1136/pn-2021-003291

Cogswell, P. M., Weigand, S. D., Wiste, H. J., Gunter, J. L., Graff-Radford, J., Jones, D. T., et al. (2021). CSF dynamics as a predictor of cognitive progression. *NeuroImage* 232:117899. doi: 10.1016/j.neuroimage.2021.117899

Dale, A. M., Fischl, B., and Sereno, M. I. (1999). Cortical surface-based analysis. *NeuroImage* 9, 179–194. doi: 10.1006/nimg.1998.0395

Ellingsen, L. M., Roy, S., Carass, A., Blitz, A. M., Pham, D. L., and Prince, J. L. (2016). "Segmentation and labeling of the ventricular system in normal pressure hydrocephalus using patch-based tissue classification and multi-atlas labeling" Proc. SPIE Int. Soc. Opt. Eng. 9784:97840G. doi: 10.1117/12.2216511

Fischl, B., Salat, D. H., Busa, E., Albert, M., Dieterich, M., Haselgrove, C., et al. (2002). Whole brain segmentation. *Neuron* 33, 341–355. doi: 10.1016/S0896-6273(02)00569-X

Guenette, J. P., Stern, R. A., Tripodis, Y., Chua, A. S., Schultz, V., Sydnor, V. J., et al. (2018). Automated versus manual segmentation of brain region volumes in former football players. *Neuroimage Clin.* 18, 888–896. doi: 10.1016/j.nicl.2018.03.026

Han, J., Kim, M. N., Lee, H. W., Jeong, S. Y., Lee, S. W., Yoon, U., et al. (2022). Distinct volumetric features of cerebrospinal fluid distribution in idiopathic normal-pressure hydrocephalus and Alzheimer's disease. *Fluids Barriers CNS* 19:66. doi: 10.1186/s12987-022-00362-8

Hashimoto, M., Ishikawa, M., Mori, E., and Kuwana, N. (2010). Diagnosis of idiopathic normal pressure hydrocephalus is supported by MRI-based scheme: a prospective cohort study. *Cerebrospinal Fluid Res.* 7:18. doi: 10.1186/1743-8454-7-18

Isensee, F., Schell, M., Pflueger, I., Brugnara, G., Bonekamp, D., Neuberger, U., et al. (2019). Automated brain extraction of multisequence MRI using artificial neural networks. *Hum. Brain Mapp.* 40, 4952–4964. doi: 10.1002/hbm.24750

Jaraj, D., Rabiei, K., Marlow, T., Jensen, C., Skoog, I., and Wikkelso, C. (2014). Prevalence of idiopathic normal-pressure hydrocephalus. *Neurology* 82, 1449–1454. doi: 10.1212/WNL.0000000000000342

Kang, K., Han, J., Lee, S. W., Jeong, S. Y., Lim, Y. H., Lee, J. M., et al. (2020). Abnormal cortical thickening and thinning in idiopathic normal-pressure hydrocephalus. *Sci. Rep.* 10:21213. doi: 10.1038/s41598-020-78067-x

Lotan, E., Damadian, B. E., Rusinek, H., Griffin, M., Ades-Aron, B., Lu, N., et al. (2022). Quantitative imaging features predict spinal tap response in normal pressure hydrocephalus. *Neuroradiology* 64, 473–481. doi: 10.1007/s00234-021-02782-z

McCarthy, C. S., Ramprashad, A., Thompson, C., Botti, J. A., Coman, I. L., and Kates, W. R. (2015). A comparison of FreeSurfer-generated data with and without manual intervention. *Front. Neurosci.* 9:9. doi: 10.3389/fnins.2015.00379

Moore, D. W., Kovanlikaya, I., Heier, L. A., Raj, A., Huang, C., Chu, K. W., et al. (2012). A pilot study of quantitative MRI measurements of ventricular volume and cortical atrophy for the differential diagnosis of normal pressure hydrocephalus. *Neurol. Res. Int.* 2012, 1–6. doi: 10.1155/2012/718150

Relkin, N., Marmarou, A., Klinge, P., Bergsneider, M., and Black, P. M. (2005). Diagnosing idiopathic Normal-pressure hydrocephalus. *Neurosurgery* 57, S2-4–S2-16. doi: 10.1227/01.NEU.0000168185.29659.C5

Roy, S., He, Q., Sweeney, E., Carass, A., Reich, D. S., Prince, J. L., et al. (2015). Subject-specific sparse dictionary learning for atlas-based brain MRI segmentation. *IEEE J. Biomed. Health Inform.* 19, 1598–1609. doi: 10.1109/JBHI.2015.2439242

Shao, M., Han, S., Carass, A., Li, X., Blitz, A. M., Shin, J., et al. (2019). Brain ventricle parcellation using a deep neural network: application to patients with ventriculomegaly. *Neuroimage Clin.* 23:101871. doi: 10.1016/j.nicl.2019.101871

Shiee, N., Bazin, P. L., Cuzzocreo, J. L., Blitz, A., and Pham, D. L. (2011). Segmentation of brain images using adaptive atlases with application to Ventriculomegaly. *Inf. Process. Med. Imaging*, 22, 1–12. doi: 10.1007/978-3-642-22092-0_1

Waters, A. B., Mace, R. A., Sawyer, K. S., and Gansler, D. A. (2019). Identifying errors in FreeSurfer automated skull stripping and the incremental utility of manual intervention. *Brain Imaging Behav.* 13, 1281–1291. doi: 10.1007/s11682-018-9951-8

Frontiers in Neuroscience

Provides a holistic understanding of brain function from genes to behavior

Part of the most cited neuroscience journal series which explores the brain - from the new eras of causation and anatomical neurosciences to neuroeconomics and neuroenergetics.

Discover the latest Research Topics

See more →

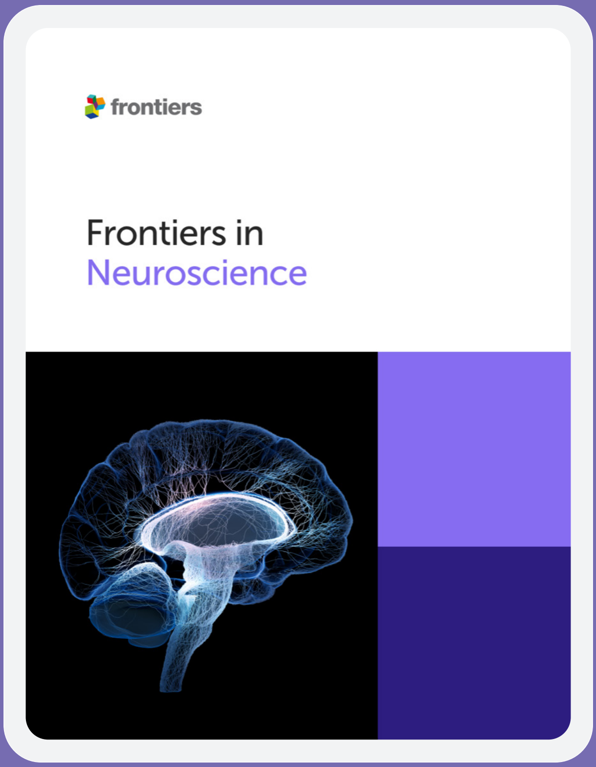

Frontiers

Avenue du Tribunal-Fédéral 34
1005 Lausanne, Switzerland
frontiersin.org

Contact us

+41 (0)21 510 17 00
frontiersin.org/about/contact

frontiers | Research Topics